

**In-situ synthesis of volatile transition-metal carbonyl complexes
produced in nuclear fusion reactions without physical preseparation.**

Dissertation
zur Erlangung des akademischen Grades
Doktor der Naturwissenschaften (Dr. rer. nat.)
im Promotionsfach Chemie

am Fachbereich Chemie, Pharmazie, Geographie und Geowissenschaften
der Johannes Gutenberg Universität Mainz



JOHANNES GUTENBERG
UNIVERSITÄT MAINZ

von
Michael Alexander Götz
geb. in Wiesbaden-Dotzheim

Mainz, 2020

1. Gutachter: -
2. Gutachter: -

Tag der mündlichen Prüfung: 18/03/2022

Table of Contents

Summary	I
Zusammenfassung	IV
<hr/>	
1 Introduction	1
1.1 Transactinide carbonyl chemistry outline	2
1.2 Motivation	5
<hr/>	
2 Theoretical fundamentals	9
2.1 Stability of the heaviest nuclei	9
2.1.1 The Liquid Drop Model (LDM)	9
2.1.2 Shell structure and shell effects	11
2.1.3 The influence of shell deformation	13
2.2 The production of Super Heavy Elements (SHE)	19
2.3 Chemical experiments with SHE	22
2.4 Carbonyl chemistry with transition metals and SHE	24
2.4.1 Bond structure of carbonyl complexes	25
2.4.2 The influence of relativistic effects on the carbonyl bond structure	32
2.5 Investigation techniques	38
2.5.1 Neutron induced fission	38
The neutron induced fission of ^{235}U	40
2.5.2 Monte Carlo Simulation	41
2.5.3 Electronic- and Nuclear Stopping Power	44
<hr/>	
3 Experimental Setup	48
3.1 The research reactor TRIGA Mainz	48
3.1.1 The target chamber at the TRIGA Mainz	50
3.1.2 The target and the target-holder of the TRIGA Mainz	51
3.1.3 The modified target chamber for carbonyl experiments	52
3.1.4 The gas-transport and gas purification system (GPS) at the TRIGA Mainz	54
3.1.5 The modified gas-transport and gas purification system (GPS) for the QMS measurements	56
3.1.6 Charcoal filter and detection system	57
3.2 The JAEA tandem Accelerator facility	58

3.2.1	The target chamber of the JAEA tandem accelerator	60
3.2.2	The gas-transport and gas purification system (GPS) at the JAEA tandem accelerator	63
3.2.3	Charcoal filter and detection system	64
<hr/>		
4	Part I: Analytical studies of 4d transition metal carbonyl complexes at the research reactor TRIGA Mainz	65
4.1	Experimental parameters	65
4.1.1	Direct catch measurements	68
4.1.2	Measurement of reference yield ϵ_{Ref} in a one-chamber approach	69
4.1.3	Measurements of the flush-out efficiency ϵ_{Flush}	70
4.1.4	Measurements of the total efficiency ϵ_{Tot}	71
4.1.5	Measurements to investigate gas purification and CO back diffusion	72
4.2	The reference efficiency ϵ_{Ref}	74
4.2.1	Results	74
4.2.2	Discussion	75
4.3	The flush-out efficiency ϵ_{Flush}	75
4.3.1	Results	76
4.3.2	Discussion	76
	The thermalization efficiency ϵ_{Stop}	77
	The transfer efficiency ϵ_{Diff}	81
	Theoretical modeling the flush-out efficiency ϵ_{Flush}	84
4.4	The overall efficiency ϵ_{Tot}	86
4.4.1	Results	87
4.4.2	Discussion	89
4.5	The investigation of CO back diffusion	90
4.5.1	Results	90
4.5.2	Discussion	92
4.6	The influence of the GPS on the gas purity	93
4.6.1	Results	93
4.6.2	Discussion	95
4.7	Summary of Part I: Carbonyl experiments at the TRIGA Mainz	97
<hr/>		
5	Part II: Analytical studies of 5d transition metal carbonyl complexes at the JAEA tandem accelerator facility	99
5.1	Experimental parameters	99
5.1.1	Isotope production and direct catch measurements	102
5.1.2	Measurements of the flush-out efficiency ϵ_{flush}	102
5.1.3	Measurements of the total efficiency ϵ_{Tot}	104
5.2	The flush-out efficiency ϵ_{Flush}	105
5.2.1	Results	105

5.2.2	Discussion	106
5.3	The overall efficiency ϵ_{Tot}	109
5.3.1	Results	109
5.3.2	Discussion	112
5.4	Summary of Part II: Carbonyl experiments at the Tandem research facility	115
<hr/>		
6	Conclusions and Future studies	117
6.1	Conclusions	117
6.2	Future studies	119
<hr/>		
7	List of Figures and Tables	122
7.1	List of Tables	124
7.2	List of Figures	134
<hr/>		
8	Bibliography	135
<hr/>		
9	Appendix	143
9.1	Python code: Monte Carlo simulation	143
9.2	Specifications gas purification cartridges	152

Summary

The present work describes experiments for the development of a novel concept for the investigation of the in-situ synthesis of transition metal carbonyl complexes. The study of the synthesis of carbonyl complexes using the classical transition metals (elements with a d-subshell that is not completely filled) was also of great importance here in preparation for experiments with superheavy elements. Typically, chemical properties can be derived from the number of electrons in the outermost electron shell of an element, including properties such as ionization energy, electron affinity, how strongly an element interacts with a metal surface, or how the chemical bonding between two reaction partners can be described. At the research reactor TRIGA, the lighter homologs of the transition metals can be produced relatively easily in neutron-induced fission reactions. With the help of these lighter homologs, studies were carried out on the mechanism of carbonyl synthesis with single fission products. The fission products, which were produced when the ^{235}U -target was irradiated with neutrons, were stopped in a gas volume located directly behind the target. The most sensitive step in the carbonyl synthesis was the subsequent purging of the non-volatile transition metal into a second, directly connected reaction chamber. The difficulty was that any collision with a metal surface of the chamber would lead to the loss of the respective fission product, as this would then deposit on the surface or, if sufficient energy was available, even implant. For this purpose, various parameters, such as the pressure in the chamber, the flow velocity of the gases, and the gas composition were investigated or the diameter of the transition channel between the two chambers was examined to obtain an optimized scavenging efficiency. Subsequently, the chemical reactivity with the injected carbon monoxide was investigated as a function of its partial pressure in the gas mixture of the reaction chamber. The various partial efficiencies were determined by positioning filters at different positions in the experimental setup. The overall efficiency was determined hereafter by the subsequent transport of the volatile transition metal-carbonyl complex to a carbon filter directly in front of the detector.

For this experiments, the target chamber of the TRIGA Mainz was modified in a way, that a second chamber could be mounted directly on its exit. This simplified setup was used to investigate the rinsing behavior of non-volatile (transition metal) fission products by mounting a ^{248}Cm source. Then experiments with fission products of ^{235}U were carried out, whereby the formation of the transition metals into their corresponding carbonyl complexes was investigated.

In order to evaluate the data obtained with respect to each of the proposed sub-steps: (a) transport of non-volatile elements from chamber 1 to chamber 2 (b) chemical formation of a carbonyl complex (c) transport of the volatile carbonyl complex to the detector, and to ensure that the data was correctly interpreted, the flush-out process was modeled with the help of a Monte Carlo Simulation based on a simplified microscopic model developed by Zvara, which was combined with TRIM simulation. This procedure allowed a theoretical

estimation of the flush out efficiency. In various measurements an overall efficiency of up to 49(2) % for the transport of ^{101}Mo could be achieved, including the partial efficiencies of $\epsilon_{\text{Flush}} = 57(5) \%$ and $\epsilon_{\text{Chem}} = 83(8) \%$ for the flush-out and the carbonyl complex formation step. It could be shown that both the flush-out- and the carbonyl complex formation step show a strong pressure dependency and that the overall efficiency could be optimized by means of high partial pressures of CO in the gas mixture. In addition, it could be shown, that the length and the shape of the transition piece in between both chambers have a strong influence on the expected yield, since unwanted turbulences and lateral diffusion of the non-volatile fission products will immediately lead to large losses in the flush-out process.

In additional experiments with a quadrupole mass analyser, the back diffusion of carbon monoxide from the second- into the first chamber was investigated. This was particularly important to exclude the process of back diffusion of CO into the TC, whereby volatile carbonyl complexes or mixed carbonyl complexes could distort the measured efficiencies. In this context, the influence of the Gas Purification Systems on the gas purity and the carbonyl complex formation was examined, whereby it could be shown that the oxisorb cartridge has the strongest influence on the complex formation. However, it could not be verified, if there was any reactive species, which was being removed by adding the cartridge into the GPS or whether the presence of oxygen was the reason for higher overall efficiency using the "less purified" gas. Whereby it is most likely the case, that the presence of oxygen will lead to the formation of volatile species with the investigated transition metals, which is disturbing the measurements. The results indicate that the gas-phase synthesis of single transition metal carbonyl complexes is not a hot-atom reaction.

The insights gained during the TRIGA experiments were used in the designing phase of the new target chamber of the JAERI tandem accelerator. In this experiments, a new type of nozzle system was used as the transition between the two chambers, which combines the advantages of a short transition channel with an on both sides conical shape in order to minimize diffusion losses. It could be demonstrated, that with this newly designed two-chamber design the formation of carbonyl complexes with fission products is feasible without physical preseparation. This design maintains a spatial decoupling of beam-environment behind the target and beam-free environment at the site of chemical complex formation, as it was established in the previous studies of carbonyl complexes using the approach of physical preseparation. In these experiments, the successful formation of ^{173}W , $^{175-178}\text{Re}$ and ^{179}Os could be observed, whereby already trace amounts of oxygen impurity in the carrier gas seemed to have a noticeable influence on the carbonyl complex formation. Whereas the yield for $\epsilon_{\text{Tot, Os}}$ was distorted in case of $\text{Os}(\text{CO})_5 \approx 94(10) \%$ by volatile OsO_4 , the opposite effect could be observed in case of $\text{W}(\text{CO})_6$, $\epsilon_{\text{Tot, W}} = 39(6) \%$, by the formation of non-volatile oxides. The successful transport of rhenium carbonyl $\epsilon_{\text{Tot, Re}} \geq 20 \%$ in the $^{nat}\text{Dy}(^{19}\text{F}, 5n)^{175-178}\text{Re}$ reaction indicates the formation of unsaturated 17 valence electron carbonyl complexes, which agrees with theoretical predictions. Despite that radical type

complexes are not common, their existence was reported already in Szilard Chalmers type experiments leading to the formation of radical-type rhenium pentacarbonyl complexes. Moreover, these experiments led to the first successful carbonyl complex formation with fusion evaporation residual nuclei without a physical pre-separation.

Zusammenfassung

Die vorliegende Arbeit beschreibt Experimente zur Entwicklung eines neuartigen Konzepts zur Untersuchung der in-situ-Synthese von 4d- und 5d- Übergangsmetallcarbonylkomplexen. Die Untersuchung der Synthese von Carbonyl Komplexen mithilfe der klassischen Übergangsmetalle (Elemente mit einer nicht vollständig gefüllten d-Unterschale) war hierbei auch für die Vorbereitung zu Experimenten mit superschweren Elementen von grosser Bedeutung. Typischerweise kann man chemische Eigenschaften aus der Anzahl der Elektronen in der äussersten Elektronenschale eines Elementes ableiten, dazu zählen Eigenschaften wie die Ionisierungsenergie, die Elektronenaffinität aber wie stark ein Element mit einer Metalloberfläche interagiert oder wie die chemische Bindung zwischen zwei Reaktionspartnern beschrieben werden kann. Am Forschungsreaktor TRIGA können die leichteren Homologen der Übergangsmetalle relative einfach in neutroneninduzierten Spaltreaktionen produziert werden. Mithilfe dieser leichteren Homologen wurden Untersuchungen zum Mechanismus der Carbonylsynthese mit einzelnen Spaltprodukten durchgeführt. Das Spaltprodukt, welches bei der Bestrahlung von ^{235}U mit Neutronen erzeugt wird, wurde hierzu in einem Gasvolumen gestoppt, welches sich direkt hinter dem Target befand. Der empfindlichste Schritt der Carbonylsynthese war der anschließende Ausspülprozess des nicht flüchtigen Übergangsmetalls in eine zweite, direkt anschließende Reaktionskammer. Die Schwierigkeit bestand darin, dass jegliche Kollision mit einer Metalloberfläche der Kammer zum Verlust des jeweiligen Spaltproduktes führt, da sich dieses dann an der Oberfläche abscheidet oder bei ausreichender Energie, sogar implantiert wird. Hierfür wurden verschiedene Parameter, wie der Druck in der Kammer, die Strömungsgeschwindigkeit der Gase und auch die Gaszusammensetzung untersucht oder der Durchmesser des Übergangskanals zwischen den beiden Kammern untersucht, um eine optimierte Ausspüreffizienz zu erhalten. Im Anschluss wurde die chemische Reaktivität mit dem eingeleiteten Kohlenstoffmonoxid in Abhängigkeit zu seinem Partialdruck im Gasgemisch der Reaktionskammer untersucht. Durch die Positionierung von Filtern an verschiedenen Positionen im Versuchsaufbau wurden die verschiedenen Teileffizienzen bestimmt. Die Gesamteffizienz wurde hierbei nach dem anschließenden Transport des flüchtigen Übergangsmetall-Carbonylkomplex zu einem Kohlefilter direkt vor dem Detektor bestimmt.

Für diese Experimente wurde die Targetkammer des TRIGA Mainz so modifiziert, dass eine zweite Kammer direkt am Ausgang montiert werden konnte. Dieser vereinfachte Aufbau wurde verwendet, um das Ausspülverhalten nicht flüchtiger (Übergangsmetall-) Spaltprodukte mithilfe einer ^{248}Cm -Quelle zu untersuchen. Anschliessend wurden Experimente mit Spaltprodukten von ^{235}U durchgeführt, wobei die Carbonylkomplexbildung der Übergangsmetalle untersucht wurde.

Um die erhaltenen Daten hinsichtlich der einzelnen Teilschritte: (a) Transport nicht flüchtiger Elemente von Kammer 1 zur Kammer 2 (b) Bildung eines Carbonyl Komplexes (c) Trans-

port des flüchtigen Komplexes zum Detektor, korrekt interpretieren zu können, wurde der Ausspülprozess von der ersten- in die zweite Kammer mit Hilfe einer Monte-Carlo-Simulation modelliert, die auf einem von Zvara entwickelten vereinfachten mikroskopischen Modell basiert, das mit der TRIM-Simulation kombiniert wurde. Dieses Verfahren ermöglichte eine theoretische Abschätzung der Ausspüeffizienz. In verschiedenen Messungen konnte eine Gesamteffizienz von bis zu 49(2) % für den Transport von ^{101}Mo erreicht werden. Dies schliesst die jeweiligen Teileffizienzen von $\epsilon_{\text{Flush}} = 57(5) \%$ und $\epsilon_{\text{Chem}} = 83(8) \%$ für den Ausspül- und den Carbonylkomplexbildungsschritt mit ein. Es konnte gezeigt werden, dass sowohl der Ausspül- als auch der Carbonylkomplexbildungsschritt eine starke Druckabhängigkeit aufweisen und dass die Gesamteffizienz durch hohe CO-Partialdrücke im Gasgemisch optimiert werden kann. Darüber hinaus konnte gezeigt werden, dass die Länge und Form des Übergangsstückes zwischen beiden Kammern einen starken Einfluss auf die erwartete Ausbeute haben, da unerwünschte Turbulenzen und die laterale Diffusion der nichtflüchtigen Spaltprodukte sofort zu großen Verlusten im Ausspülprozess führen.

In weiterführenden Experimenten mit einem Quadrupol-Massenanalysator wurde die Rückdiffusion von Kohlenstoffmonoxid aus der zweiten- in die erste Kammer untersucht. Dies war besonders wichtig um den Prozess der Rückdiffusion von CO in den TC auszuschliessen, wodurch flüchtige Carbonylkomplexe oder gemischte Carbonylkomplexe die gemessenen Effizienzen verfälschen könnten. In diesem Zusammenhang wurde auch der Einfluss des verwendeten Aufreinigungssystems auf die Gasreinheit und die Carbonylkomplexbildung untersucht, wobei gezeigt werden konnte, dass die Oxisorb-Kartusche den stärksten Einfluss auf die Komplexbildung hat. Es konnte jedoch nicht gezeigt werden, ob durch das Hinzufügen der entsprechenden Patrone zum Reinigungssystem eine reaktive Spezies entfernt wurde oder ob die Existenz von Sauerstoff der Grund für eine höhere Gesamteffizienz unter Verwendung des "weniger gereinigtem" Gases war. Wobei es am wahrscheinlichsten ist, dass die Anwesenheit von Sauerstoff zur Bildung flüchtiger Spezies mit den untersuchten Übergangsmetallen führt, welche die Messungen störte. Die Ergebnisse zeigen, dass die Gasphasensynthese von Carbonylkomplexen mit einem Übergangsmetall keine "hot-atom reaction" ist.

Die während der TRIGA-Experimente gewonnenen Erkenntnisse wurden abschliessend für den Entwurf einer neuen Targetkammer für den JAEA-Tandembeschleuniger verwendet. In diesen Experimenten wurde ein neuartiger Typ einer Düse als Übergang zwischen den beiden Kammern verwendet, der die Vorteile eines kurzen Übergangskanals mit einer beidseitig konischen Form kombiniert, um Diffusionsverluste zu minimieren. Es konnte gezeigt werden, dass mit diesem neu entworfenen Zweikammerdesigns die Bildung von Carbonylkomplexen mit Fusionsprodukten ohne physikalische Trennung möglich ist. Dieses Design ermöglicht eine räumliche Entkopplung der Strahlunggebung hinter dem Target und der strahlungsfreien Umgebung am Ort der Bildung chemischer Komplexe bei, wie dies in früheren Studien zu Carbonylkomplexen unter Verwendung des Ansatzes der physikalischen Präparation

genutzt wurde. In diesen Experimenten konnte die erfolgreiche Bildung von ^{173}W , $^{175-178}\text{Re}$ und ^{179}Os beobachtet werden, wobei bereits Spuren von Sauerstoffverunreinigungen im Trägergas zu einem merklichen Einfluss auf die Carbonylkomplexbildung führten. Während die Gesamteffizienz für die Bildung von Osmiumpentacarbonyl $\epsilon_{\text{Tot,Os}}$ bei ungefähr 94(10) % lag und durch flüchtiges OsO_4 zu hohe Ausbeuten verfälscht wurden, wurde der gegenteilige Effekt im Fall von Wolframhexacarbonyl $\epsilon_{\text{Tot,W}} = 39(6) \%$ beobachtet, da die Bildung nichtflüchtiger Oxide zu keinem Transport aus dem Zweikammersystem führt. Der erfolgreiche Transport von Rheniumcarbonyl $\epsilon_{\text{Tot,Re}} \geq 20 \%$ in der $^{nat}\text{Dy}(^{19}\text{F}, 5n)^{175-178}$ Reaktion weist auf die Bildung ungesättigter 17-Valenzelektronen-Carbonylkomplexe hin, was mit theoretischen Vorhersagen übereinstimmt. Obwohl Komplexe vom Radikaltyp nicht üblich sind, wurde ihre Existenz bereits in Experimenten vom Typ Szilard Chalmers berichtet, die zur Bildung von Rheniumpentacarbonylkomplex-Radikalen führten. Darüber hinaus führten diese Experimente zur ersten erfolgreichen Carbonylkomplexbildung mit Fusionsverdampfungsrestkernen ohne eine physikalische Vorseparation.

The periodic table is the basic scheme for ordering the elements by their respective atomic numbers and their associated number of electrons. This leads to elements in a specific group typically exhibiting similar chemical properties. Nevertheless, the predictive power of periodic table is affected by relativistic effects, as they influence the electronic structure of an element and therefore affect trends established by lighter homologs, thus affecting the predictive power of the periodic table [1]. These effects scale with Z^2 and are hence most pronounced in the heaviest elements. The reason for the relativistic effect lies in the mass of the electron, which increases for heavier elements compared to the electron rest mass m_0 , e.g.: $m/m_0 = 1.000027$ for H and exceeds by 10% for elements of the sixth period onward and reaches values of 1.70 for Fl and 1.95 for Og, with v is the velocity of the electron and c the speed of light [2, 3]:

$$m = \frac{m_0}{[1 - (v/c)^2]^{1/2}} \quad (1.1)$$

The relativistic effects can be divided into two categories as shown in Fig. 1.1. As the Z of the heavy elements increases, the stronger attraction causes a faster movement of the electrons around the core and therefore, the resultant mass of the electron increases which leads to a decrease in the effective Bohr radius $a_B = a_B^0 [1 - (v/c)^2]^{1/2}$. This so called direct relativistic effect can be described as an orbital contraction and stabilization of the spherical s and $p_{1/2}$ electrons. This effect goes hand in hand with the indirect relativistic effect, which is the expansion of outer d and f orbitals, which is caused by the more efficient screening of the nuclear charge. Since the electrons, which are sitting in the orbitals far away from the core, will see less positive attraction of the core, these orbitals will expand and destabilize. The third relativistic effect is the spin-orbit splitting of levels with $l > 0$ [3, 4].

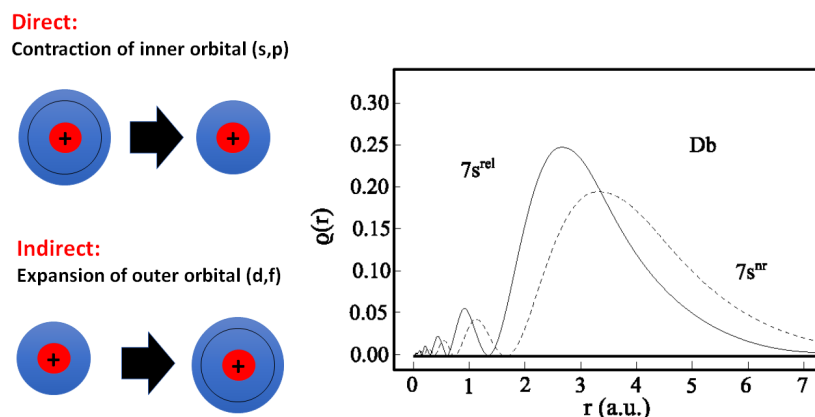


Fig. 1.1: Schematic of the direct and indirect relativistic effect and the influence of the radial distribution of the 7s valence electrons in element 105, Db. The relativistic calculations are shown as solid line, whereas the non-relativistic distribution is shown as dashed line. Figure adapted from [3].

As mentioned before, the relativistic effects are most pronounced in the transactinide elements (elements with atomic number $Z \geq 104$) which can only be produced by nuclear fusion reactions. The synthesis of these "superheavy" elements can be classified as cold fusion or hot fusion, depending on the target-projectile combination, which can result in significantly different excitation energies of the compound nucleus. In these accelerator based experiments, the Coulomb barrier between the two approaching positively charged nuclei has to be overcome, which is the reason for the fused system to carry a certain amount of excitation energy. Typically cold-fusion reactions are characterized by low minimum excitation energies of about 10-15 MeV, whereas hot fusion reactions can be characterized by minimum excitation energies of about 40-50 MeV [3, 5]. Depending on this excitation energy, the compound nucleus has to undergo several neutron-evaporation steps, before the nucleus has finally cooled, whereby this step competes with the predominantly strong nuclear fission process in the deexcitation process, which leads to small production rates. Therefore, the studies of the chemical properties of transactinide elements ($Z \geq 104$) are challenging due to small production rates and short half-lives [6]. Transactinides are produced in nuclear fusion reactions at rates of single atoms per minute, day, or even week, and the typical half-lives are in the range of minutes at most, with very few exceptions [7]. Therefore, studies of the heaviest elements of the periodic table require the development of appropriate methods to isolate single atoms with half-lives of a few seconds at most.

1.1 Transactinide carbonyl chemistry outline

Current fast chemical-isolation procedures are suitable for studies of nuclei with half-lives of about one second or more. Despite of these challenges, basic chemical properties of

many transactinide elements have been studied [6, 8, 9]. For the liquid-phase chemistry experiments, separation of transactinides is typically performed in batch-wise operations [10], coupled with the detection of characteristic α -signals or the spontaneous fission (sf) fragment energy measurements. Chemical studies of transactinides in the aqueous phase has been performed for elements up to seaborgium, Z=106. For heavier, mostly more short-lived elements, gas phase chemistry is still the method of choice. Therefore, gas phase chromatographic approaches have proven especially powerful as they are fast and efficient. Typically, for elements up to hassium volatile and thermally stable inorganic compounds such as halides, oxyhalides, hydroxides, or oxides have been studied [3, 11–13] as shown in Fig. 1.2.

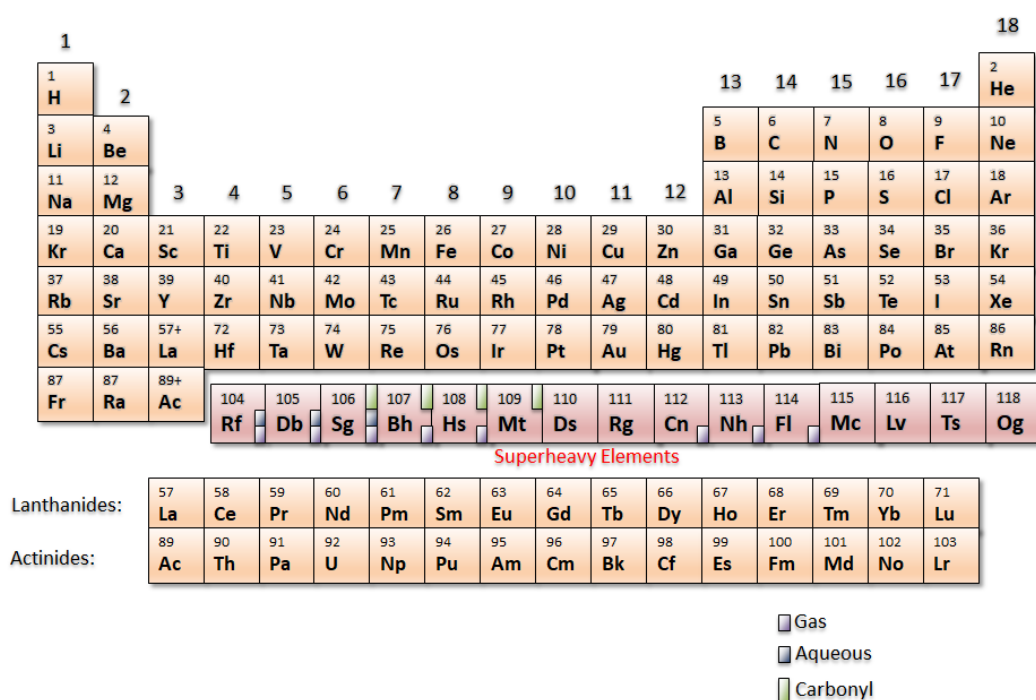


Fig. 1.2: Periodic table of elements. The transactinides (Superheavy elements, $Z < 104$) are shown in red. Elements, for which successful gas- and liquid phase experiments have been performed are indicated by violet and blue boxes. Elements supposed to be accessible with carbonyl experiments are indicated with green boxes.

The production of transactinide carbonyl complexes could diminish the existing gap between element 108 (hassium) and element 112 (copernicium), as for the elements 109 (meitnerium) up to element 111 (roentgenium), no chemical experiments have been performed so far [14]. The accessibility of volatile transition metal carbonyl complexes could be shown by the synthesis of $\text{Mo}(\text{CO})_6$ from the irradiation of a mixture of $\text{Cr}(\text{CO})_6$ and U_3O_8 according to $\text{Cr}(\text{CO})_6 + \text{U}(n,f) \text{ } ^{99}\text{Mo} \rightarrow \text{ } ^{99}\text{Mo}(\text{CO})_6$, which was reported in [15] and described as a Szilard-Chalmers-type reaction. In these kind of reactions, isotopic nuclides produced by nuclear reactions can be separated by chemical methods from the target nuclides due to the

chemical effects of the nuclear reactions, such as changes in the oxidation state or other chemical changes. These kind of reactions are applicable to elements existing in different stable oxidation states or forming substitution-inert complexes. However, experiments with the lighter homologues of the transition metals show that the formation of carbonyl complexes is feasible for elements of group 6 to 9 [16]. In case of transactinide elements, the existence and volatility of such complexes was predicted by theoretical calculations of the molecular properties in e.g.: $M(\text{CO})_4$ ($M = \text{Rh, Ir, Mt}$) with Density Functional Theory (DFT) and Couple-Cluster methods (CCM)[2, 17–20].

Carbonyl complexes of single short-lived transition metal isotopes have become experimentally accessible [21], employing gas phase formation in a carbon-monoxide containing atmosphere. This technique also proved successful in studies of Sg carbonyl complexes [22]. This prompted many follow-up experiments on several d elements. Typically, 4d elements can be produced in nuclear fission processes (thermal neutron induced fission of, e.g., ^{235}U or ^{249}Cf , or spontaneous fission of ^{248}Cm or ^{252}Cf) [21, 23–26], whereas the carbonyl complexes of 5d elements are only available in fusion-evaporation reactions in accelerator-based experiments [27–29]. Isothermal chromatography studies for the interaction of the volatile compounds with a quartz or gold surface were reported by Even et al. [21, 26, 27], Cao et al. [24] and Wang et al. [25], where the formation of volatile carbonyl compounds of several 4d- and 5d-elements, were reported. The thermal decomposition was studied by Usoltsev et al. [30, 31]. Studies on the most stable species in single atom chemistry of group 7 carbonyl complexes deduced from the laser-ablation time-of-flight-mass-spectrometric investigation of $\text{Re}(\text{CO})_5$ were reported in [29]. Theoretical calculations on the properties of single ion carbonyl complexes can be found in the work of Nash et al. [32], Davidson et al. [33], Pershina et al. [34, 35] and Iliáš et al. [17]. The yield of gas phase carbonyl complex formation as a function of different parameters including total gas pressure as well as carbon monoxide partial pressure was studied, indicating that high CO partial pressure is beneficial for high yields. For accelerator-based experiments, the technique of physical preseparation [26, 27, 29, 36] was applied. In this technique, the beam and unwanted side products are removed from the product trajectory inside the physical preseparator. This ensured that the carbon monoxide filled gas-volume is not exposed to the intense heavy-ion beam needed for the production of the isotopes of interest. Experiments, in which no preseparator was employed and carbonyl complex formation was attempted in a recoil gas volume directly behind the target showed substantial decomposition of the carbon monoxide [25, 37]. This is due to the formation of a plasma induced by the beam. The presence of the decomposition products prohibited the study of carbonyl complexes.

1.2 Motivation

The synthesis of carbonyl complexes with transactinide elements in single-atom reactions is a powerful tool to investigate the influence of relativistic effects on the chemical behaviour of these elements [1]. The metal atom in carbonyl complexes typically remains uncharged, whereas the relativistic effects are affecting the chemical bond structure (details see Sec. 2.4). Therefore, the M-CO bond can be used to investigate the influence of relativistic effects on chemical bonding, whereby the σ - and π -bond is directly influenced by these effects (for details see Sec. 2.4.2). The carbonyl complexes of the heaviest elements are solely accessible in nuclear fusion reactions with heavy ion beams. Isotopes with long enough half-lives for chemical studies are produced in hot fusion reactions with comparatively light ion beams and suitable actinide targets. Successful techniques include the thermalization of the nuclear fusion products in a gas-filled recoil chamber behind a physical preseparator [7].

The physical preseparation [36, 38] of the evaporation residues from the primary beam coupled with the subsequent thermalization in a gas-filled volume behind such a recoil separator [39] turned out to be a suitable method for the investigation of more fragile compounds, e.g., carbonyl complexes of transition metals. Nevertheless, such a physical preseparation step comes with some limitations. The evaporation residues of asymmetric fusion reactions (reactions with comparatively light projectiles and heavy targets), as they are employed for the production of comparatively long-lived isotopes of seaborgium and also of bohrium and hassium, have relatively large angular and energy spreads. This leads to a low transmission in a recoil separator. In case of the studies of $\text{Sg}(\text{CO})_6$, which were performed at the GAS-filled Recoil Ion Separator (GARIS) at RIKEN, Wako, Japan, this partial efficiency is on the order of only 13 % for ^{265}Sg produced in the $^{248}\text{Cm} (^{22}\text{Ne}, 5n)^{265}\text{Sg}$ [40] reaction. Consequently, only 18 decay chains attributed to ^{265}Sg were observed in this study in 14 days of beamtime [22], despite the cross section of this reaction being comparatively large, e.g.: $\sigma(^{265}\text{Sg}) = 380_{-70}^{+90}$ pb in the $^{22}\text{Ne} + ^{248}\text{Cm}$ reaction.

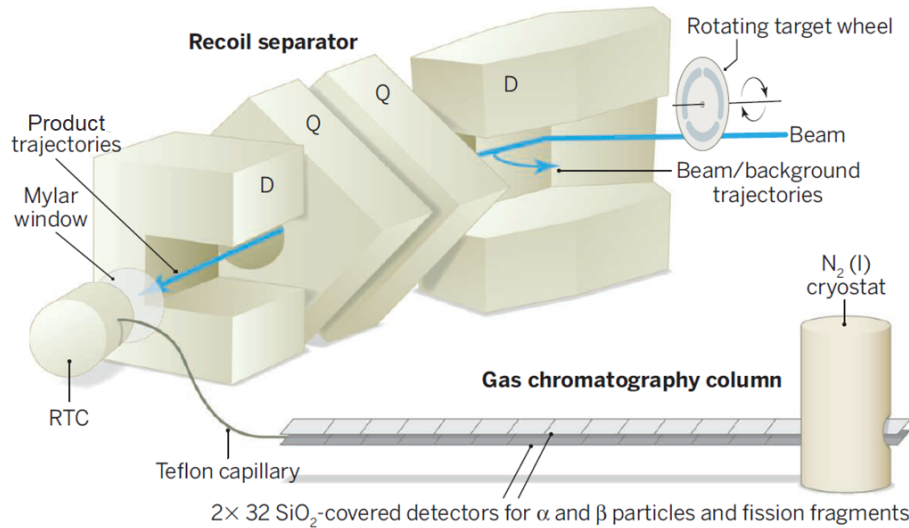


Fig. 1.3: Schematic of the experimental setup used for the $^{248}\text{Cm}(^{22}\text{Ne},5n)^{265}\text{Sg}$ reaction at the recoil separator GARIS at RIKEN. The reaction products are transported through GARIS, and slowed down in the recoil transfer chamber (RTC), where they react with the carbon monoxide. The resulting $\text{Sg}(\text{CO})_6$ products are transported to the thermochromatography apparatus COMPACT for analysis. Picture is taken from [22].

To progress to heavier elements a more efficient concept is highly desirable as production rates for elements beyond Sg fall drastically, as follows from cross sections of $\sigma(^{265}\text{Sg}) = 380_{-70}^{+90}$ pb in the $^{22}\text{Ne} + ^{248}\text{Cm}$ reaction, $\sigma(^{266}\text{Bh}) = 57_{-14}^{+14}$ pb in the $^{23}\text{Na} + ^{248}\text{Cm}$ [41] and 58_{-15}^{+33} pb in the $^{22}\text{Ne} + ^{249}\text{Bk}$ reactions [42] and $\sigma(^{269}\text{Hs}) = 7.0_{-2.8}^{+3.3}$ pb in the $^{26}\text{Mg} + ^{248}\text{Cm}$ reaction [43] and $\sigma(^{270}\text{Hs}) = 16_{-7}^{+13}$ pb in the $^{48}\text{Ca} + ^{226}\text{Ra}$ reaction [44]. The cross sections for $^{248}\text{Cm}(\text{X},5n)$ based nuclear reactions are shown in Fig. 1.4, where the decrease in production cross section is illustrated.

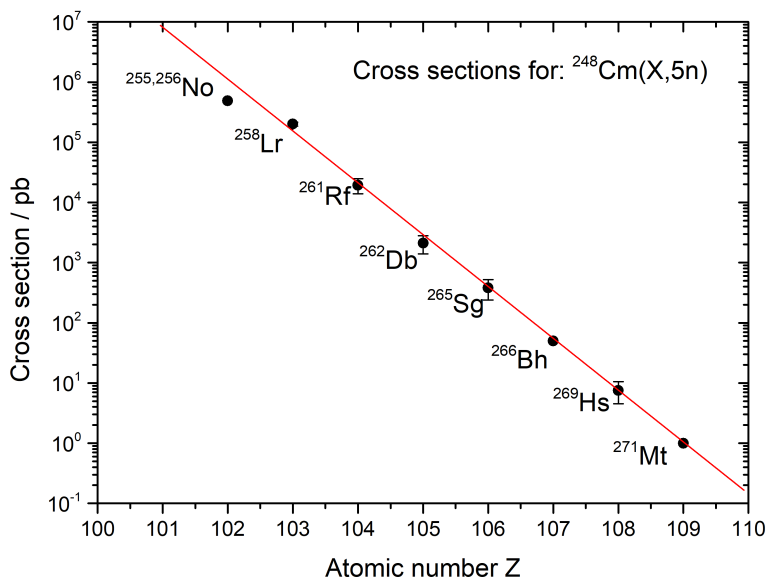


Fig. 1.4: Production cross sections for the $^{248}\text{Cm}(X,5n)$ reactions for the elements nobelium up to meitnerium. Cross sections were taken from references [40, 43, 45–49].

With the cross sections depicted in Fig. 1.4 and estimated efficiencies in a similar range as that for the measured $^{248}\text{Cm}(^{22}\text{Ne},5n)^{265}\text{Sg}$ reaction, the detection rate of $^{266,267}\text{Bh}$ would be expected to be $\lesssim 0.4$ events/day. Therefore, the synthesis of carbonyl complexes beyond seaborgium by the method of physical preseparation can still be feasible but will demand long beamtimes. However, the need of adequate statistics makes a more efficient and less beamtime-demanding concept highly desirable. In this thesis an exploration to find a more efficient way to synthesize carbonyl compounds is described.

The method is based on the spatial decoupling of the evaporation residue production and the subsequent thermalization from the chemical bond formation step. This idea builds up on an approach, which has already been used at FLNR Dubna in the investigation of (oxo)chlorides of group 4-6 elements including Rf, Db and Sg [50–53]. By this method, the very harsh ionizing conditions caused by the highly intense primary beam, which heats up the gas and creates a plasma in the recoil chamber, will be avoided in the carbonyl complex formation step [54].

In this thesis, the performance of a novel concept aimed at superseding the efficiency-limiting component of physical preseparation, using single short-lived radioisotopes of 4d elements obtained as fission fragments, and 5d elements obtained as fusion evaporation products, is described. These experiments reproduce the conditions under beam-influence for the heavier homologues and therefore, they are ideally suited to study the transfer of

the isotopes of interest from the thermalization chamber into the reaction chamber and the formation of volatile carbonyl complexes, thus providing a basic validation of this approach before experiments with transactinide elements are conducted.

2.1 Stability of the heaviest nuclei

Each atomic nucleus consists of neutrons and protons, whereby the atomic core carries more than 99% of the mass of an atom, whereas it only occupies a small fraction ($d_{\text{Nuc}} \approx 10^{-15}$ m) of the atomic volume. Despite their repulsive nature, the protons are held together by strong short-range nuclear cohesive forces. Nevertheless, with an increasing number of protons (Z), the Coulomb repulsion of the protons inside the nucleus will also increase and at a certain number of protons, will exceed the binding energy of a nucleus. This energy is described by the Liquid Drop Model (LDM), which was first proposed by Weizsäcker [55] and Bethe [56].

2.1.1 The Liquid Drop Model (LDM)

In this model, the nucleus is described as a charged droplet of an incompressible liquid of constant density. The phenomenon is analogous to a liquid drop in which the molecules are subjected to the same van der Waals forces, independent of the size of the drop. The semi-empirical mass formula quantifying mass defect or nucleon binding energy is called the WEIZSÄCKER equation shown in Eq. 2.1. In this approach, the nucleon binding energy is described by cohesive and repulsive forces as a derivative of the mass number A and the individual numbers of protons Z and neutrons N responsible for that value of A . The positive contributions to binding energy are depicted in red and negative contributions are depicted in blue:

$$BE(A, Z) = a_v A - a_f A^{2/3} - a_c \frac{Z(Z-1)}{A^{1/3}} - a_s \frac{(A-2Z)^2}{A} \pm E_p \quad (2.1)$$

with

$$E_p = \begin{cases} +E_p & \text{N, Z both even} \\ 0 & \\ -E_p & \text{N, Z both odd} \end{cases} \quad (2.2)$$

The volume energy ($a_v A$) describes the way each nucleon contributes to the binding energy.

Bound nucleons are of lower potential energy compared to the non-bound situation. It can be described as the energy which is gained, whenever a nucleon is getting bound. This energy depends exclusively on A and is according to a direct proportionality. This can be explained by the short range of the nucleon-nucleon interaction, where a nucleus in the interior is only bound to its nearest neighbors resulting in A bindings where the fit parameter a_v is the energy by which each nucleon is bound.

The surface energy ($-a_f A^{2/3}$) considers, that nucleons at the surface are less bound, due to their reduced numbers of direct neighbours, since they do not feel the attractive nuclear force on all sides. The surface of a nucleus is $4\pi R^2$ with $R^2 \sim A^{2/3}$.

The coulomb energy ($-a_c \frac{Z(Z-1)}{A^{1/3}}$) describes the Coulomb repulsion between the positively charged protons. The Coulomb energy of a uniformly charged sphere is proportional to Z^2/R .

The asymmetry energy ($-a_s \frac{(A-2Z)^2}{A}$) comes from a quantum-mechanical origin, which is related to the difference in binding energy of a nucleus with $N \neq Z$ and one with $N = Z$. It reflects the increased stability of nuclei with approximately equal numbers of protons and neutrons. The change in energy required for the transformation of an $N = Z$ into an $N \neq Z$ is $p^2 D = (N - Z)^2 D/4$ with $D \sim 1/A$ to take care of the level spacing, which gets smaller as the total number of nucleons increases.

The pairing energy (E_p) describes the enhanced stability of paired nucleons in an even-even nucleus and the relatively low stability of odd-odd nuclei. It considers the overall spin quantum numbers and that non-paired nucleons contribute to weakening the binding energy [57, 58]. This effect is also reflected in the abundance of stable nuclei in the chart of nuclides, with 158 even-even nuclei, compared to the relatively small number of stable odd-odd nuclei of only 6. The influence of the pairing energy can easily understood by taking a closer look on the β -decay of the isobars with the mass number 64 as shown in Fig. 2.1. There the semiempirical mass equation is written as a function of Z in the form of:

$$BE(A, Z) = aZ^2 + bZ + c \pm \frac{d}{A^{3/4}} \quad (2.3)$$

The binding energy for a fixed mass number, plotted as a function of Z gives two parabola of different energies, where the binding energy is consistently higher for the even-even nuclei [6, 59]. Consequently, the most stable nuclei lie at the bottom of the parabola. Nuclides on the left hand of the parabola are unstable to β^- decay, whereas isobars to the right of the valley of stability are unstable to β^+ emission. The most stable nuclei ^{64}Ni (largest binding energy), shows a positive contribution of (E_p) to the binding energy.

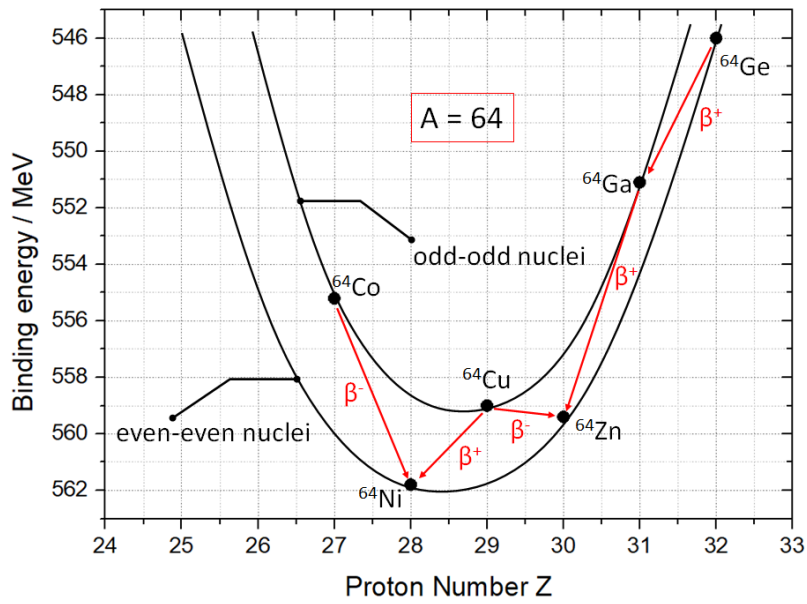


Fig. 2.1: Binding energies and β decays of nuclides with even mass number. ^{64}Ni (even-even), is the minimum of the mass parabola, which undergoes no further decay as a stable nucleus. Data adapted from [10].

2.1.2 Shell structure and shell effects

The overall behaviour of masses and binding energies can be described with the LDM [Sec. 2.1.1](#), whereby the theoretical predictions are correlating well with experimental observations. Nevertheless, at certain numbers of protons or neutrons (2, 8, 20, 28, 50 and 82) differences from calculated LDM values that are most pronounced can be observed as shown in [Fig. 2.2](#). These numbers are typically known as the magic numbers for " Z^{mag} " and " N^{mag} ".

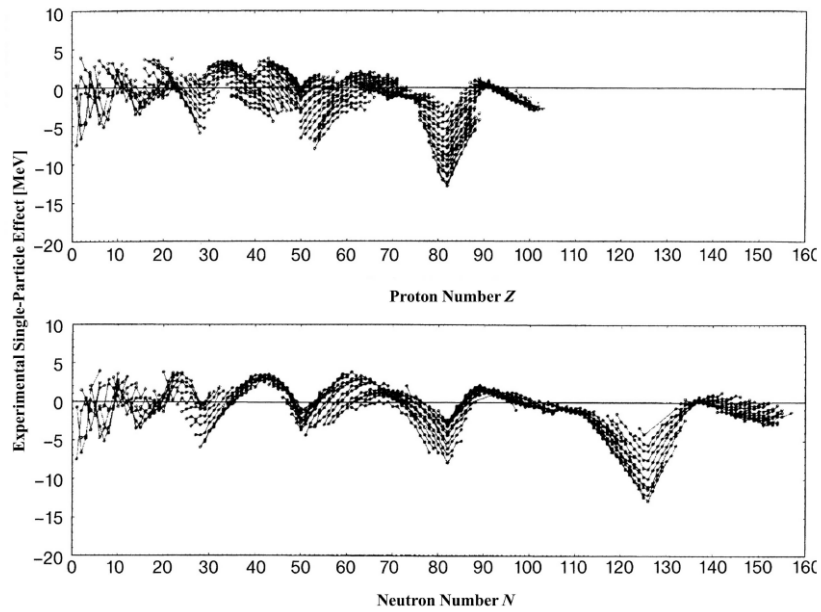


Fig. 2.2: Differences between experimental atomic masses and the LDM drop model masses as a function of their proton (top)- and neutron (bottom) numbers. A noticeable difference is pronounced at the numbers 28, 50, 82 and 126. Picture taken and adapted from [10].

Nuclei with one or even two magic numbers generally show more stable isotopes or isotones compared to non-magic nucleon compositions. The additional binding energy and the enhanced stability of these magic or doubly-magic nuclei can be explained by the nuclear shell model, which considers each nucleon to be moving in a single-particle orbit with the nucleus.

In the shell model, nuclear binding energy has to be considered. Considering the approach of a neutron of low kinetic energy closely approaches a nucleus. Since the uncharged nature of a neutron, it is not affected by the Coulomb field and may approach close to the nucleus without interaction until it is close enough (r_n) to experience a strong attractive force at close ranges which leads to adsorption of the neutron. This adsorption is caused by an attraction from the nearest-neighbour nucleons, which will pull the neutron into the nucleus, as shown in Fig. 2.3. This attraction will increase rapidly in the surface region as the nucleon comes in contact with other nucleons until it is surrounded by nucleons and is in the interior of the nucleus [60]. This decrease in energy is commonly referred as a potential well [57, 61] and the nucleons can occupy different levels in such a potential well.

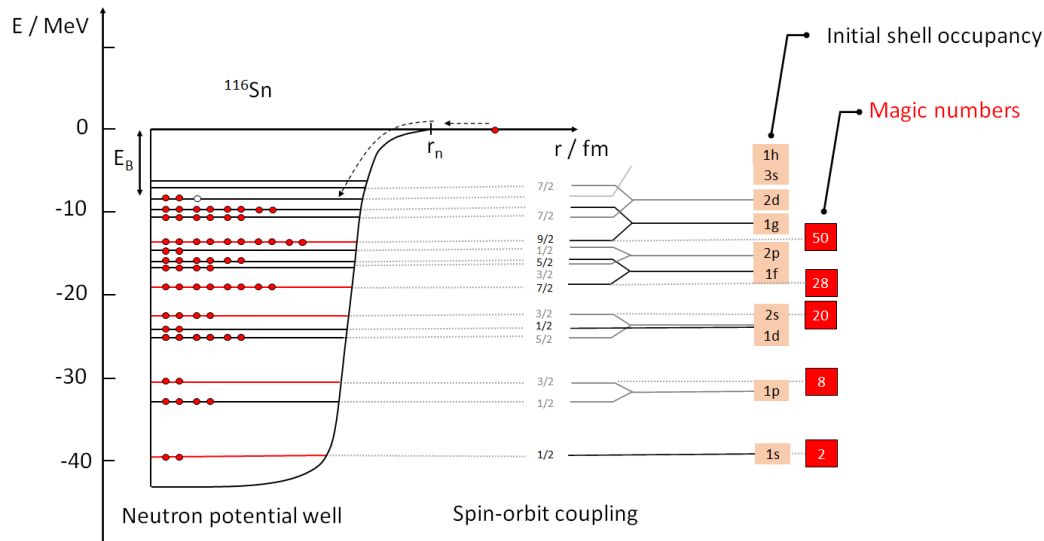


Fig. 2.3: The approach along the x-axis of a neutron (orange) to a ^{116}Sn nucleus. The single-neutron levels in the potential well are indicated. The neutron is trapped at a certain energy level. The distance r_n indicates the range of the cohesive forces at which the approach neutron is adsorbed and pulled inside the potential well. Adapted from [62].

In difference to neutrons, protons experience a strong, long range repulsive nuclear force when they approach at the nucleus due to the Coulomb interaction, which leads to a different behaviour. The nucleus will repel the approaching proton until the proton approaches that closely to the nucleus that the strong attractive forces will exceed the Coulomb repulsion and pull the proton in the potential well. The proton will then be surrounded by nucleons as in the neutron case, but since the proton will always feel a net repulsion from other protons, the proton well will never be as deep as the neutron well. The shape of the potential well can be assumed to be similar to a harmonic oscillator potential which features equally-spaced energy levels. By applying spin-orbit coupling to the harmonic oscillator, the relativistic particles will align their orbital and intrinsic angular momenta (spins), which leads to a further splitting in energy of the given levels according to the alignment of the orbital and the intrinsic spin [63, 64]. With increasing angular momentum number (l) the magnitude of the splitting increases, which leads to the well known energy gaps, see right hand panel in Fig. 2.3. If all shells in between two gaps are filled with nucleons, the nucleon shell can be considered to be filled, which leads to enhanced stability of the nucleus.

2.1.3 The influence of shell deformation

The classical shell model described in Sec. 2.1.2 can be used to describe particles moving in a spherically symmetric central potential. Additional insights were proposed by Strutinsky et al. who proposed a method to extend the harmonic oscillator potential to deformed nuclei [65, 66].

In his model Strutinsky show that shell corrections for a given nucleus must not occur only as a function of nucleon number. Furthermore, shell corrections can also be referred as a function of shell deformation. Indeed, most nuclei are deformed, whereby the energy of the nucleus is minimized by arranging the nucleons in a deformed configuration. In Fig. 2.4 the energies of a deformed harmonic oscillator as a function of the deformation are shown. In the spherical model the gaps for the initial shell occupancy or the basic harmonic oscillator can be seen (cf. Fig. 2.3). Due to deformation, the basic levels are changing their energies and new shell gaps will occur.

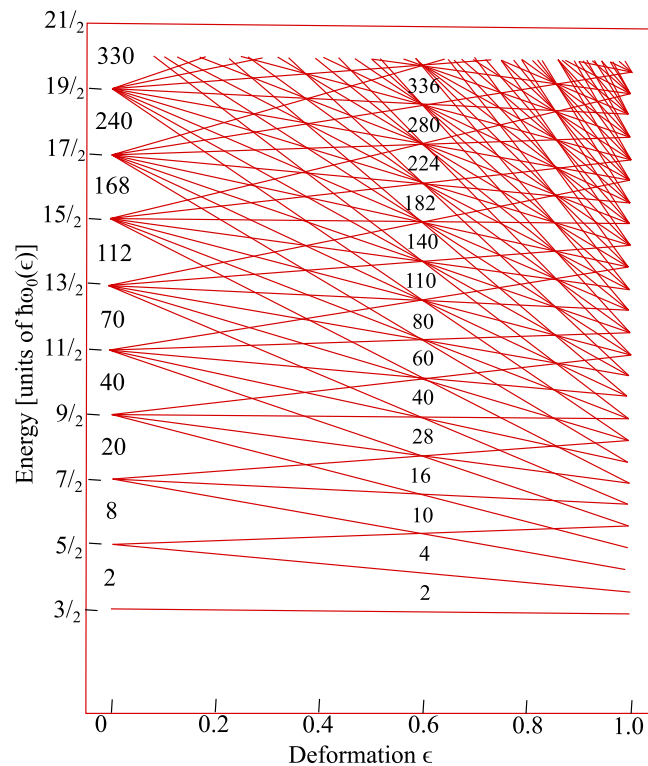


Fig. 2.4: Single-particle levels of a deformed harmonic oscillator as a function of the deformation. The graph is taken from [10].

Whereas the classical (collective) model gives is accurate for even-even nuclei, there is some discrepancy between observed spins and the spin values expected from the single-particle shell model. In the classic model, a nucleon can move freely in a symmetrical potential well, an assumption which is sufficiently accurate for nuclei near closed shells. However, the angular momentum of an odd-numbered (deformed) core is based on both, the angular momentum of the deformed core and of the odd nucleon and as a consequence, the energy levels for such a nucleus are differen from those of the symmetric shell model.

For this occasion, Nilsson developed a shell model, in which the energy levels are cal-

culated for odd nuclei as a function of the nuclear deformation. In case of the Nilsson states, the spherical states (deformation parameter: $\epsilon_D = 0$) with angular momentum j will split into $j+1/2$ levels, since the nucleons will no longer moving freely in a fully symmetrical potential well. If the deformation increases, this can lead to a reversal in order for some levels, which is called the cross-over of the Nilsson states. This cross-over can be seen at a deformation parameter $\epsilon_D \approx \pm 0.6$, which corresponds to an axis ratio of 2:1 leading to so called super-deformed nuclei. Nuclei with magic numbers are spherical and have sharp boundaries. As the values of N and Z depart from the magic numbers the nucleus increases its deformation. Fig. 2.5 shows the oblately and prolately ellipsoidal-distorted nuclei:

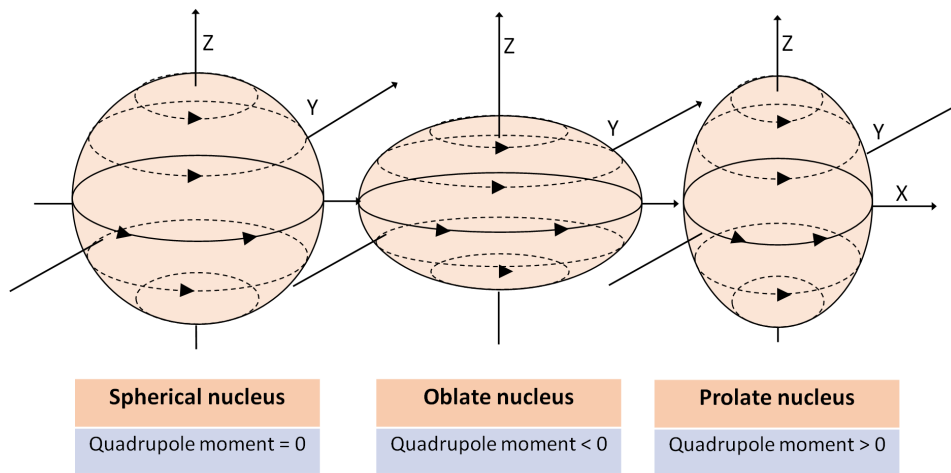


Fig. 2.5: Schematic representation of the prolate and oblate deformations, compared to a spherical nucleus.

The macroscopic-microscopic model combines the liquid-drop model Sec. 2.1.1 with shell corrections. Therefore, the shell effects are considered to be small deviations from the original energy level distribution. The new total energy is calculated by considering the discussed necessary correction as a sum of the macroscopic liquid-drop model energy (E_{LDM}) and the microscopic shell(δU)- and pairing corrections(δP) as follows [10]:

$$E = E_{LDM} + \underbrace{\sum_{n,p} (\delta U + \delta P)}_{E_{Shell}} \quad (2.4)$$

The shell corrections increase consistently from uranium to meitnerium, reaching a maximum of up to 6 MeV (compared to 12 MeV for the doubly magic lead). This stabilization is due to the energy levels in the atomic nucleus, which are still quite easy to calculate for symmetric systems. In deformed nuclei, however, a changed nuclear potential is present and the symmetry is lost. As a consequence, the degenerated energy levels are split. In

Fig. 2.6 this process is shown schematically. The raising and lowering of the energy levels with increasing deformation leads to (a) a very dense arrangement of the core levels and (b) to regions with gaps between the energy levels, which are corresponding to regions of increased stability. This effect was already shown in **Fig. 2.4** and describes deformed shells and changes with increasing core deformation.

The energy, mandatory to deform a nuclei, is an expression for the stability of the nucleus against fission. In **Fig. 2.6** the fission barrier as function of ϵ_D is shown. The most stable form against fission is the spherical shape with no deformation. After deforming the nuclei to a certain point (saddle point), the nuclei can not return to the original (spherical) shape and fission occurs.

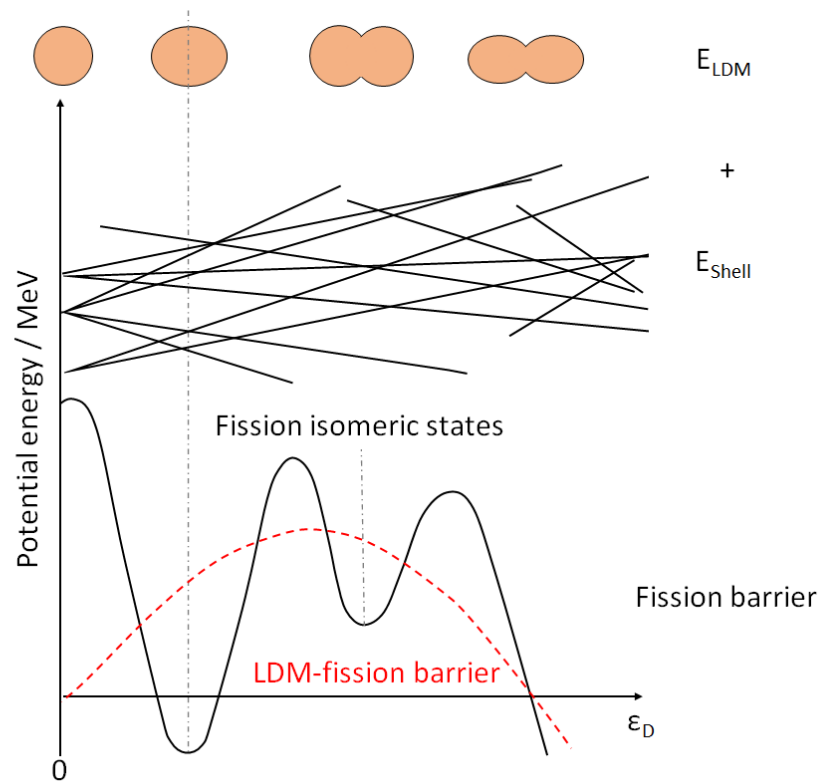


Fig. 2.6: Double humped fission barrier (solid line) as a function of the deformation parameter ϵ_D . The fission barrier equals the deformation energy and can be calculated as shown in **Eq. 2.4**. E_{LDM} shows the deformation of the nucleus, which leads a split in energy levels, shown by E_{Shell} . The sum of these two energies gives the fission barrier and characterizes the stability of the nucleus against fission. For details, see text above. Picture adapted from [10].

In the case of the transuranic elements, the core deformation leads to a lowering of the energy. This is equivalent to the fact that the nuclei are in a deformed state in the ground state and are not spherical. In **Figure Fig. 2.7** the fission barriers for the elements plutonium, rutherfordium and flerovium are shown. It can be seen, that the contribution to the fission

barrier from the LDM is decreasing strongly with increasing Z . For element 114, flerovium, the stability of the nuclei is almost exclusively distributed from the shell stabilisation effects. Therefore, the transactinides are exclusively shell stabilized elements. Experimentally, this effect can be understood by looking at the fission half-lives. The actinoids up to uranium have a fission barrier, which is stabilized by a contribution of the droplet barrier. The decrease of this contribution to the fission barrier with increasing nuclear charge ($Z > 92$) leads to shorter half-lives and a reduced stability against fission.

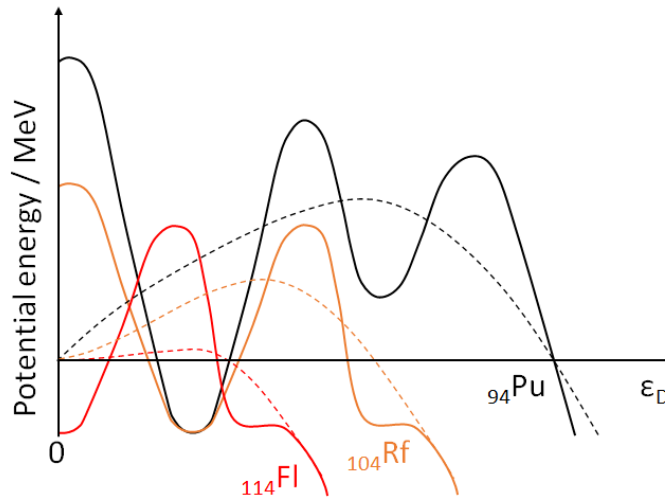


Fig. 2.7: Double humped fission barrier (solid line) as a function of the deformation parameter ϵ_D . The fission barrier equals the deformation energy and can be calculated as shown in Eq. 2.4. Picture adapted from [10].

The stability of the deformed cores can also be understood by theoretical calculations. Here, spherical nuclei are assumed, which are deformed to ellipsoids as shown in Fig. 2.5. In reality, however, this deformation is much more complex, since the nuclei oscillate in complicated shapes. These oscillations can be calculated by quadrupole deformations and hexadecapole deformations. The result is a region of low level density (gap) at $N = 152, 162$ and 182 [67, 68]. Theoretical calculations with spherical nuclei made in the middle of the 1960s concluded that element flerovium ($Z=114, N=184$) could be a candidate for a closed shell configuration [69, 70]. The nuclear shell model states that nuclei are most stable when both protons and neutrons fully occupy closed shells (double magic nuclei). This prediction was adopted in enhanced calculations of deformed shell structures in the 1980s [70]. Relatively long half-lives were predicted by several modern theoretical approaches, using Hartree-Fock or relativistic mean-field theory [71, 72] which can also be explained with the large shell effects. In Fig. 2.8 some theoretical calculations of E_{Shell} are given. This figure also shows that a new region of shell-stabilized, deformed superheavy nuclei with similarly high shell stabilization has formed between the double-magic spherical nuclei ($^{298}_{114}\text{F}$) and isotopes

with $N > 152$ at the upper end of the nuclide chart.

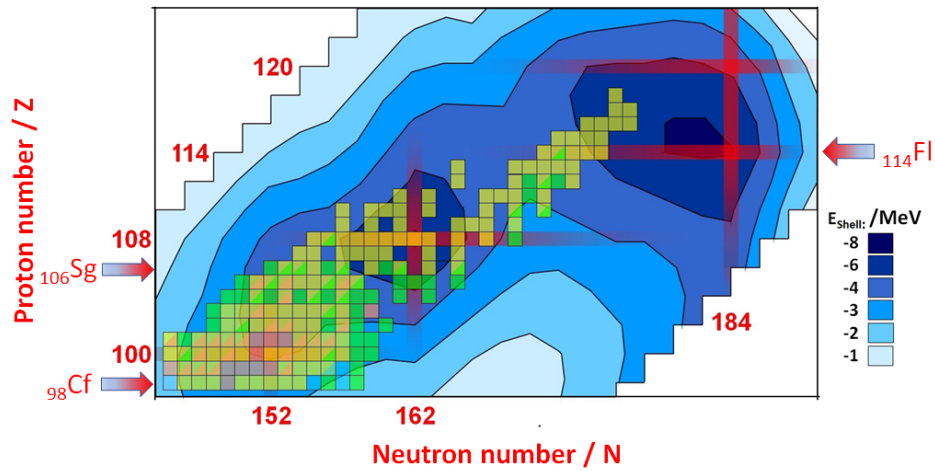


Fig. 2.8: Excerpt from the upper end of the Chart of Nuclei and the shell correction energies calculated for the given area of interest. Estimated magic numbers are highlighted in red. Picture adapted from [73] with calculations taken from Möller et al. [74, 75].

To estimate the half-lives of these isotopes, the level of deformation has to be considered. In case of ^{250}Cf the ground state is deformed as shown in Fig. 2.6, the double humped fission barrier is strongly influenced from E_{LDM} . Going to elements with higher Z like ^{106}Sg , the influence of E_{LDM} is so small that it only contributes marginally to stabilization, as shown for ^{106}Sg in Fig. 2.9. In this case, the second hump of the shell stabilization is disappearing and a high but thin stabilization caused by the shell effect remains [76].

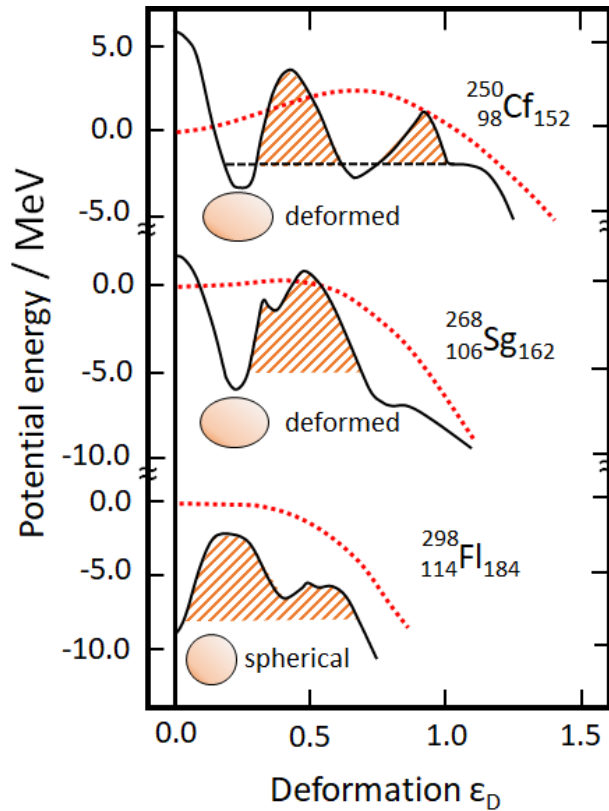


Fig. 2.9: Calculated fission barriers for ^{250}Cf (actinide), ^{268}Sg (transactinide) and ^{298}Fl (spherical transactinide). The macroscopic fission barrier is shown as a red dotted line. The ground state deformation is shown based on calculations performed by A. Sobiczewski. Pictured adapted from [77].

From the width of the fission barrier (shown as shaded area in Fig. 2.9), the lifetime of the corresponding radioisotope can be estimated. For fission to occur, the nucleus must tunnel through the fission barrier. If the barrier is high and wide (actinides), the tendency to fission is comparatively small and the nuclides have long lifetimes. If the height of the barrier remains comparable, but decreases in width as the macroscopic portion of the stabilization (ELPF) is disappearing, the half-lives decrease rapidly (transactinides). In this view, it is then irrelevant whether the core is deformed or spherical in the ground state, the half-lives are then roughly similar.

2.2 The production of Super Heavy Elements (SHE)

The heaviest element known to occur commonly in nature is uranium which contains 92 protons, putting it far below the heaviest elements in the periodic table. All transuranium elements have been discovered in the laboratory with neptunium and plutonium later also discovered in nature, formed by neutron capture in uranium ore with subsequent beta decay:

$^{238}\text{U} + \text{n} \rightarrow ^{239}\text{U} \rightarrow ^{239}\text{Np} \rightarrow ^{239}\text{Pu}$. However, all elements heavier than plutonium are entirely synthetic and created in nuclear reactions.

The neutron capture process followed by the subsequent β^- -decay in a high neutron flux nuclear reactor can be used for the synthesis and production of transuranium elements with Z up to fermium ($Z=100$). The even heavier transfermium elements can only be produced in heavy ion accelerators based nuclear fusion reactions [78].

The reason for this lies in the nature of the neutron capture process. The elements einsteinium and fermium were produced in 1952 after a first test thermonuclear explosion (code name Mike) at Eniwetok Island in the Pacific. The strong neutron flux during the short explosion of Mike had been so intense that it resulted in capture by ^{238}U of as many as 17 neutrons. This multi-neutron capture ended as the device blew apart and was followed by a sequence of β^- decays [79]. Such strong neutron fluxes might also be provided by nuclear reactors or supernova explosions in nature. However, the "fermium gap", consisting of the short-living fermium isotopes $^{258-260}\text{Fm}$ located on the β stability line and having very short half-lives for spontaneous fission, impedes the formation of nuclei with $Z > 100$ by the "weak" neutron fluxes realized in common reactors. In case of fast neutron capture e.g.: within nuclear- or supernova explosions this gap may be bypassed if the total neutron fluence is high enough and the neutron capture can occur faster than the competing fission [80].

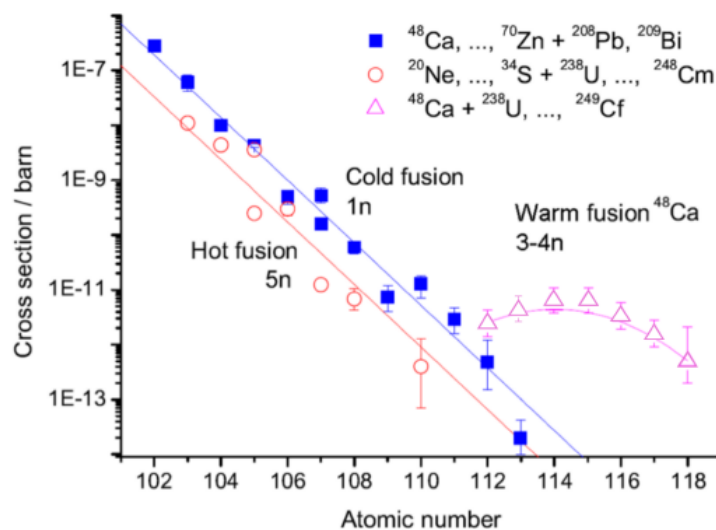


Fig. 2.10: Plot of the observed cross section for the production of heavy elements by cold and hot fusion reactions with $Z \geq 102$ in the $1n$ (cold fusion) and $5n$ (hot fusion) evaporation channel. Figure taken from [12] and adapted with values from Ref. [81]

In a simplified model, fusion can be considered to start at the touching point of the two nuclei, when the nuclear forces become effective and drive the dinuclear system (DNS) towards a mono-nucleus. For the synthesis of superheavy elements ($Z \geq 104$), the minimum in kinetic

energy of the projectile has to exceed the Q-Value needed for the formation of the compound system. After a successful fusion, the compound nucleus will be created above ground state and the excitation energy is dissipated by fission or by particle-evaporation (neutron- and γ emission).

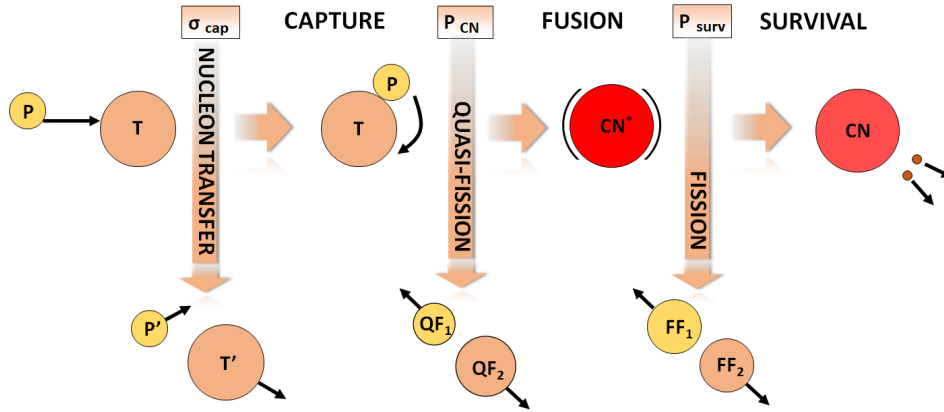


Fig. 2.11: The sketch of the sequences of the nuclear reaction mechanism in heavy ion collisions. When the projectile (P) collides with the Target (T), the formation of a compound nucleus (CN) competes always with other reaction channels, e.g.: nucleon transfer, quasi-fission and fission [82]

Unfortunately, the de-excitation process is strongly dominated by fission. Typically the collision between target and projectile will not exclusively be central collisions and therefore, the compound nucleus will be produced carrying an angular momentum, which can limit fusion probabilities by fission. In general the fusion-evaporation can be described as a three-step process whereby the production cross section σ_p is defined by the capture cross section σ_{cap} , the probability of forming a compound nucleus P_{CN} and the survivability P_{surv} of the excited intermediate compound nucleus as shown in Fig. 2.11:

$$\sigma_p = \sigma_{cap} \cdot P_{CN} \cdot P_{surv} \quad (2.5)$$

In general, the chance for a successful fusion is relatively low due to the high probability of re-separation in the entrance- and the high probability of fission in the exit-channel. Therefore, P_{surv} can be described as the fraction of compound nuclei, which reach de-excitation by neutron evaporation. Since this neutron evaporation has to be repeated a couple of times, depending on the amount of excitation energy of the compound nucleus and therefore as long as its remaining excitation energy is higher than the energy threshold for the competing fission process, the survivability can be described as shown in Eq. 2.6 for the evaporation of

x neutrons [83, 84]:

$$P_{surv} = \prod_{i=1}^x \frac{\Gamma_n}{\Gamma_f} \quad (2.6)$$

with

$$\frac{\Gamma_n}{\Gamma_f} = \exp\left(\frac{B_f - B_n}{T}\right) \quad (2.7)$$

The process is strongly influenced by the difference between the height of the fission barrier B_f and the neutron binding energy B_n of the compound nucleus, T is the temperature of the nucleus associated with its excitation energy [85, 86].

2.3 Chemical experiments with SHE

Chemical experiments with SHE are very different from the classical chemistry experiments due to some significant requirements and limitations. Typically, unique experimental methods have to be developed due to the constant competition against the nuclear decay of the investigated nuclei and their short half-lives. Additionally, the artificial production of SHE will only provide single atoms (one-atom-at-a-time), which requires performing a chemical experiment with just one atom, in a highly efficient and rapid kind of reaction, coupled with a highly selective separation method and a sensitive detection method.

Already the production of SHE is a very difficult process, with special challenges being involved in the study of chemical properties because of their typical short half-lives, low production rates, the presence of many unwanted activities and the necessity for producing them with high-intensity beams. For chemical studies often the longest-lived known isotope of the element is used, since this studies require use of an isotope with a half-life long enough to permit chemical separation and a reasonable production and detection rate. In case of transactinide elements this may range from a few atoms per minute (e.g.: Rf) to only one atom a week (e.g.: Hs) [87]. This also requires exotic and highly radioactive target nuclides such as e.g. ^{249}Bk or ^{249}Cf , which are bombarded with intense ion beams. The production of the SHE elements with $Z \geq 112$ is usually followed by a physical pre-separation step to deliver clean products. Since during the bombardment of a target with a heavy ion beam, not exclusively fusion will be observed. Usually a multitude of different reactions will take place, depending on how the projectile collides with the target as shown in Fig. 2.12 [88], which will populate a lot of different exit channels, leading to unwanted side products. This makes it difficult to unambiguously identify a single decay of interest of a SHE in a detection system, even when very sensitive detectors are used. These sensitive detectors are also damaged by high energy fluxes of ions, therefore the irradiation of such a detector with the ion beam should be avoided. The physical pre-separation with gas-filled separators or

vacuum separators are used to realize chemical experiments with transactinide elements [38].

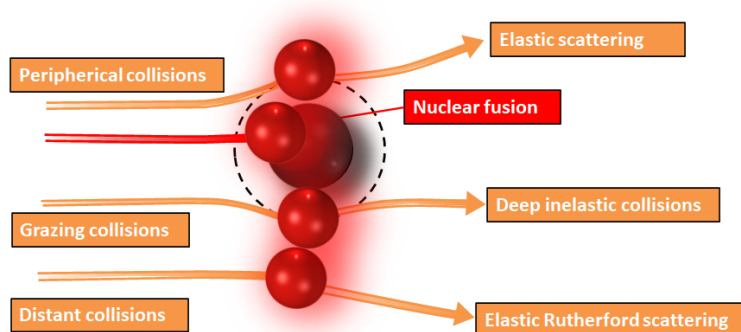


Fig. 2.12: Classification of heavy-ion collisions. Figure adapted from Ref. [88]

The investigation of chemical properties of transactinides was realized by the development of new experimental techniques such as computer-controlled systems to enhance the reproducibility of experiments like e.g., large numbers of chromatographic separations in the liquid phase. In addition to liquid phase chemical experiments a variety of gas-phase experiments have been performed in conjunction with theoretical modeling of chemical species with improved quantum-chemical codes [18, 20, 89–91].

Considering the low production rates shown in Tab. 2.1 it is quite unlikely that more than a couple or in some cases just one single atom is available at a time. Therefore, in the following chemical reaction Eq. 2.8, the change of the Gibbs free energy ΔG for a reversible reaction can be described in macroscopic quantities as shown in Eq. 2.9:



$$\Delta G = \Delta G_0 + RT \frac{[X]^x [Z]^z}{[A]^a [E]^e} \quad (2.9)$$

For the chemistry reactions with only one available atom available, this atom cannot be constituent of A and X simultaneously and at least one of these activities will be zero. Therefore, we can no longer talk about a chemical equilibrium with a single atom. Guillaumont et al. [110, 111] described the chemical specification at a tracer scale, in which concentrations are replaced with probabilities for finding a single atom in a given state and a given phase. The consequence for single atom chemistry is that the studied atom must be subjected to a repetitive partition experiment to ensure a statistically significant behaviour.

Tab. 2.1: Target(Tar.) and projectile(Proj.) combinations for the synthesis of nuclides from nuclear fusion reactions used in transactinide chemistry are shown with their cross sections (σ), neutron evaporation channels(NEC) and estimated production rates (Prod. rate).

Nuclide	T _{1/2}	Tar.	Proj.	NEC	σ	Prod. rate ^a	Ref.
^{257m} Rf	4.1 s	²⁰⁸ Pb	⁵⁰ Ti	1 n	10 nb	2 min ⁻¹	[92]
²⁵⁹ Rf	2.5 s	²³⁸ U	²⁶ Mg	5 n	1.6 nb	0.5 min ⁻¹	[93]
^{261a} Rf	78 s	²⁴⁸ Cm	¹⁸ O	5 n	10 nb	2 min ⁻¹	[94]
^{261b} Rf	3.0 s	²⁴⁸ Cm	²⁶ Mg	5 n, 2 α	6 pb	3 day ⁻¹	[43, 95]
		²⁴⁸ Cm	¹⁸ O	5 n	11 nb	2 min ⁻¹	[96]
²⁶² Db	34 s	²⁴⁹ Bk	¹⁸ O	5 n	6 nb	2 min ⁻¹	[97]
		²⁴⁸ Cm	¹⁹ F	5 n	1 nb	0.5 min ⁻¹	[98]
²⁶³ Db	27 s	²⁴⁹ Bk	¹⁸ O	4 n	10 nb	2 min ⁻¹	[97]
^{263a} Sg	0.9 s	²⁴⁹ Cf	¹⁸ O	4 n	0.3 nb	6 h ⁻¹	[99]
^{265a} Sg	9.0 s	²⁴⁸ Cm	²² Ne	5 n	0.2 nb	4 h ⁻¹	[40, 100]
^{265b} Sg	16 s	²⁴⁸ Cm	²⁶ Mg	5 n, α	6 pb	3 day ⁻¹	[100]
		²⁴⁸ Cm	²² Ne	5 n	0.18 nb	3.5 min ⁻¹	[40]
²⁶⁶ Bh	0.7 s	²⁴⁸ Cm	²³ Na	5 n	50 pb	1 h ⁻¹	[101]
		²⁴⁸ Cm	²³ Na	5 n	57 pb	1.1 h ⁻¹	[40]
²⁶⁷ Bh	17 s	²⁴⁹ Bk	²² Ne	4 n	≈70 pb	1.5 h ⁻¹	[102]
		²⁴⁸ Cm	²³ Na	4 n	14 pb	0.3 h ⁻¹	[40]
²⁶⁹ Hs	9.0 s	²⁴⁸ Cm	²⁶ Mg	5 n	≈6 pb	3 day ⁻¹	[103]
²⁷⁰ Hs	23 s	²⁴⁸ Cm	²⁶ Mg	4 n	≈3 pb	1.5 day ⁻¹	[43, 95]
		²³⁸ U	³⁶ S	4 n	2.9 pb	1.5 day ⁻¹	[104]
²⁷¹ Hs	4.0 s	²⁴⁸ Cm	²⁶ Mg	3 n	≈3 pb	1.5 day ⁻¹	[43, 95]
²⁸³ Cn	3.8 s	²⁴² Pu	⁴⁸ Ca	3 n	≈3 pb	1.5 day ⁻¹	[105]
²⁸⁵ Nh ^a	3.3 s	²⁴³ Am	⁴⁸ Ca	2 n	≈1.5 pb	0.8 day ⁻¹	[106, 107]
²⁸⁹ Fl	1.9 s	²⁴⁴ Pu	⁴⁸ Ca	2 n	≈5.3 pb	2.7 day ⁻¹	[108, 109]

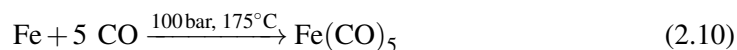
Assuming values of 0.8 mg/cm² target thickness and 3 x 10¹²s⁻¹ beam particles.

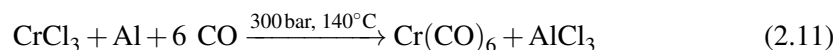
^a Not directly produced: Nihonium will be received by α -decay of moscovium

2.4 Carbonyl chemistry with transition metals and SHE

Carbonyl complexes were discovered already more than 130 years ago, when Mond reported on the synthesis of nickel tetracarbonyl [6]. The industrial and also scientific importance of these compounds is reflected in their large number [7, 8, 120]. Even in radio-pharmaceutical applications, carbonyl complexes are a focus of interest [121-122].

Carbonyl compounds are commonly synthesized involving high carbon monoxide pressure [16], either in direct reactions of metals with carbon monoxide Eq. 2.10 or the reduction of metal salts and oxides Eq. 2.11.





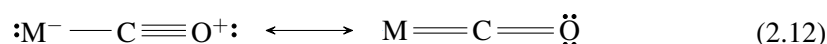
These stable, binary, mononuclear, neutral and volatile metal carbonyl complexes are formed by almost all transition metals [112–116]. In addition to these mononuclear complexes, a huge variety of polynuclear compounds can be formed with metal carbonyls, like the dimetal decacarbonyl complexes of group 5 elements, the tetrametal dodecacarbonyl complexes of cobalt and iridium, or the octarhodium hexadecacarbonyl complexes, as shown in table Tab. 2.2. Neutral, binary complexes of some of the more noble transition metals like palladium, platinum, silver or even gold were only observed in matrix isolation experiments at low temperatures [117, 118]. Due to the ability of being easily exchanged by Lewis bases, olefins or arenes, metal carbonyls can also form mixed carbonyl complexes with ligands like nitrosyl, hydrogen or oxygen as known for transition metals of almost all groups.

Tab. 2.2: Stable, neutral binary metal-carbonyl complexes. Data taken from [16].

Group in PSE							
4	5	6	7	8	9	10	11
Ti	V(CO) ₆	Cr(CO) ₆	Mn ₂ (CO) ₁₀	Fe(CO) ₅ Fe ₂ (CO) ₉ Fe ₃ (CO) ₁₂	Co ₂ (CO) ₈ Co ₄ (CO) ₁₂ Co ₆ (CO) ₁₆	Ni(CO) ₄	Cu
Zr	Nb	Mo(CO) ₆	Tc ₂ (CO) ₁₀ Tc ₃ (CO) ₁₂	Ru(CO) ₅ Ru ₃ (CO) ₁₂	Rh ₂ (CO) ₈ Rh ₆ (CO) ₁₆	Pd	Ag
Hf	Ta	W(CO) ₆	Re ₂ (CO) ₁₀	Os(CO) ₅ Os ₆ (CO) ₁₈	Ir ₄ (CO) ₁₂ Ir ₆ (CO) ₁₆	Pt	Au

2.4.1 Bond structure of carbonyl complexes

Pauling (1935) [16] described the bonding in transition metals in their resonance structure, which leads to a bonding order in between of one and two for the metal-carbon bond, following the principle of electro neutrality as shown in Eq. 2.12



In Fig. 2.13 the molecular orbital diagram (MO diagram) of carbon monoxide is depicted. Mostly relevant for the M-CO bond are the so called frontier orbitals with 2π as the lowest unoccupied molecular orbital (LUMO), 5σ as the highest occupied molecular orbital (HOMO) and 1π as another group of frontier orbitals. The LUMO is shown with a weak

anti bonding character.

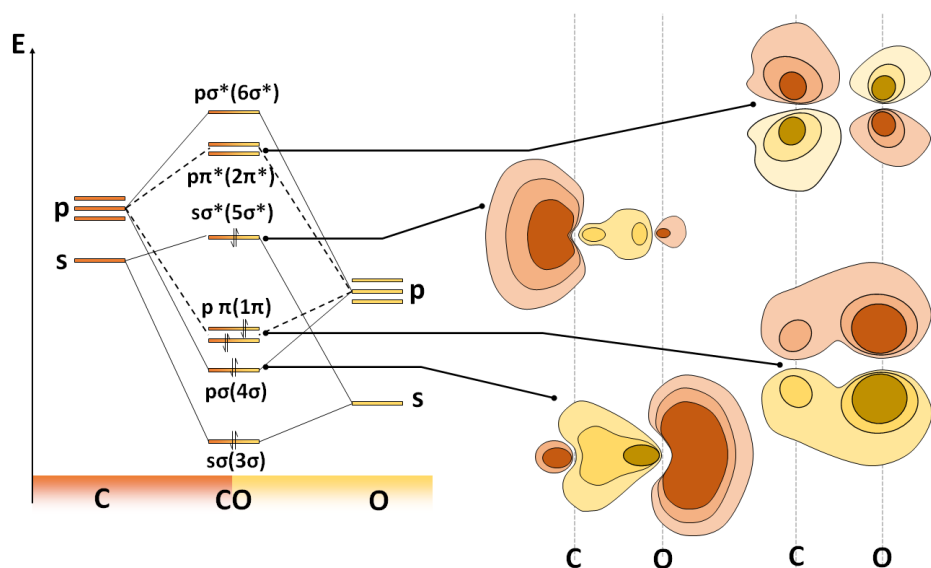


Fig. 2.13: (left) Schematic of the molecular orbital diagram of carbon monoxide before and after s - p mixing. With quantum mechanical calculations the contour-line (right) diagrams for the orbitals can be visualized, which are used to describe the shape of the M - C - O bond. Picture adapted from [16].

Typically the transition metal carbonyl bond is described with a donor-acceptor interaction between the (a) HOMO ($5\sigma^*$) of the carbon monoxide molecule with an empty transition metal atomic orbital (AO), which fits the σ -symmetry (e.g., d_{z^2}) and (b) an occupied π type d -orbital of the transition metal and the degenerated $2\pi^*$ LUMO of the carbon monoxide [119]. During the M - C bond formation, three different bonds can be discussed as shown in Fig. 2.14.

- σ -donation from the carbon monoxide to the transition metal
- π -donation of the carbon monoxide to the transition metal
- π -backbonding of the carbon monoxide

Tab. 2.3: The change of bond length d and stretching frequencies ν , when the CO molecule is getting bonded to a transition metal. CO describes the ground state ($X^1\Sigma^+$), whereas CO^* describes the electronically excited state in $a^3\Sigma^+$ (TS), and $a^3\Pi_r$ (TP). Data taken from [130]

Species	Configuration	d(C-O) / pm	ν (CO) / cm^{-1}
CO	$(5\sigma^2)$	113	2143
CO^+	$(5\sigma^1)$	111	2184
CO^*	$(5\sigma^1)(2\pi^1)$ TS	124	1489
CO^*	$(5\sigma^1)(2\pi^1)$ TP	121	1715
N_2	$(5\sigma^2)$	110	2330

In Fig. 2.14 a schematic representation of the transition metal carbonyl orbital (M-C-O) interactions is depicted following the (DCD) Dewar-Chat-Duncanson [120] model. After binding to a transition metal, the electronic structure of the carbon monoxide will be changed, whereby the frequency of ν_{CO} will be shifted hypsochromic. Removal of an electron out of the carbon-centred 5σ MO will leave the carbon positively charged, which will strengthen the C-O bond, by lessening the charge difference between the carbon and oxygen atom ($5\sigma^*$ has a slightly anti-bonding character). In addition, π -backbonding from the metal to the carbon monoxide will move an electron into the $2\pi^*$ orbital, which has a strongly anti-bonding character and therefore, will lessen the C-O bond strength [16].

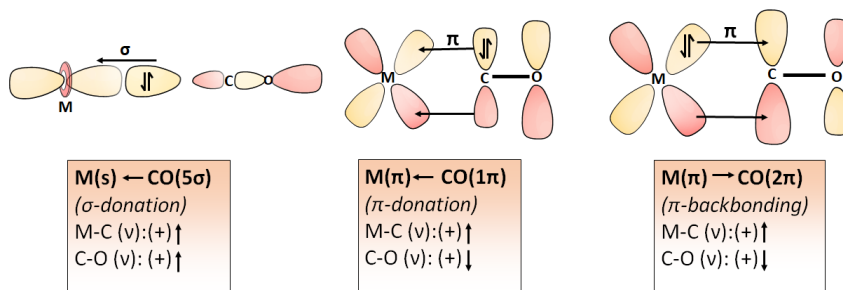


Fig. 2.14: Scheme of synergistic σ -donation, π -donation and π -backbonding in the transition metal carbonyl bonding. The bond strength of the C-O bond is influenced by the difference in charge between the oxygen and carbon atom, therefore moving electrons away in a donation to the transition metal will strengthen the C-O bond, whereas the addition of electrons has the opposite effect. Picture adapted from [16].

In quantum mechanical calculations it can be shown that the most significant contribution to the M-C-O bond is distributed by the π -backbonding, which agrees with qualitative models such as the popular DCD. Davidson et al. calculated with density functional theory (DFT) and extended transition state method (ETS) that the strength of the π -backbonding arises from the penetration of the 5σ (lone pair) electrons of the carbon, into the transition metal valence shell [33]. Nevertheless, the influence of the π -backbonding would not explain

the bond stabilization in the positively charged carbonyl complexes. In **Tab. 2.3** the (C-O) stretching frequencies of carbon monoxide are shown, whereby the existence of $M(\text{CO})_n^{m+}$ complexes with stretching frequencies higher than free CO were observed. Theoretical investigation by Frenking and Szilagyí using the (CDA) charge decomposition analysis [121] of the structure and bonding of isoelectronic hexacarbonyls $M(\text{CO})_6^q$ showed, that the C-O stretching frequency increased with the positive charge on the transition metal. In addition, the first bond dissociation energy (FBDE) was found to show a reversed U-shaped curve form ($M^q = \text{Hf}^{2-}, \text{Ta}^-, \text{W}, \text{Re}^+, \text{Os}^{2+}, \text{Ir}^{3+}$) with its minimum at the un-charged complex, shown in **Fig. 2.15**, indicating stabilizing effects for positively charged carbonyl complexes.

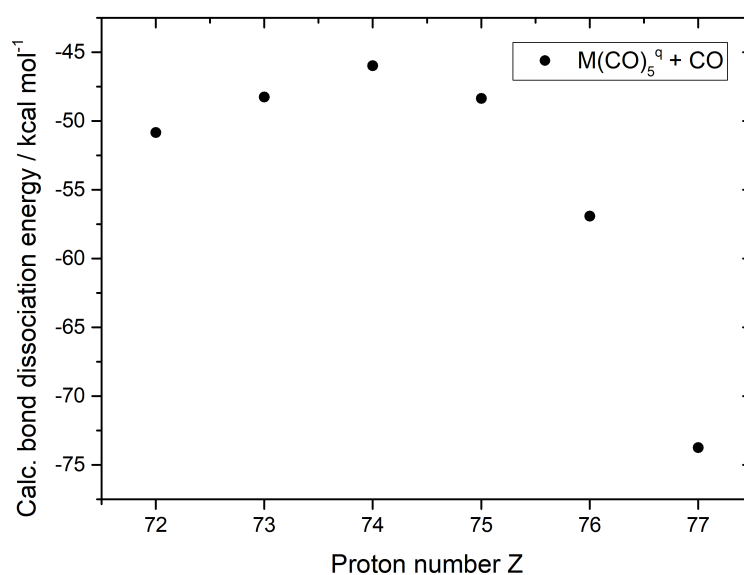


Fig. 2.15: Calculated Bond dissociation energies (kcal/mol) as a function of the charge of the complex for isoelectronic $M(\text{CO})_6^q$ ($M^q = \text{Hf}^{2-}, \text{Ta}^-, \text{W}, \text{Re}^+, \text{Os}^{2+}, \text{Ir}^{3+}$) hexacarbonyl complexes [122].

The influence of the charge of the complex on the M-C-O bond strength can be explained by an increasing influence of the σ -donation to the bond energy in case of carbonyl cations or by an increased electrostatic interaction in positively charged species. In case of negatively charged complexes, a larger π -backbonding contribution to the bonding energy is expected. In general, in an octahedral complex $(\text{ML})_6$ the σ -donation from the ligand to the transition metal involves empty d(σ), p and s orbitals of the metal, with t_{1u} , e_g and a_{1g} symmetry, while π -backbonding arises from orbitals with t_{2g} symmetry as shown in **Fig. 2.16**.

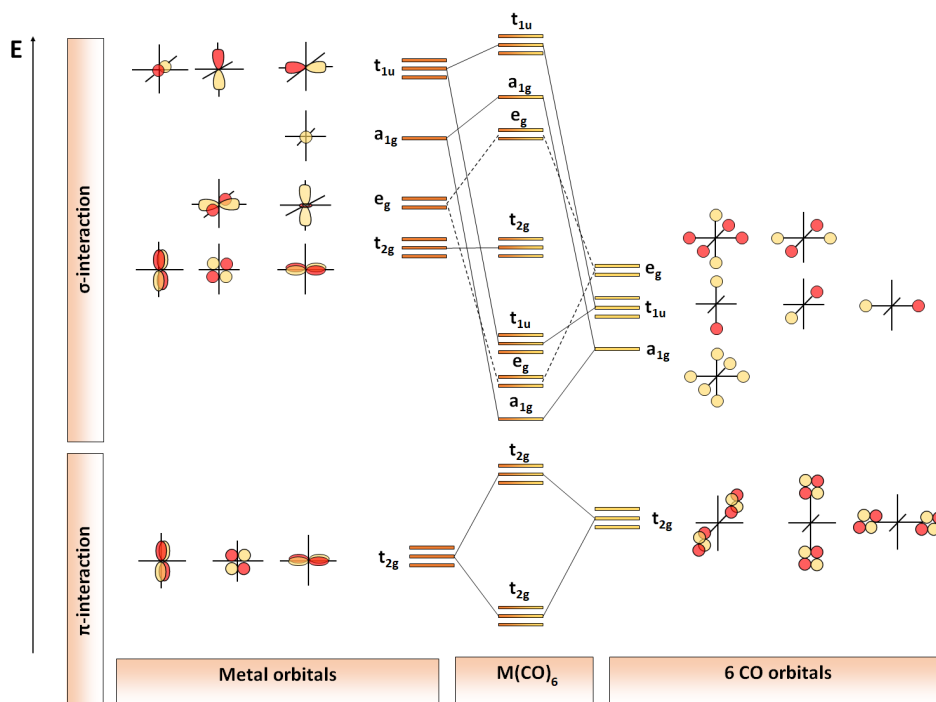


Fig. 2.16: Splitting of the orbital energy levels of an octahedral d^6 transition metal complex ML_6 , where the ligand L has occupied donor orbitals with σ symmetry and empty acceptor orbitals with π symmetry [16].

In case of transition metal carbonyl complexes, the bond energy can be described by several contributions as shown in Eq. 2.14. In the octahedral ligand field (c.f., Eq. 2.13), the carbon monoxide building a cage surrounding the transition metal:



Based on calculations of Davidson et al. [33], the bond energy ΔE can be described with ΔE_M as the promotion energy, necessary to promote the ground state transition metal into the complex, ΔE_{CO} as the energy necessary for changing the carbon monoxide bond length, ΔE_{Cage} as the energy necessary to build an octahedron with the carbon monoxide molecules against the van der Waals repulsion and ΔE_{Bond} , as the basic bonding energy.

$$\Delta E = \Delta E_M + n \Delta E_{CO} + \Delta E_{Cage} + \Delta E_{Bond} \quad (2.14)$$

The energies shown in red are endothermic in their nature and only ΔE_{Bond} causes the energy to be lowered. ΔE_{Bond} can be divided into two different parts:

(1) Introduction of the 5 σ electron pair into the 3 s,p,d-electron shell of the transition metal, which leads to an expansion of the M(t_{2g}) orbitals, e.g., by a mixture with the 4d-orbitals. This will enhance the 2 π interaction with the carbon monoxide ligand orbitals. (2) Correlation of the 5 σ orbital from the carbon monoxide (HOMO) with the LUMO of the transition metal M3d(t_{2g}), which can be split into a σ -donation via the t_{1u} and the a_{1g} -orbitals and a π -backbonding contribution via the t_{2g} orbitals. In the negatively charged complexes, as well as the neutral tungsten complex, the π -backbonding contributes the major fraction to ΔE , while the positively charged complex has a stronger σ -donation.

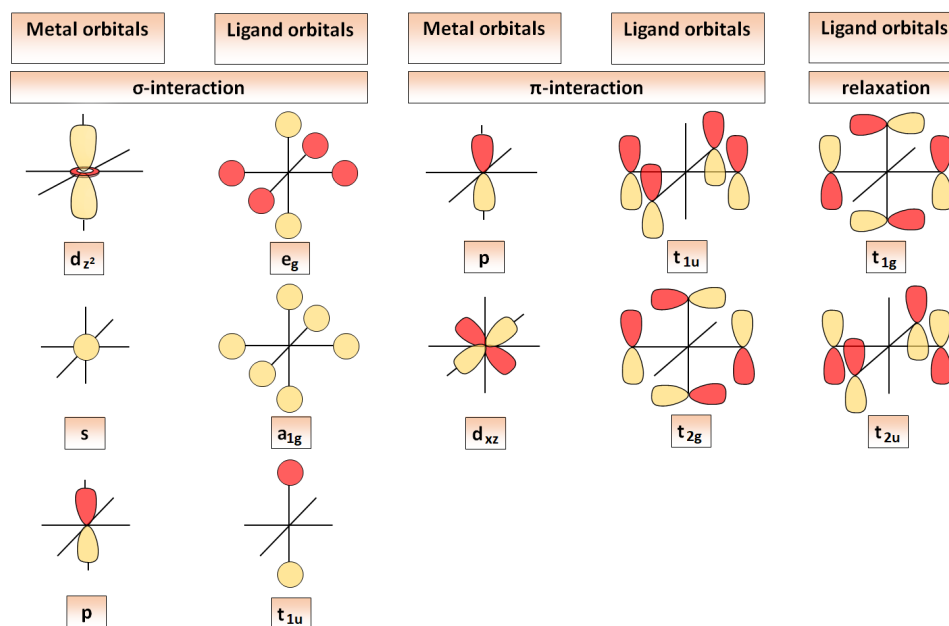
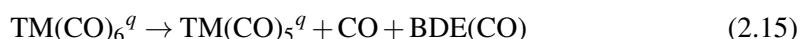


Fig. 2.17: Orbital interaction diagram of the splitting d , s , p valence orbitals of a transition metal in an octahedral ligand field [16].

Typically the strength of the M-CO bonds can be described by its bond dissociation energies (BDEs). This energies can be calculated, e.g.: in case of hexacarbonyls for the loss of one CO ligand yielding $\text{TM}(\text{CO})_5^q$ and CO as shown in Eq. 2.15



In Fig. 2.17 the orbital interactions of the decomposition of $\text{M}(\text{CO})_6^q$ are depicted [119]. In case of the positively charged complexes like $\text{Ir}(\text{CO})_6$, a energy contribution to ΔE arises solely from the relaxation of the ligand orbitals. With no metal orbitals available in t_{1g} and t_{2u} symmetry, the orbital interactions existing with t_{1u} symmetry can be split into two different contributions: (1) σ -donation into the $p(\sigma)$ -orbitals of the metal and a π -donation from the filled π -orbital of the carbon monoxide in the $p(\pi)$ orbitals of the metal, which is also shown

in Fig. 2.14 as a π -donation interaction. Therefore, positively charged carbonyl complexes are stabilized by the π -donation interaction of the carbon monoxide. However, the influence of the π -donation is mostly neglected and rather small.

In order to calculate the corresponding BDEs, it is mandatory to understand what influence the M-CO bond dissociation has on ΔE_{Bond} and in which state the $\text{TM}(\text{CO})_5^q$ complex remains after the removal of one carbon monoxide ligand. Typically the M-CO bond can have two different kind of natures: (1) A covalent bonding nature (ΔE_{cov}) and (2) a electrostatic bonding nature (ΔE_{els}):

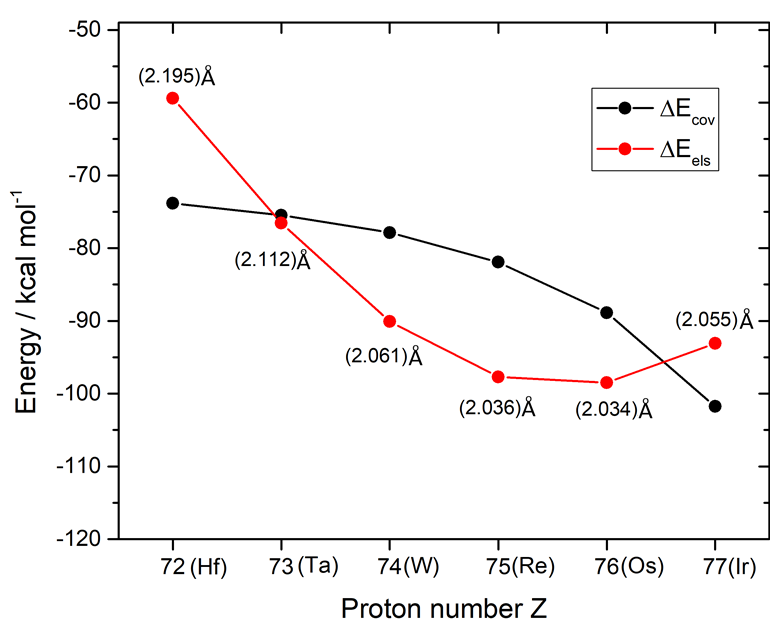


Fig. 2.18: Trend of the covalent- and electrostatic energy contributions to the interaction energy between $\text{TM}(\text{CO})_5^q$ and CO. The numbers in brackets indicate the interatomic distances. Data taken from [122].

In In Fig. 2.18 it can be seen that for $\text{Hf}(\text{CO})_6^{2-}$ and $\text{Ir}(\text{CO})_6^{3+}$, the covalent bonding contribution to the interaction energy is larger than the electrostatic bonding. This result indicates, that the complex with the highest charge have the smallest degree of ionic character in the M-CO bond. Furthermore it can be seen that, ΔE_{els} follows the trend of the bond length of the M-CO bond and is clearly smaller in its absolute value than for the $\text{Re}(\text{CO})_6^+$ and $\text{Os}(\text{CO})_6^{2+}$ and therefore, the increased bond dissociation energy for the $\text{Ir}(\text{CO})_6^{3+}$ complex shown in Fig. 2.15 cannot be explained by only the charge within the complex.

The stabilization of the carbonyl complex to $\text{TM}^q \leftarrow \text{CO}$ σ -donation increases from $\text{Hf}(\text{CO})_6^-$ to $\text{Ir}(\text{CO})_6^{3+}$, while the $\text{TM}^q \rightarrow \text{CO}$ π -backdonation shows the opposite trend. Therefore,

the latter one is stronger for the negatively charged complexes, whereas the σ -donation exhibits a stronger influence for the positively charged complexes like $\text{Ir}(\text{CO})_6^{3+}$. This trend can be explained with the lowering of the orbital energies of the π HOMO and σ LUMO. In Fig. 2.19 the HOMO and LUMO energies of the pentacarbonyls are shown. The large difference of more than 30 eV explains the difference in stabilization by matching orbital energies, whereby the π -HOMO of hafnium pentacarbonyl ($Z=72$) sits at high energy and the σ -LUMO of the iridium pentacarbonyl ($Z=77$) is considerably low.

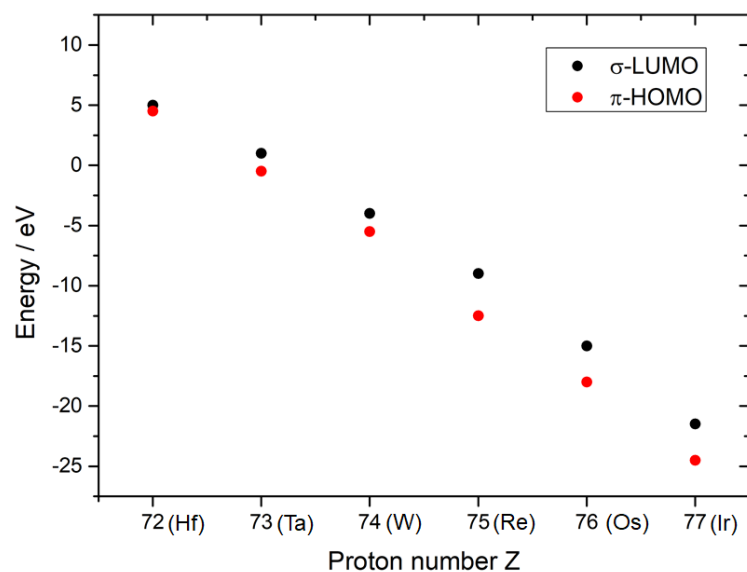


Fig. 2.19: Trend of the frontier orbital energy levels of the pentacarbonyls. Data taken from [122].

As a result of this matching orbital energies, the σ -donation will increase with an increasing positive charge on the carbonyl complex: $[\text{M}(\text{CO})_6]^q$ with $3^+ > q > 2^-$, whereas with an increasing negative charge, the π -backbonding will be preferred, as is, e.g.: visible in ν_{CO} of 1757 cm^{-1} in $[\text{Hf}(\text{CO})_6]^{2-}$ compared to 2254 cm^{-1} in $[\text{Ir}(\text{CO})_6]^{3+}$ [16, 119]. Therefore, the charge of the complex will be de-localised, whereas the transition metal remains partially negatively charged and the remaining charge will be distributed to the ligands.

2.4.2 The influence of relativistic effects on the carbonyl bond structure

The first transactinides ($Z= 104$ to 112) were assigned to the group of the transition metals in the periodic table of elements (cf. Fig. 1.2), as their chemical behaviour is characterized by the filling of the 6d-orbitals. The electronic structure of the transition metal influences the interaction of the metal atom with the carbonyl ligands in terms of σ - and π donation, as well as the π -backbonding and therefore influences the stability M-CO. As discussed in Sec. 2.4, the M-CO bond forms by the overlap of specific orbitals (cf. Fig. 2.14 and Fig. 2.17).

With increasing number of protons in the nuclei of the heavy elements, the attraction of the electrons to the core becomes stronger [19, 123]. Therefore, the distance to the nucleus decreases and the electrons begin to move on a smaller orbit with an increased velocity v , which can be described with the rest mass m_0 and the speed of light c as follows [87]:

$$m = \frac{m_0}{\sqrt{1 - \left(\frac{v}{c}\right)^2}} \quad (2.16)$$

The orbit of an electron can be described with the Bohr model for hydrogen-like species, where the radius r is set in relation to the mass m , velocity v , atomic number Z and charge of the electron e as follows:

$$r = \frac{Ze^2}{mv^2} \quad (2.17)$$

According to the electron mass being located in the denominator of Eq. 2.17 the direct relativistic effect leads to a shrinking and stabilisation of the spherical s and $p_{1/2}$ orbitals. The energetic stabilization E of the orbital can be calculated as shown in Eq. 2.18, including the principal quantum number n and the Planck constant h :

$$E = \frac{2\pi e^4}{n^2 h^2} m Z^2 \quad (2.18)$$

The relativistic stabilization of the s-orbitals was calculated by Pershina et al. [35, 123] and the influence can be seen by comparing the different radii R_{\max} of maximum charge density of group 8 elements (Fe, Ru, Os and Hs), as shown in Fig. 2.20.

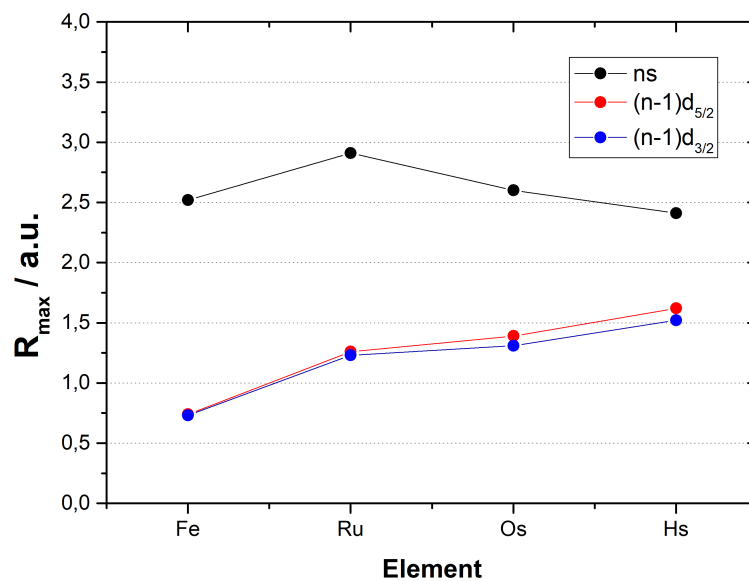


Fig. 2.20: Trend of the radii of maximum charge density of group 8 elements. Data taken from [35].

In Fig. 2.20 additional information about the shape of the d orbitals is given. Due to the relativistic contraction of the s and $p_{1/2}$ orbitals, the nuclear charge is shielded more effectively, which leads to a destabilization and expansion of the $p_{3/2}$, d and f orbitals. Since this effect is a consequence of the first effect, this behaviour is called the indirect relativistic effect. The indirect relativistic effect manifests itself in the outer core shells. The strong influence of the relativistic can be seen for element 108, Hs, where the level sequence of 7s and 6d orbitals is inverted as shown in figure Fig. 2.21.

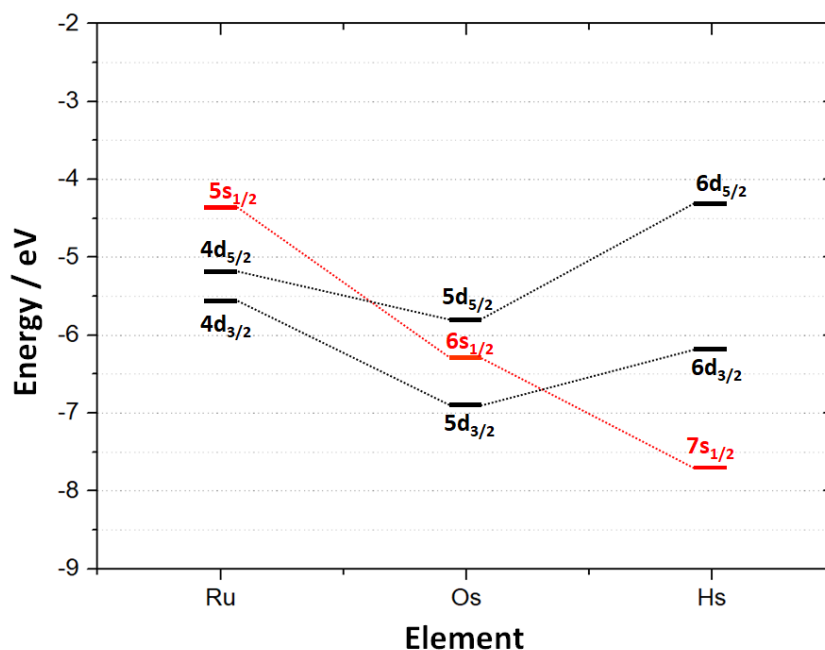


Fig. 2.21: SO ZORA energies of the ns and $(n-1)d$ valence AOs of group 8 elements. Data taken from [35].

The third and last relativistic effect is the spin-orbit splitting. The levels with an azimuthal quantum number $l > 0$ (p, d and f orbitals) will split into sublevels with the total angular momentum quantum number $j = l \pm 1/2$. The SO splitting decreases with increasing number of subshells and therefore, is much stronger for inner shells than outer shells. For orbitals with the same principal quantum number n , the influence will decrease with higher angular momentum [3, 124]. In transactinide compounds the SO coupling can exceed typical bond energies, as seen in the splitting of 7p electrons in element 118, which is in the order of 11.4 eV [125].

Typically, chemical bonding can be visualized by creating Molecular Orbital (MO) schemes of the bond formation. In Fig. 2.22 the bond formation of $M(\text{CO})_5$ ($M = \text{Ru}, \text{Os}$ and Hs) is shown, considering the symmetries, occupation numbers and energies of the selected MOs.

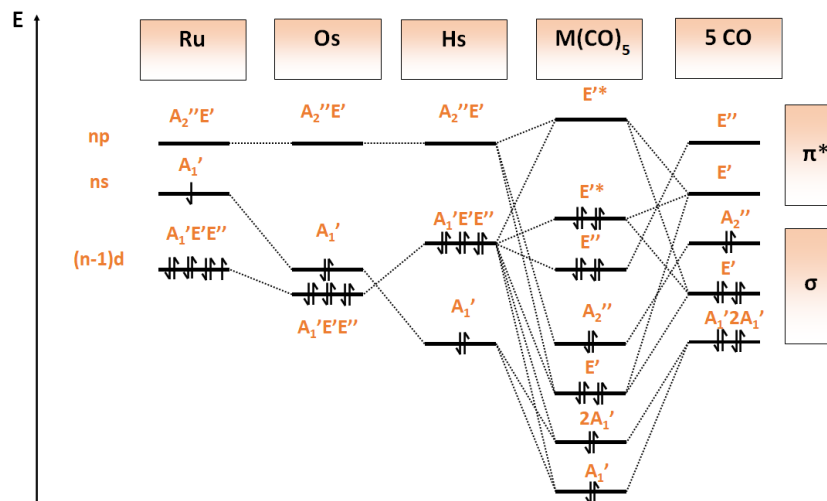


Fig. 2.22: Schematic of the $M(\text{CO})_5$ bond formation of group 8 transition metals. Picture adapted from [35].

Basically, a distinction can be made between two different types of bonding: (a) σ -interactions and (b) π -interactions. In case of ruthenium ($4d^75s^1$), seven electrons are located in the 4d AOs and one electron is located in the 5s AO. The corresponding σ -interactions are shown in Fig. 2.23. In the D_{3h} representation the orbital interactions between the filled d(M) AOs of the E' and E'' symmetries are strongly repulsive with the σ orbitals of the carbon monoxide in the equatorial plane, whereas the interactions along the A'_1 and A''_2 mode with the empty d_{z^2} , np and ns AOs are bonding.

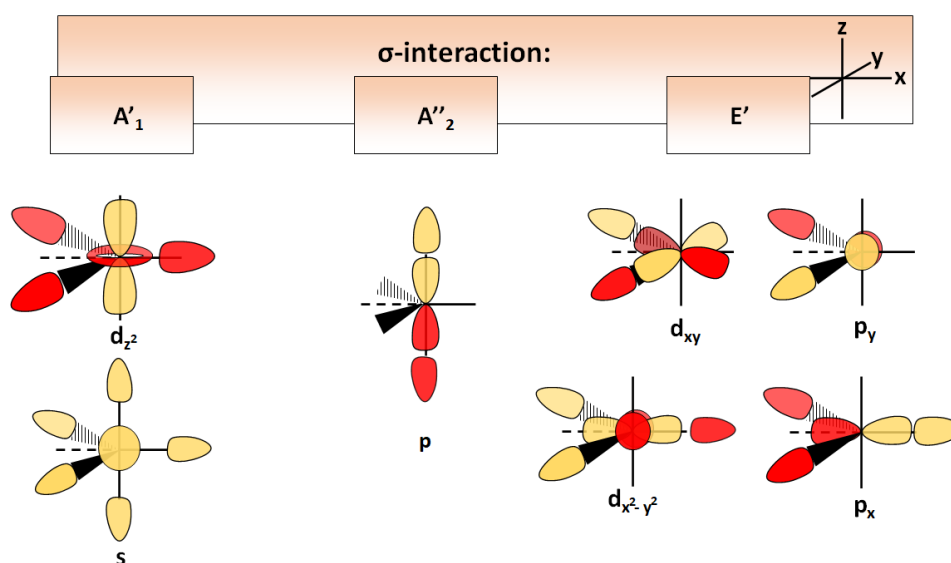


Fig. 2.23: Schematic of the σ -interactions in the D_{3h} representation. Figure is adapted from [126].

In addition to the σ interaction, the π back-donation from the occupied (n-1)d AOs of the metal atom along the E' and E'' mode into vacant $\pi(\text{CO})$ AOs will stabilize the M-CO bond and partially compensates for the repulsive interactions with the equatorial ligands. The corresponding π -interactions are shown in Fig. 2.24.

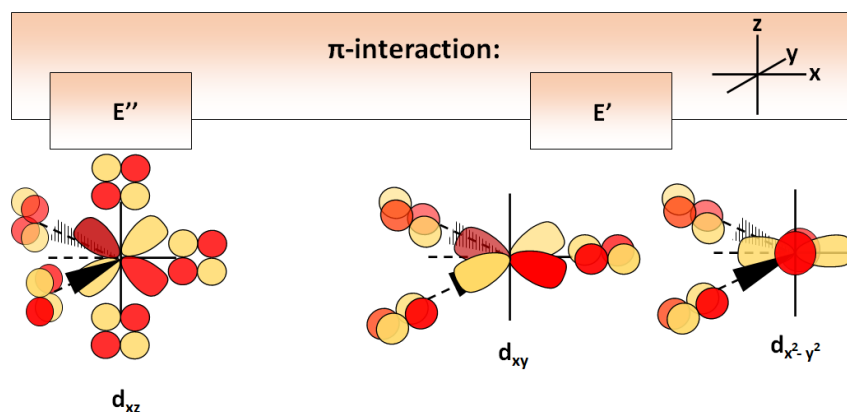


Fig. 2.24: Schematic of the π -interactions in the D_{3h} representation. Figure is adapted from [126].

In the case of more relativistic orbitals, beginning from osmium, the situation changes. As shown in Fig. 2.21, the direct and indirect relativistic effects lead to a change in the level sequence, whereby the 6s AO of osmium drops in between the (n-1) $d_{3/2}$ and (n-1) $d_{5/2}$ orbitals. This effect is even more pronounced for hassium, where the 7s drops under the corresponding d-orbitals. Due to this change, the 6s orbital will be filled with an additional electron, leading to a change of bond structure in case of $\text{Os}(\text{CO})_5$ and $\text{Hs}(\text{CO})_5$. Since the ns orbital is no longer available for bonding, the σ -interaction will happen along the A''_2 , E' and A'_1 modes with the (n-1)d metal orbitals, whereas the ns orbital along the A'_1 will lead to a strong repulsive interaction, weakening the σ -bonds in the M-CO bond structure. In addition to the weaker σ -bonding the π -backbonding will also be influenced by the relativistic effects. As shown in Fig. 2.22, the energetic character of the (n-1)d orbitals will be more similar to the vacant π^* orbitals of the carbon monoxide, whereby a stronger interaction can be expected. However, despite the stronger overlap of the metal d orbitals with the $\pi(\text{CO})$ orbitals, the π -backbonding is weaker. The backbonding can be considered as a delocalization of an electron from the metal to the CO. Due to the more diffuse character of the more relativistic 5d and 6d orbitals compared to the 4d one of ruthenium, the delocalization of an electron from the less relativistic 4d orbitals is electronically more beneficial for the M-CO bond than the larger overlap, which leads to a stronger backbonding for ruthenium compared to osmium or even hassium.

As a result, it can be assumed that $\text{Hs}(\text{CO})_5$ will form a carbonyl complex in the D_{3h}

and D_{2d} symmetries, similar to its lighter homolog Os. The bond length of the M-CO bond is assumed to increase, which is typical for group 4 through group 8 compounds [35] going from 5d to 6d elements. As a consequence, the polarizability is expected to decrease, whereas the ionization potential should decrease with increasing Z due to the indirect relativistic effect and the destabilization of the d AOs. In case of adsorption studies on different surface, e.g.: quartz and teflon surfaces as shown in Fig. 2.25.

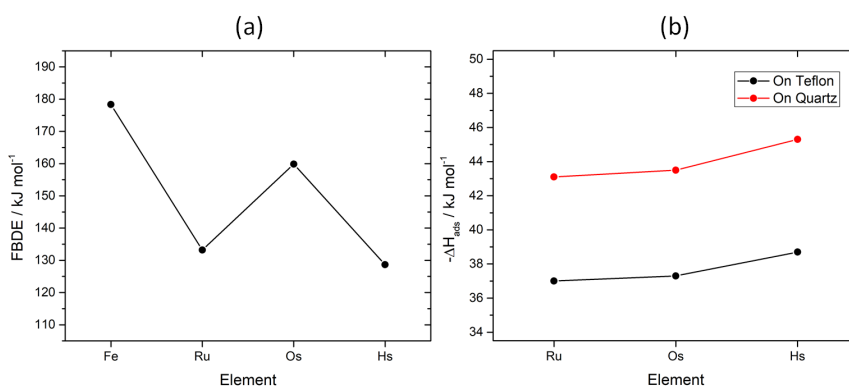


Fig. 2.25: (a) Calculated first bond dissociation energies of group-8 $M(\text{CO})_5$ carbonyl complexes and (b) predicted adsorption enthalpies via ADF (SO) on quartz and teflon surfaces. Data taken from [35]

2.5 Investigation techniques

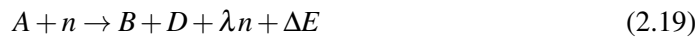
This section gives an overview about the most important techniques, necessary to understand the experimental procedures used for the evaluation of data. For more details, see the references given in the respective sections.

2.5.1 Neutron induced fission

In Sec. 2.1.1 - Sec. 2.1.3 the classical shell model and the stability of nuclei against fission have been discussed. Whereas spontaneous fission is a tunnelling process, induced fission can be observed when excitation energy is available for a compound nucleus to overcome the fission barrier. In case of neutron induced fission reactions the energy that is released by binding the neutron to the nucleus is sufficiently high to excite the nucleus above the fission barriers shown in Fig. 2.6. Considering Eq. 2.1 the binding energy is very low especially for odd numbers of protons and neutrons. As an example the fission of two different uranium isotopes can be considered: (1) For the fission of ^{235}U the fission cross section is large even for thermal energies, because the neutron binding energy is larger than the maximum of the fission barrier so that, after absorption of a neutron, the compound nucleus ^{236}U is unstable against fission. Heavy nuclei like ^{235}U with an odd number of neutrons are fissioned

by thermal neutrons with high cross-sections (586 b in case of ^{235}U), because the captured neutron is paired and the pairing energy results in an excitation energy exceeding the fission barrier, as shown in Fig. 2.6. As the neutron energy increases, the fission cross section decreases with $1/v$, with v being the velocity of neutron. (2) In ^{238}U we find the opposite case, with a barrier higher than the neutron binding energy, so that only neutrons above a threshold energy can lead the nucleus to fission. This value is called “fission threshold” and is absent in the case of ^{235}U [127].

In general, the low-energy fission can be described by Eq. 2.19:



Hereby, the fission of a nuclide A , induced by the capture of one neutron n leads to the production of two nuclides: B and D as well as the emission of λ neutrons and the emission of the energy ΔE . The released neutrons typically can be used to maintain the chain reaction of neutron-induced fission, as it is done in nuclear reactors.

In neutron induced fission reactions with thermal neutrons on targets like ^{235}U or ^{239}Pu or ^{249}Cf , predominantly asymmetric mass distributions result [128]. The illustration of the asymmetric neutron induced fission is shown in Fig. 2.26. The fission process is initiated by the capture of a neutron, which is followed by the excitation of the nucleus, which undergoes strong deformation caused by vibrations, whereas the nuclear forces act to constrain the nucleus back to the ground state shape. After about 10^{-15} s the deformation is so drastic, that the nucleus cannot recover from its critical deformation and a saddle point is reached. Due to the Coulomb repulsion the two fragments will separate after an additional 10^{-20} s (scission point). The fission fragments will release an average of two to three neutrons. Additional kinetic energy can be emitted in form of emitting γ rays. In the final step, the fission products will lose their excess energy by radioactive decay over a lengthy time period (seconds to years) before they will reach a final stable state [129].

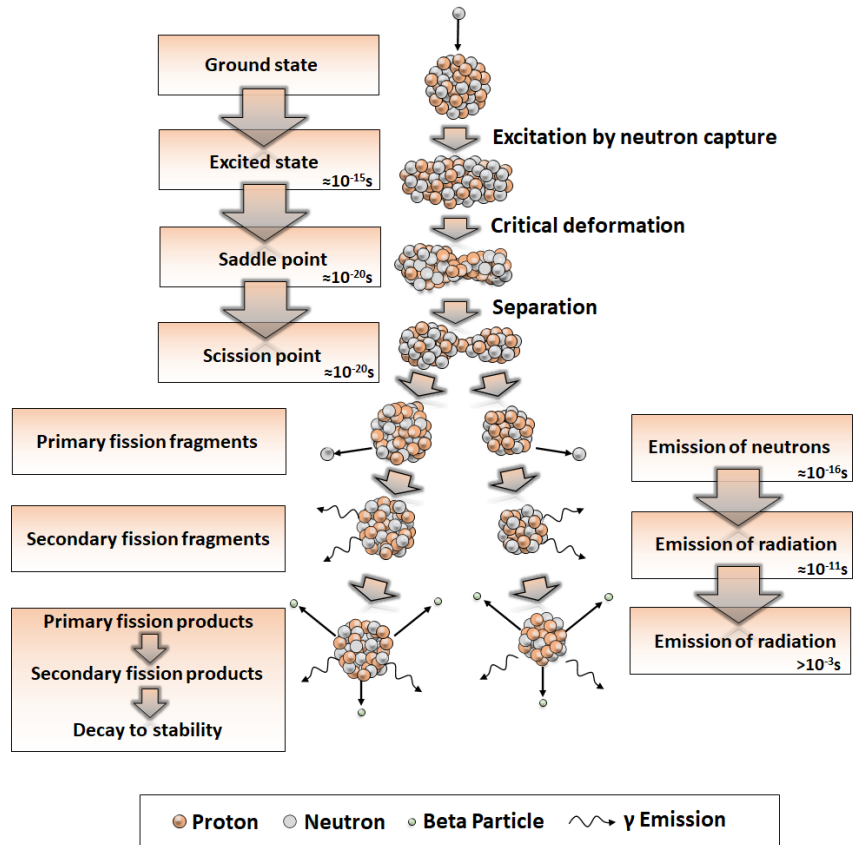


Fig. 2.26: Schematic of the different steps during nuclear fission. After neutron capture, the fission products will gain kinetic energy of up to 100 MeV, emit neutrons and γ rays until they end as stable nuclei.

The neutron induced fission of ^{235}U

The maxima for the asymmetric fission of ^{235}U are located at mass numbers $A \approx 100$ and $A \approx 138$, (cf. Fig. 2.27). Nuclides apart from the maxima are typically produced with several orders of magnitude smaller yields. The heavy-mass peak is located around the shell closure at $Z=50$ and $N=82$, which is caused by a preferred fine structure in the fission yields near closed shells.

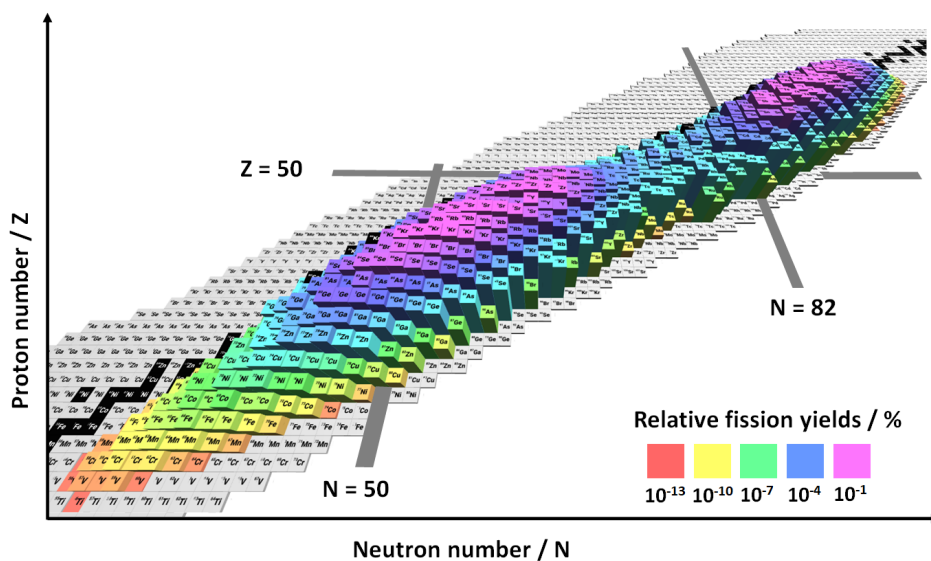


Fig. 2.27: Asymmetric thermal neutron fission yields of ^{235}U . The thermal neutron induced fission yield mass distribution shows a ratio of the heavy to light mass >1.0 for the fission of most nuclei [10].

In case of high energetic neutrons, the fission yields for ^{235}U become more symmetric due to the faster direct fission process at higher energies. In addition, other nuclear reactions like the emission of an α -particle or proton emission can occur.

2.5.2 Monte Carlo Simulation

In Sec. 2.3 some challenges for chemistry experiments with the heaviest elements are described. However, gas chromatographic experiments proved to be a powerful tool for the investigation of chemical properties of these heavy elements and therefore, chromatographic techniques are an established tool for the physico-chemical characterization of these elements, which are mostly available only in trace amounts. Therefore, comparison between experimental data and predictions on thermodynamic arguments and model calculations can be used for improving the understanding of the reaction mechanisms which are involved in chemical experiments.

A Monte Carlo Simulation (MCS) procedure based on a simple microscopic model of adsorption processes [37, 130] was developed to describe the chromatographic behaviour and the reversible adsorption/desorption of an process without superimposed chemical reaction, which takes place within a gas-chromatographic column. This MCS can be used to simulate deposition (zone) profiles or to calculate expected yields of specific chemical species for a given adsorption enthalpy ad column temperature. This MCS was already successfully used for the evaluation of isothermal online gas chromatography experiments of transactinide elements in the synthesis of a variety of compounds, such as e.g., halides, oxides and oxo-

halides [131–133].

In the Zvara model, the down stream migration of a sample molecule is described, in which the movement can be simplified as a number of effective random displacements and a sequence of adsorption/desorption events. The relevant probability density distributions are thereby derived. In Fig. 2.28 a schematic of the modeling process is shown.

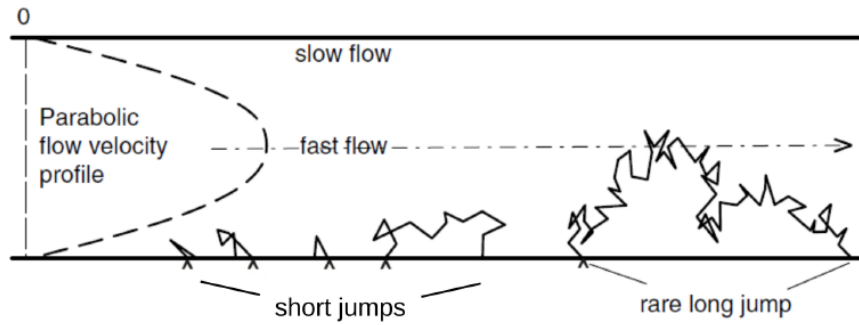


Fig. 2.28: Schematic of the description of a molecule in the downstream migration inside a chromatography column. Picture taken from [37].

The simulation is typically started with a random lifetime, based on the half-life of the isotopes. Two states can be discussed for the respective molecule: (1) the molecule is in a desorbed state, migrating in the carrier gas down stream, or (2) the molecule is adsorbed on the surface of the column. The average time which a molecule spends adsorbed on the surface $\bar{\tau}_a$ can be calculated by the total adsorption time t_{ads} divided by the number of reoccurring collision with the surface. The latter can be calculated by the mean number of collision ν_t per unit length segment and the length of the column L .

$$\bar{\tau}_a = \frac{t_{ads}}{\nu_t \cdot L} \quad (2.20)$$

In the microscopic model for the reversible adsorption and desorption, $\bar{\tau}_a$ is defined by the Frenkel equation and the period of oscillation of the adsorbed molecule in the adsorbed state perpendicular to the surface, τ_0 .

$$\bar{\tau}_a = \tau_0 \cdot \exp\left(\frac{-\Delta H_{ads}^0}{RT}\right) \quad (2.21)$$

The adsorption can be calculated in dependency of the adsorption enthalpy $-\Delta H_{ads}^0$, the universal gas constant R and the gas temperature T . τ_0 can be defined depending on the surface properties, e.g., reciprocal of Debye's phonon frequency of the column surface [134]. The adsorption process described by the Frenkel equation is strongly influenced by the temperature. The weak interaction between the molecule and the surface with, e.g., $\Delta H_{ads} \approx 25 \text{ kJ mol}^{-1}$ at STP conditions leads to only short adsorption times of $\approx \tau_a = 10^{-18} \text{ s}$ [37]. The species

migrates quickly at high temperatures and moves very slowly at low temperatures. This is indicative of a physisorption process.

The length of a jump of a respective molecule l in between two collision may vary from very short to rare long jumps. However, it should be noted that a just recently desorbed molecule has a high chance of colliding with the wall again, since the velocity of the gas in the thin layer close to the surface is rather small. Therefore, there will mostly occur very short displacements of the order of a few free paths as shown in [Fig. 2.28](#). In case of rare long jumps, the molecule needs to diffuse far enough from the wall to be carried over a rather large distance before hitting the surface again. Therefore, each jump-length can be assigned to a corresponding probability that this jump occurs, whereby the probability for very long jumps approaches zero. For a laminar flow in a cylindrical tube, the probability density distribution for a given down stream distance η can be described as:

$$\rho(\eta) = \frac{1}{\bar{\eta}} \exp\left(-\frac{\eta}{\bar{\eta}}\right) \quad (2.22)$$

With the effective mean length of the jumps $\bar{\eta}$ at high laminar carrier gas velocities:

$$\bar{\eta} = \frac{11Q}{48\pi D_{1,2}} \quad (2.23)$$

Here, Q describes the volume flow rate and $D_{1,2}$ is the diffusion coefficient. The diffusion can be described as the compensation of an imbalance in concentrations of a specific species within a gas or a fluid. It is based on a statistical movement which is described within the kinetic gas theory. According to Maxwell's velocity distribution the molecules will move in all directions statistically and will be scattered by collisions with other molecules. This results in a superimposed movement J , which is directed to the volume with a lesser concentration of the respective molecules and is directly proportional to the gradient in concentration, which is described well by Fick's law:

$$J_{1 \rightarrow 2} = D \cdot A \frac{c_1 - c_2}{\Delta x} \quad (2.24)$$

In [Eq. 2.24](#), A describes the area, which has been passed by the diffusional movement J and D is the molecule specific diffusion coefficient, which is temperature- and pressure dependent and strongly influenced by the size of the given molecules. For a binary gas mixture, the diffusion coefficient is calculated by the semi-empirical Gilliland's equation [[135](#)]:

$$D_{1,2} = \frac{0.0044 \cdot T^{3/2}}{p[(V_{m,1}^{1/3} + V_{m,2}^{1/3})]} \left(\frac{1}{M_1} + \frac{1}{M_2}\right)^{1/2} \quad (2.25)$$

In [Eq. 2.25](#), T is the temperature, p is the gas pressure, M_1 and M_2 are the molecular masses

of each gas species, as well as the molecular Volumes $V_{m,1}$ and $V_{m,2}$ of the diffusing gas and medium, respectively.

2.5.3 Electronic- and Nuclear Stopping Power

The most important parameter in the context of range determination is the so-called stopping power. It is defined as the average energy loss of a particle along a given path length in a medium. It is given by a correlation on the type of the particle and its specific energy, as well as the properties of the matter which the particle traverses. Charges play a decisive role in the interaction of atoms or ions with matter. Since the creation of an ion pair requires always a certain energy, the ionization density along a unit of length is proportional to the stopping power of the corresponding material. It is important that the particle loses energy when it traverses through media, regardless of its charge.

The stopping power $STP(E)$ is seen as a material property of the medium to be traversed, while dE/dx describes the energy loss per unit length of the corresponding particle that traverses the medium. Nonetheless, this is a description of the same phenomenon and the unit and numerical value of the quantities are considered to be identical.

$$STP(E) = -\frac{dE}{dx} \quad (2.26)$$

The term Electronic Stopping Power (STP_e) describes the reduction in kinetic energy of a particle by inelastic collisions between bound electrons within the stopping medium and the ion that passes through it. The term inelastic is used here to indicate that the collisions can result in an excitation of the bound electrons of the medium and the electron cloud of the ion [136]. It can be described as an energy transfer, based on the kinetic energy of the ion, to the electrons of the medium passed through. Since the number of collisions when passing through matter takes on a very large numerical value and the charge of the ion can constantly change during this process, it is very difficult to quantify these interactions. At this point the Electronic Stopping Power is often described as a function, which describes an average energy loss for different ion velocities [137, 138]. At high particle speeds, this effect represents the main part of the energy loss of the ions. The electronic stopping as a function of the ion velocity is depicted in Fig. 2.29 for the stopping of silicon ions in silicon targets.

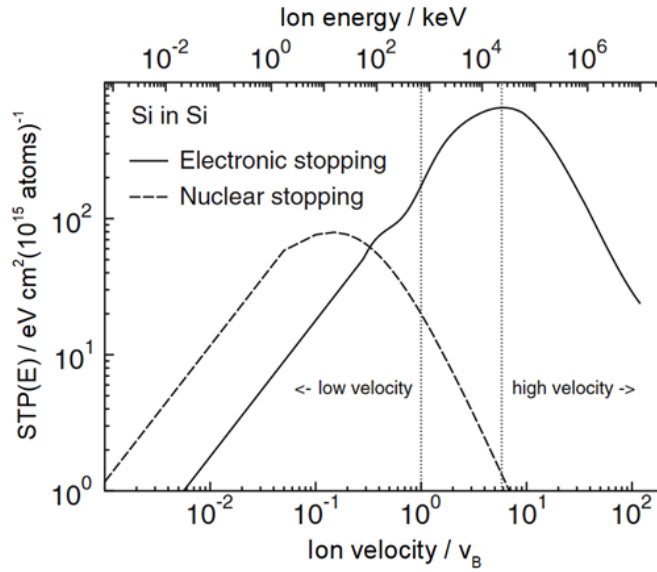


Fig. 2.29: Stopping Powers for silicon ions in a silicon target as a function of the ion velocity and the ion energy. The ion velocity is given in the units of Bohr velocity v_B . The picture is adapted from [138].

The Nuclear Stopping Power (STP_n), on the other hand, refers to elastic collisions and energy loss due to Coulombic interaction between the target and the projectile nuclei. They are less relevant at high kinetic energies of the particle. By scattering at the nuclei of the decelerating medium, according to Rutherford's theory (assuming point-like charge carriers) the trajectory of the ions can change strongly [139]. This leads to a large number of statistically distributed deflections, and therefore to a broadening of the angular distribution in the range of low energies. In the collisions, a specific fraction of the energy is also dissipated to the surrounding medium. A schematic of the STP_e and STP_n is shown in Fig. 2.30.

In general, the total stopping power is given by Eq. 2.27:

$$STP(E) = STP_e(E) + STP_n(E) \quad (2.27)$$

There are various theoretical approaches for calculating energy losses, each of which is valid in different energy ranges, starting from the classical impact theory [140], where the mean energy loss is calculated using classical mechanics [141], up to quantum mechanical theories [142] considering relativistic effects [143]. Within this thesis, the ZBL theory by Ziegler, Biersack and Littmark was used [144].

The maximum of the electronic stopping power occurs at much higher velocities than that of the nuclear stopping, (cf. Fig. 2.29). With decreasing velocity, the electronic stopping decreases before the nuclear stopping. This leads to the fact that for heavy ions, the nuclear

stopping power dominates at low velocities.

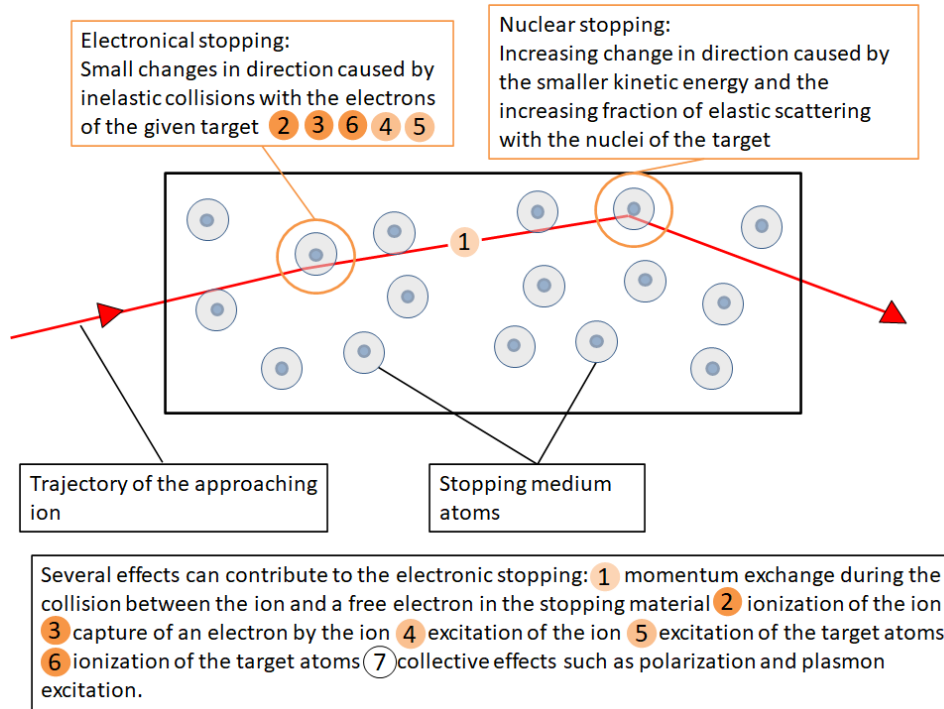


Fig. 2.30: Schematic trajectory of a particle passing through a stopping medium. The electronic stopping affects the ion both during the collision and thereafter. Between two collisions, the ion is slowed by a constant force owing to the momentum exchange with the electrons in the material (1). The energy loss during a collision is connected to electron exchange (4)+(5) between the ion and the target. In addition, charge-exchange events will occur (2)+(3)+(6).

The range of an ion in a stopping medium can be calculated by the integration of the STF, beginning with the kinetic energy the particle had when it was entering the medium, up to the kinetic energy when the particle is leaving the medium or until it is finally stopped, as shown in Eq. 2.28:

$$R = \int_0^E \frac{1}{STP(E)} dE \quad (2.28)$$

The calculation of an effective stopping power (ESP) is more complex due to its inelastic nature, whereby electrons can have charge effects on atoms of the stopping medium due to the energy dissipation of the particle, which can lead to ionization of the medium and the change of the stopping probabilities [144].

In the ZBL theory, the definition of a local charge density is used. This is based on the assumption that the interactions between the electrons of the nuclei, in every infinitesimally small volume unit, only depend on the electron density of the surrounding medium in this volume element. To calculate a stopping range, the energy loss due to a certain number of impacts (nuclear stopping power, proportional to the film thickness) is simulated, whereby

each impact is assumed to be independent of one another and the ions between the individual impacts move linearly.

The stopping power of an ion is a description of a partial loss of energy per unit of distance. As the ion traverses matter, it will continuously lose energy until the kinetic energy is reduced to zero or the material is exited. In the first case a calculation of the sum over all distance units performed to obtain a range. Alternatively, the ranges can also be calculated using the integral of the energy loss per unit distance. If one integrates over $E = 0$ to $E_0 = E_{kin,max}$, one obtains the distance which corresponds to the complete energy loss of the ion and therefore will refer to the range of the particle given in [Eq. 2.28](#):

Since the direction of movement depends on the scattering vector and therefore is dependent on the speed of the ion, a correction factor must be introduced. Only at lower velocities and a higher fraction of elastic interaction in the energy loss, a significant deviation from the direction of movement will occur and the correction factor is defined depending on the ratio of elastic to inelastic energy loss as shown in [Eq. 2.29](#):

$$\tau(E, E_0) = -\frac{\kappa}{4} \int_{E_0}^E \frac{STP_n(E) dE}{STP(E) E} \quad (2.29)$$

In [Eq. 2.29](#), κ corresponds to the mass ratio of the heavy ion fragment to the stopping material. Considering the correction factor, [Eq. 2.27](#) can be modified to give the range of an ion in matter ($R(E)$), shown in [Eq. 2.30](#):

$$R(E) = \int_0^{E_0} e^{-2\tau(E_0, E)} (STP(E))^{-1} dE \quad (2.30)$$

The experiments performed during this thesis were conducted at the research reactor TRIGA Mark II in Mainz, Germany and at the TANDEM accelerator facility at the Japan Atomic Energy Agency (JAEA) in Tokai-mura, Japan. In this chapter, the different experimental setups will be introduced. The experimental parameters and more experiment related explanations will be given in [Sec. 3.1](#) and [Sec. 3.2](#).

3.1 The research reactor TRIGA Mainz

The Training, Research, Isotope, General Atomics MARK-II (TRIGA) was established in Mainz in 1965 by the company General Atomic [145] and is a free-standing reactor associated to the Institute of Nuclear Chemistry at the Johannes Gutenberg University Mainz. The reactor core contains 76 fuel moderator elements of an alloy of uranium-zirconium-hydride (UZrH, 8 wt% uranium, 91 wt% zirconium, 1 wt% hydrogen) with an average enrichment of about 20% in ^{235}U . Each of the cylindrical elements has a length of 72.2 cm and a diameter of 3.75 cm. The reactor core is loaded with 2.3 kg of ^{235}U and is water cooled, whereby the water also serves as a moderator for the emitted neutrons. A graphite-reflector is used at the outer rings of the core grid plate for bundling of the neutrons and enhancing thermal neutron fluxes by reducing the fuel needed for criticality [146]. The reflector is surrounded by a 20 m³ reactor tank and a concrete shield [147, 148]. The reactor contains three control rods made of boron carbide (two) or boron nitride (one), each with an individual thickness and graphite containing dummy elements, filling up empty positions.

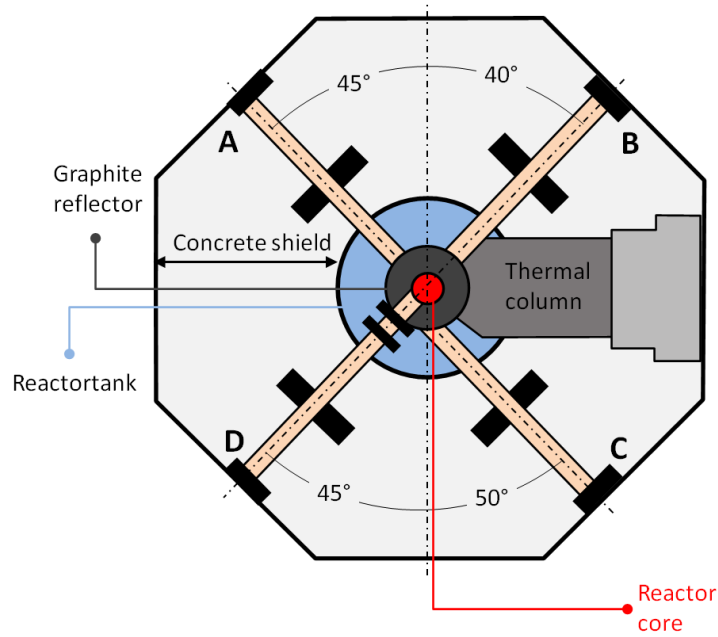


Fig. 3.1: Schematic of the beam tube arrangement at the research reactor TRIGA Mainz. The experiments described in the thesis were performed at beamport A, which offers the possibility for long-term experiments. The thermal neutron flux among the beamports varies significantly, for instance beamport D points directly at the reactor core and therefore, the neutron flux is substantially higher than at the others. The picture was taken and adapted from [148, 149]

The reactor can be operated in two different modes: (i) In the steady-state mode, in which the reactor can maintain power levels of $100 \text{ mW}_{\text{th}}$ to $100 \text{ kW}_{\text{th}}$, which corresponds to thermal neutron fluxes in the order of $10^5 \text{ n/cm}^2\text{s}$ to $10^{11} \text{ n/cm}^2\text{s}$ [148]. The maximum available neutron flux varies depending on the measurement position, for details see Tab. 3.1. (ii) The TRIGA reactor can also be operated in transient operation, the so-called pulse mode [150] with a maximum power of $250 \text{ mW}_{\text{th}}$, whereby a neutron pulse with a length of approximately (10-30) ms will be emitted with a prompt pulse energy yield of 10 MW/s. The reactor cannot maintain this overcritical state due to an inherent safety mechanism. The fuel matrix [151] moderates the neutron flux by interactions with the hydrogen in the UZrH alloy. During the transient operation mode, the maximum fuel temperature will reach $360 \text{ }^\circ\text{C}$ approximately nine seconds after the neutron pulse itself [152], whereby the moderating capacity of the UZrH alloy is reduced and the neutrons will lose less energy in collision with the hydrogen atoms due to the high thermal energy of the hydrogen itself. Thus the neutrons will cause fewer fissions due to the smaller neutron capture cross section for the higher energetic neutrons of the ^{235}U and will escape to the water. Hence, the chain reaction will be aborted in a few milliseconds.

The TRIGA reactor offers four measurement positions for the irradiation of samples in

the reactor core. The central experiment tube (CET), which reaches vertically from the reactor platform in the center of the core, and three pneumatic transfer tubes (PTS) which are connected to the surrounding laboratories and are located in the periphery of the core. The reactor core is surrounded by a rotary specimen rack which can be used for isotope production and neutron activation analysis and offers 40 different irradiation positions at a rather constant neutron flux, whereby a sample will continuously rotate around the core. The thermal column offers a lower thermal neutron flux. It is covered by 13 mm of aluminium and has a boral liner. The front part is connected to the reactor core and widens towards its cuboid main part. The complete volume of the column is filled with graphite, hence providing an isotropic, predominantly thermal neutron field. All thermal neutron fluxes available at the TRIGA Mainz are summarized in [Tab. 3.1](#).

Tab. 3.1: *Thermal neutron fluxes at different irradiation positions at the TRIGA MARK II research reactor in Mainz.*

Irradiation position	Sample positions	Thermal neutron flux / n/cm²sW
Central experiment tube	1	4.0 x 10 ⁷
Pneumatic transfer system	3	2.0 x 10 ⁷
Rotary specimen rack	40	7.0 x 10 ⁶
Radial beam tubes	4	5.0 x 10 ⁵ to 5.0 x 10 ⁶
Thermal column	1	3.0 x 10 ² to 2.0 x 10 ⁵

3.1.1 The target chamber at the TRIGA Mainz

The target chamber of the TRIGA research reactor offers three connectors, two lateral and a central one, to which tubes can be attached. One lateral port is designated to connect to a pressure gauge to monitor the pressure inside the target chamber. The second lateral port is used as a gas-inlet whereby the gas is guided into a volume behind the target from which it can stream through holes in the back-plate of the target holder into the inner volume of the TC. Details can be seen in [Fig. 3.2](#). Fission products emitted from the target will be thermalized inside the gas volume and guided through the central exit towards the reaction chamber.

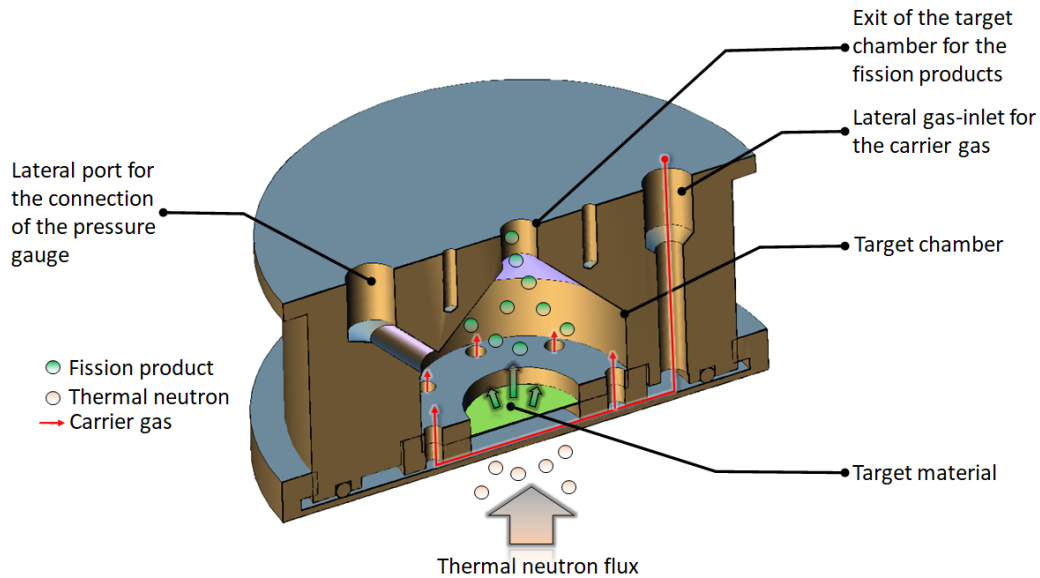


Fig. 3.2: Schematic of the original target chamber which is placed inside of beamport A close to the core. The carrier gas (red line) enters the chamber through a lateral inlet. The fission products (green circles) produced by neutron induced fission will be extracted through the central exit port.

3.1.2 The target and the target-holder of the TRIGA Mainz

The target-holder used for the experiments at the TRIGA Mainz is made out of two plates. The target is typically made by molecular plating [153, 154] and therefore, will be deposited on a thin metallic foil. This thin metal foil can be held in position between this two plates (cf. Fig. 3.4).

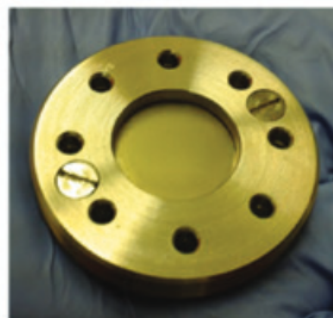


Fig. 3.3: Target-holder of the TRIGA Mainz. The front- and back-plate of the target-holder hold the target in place between of each other. The eight surrounding holes, which offer a possibility for the gas to enter the target chamber are also visible.

The target usually faces towards the front-plate through a 18 mm hole in the middle of the target holder, which is also limiting the maximum target area available at the TRIGA Mainz, whereby typically sizes of approximately 15 mm will be used. The target itself is surrounded by eight holes, which will guide the carrier gas from a gas volume behind the target to the inner volume of the TC, on the bottom of which the target can be mounted. A schematic showing the gas flow around the target are depicted in schematic Fig. 3.4. Both plates are kept together by two 3 mm screws. The entire target-holder has a diameter of 41 mm, whereby the maximum distance between two gas outlets is 34 mm.

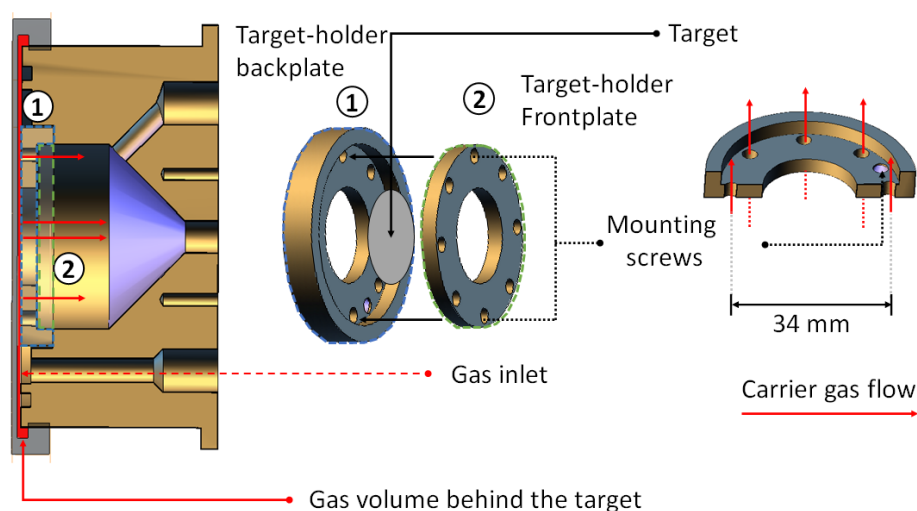


Fig. 3.4: Schematic of the target-holder in side- and isometric view. The target-holder consists of two parts: (1) Back-plate and (2) Front-plate.)

The target-holder offers the possibility to clamp a cover foil over the target on the side facing the inner volume of the chamber. This foil typically serves to suppress fission products of the heavy mass peak. These fission products have a shorter residual range in matter than those of the light mass peak. However, some fission products from the heavy mass branch which have high kinetic energies and were produced with high cumulative yields, can usually penetrate the cover foil and will not be completely stopped by the cover foil.

3.1.3 The modified target chamber for carbonyl experiments

For the carbonyl experiments, the target chamber usually used for experiments at the TRIGA Mainz is modified, so that a second chamber, the so called reaction chamber (RC) could be mounted on the exit of the original target chamber, which will be called thermalization chamber (TC) within this thesis to avoid misunderstanding. The TC was made from titanium with a depth of 32 mm and an diameter of 35 mm. A picture of the disassembled TC is shown in Fig. 3.6(a), whereby Fig. 3.6(b) depicts the chamber in its assembled state.

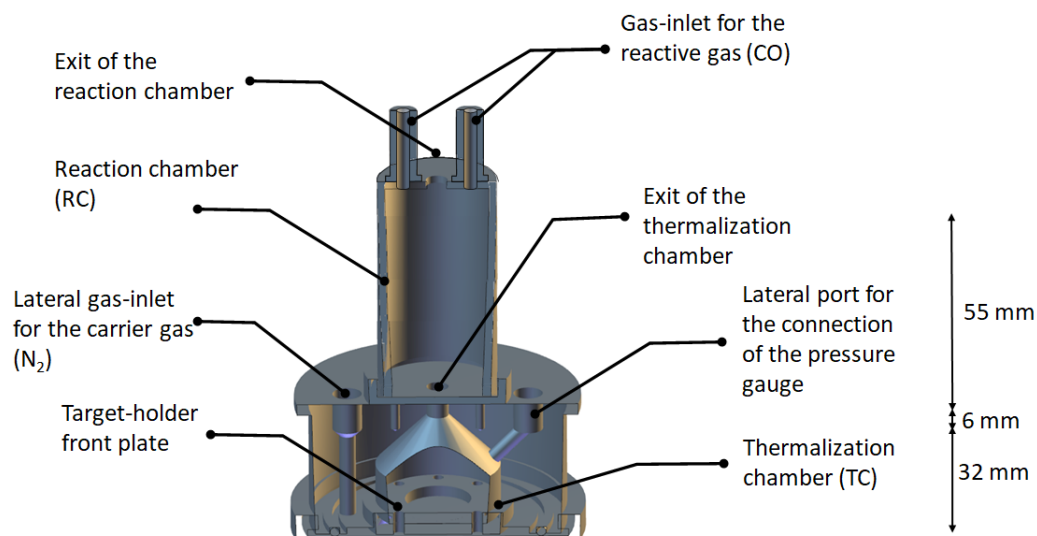


Fig. 3.5: Schematic of the modified thermalization chamber which is placed inside of beam-port A. The thermalization chamber can be flushed with a carrier gas (nitrogen) and the reactive gas can be introduced separately into the reaction chamber, which can be mounted on the former exit of the thermalization chamber.

The RC is usually mounted directly on the exit of the TC. The gas has to pass through a small connection piece with a length and a diameter of 6 mm each, to reach the RC. During the experiments, the dimensions of this connection piece could be changed by inserting a small aperture, which increased the length of the connection to 8 mm, with an inner diameter of 4 mm. The RC is made from titanium and has a diameter of 18 mm and a depth of 55 mm and offers 3 ports. Two of these ports can be used as gas-inlets for the reactive gas or for the connection of a pressure gauge to monitor the pressure inside the RC. On the gas-outlet a pneumatic push-fit connector made out of Polytetrafluoroethylene (PTFE, from SERTO, type FP3), could be mounted. This push-fit connector allows the direct connection of the gas-outlet to a capillary with an inner diameter of 4 mm, which was made out of PTFE, to guide the gas to the detection system.

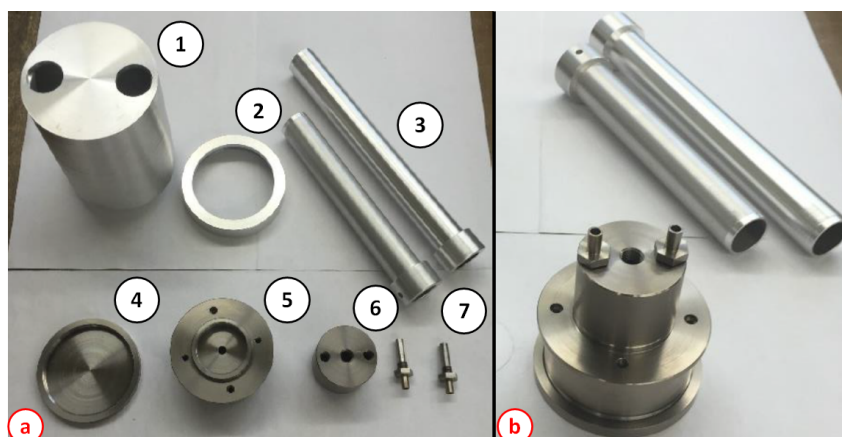


Fig. 3.6: (a): The modified target chamber consists of 7 main elements shown in its disassembled state: (1) Aluminum shell of the chamber (2) Screw bracket of the aluminum shell (3) Aluminum shells for the connection ports of the chamber (4) Back-plate of the target chamber (5) Thermalization chamber (6) Reaction chamber (7) Connections for the gas inlets of the reaction chamber (b) Target chamber in its assembled state.

3.1.4 The gas-transport and gas purification system (GPS) at the TRIGA Mainz

For carbonyl experiments a simple gas flow system was implemented, which was directly connected to the exhaust. Nitrogen with a purity of 99.999 vol.% was used as a carrier gas and carbon monoxide with a purity of 99.997 vol.% was used as reactive gas. Notable impurities include oxygen, nitrogen, argon (<25 ppm), hydrogen (1 ppm by volume) and water (<3 ppm). Both gases were purified by using purification cartridges to remove unwanted impurities whereby the applied processes are based on chemisorption and physisorption. The reactive components and specifications of the cartridges are given in the appendix. For the removal of moisture and oxygen, the following cartridges were used:

Moisture: Spectromol hydrosorb (SPECTRON INC, moisture content: <20 ppb) and MT Series molecular sieve 13X and 4 moisture trap (Agilent, MT400-4, maximum moisture: <14 ppb). Physisorption of moisture on Silica gel or SICAPENT (Phosphorpentoxide).

Oxygen: Spectromol oxisorb (SPECTRON INC, maximum oxygen: <5 ppb). Chemisorption of oxygen on the Silica gel with chromium oxide.

The gas flow was regulated by mass flow controllers (MKS Type 1179-B and GE-50-A) from MKS instruments, whereby the mass flow readout was realized with two PR-4000B control units from MKS instruments. A third PR-4000B was used for monitoring the pressure of

both chambers with two 628F-Baratron capacitance manometers from MKS instruments. A schematic of the experimental setup is depicted in Fig. 3.7.

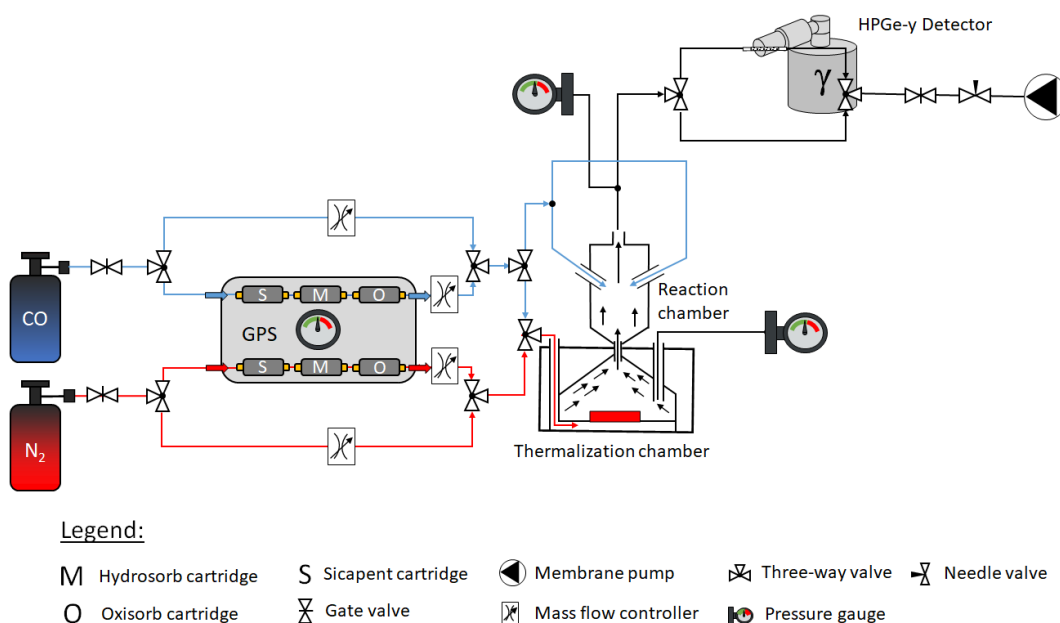


Fig. 3.7: Simplified schematic of the experimental setup used for the experiments at the TRIGA Mainz. The respective gases were introduced via the gas purification system (GPS). Nitrogen and carbon monoxide could be fed into the TC, whereas the RC could only be flushed with carbon monoxide. The pressure was monitored inside the GPS and both chambers. For more details, see text.

For the tubing, PTFE was used, since it offers less diffusion of oxygen through the capillary into the used gases than the usually used Polyethylene tubing. It should be mentioned that the condition of the PTFE was tested every day before beam operation was started, due to a rising brittleness of the material when it is exposed to the neutron field of the reactor. In addition to the PTFE, stainless steel tubing was used for all non-flexible parts of the setup, which includes all tubing leading into the beamport and out of the beamport. Only tubes with an inner diameter of 4 mm were used, whereby the charcoal filters were connected to the tubing with pneumatic fittings type QSM-6 from FESTO. A schematic of these tools is depicted in Fig. 3.8. These pneumatic quick connectors allowed a fast sampling procedure.

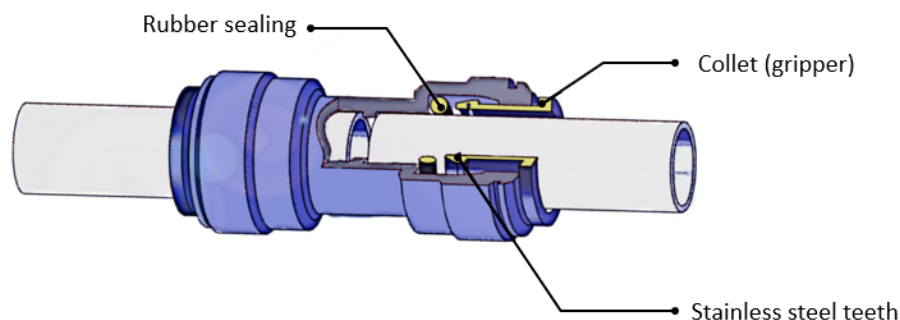


Fig. 3.8: The pneumatic fitting type QSM-6 provides a leakproof sealing up to 14 bar. A collet keeps the capillary in position by the help of small stainless steel teeth.

3.1.5 The modified gas-transport and gas purification system (GPS) for the QMS measurements

In Fig. 3.9 a simplified scheme of the gas composition measurements utilizing a Quadrupole Mass Spectrometer (QMS) is depicted. The system was used for two different series of measurements: (a) Investigation of a possible back diffusion of carbon monoxide from the reaction- into the thermalization chamber and (b) investigation if the carbonyl formation is catalysed by an active species (impurity) within the used gases. For the former, the experimental setup which was also used during the online measurements described in this previous section (cf. Sec. 3.1.4) was replicated. The gas purification system was also identical to that used in the previous measurements.

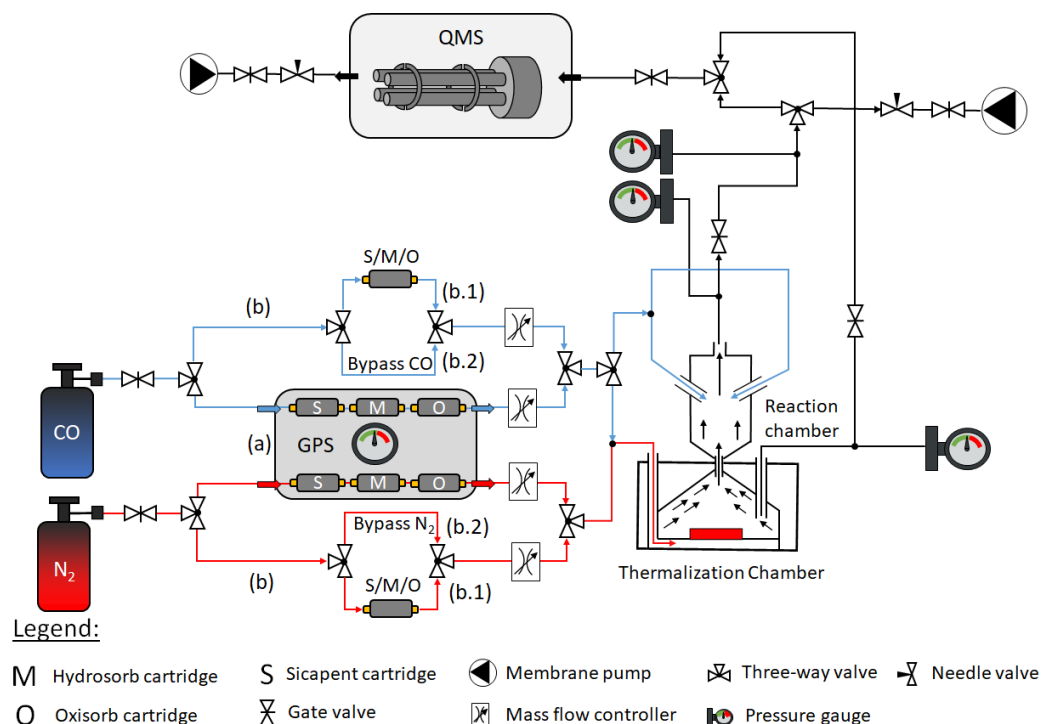


Fig. 3.9: Schematic of the experimental setup used for the mass spectrometry measurements. The respective gases were either introduced: (a) via the gas purification system (GPS) used during the experiments at TRIGA or (b) via a bypass, which either allowed the installation of specific purification cartridges or any combination of them (b.1) or was directly connected to the two-chamber system (b.2). The nitrogen gas was introduced into the thermalization chamber (TC), whereas the carbon monoxide gas was connected to the reaction chamber (RC). Samples could be extracted from either, the TC and the RC and were transported to the quadrupole mass analyzer (QMS).

For the investigation of back diffusion, the nitrogen-line was connected to the thermalization chamber, whereas the carbon monoxide was fed into the reaction chamber. A quadrupole mass analyser type Microvision 2, LM105-00512010 from MKS instruments was connected to the exit of both chambers, whereby the flow was regulated by two needle valves to ensure optimal sampling conditions for the QMS. During the back diffusion measurements, samples were exclusively taken out of the thermalization chamber and the experimental conditions from the online measurements were imitated. No transition piece was used in between TC and RC.

3.1.6 Charcoal filter and detection system

Filters consisting of PTFE tubes with an inner diameter of 4 mm were used to adsorb the volatile metal-carbonyl complexes. Each filter was made by filling a 8 cm long tube with ≈ 250 mg activated charcoal from MERCK (Type: extra pure) with a particle size in between of (20-40) mesh. On both sides of the charcoal, quartz wool plugs were added,

to keep the charcoal in position. For the measurements performed in high-flow regimes ($>1000 \text{ mL min}^{-1}$ total flow-rate) a blocker was added to prevent the charcoal from being blown through. The blocker was made out of a PTFE tube with an outer diameter of 4 mm and an inner diameter of 2 mm and was just added at each side. A schematic of the used charcoal filters is shown in Fig. 3.10.

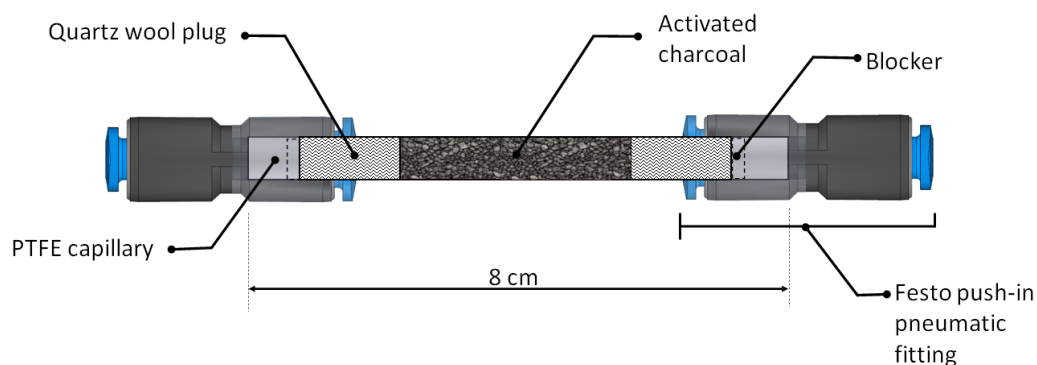


Fig. 3.10: Schematic of the used charcoal filters, plugged into two push-in fittings from FESTO. The filters could be used up to flow-rates of 1500 mL min^{-1} .

For all measurements performed at the TRIGA Mainz, a germanium detector type EG&G Ortec GEM-50195 S with an efficiency of 55 % was used. The corresponding γ spectra were analysed with the computer program GENIE 2000, whereby the respective γ lines were identified by their γ energies listed in [155]. The identification of the primary- and secondary fission products was realized in conjunction with the computer program [156], based on the ENDF-349 database published from England et al. [157].

3.2 The JAEA tandem Accelerator facility

The tandem accelerator at JAEA Tokai was established in 1982 and was built up by National Electrostatic Corp. (NEC, Wisconsin, USA). The model 20 UR Pelletron accelerator was commissioned at a terminal voltage of up to 18 MV with both, continuous and pulsed beams for heavy ion experiments. The electrostatic accelerator is installed in vertical configuration inside a tank filled with 5.5 bar SF_6 insulating gas. The accelerator column including the high voltage terminal is 16 m high and is placed inside of a high pressure vessel of 8.2 m in diameter and 26 m in height. [158]. A pellet chain, which is made out of short conductive tubes connected by links made of insulating material, is used to deliver charge to the terminal in order to generate high voltage [159]. The injection energy for negative ions is in between of 50 keV up to 350 keV. The tandem accelerator is a type of electrostatic accelerator [160], where negative ions are produced at ground potential and will pass a mass analyzing magnet. The ions then will be accelerated to a high-voltage positive terminal. Inside the terminal, the fast moving negative ions are stripped of electrons by a thin carbon foil, and switch into a positive charge state. The stripped positive ions are bent back by a 180 degree bending

and charge analyzing magnet. After passing the magnet, the ions then receive an additional acceleration from the terminal to the ground potential. Thus, the ions receive two stages of acceleration as shown in Fig. 3.11. The maximum beam current available is in the order of several particle microamperes (μA , e.g.: Hydrogen: $3 \mu\text{A}$) [161].

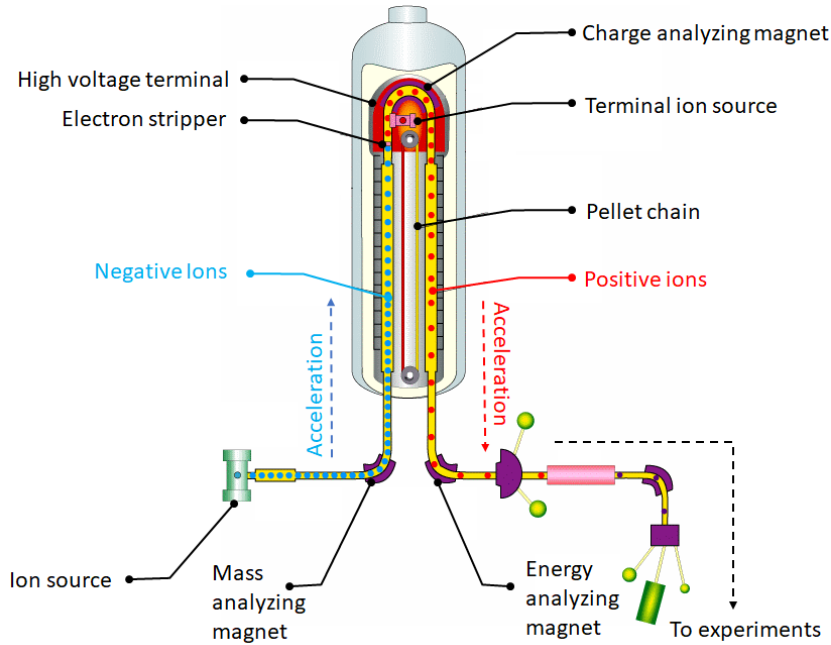


Fig. 3.11: Simplified schematic of the tandem accelerator facility. Ions will be produced by a pellet chain and will be accelerated in two stages. First, in the form of negative ions up to the high voltage terminal and after electron stripping, downwards as positively charged ions. Figure taken and adapted from Ref. [161]

The JAEA tandem facility comprises a total of ten different beamlines and a linear accelerator (LINAC) Booster. The accelerator can provide ion beams from hydrogen to bismuth with different beam intensities and energies. The different beamlines are distributed among five research rooms as shown in figure Fig. 3.12. The superconducting booster can provide an additional step of ion acceleration, in order to provide access to nuclear reactions between any combination of projectile ions and target elements up to a mass number of about 200 amu [161]. The beam size of the accelerator is rather small with a diameter of 1 mm only. The experiments described in this thesis were conducted at the R-2 beamline.

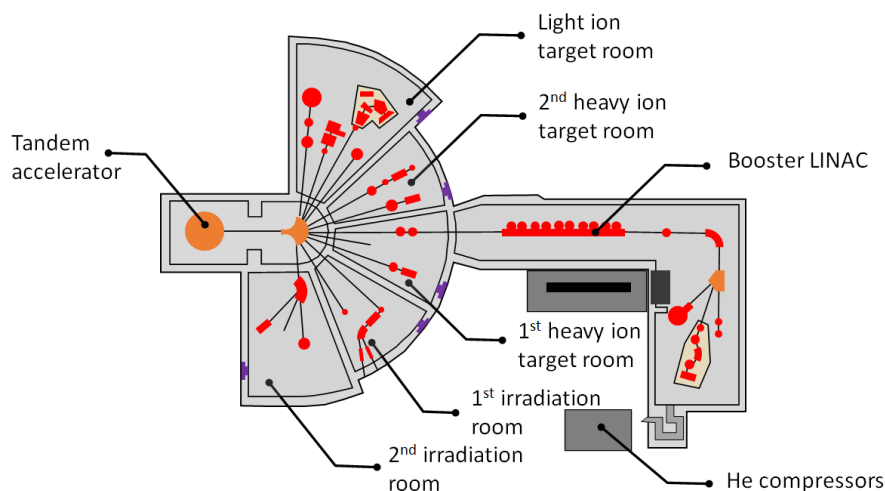


Fig. 3.12: Schematic of the JAEA tandem research facility. The tandem accelerator provides ion beams ten beam lines, distributed among 5 different research rooms. The JAEA tandem accelerator also includes a LINAC booster, which can be used as an additional "third" acceleration step for heavy ions. Figure was adapted from [161].

3.2.1 The target chamber of the JAEA tandem accelerator

For the experiments performed at the JAEA tandem accelerator a newly designed combined chamber system (TC + RC) was used. The new design was based on insights gained from the experiments with the TC of the TRIGA Mainz described in [Sec. 3.1.1](#).

For the experiments a newly designed double-chamber setup was developed, which is depicted in [Fig. 3.13](#). The TC and RC are built as one single module to fit into the beamline of the tandem accelerator. The entire module is made from stainless steel, coated with a thin teflon layer. At the entrance of the chamber, a metal foil (window) can be mounted. Behind the target the TC offers a gas volume with a diameter of 30 mm and a depth of 25 mm, whereas the RC had a diameter of 30 mm and a depth of 78 mm (volume: 55.1 cm³). The TC has one gas-inlet, which is mounted perpendicularly to the beam axis, for the introduction of the carrier gas. The reaction chamber is attached to the exit of the TC and offers a total of four gas-inlets for the introduction of the reactive gas and one gas-outlet usually connected to the capillary which is guiding the gas towards the chemistry laboratory. A schematic of both chambers is shown in [Fig. 3.13](#)

In the design of this chamber a novel nozzle-system is implemented. This novel nozzle-system allows the collection of the non-volatile fusion products directly at the conical tapering by the carbon monoxide gas stream. The connection piece resembled a nozzle that

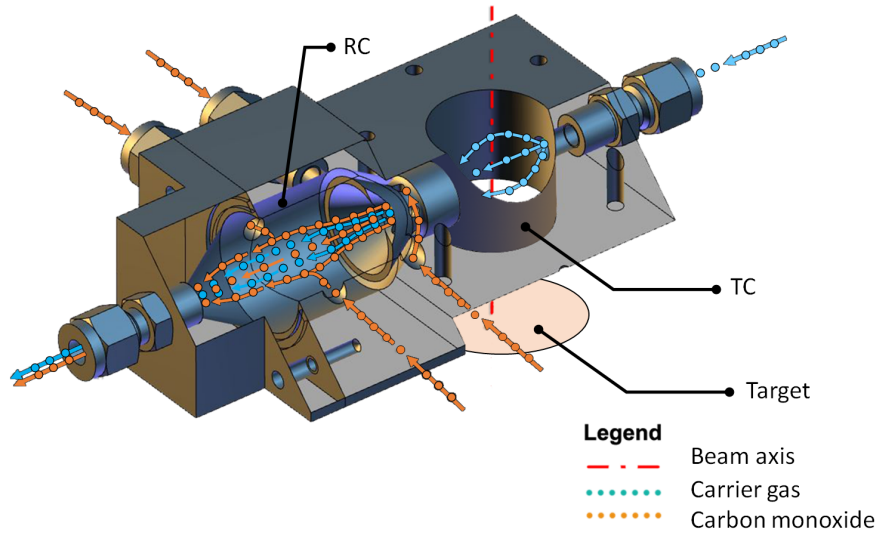


Fig. 3.13: *Isometric view of the thermalization- (TC) and the reaction chamber (RC). The TC is mounted perpendicularly to the beam axis and flushed with the carrier gas (He/Ar in a mixture of 9:1, shown as blue dots). The gas is guided into a conically-shaped nozzle. Carbon monoxide was introduced through gas inlets inside the nozzle directly behind the tapering (shown as orange dots). Additional carbon monoxide was introduced to the RC over two further inlets in the middle of the chamber.*

converges conically on both sides to avoid diffusion related wall collisions inside the narrow connection. A detailed view on the gas-stream and the newly designed nozzle-connection is depicted in Fig. 3.14.

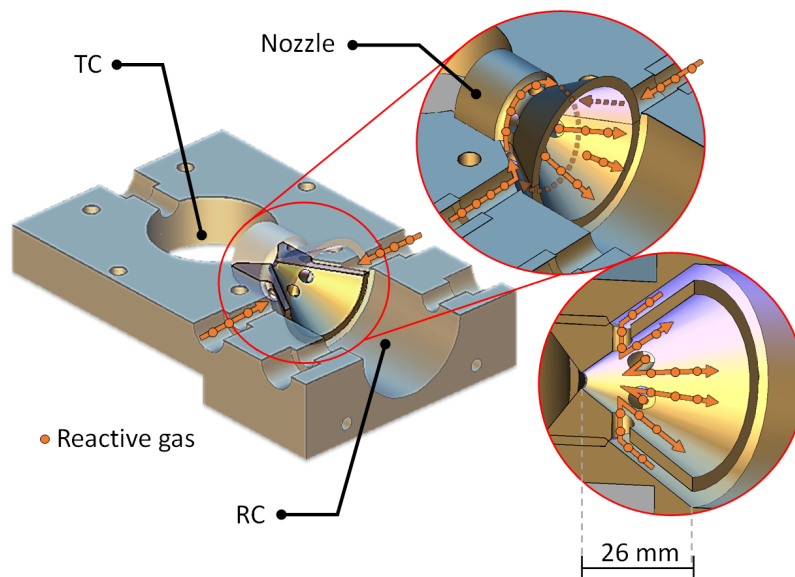


Fig. 3.14: Isometric view of the thermalization- (TC) and the reaction chamber (RC) in conjunction with the newly designed nozzle connecting the two chambers. The gas flow of the reactive gas (CO) is shown in orange.

The nozzle has a length of 26 mm in total and converges conically on both sides. A direct connection between the two chambers is established by a hole with a diameter of 3 mm in the center of the nozzle for the standard transition piece. In total, four different nozzles were prepared for the experiment, covering hole sizes of 2 mm up to 5 mm. The reactive gas can be fed into a small volume next to the nozzle via the SWAGELOK connection. This small volume is directly connected to the inner volume of the RC, but also directs a certain fraction of the reactive gas into the nozzle. The nozzle offers six drilled holes which are arranged in a circle around the central connection hole to feed the gas directly behind the tapering into the reaction chamber.

When designing the nozzle, it was taken into account that the narrowest point should be as short as possible to reduce losses caused by lateral diffusion. The conical shape of the nozzle should suppress back diffusion of carbon monoxide from the RC into the TC. In addition, the carbon monoxide reactive gas should be introduced as close as possible to the tapering to increase the chance of carbonyl complex formation.

3.2.2 The gas-transport and gas purification system (GPS) at the JAEA tandem accelerator

For the experiments at the JAEA tandem accelerator a similar open gas system as described in [Sec. 3.1.6](#) was used. Only gases of high purity were used during the experiment. Therefore, helium and argon with a purity of 99.999 vol.% were used as carrier gases in addition to the carbon monoxide reactive gas with a purity of 99.997 vol.%. Similar to the experiments at the TRIGA Mainz, a GPS was used to reduce unwanted impurities including oxygen (<3 ppm) and moisture (<3 ppm). Additional notable impurities are: hydrocarbons (<0.2 ppm), nitrogen (<5 ppm) and hydrogen (<1 ppm). The GPS was improved compared to the previous TRIGA experiments, whereby again gas purification cartridges were used to remove unwanted impurities. The existing GPS was modified by adding Big Oxygen Traps (BOT Series), which are extra large gas purifiers (750 cm³ Big Traps), ideal for bulk purification applications and for open gas systems, due to their enlarged active volume for the adsorption of impurities in a single pass through. The reactive components and specifications of the cartridges are given in the appendix. For the removal of moisture and oxygen, the following cartridges were used:

Moisture: Spectromol hydrosorb (SPECTRON INC, moisture content: <20 ppb) and MT Series molecular sieve 13X, 4 moisture trap (Agilent, MT400-4, maximum moisture: <14 ppb) and Big Moisture Trap (Agilent, BMT-4, maximum moisture: <20 ppb). Physisorption of moisture on Silica gel or SICAPENT (Phosphorpentoxide).

Oxygen: Spectromol oxisorb (SPECTRON INC, maximum oxygen: <5 ppb) and Big Oxygen Trap (Agilent, BOT-4, maximum oxygen: <5 ppb). Chemisorption of oxygen on the Silica gel with chromium oxide.

During the experiments, the mass flow readout was realized with a 946-vacuum system controller from MKS instruments and one PR-4000B control unit from MKS instruments. The pressure inside the chambers was monitored with a digital manometer (Yokogawa, type 2654) at the carrier gas inlet, whereas the pressure inside the GPS was monitored with a 628F-Baratron capacity manometer (MKS instruments). A simplified schematic of the experimental setup is depicted in [Fig. 3.15](#).

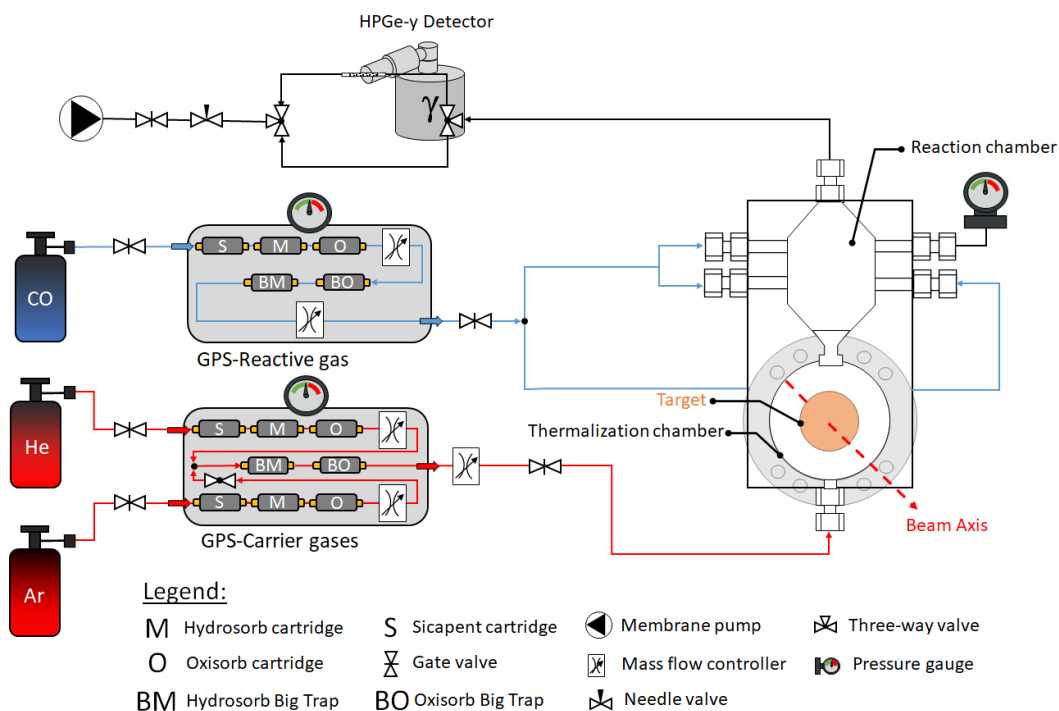


Fig. 3.15: Simplified schematic of the experimental setup used for the experiments at the JAEA tandem accelerator. The respective gases were introduced via the gas purification systems (GPS-Reactive gas, GPS-Carrier gases). A mixture of helium and argon was used as carrier gas, whereas carbon monoxide remains the reactive gas. The pressure was monitored inside the gas system and both chambers. For more details, see text.

Tubes made out of stainless steel with an inner diameter of 4 mm were used for the GPS. The gas-inlets were connected with short PTFE tubes (<10 cm) with an inner diameter of 4 mm to add more flexibility to the system, needed for dismantling the chamber. The gas-outlet was connected to a 30 m long PTFE tube, also with an inner diameter of 4 mm, which was connected to the chemistry laboratory.

3.2.3 Charcoal filter and detection system

The preparation of the charcoal filters was identical to that for the previously described TRIGA experiments (cf. Sec. 3.1.6). For the γ -spectrometry a HPGe-detector (Ortec, GMX type) was used to assess γ emitting nuclides. The corresponding γ spectra were analysed with the computer program GENIE 2000, whereby the respective γ lines were identified by their γ energies listed in [155].

4.1 Experimental parameters

The synthesis of 4d transition metal carbonyl complexes within the two-chamber approach was investigated using short-lived fission products produced via $^{235}\text{U}(n,f)$ at the research reactor TRIGA Mainz [148] and via $^{248}\text{Cm}(sf)$. A schematic of the setup is shown in Fig. 3.7. A cut-out of the chart of nuclides showing the isotopes relevant to this work is shown in Fig. 4.1.

Ru 100 stable 5.6E-6% 2.1E-10%	Ru 101 stable 5.17% 1.6 E-8%	Ru 102 stable 4.30% 9.8 E-7%	Ru 103 39.2 d 4.80% 3.03% 2.4 E-5%	Ru 104 stable 1.88% 3.4 E-4%	Ru 105 4.44 h 0.96% 1.1 E-7%	Ru 106 374 d 0.40% 9.1 E-7%	Ru 107 3.75 m 0.15% 4.9 E-6%	Ru 108 4.55 m 0.05% 1.7 E-5%	Ru 109 34.5 s 0.03% 8.6 E-4%	Ru 110 14.6 s 0.03% 0.01%
Tc 99 6.0 h 5.38% 2.9E-8%	Tc 100 2.1E5 a 6.11% 1.2E-7%	Tc 101 15.8 s 5.59E-6% 5.59E-6%	Tc 102 14.2 m 5.17% 1.61 E-4%	Tc 103 4.3 m 5.3 s 4.29% 0.22% 9.6E-3%	Tc 104 54.2 s 3.03% 0.08%	Tc 105 18.3 m 1.88% 0.09%	Tc 106 7.60 m 0.96% 0.05%	Tc 107 35.6 s 0.40% 0.03%	Tc 108 21.2 s 0.15% 0.02%	Tc 109 5.17 s 0.05% 0.02%
Mo 98 stable 5.79% 9.6 E-5%	Mo 99 65.9 h 6.11% 0.04%	Mo 100 7.1E19 a 6.29% 0.07%	Mo 101 14.6 m 5.17% 0.19%	Mo 102 11.3 m 4.28% 0.65%	Mo 103 67.5 s 2.95% 1.04%	Mo 104 60.0 s 1.79% 1.13%	Mo 105 35.6 s 0.92% 0.67%	Mo 106 8.40 s 0.38% 0.36%	Mo 107 3.50 s 0.12% 0.12%	Mo 108 1.09 s 0.03% 0.03%
Nb 97 52.7 s 5.63% 2.5E-3%	Nb 98 72.1 m 6.00% 0.01%	Nb 99 51.3 m 2.86 s 0.04% 5.75% 0.12%	Nb 100 2.6 m 15.0 s 2.10% 3.97% 0.41% 0.03%	Nb 101 2.99 s 1.50 s 3.11% 3.11% 0.32% 0.32%	Nb 102 7.10 s 4.99% 1.92%	Nb 103 4.3 s 1.3 s 1.50 s 0.92 s 4.8 s 1.91% 0.29% 0.37% 0.29% 0.29%	Nb 104 0.92 s 4.8 s 0.25% 0.14%	Nb 105 2.95 s 0.38% 0.14%	Nb 106 1.06 s 0.12% 0.02%	Nb 107 330 ms 2.3E-3% 2.3E-3%
Zr 96 3.9E19 a 6.34% 0.34%	Zr 97 16.8 h 5.98% 1.09%	Zr 98 30.7 s 5.64% 2.57%	Zr 99 2.20 s 5.63% 3.58%	Zr 100 7.10 s 5.58% 4.98%	Zr 101 2.30 s 3.07% 2.79%	Zr 102 2.90 s 2.05% 1.78%	Zr 103 1.38 s 0.50% 0.50%	Zr 104 920 ms 0.08% 0.08%	Zr 105 670 ms 0.12% 0.12%	Zr 106 186 ms 1.6E-6% 1.6E-6%

Fig. 4.1: Cut-out of the chart of nuclides, including their half-lives and independent-, as well as cumulative yields in the neutron induced fission reaction of ^{235}U . Data is taken from the ENDF/B-VI fission library.

The TRIGA was operated in continuous operation mode, providing a thermal neutron flux of $9.8 \cdot 10^{10}$ neutrons/cm²s. The thermalization chamber (TC) was equipped with a ^{235}U -target or a ^{248}Cm -source and was flushed with inert gas. The ^{235}U -target was made by molecular plating [153, 154], containing 1100 μg ^{235}U segregated over a spot of 15 mm in diameter, corresponding to an areal density of 625 $\mu\text{g}/\text{cm}^2$. The ^{235}U -target was covered with a 10 μm aluminum foil to suppress fission products of the heavy mass branch, which have a shorter residual range in matter than those of the light mass peak. Still, some fission products from the heavy mass branch which had high kinetic energies and were produced with high cumulative yields (e.g., ^{138}I , ^{131}Te and ^{134}Te), could be identified in the corresponding γ spectra and were not completely removed by the aluminum foil, cf. Fig. 4.3 and Fig. 4.4. The ^{248}Cm -source was also deposited by molecular plating over a spot of 6 mm in diameter,

containing a total activity of 1 kBq, corresponding to an areal density of $389 \mu\text{g}/\text{cm}^2$. The ^{248}Cm was used as a spontaneous fission source, owing to its fission branch of 8.4 %.

The performed measurement series are summarized in [Tab. 4.1](#). The procedure for feeding the gases into their respective chambers was identical for all measurements as follows: after evacuating both chambers, N_2 was fed into the TC to establish the pressure needed for the next measurement. After this pressure was reached, CO was added into the system (into the RC for ϵ_{Tot} or TC for ϵ_{Ref}) and the needle valves in front of the pumping system were adjusted to increase the pumping capacity as needed to maintain this pressure. The effect of back-diffusion of carbon monoxide from the RC into the TC was investigated in preceding offline studies, where the setup was connected to a quadrupole mass analyser (Microvision 2, MKS instruments). Note that the masses of CO and N_2 are identical. However, CO -decomposition inside the QMS leads to a signal rise on masses 12 and 16. This was sensitive to the presence of 1% or more CO in pure N_2 . No signal increase was observed, though, which allows placing an upper limit of 1% for the CO -content in the N_2 inside the TC.

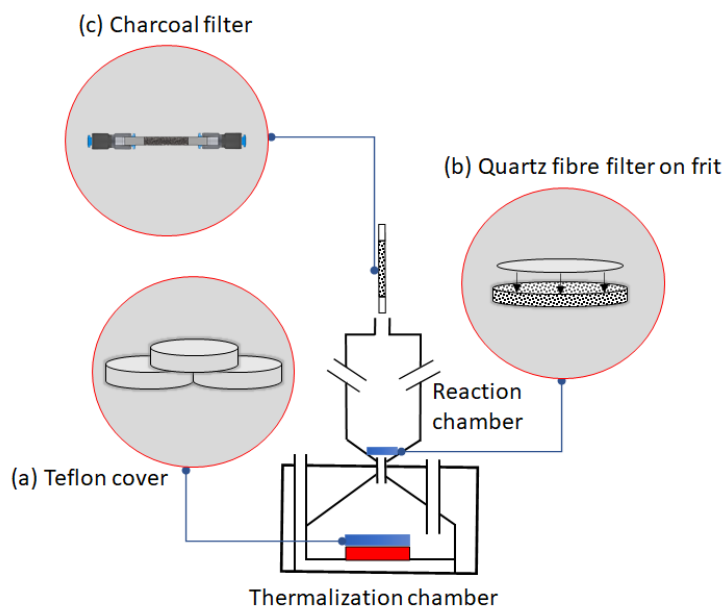


Fig. 4.2: Schematic of all measurement positions where samples could be taken. For details see text.

The original thermalization chamber of the TRIGA Mainz, which had a depth of 32 mm and an diameter of 35 mm, had been modified to allow the reaction chamber to be mounted directly onto its exit. Gas, which was fed into the TC, had to pass through a small transition piece with a length of 6 mm and a diameter of 4 mm to reach the RC. The RC itself had a diameter of 18 mm and a depth of 55 mm. Samples could be taken at three different

positions shown in Fig. 4.2. The direct catch measurement, taken at position (a), was used as a reference for the calculation of absolute yields, whereas the flush-out measurement, taken at position (b) allowed determining the fraction of radioisotopes that reached the reaction chamber (ϵ_{Flush}). Samples taken at position (c) were used to determine the overall efficiency ϵ_{Tot} . From this, the combined efficiency ϵ_{Chem} for carbonyl formation in the reaction chamber and for transport to filter (c) could be determined via:

$$\epsilon_{\text{Tot}}^{(a \rightarrow c)} = \epsilon_{\text{Flush}}^{(a \rightarrow b)} \cdot \epsilon_{\text{Chem}}^{(b \rightarrow c)} \quad (4.1)$$

The flush-out efficiency can be considered to be a two step process: first, the fission products thermalize in the bulk gas, and second, they enter the reaction chamber. The efficiency of the second step is reduced due to diffusion to the wall of the connection between the two chambers:

$$\epsilon_{\text{Flush}}^{(a \rightarrow b)} = \epsilon_{\text{Stop}} \cdot \epsilon_{\text{Diff}} \quad (4.2)$$

Due to the different geometries of the used filters for the ϵ_{Tot} and the direct catch measurements, an individual detection efficiency calibration was performed, using an aliquot of a γ standard containing the following isotopes listed by the energy of their γ lines: ^{241}Am , ^{109}Cd , ^{57}Co , ^{139}Ce , ^{203}Hg , ^{113}Sn , ^{85}Sr , ^{137}Cs , ^{88}Y and ^{60}Co (QCY48, Amersham, UK). The difference in geometric efficiency of the two geometries was a factor of 1.4, and we estimate the uncertainty to be less than 3%.

Tab. 4.1: Overview of the performed parameter studies, listing measurement sequence and gas flow rates of N_2 and/or CO entering the thermalization chamber (TC) and reaction chamber (RC), respectively. All given positions refer to Fig. 4.2.

Measurement sequence	N_2 in TC ($mL\ min^{-1}$)	CO in TC ($mL\ min^{-1}$)
Reference: Pos.:(c) p_{pC} (Ref) I-III	250	250
	250	500
	500	250
	500	500
	1000	500
	500	1000
<hr/>		
	N_2 in TC ($mL\ min^{-1}$)	CO in RC ($mL\ min^{-1}$)
Overall: Pos.:(c) p_{pC} (Tot) I-III	250	250
	250	500
	500	250
	500	500
	1000	500
	500	1000
<hr/>		
	N_2 in TC ($mL\ min^{-1}$)	N_2 in RC ($mL\ min^{-1}$)
Flush out ^a : Pos.:(b) p_{pC} (Flush) I-X	250	250
	250	500
	500	250
	500	500
	1000	500
	500	1000

The reference- and the overall measurement sequence comprises three different series, where the pressure inside the TC and RC, p_{pC} was changed from Series I:(1000 mbar) over Series II:(1200 mbar) to Series III(1500 mbar). The Flush out measurement sequence was expanded to a total of 10 measurement series to cover pressures within (800-1500) mbar.

^a Measurement series were taken at the following pressures in mbar in ascending order (I-X): 500, 600, 700, 800, 900, 1000, 1200, 1300, 1400, 1500. The measurement series was repeated for the 4 mm diameter transition piece.

4.1.1 Direct catch measurements

The ^{235}U -target was mounted in the TC. This was then irradiated with a thermal neutron flux of $9.8 \cdot 10^{10}$ neutrons/cm²s from the TRIGA Mainz. The TC was flushed with 500 mL/min N_2 . The pumping capacity was adjusted to maintain a pressure of 1000 mbar in the TC. A 10- μ m thick aluminum foil was mounted, covering the target. At a distance of ~ 3 mm a 4-mm thick teflon disc was mounted to catch recoiling fission products. The target was irradiated for 10 min for the direct catch measurements. After end of irradiation, the target chamber was dismounted and the teflon disc retrieved and placed in front of a HPGE detector. Counting started 47 min after the end of irradiation and lasted for 30 min. The decaying isotopes were identified by their respective γ lines. The corresponding γ spectrum is shown in Fig. 4.3 (a). The γ lines of several d element isotopes could be identified, with the lines of ^{101}Mo , ^{101}Tc and ^{104}Tc being the most intense ones.

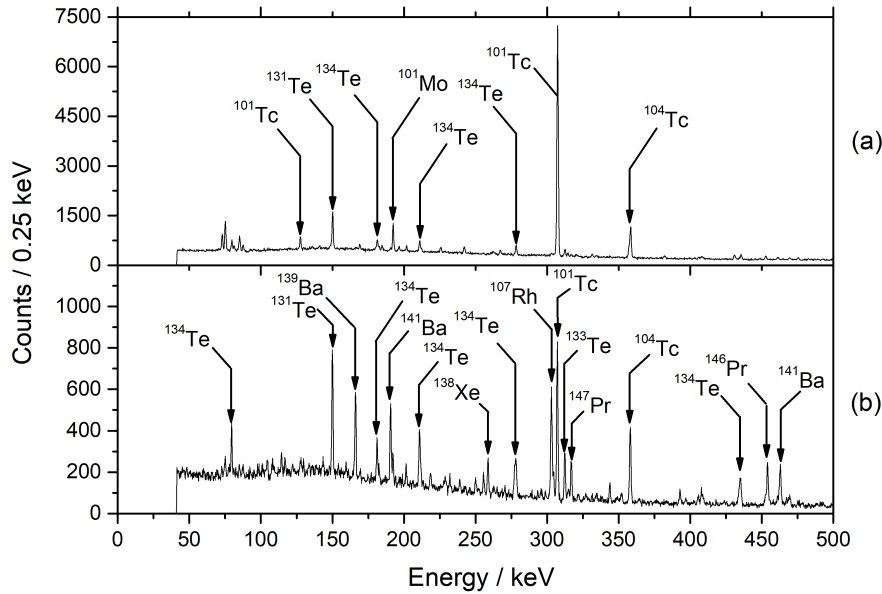


Fig. 4.3: (a) γ -ray spectrum observed for the direct catch measurement with a teflon disc using the Al-covered ^{235}U -target. Counting started 47 min after the end of irradiation and lasted for 30 min. This spectrum was used as a reference measurement for the calculation of absolute yields, referring to the amount of ^{101}Tc entering the TC. (b) γ -ray spectrum for the direct catch measurement using the non-covered ^{248}Cm -source. Counting started 5 min after the sample collection ended and lasted for 90 min. Both measurements were performed under similar conditions with 500 mL/min of nitrogen flow and $p_C = 1000$ mbar.

Similar direct catch measurements were performed, when the thermalization chamber was equipped with the ^{248}Cm -source. With regard to the nitrogen flow rate, p_C and the used teflon disc, the same specifications were used as for the previous measurements with the ^{235}U -target. Due to the low fission branch, each direct catch sample was collected for 90 minutes, followed by a 5 min break and 90 min of measurement in front of the Ge-Detector, where the respective γ lines of the decaying isotopes were identified. One direct catch measurement is depicted in Fig. 4.3 (b).

4.1.2 Measurement of reference yield ε_{Ref} in a one-chamber approach

The TC with the mounted ^{235}U -target was placed in the same beam port as used for the direct catch measurements. Initial experiments were conducted to verify that no transport of non-volatile elements attached to aerosol particles was present and disturbed the experiment series. For this, 1000 mL/min of nitrogen was fed into the TC, and no additional gas was fed into the RC. The pressure was 1000 mbar. A charcoal filter mounted in pos. (c) was counted by a Ge detector.

For studies of carbonyl complex formation, the TC was continuously flushed with a gas mixture of nitrogen and carbon monoxide as shown in the p_{pC} (Ref) I-III reference measurement sequence in Tab. 4.1. Each measurement sequence consisted of three different measurement series ((1000/1200/1500) mbar), each consisting of six individual measurements representing the different gas mixtures, cf. Tab. 4.1. Volatile fission products and the fission products forming volatile carbonyl complexes were transported with the gas stream through a capillary until they were trapped on a charcoal filter in position (c) of Fig. 4.2 and the γ lines of the decaying isotopes were identified. Each sample was collected for 10 minutes, followed by a 5 minute break and then measured for 10 minutes.

4.1.3 Measurements of the flush-out efficiency ε_{Flush}

The ^{248}Cm -source was mounted in the TC. This was continuously flushed with pure nitrogen as shown in the p_{pC} (Flush) I-X measurement sequence in Tab. 4.1. The non-volatile fission products were collected with a quartz fibre filter at the entrance of the reaction chamber (position (b) in Fig. 4.2). Each sample was collected for 90 minutes, followed by a 5 min break and was then measured for 90 min in front of the Ge-Detector, where γ lines of the decaying isotopes were identified. The γ spectrum of one sample is depicted in Fig. 4.4. In measurements with charcoal filters installed at sample position (c) (cf. Fig. 4.2), using a shortened capillary behind the RC (3 cm long instead of 12 m), no efficient transport could be observed.

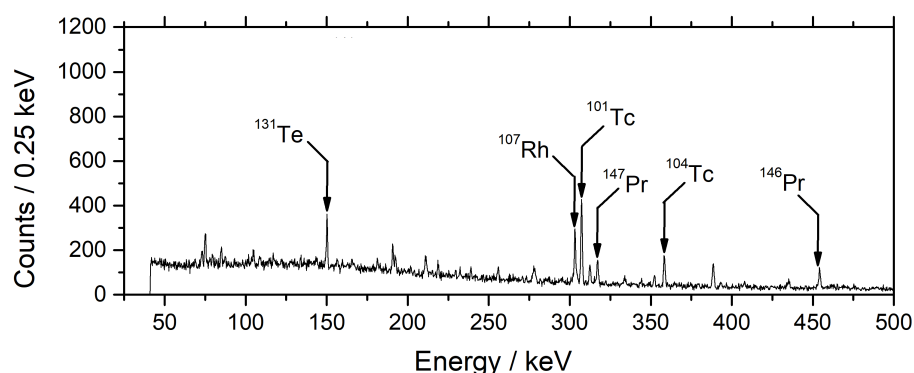


Fig. 4.4: γ -ray spectrum of ^{248}Cm fission products of the p_{pC} (Flush) I-X measurement sequence transported in 500 mL/min N_2 fed into the TC and 500 mL/min N_2 fed into the RC, collected on a quartz fibre filter at $p_C = 1000$ mbar. The sample was measured 5 min after 90 min of collection.

4.1.4 Measurements of the total efficiency ε_{Tot}

With a similar experimental setup as for the measurements of (ε_{Ref}), the TC with the mounted ^{235}U -target was flushed with pure nitrogen. Carbon monoxide was added into the RC as shown in the $p_{\text{pC}}(\text{Tot})$ I-III measurement sequence in Tab. 4.1. Fission products were flushed by the gas flow into the RC, where the appropriate transition metals converted into carbonyl complexes. All volatile products were transported with the gas stream through a 15-m long teflon capillary with an inner diameter of 4 mm to a charcoal filter placed in front of a HPGe detector and the γ lines of the decaying isotopes were identified. Each sample was collected for 10 minutes, followed by a 5 minute break and then measured for 10 minutes. Absolute yields were calculated using as a reference the direct catch measurement (cf. Sect. 2.2) which was performed with the same time sequence. To allow for such a direct comparison, five charcoal filters in position (c) were also measured 47 minutes after irradiation for 30 min in addition to their usual measurement sequence (i.e., 10 min. irradiation - 5 min. cooling - 10 min. measurement - 32 min. cooling - 30 min. measurement). Absolute efficiencies of the other samples were calculated relative to the average of these five measurements.

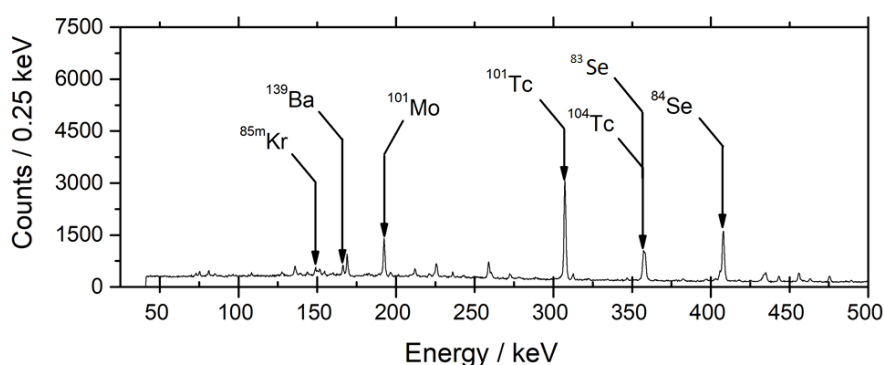


Fig. 4.5: γ -ray spectrum of fission products of the $p_{\text{pC}}(\text{Tot})$ I-III measurement sequence transported in 500 mL min^{-1} nitrogen and 500 mL min^{-1} carbon monoxide, collected on a charcoal filter at $p_{\text{C}} = 1000 \text{ mbar}$. The charcoal filters were measured 5 min after the end of irradiation.

In the late measurements starting 47 min after the end of irradiation, the γ lines of several d elements were identified, with the lines of ^{101}Mo ($T_{1/2} = 14.6 \text{ min}$) and ^{101}Tc ($T_{1/2} = 14.2 \text{ min}$) being the most intense ones. Only volatile elements or elements capable of forming volatile carbonyl complexes were expected to reach the charcoal filter in position (c). The lines of ^{139}Ba as β -decaying granddaughter of ^{139}I , as well as ^{84}Se , which forms the volatile CO_2 -equivalent molecule COSe [162], were observed in addition to those of ^{101}Mo and its daughter ^{101}Tc . Due to the relatively long time between the end of irradiation and the start of the measurement, ^{101}Mo was already substantially decayed and was not suitable for the calculation of absolute yields since only $\simeq 10\%$ of the initial amount of ^{101}Mo remained 47 min after irradiation. For this reason, its β -decay daughter ^{101}Tc was chosen for the

calculation of absolute yields. This shows intense gamma lines [$I\gamma(306\text{ keV}): 89\%$ and $I\gamma(545\text{ keV}): 6\%$ [156]]. The independent fission yield of ^{101}Tc for the $^{235}\text{U}(n,f)$ reaction is low ($< 2.0 \cdot 10^{-4}\%$)[163], whereas the primary fission product in the $A=101$ isobar is the short-lived ^{101}Nb ($T_{1/2} = 7.1\text{ s}$), which does not form volatile carbonyl complexes [27]. The corresponding β -decay daughter ^{101}Mo , however is known to form $\text{Mo}(\text{CO})_6$, see, e.g.,[27]. Therefore, we assume that ^{101}Tc originates almost exclusively from the β decay of ^{101}Mo . Whereas also Tc is known to form volatile carbonyl species, the efficiency of forming these was reported to be significantly lower than for group 6 elements [164].

The main goal of these studies is the determination of the four efficiencies, ϵ_{Ref} , ϵ_{Stop} , ϵ_{Diff} and ϵ_{Tot} in the two-chamber approach. Initially, the absence of any aerosol-based transport of non-volatile elements was confirmed. In experiments with pure nitrogen transport, only γ lines of $^{137-139}\text{Xe}$ and their daughters and $^{89-92}\text{Kr}$ and their daughters were registered at position (c).

4.1.5 Measurements to investigate gas purification and CO back diffusion

For this experimental series the pressure was kept in the range of (500-1500) mbar. The flow-rates were adjusted in the range of (250-1000) mL min^{-1} for each of the applied gases, which added to a total flow-rate of (500-1500) mL min^{-1} in the system. The QMS took samples with a flow rate of $0.05\text{ mbar L s}^{-1}$ with a pressure of around 0.04 mbar. Each sample was measured for 30 min and the information was evaluated with the program Process Eye Professional. After taking a sample from one of the chambers, the whole system could be evacuated with the help of a membrane pump, which was connected to both chambers. The evacuation of the system was monitored with a third pressure gauge connected to the connection in the pump-line. The system was evacuated for 5 min before new gas was reintroduced into the system. During all measurements, nitrogen was added into the TC first, to establish the pressure needed for the next measurement. After the given pressure was reached, CO was added into the RC and the needle valves in front of the pumping system were adjusted to maintain the given pressure by increasing the pumping capacity. The corresponding measurement sequences are summarized in Tab. 4.2.

For its second purpose, the experimental setup provided the possibility to bypass the entire gas purification system or to install a single purification cartridge of interest or any combination of them separately. The connection to the QMS itself remained unchanged, which allowed an identical sampling process to the back diffusion measurements. For the cartridge test, the samples were exclusively taken out of the RC, whereby both gases were fed into the chambers with a flow rate of (250-500) mL min^{-1} each. p_C was kept at 1000 mbar for all measurements. A detailed overview over the specific combination of cartridges is shown in Tab. 4.3 and Tab. 4.4.

Tab. 4.2: Overview of the measurement sequences performed during the back diffusion tests. The carbon monoxide fraction in the gas mixture was gradually increased during the $BDiff_{CO}$ measurement sequence, whereas the N_2 to CO ratio was kept at 1:1 during $BDiff_{TF}$, $GPur_1$ and $GPur_2$. In the sequence $BDiff_{PC}$ the N_2 to CO ratio was changed in the ratio of 1:2/1:1/2:1.

Measurement sequence	Total flow rate ($N_2 + CO$) / $mL\ min^{-1}$	p_C / mbar	Nitrogen flow rate / $mL\ min^{-1}$	Carbon monoxide flow rate / $mL\ min^{-1}$
$BDiff_{CO}$	1500	1000	1500 \Rightarrow 500	0 \Rightarrow 1000
$BDiff_{TF}$	500 \Rightarrow 1500	1000	250 \Rightarrow 750	250 \Rightarrow 750
$BDiff_{PC}$	1000	500 \Rightarrow 1500	333 \Rightarrow 666	666 \Rightarrow 333
$GPur_1$	500 \Rightarrow 1000	1000	250 \Rightarrow 500	250 \Rightarrow 500
$GPur_2$	1000	1000	500	500

Tab. 4.3: Detailed overview of the measurement sequences performed during the gas purification tests $GPur_1$. Cartridges included into the purification system are marked with \checkmark , whereas cartridges which were excluded from the system are marked with \times . The influence of the following cartridges was investigated: Sicapent (S), Hydrosorb (M) and Oxisorb (O)

Measurement sequence	Nitrogen purification	Carbon monoxide purification	Nitrogen flow rate / $mL\ min^{-1}$	Carbon monoxide flow rate / $mL\ min^{-1}$
1	S: \checkmark M: \checkmark O: \checkmark	S: \checkmark M: \checkmark O: \checkmark	250	250
2	S: \checkmark M: \checkmark O: \checkmark	S: \times M: \checkmark O: \checkmark	250	250
3	S: \checkmark M: \checkmark O: \checkmark	S: \times M: \times O: \checkmark	250	250
4	S: \checkmark M: \checkmark O: \checkmark	S: \checkmark M: \checkmark O: \times	250	250
5	S: \checkmark M: \checkmark O: \checkmark	S: \times M: \times O: \times	250	250
6	S: \checkmark M: \checkmark O: \checkmark	S: \checkmark M: \checkmark O: \checkmark	500	500
7	S: \checkmark M: \checkmark O: \checkmark	S: \times M: \checkmark O: \checkmark	500	500
8	S: \checkmark M: \checkmark O: \checkmark	S: \times M: \times O: \checkmark	500	500
9	S: \checkmark M: \checkmark O: \checkmark	S: \checkmark M: \checkmark O: \times	500	500
10	S: \checkmark M: \checkmark O: \checkmark	S: \times M: \times O: \times	500	500
11	S: \checkmark M: \checkmark O: \checkmark	S: \checkmark M: \checkmark O: \checkmark	500	500
12	S: \times M: \checkmark O: \checkmark	S: \checkmark M: \checkmark O: \checkmark	500	500
13	S: \times M: \times O: \checkmark	S: \checkmark M: \checkmark O: \checkmark	500	500
14	S: \checkmark M: \checkmark O: \times	S: \checkmark M: \checkmark O: \checkmark	500	500
15	S: \times M: \times O: \times	S: \checkmark M: \checkmark O: \checkmark	500	500

Tab. 4.4: Detailed overview of the measurement sequences performed during the gas purification tests GPur₂. Cartridges included into the purification system are marked with ✓, whereas cartridges which were excluded from the system are marked with ✗. The influence of the following cartridges was investigated: Sicapent (S), Hydrosorb (M) and Oxisorb (O)

Measurement sequence	Nitrogen purification	Carbon monoxide purification	Nitrogen flow rate / mL min ⁻¹	Carbon monoxide flow rate / mL min ⁻¹
1	S:✓ M:✓ O:✓	S:✓ M:✓ O:✓	500	500
2	S:✓ M:✓ O:✓	S:✗ M:✓ O:✓	500	500
3	S:✓ M:✓ O:✓	S:✓ M:✗ O:✓	500	500
4	S:✓ M:✓ O:✓	S:✗ M:✗ O:✓	500	500
5	S:✓ M:✓ O:✓	S:✓ M:✓ O:✗	500	500
6	S:✓ M:✓ O:✓	S:✗ M:✓ O:✗	500	500
7	S:✓ M:✓ O:✓	S:✓ M:✗ O:✗	500	500
8	S:✓ M:✓ O:✓	S:✗ M:✗ O:✗	500	500

4.2 The reference efficiency ϵ_{Ref}

In this section, the results for the reference efficiency ϵ_{Ref} will be presented. As described before, the ²³⁵U-target was mounted in the TC for these measurements. Both gases, N₂ and CO were fed into the TC. The data presented in this section were collected during the measurement sequences p_{pC}(Ref) I-III, which in total consists of 18 different data points. For details see Tab. 4.1. ϵ_{Ref} can be understood as the maximum efficiency for the two-chamber approach, whereby chemistry- and transport losses are minimal.

4.2.1 Results

Experiments with simultaneous gas introduction of nitrogen and carbon monoxide into the TC of the TRIGA Mainz were already performed by Even et al. and the dependency of the carbonyl complex formation and transport efficiency on the carbon monoxide concentration in the gas mixture was described in [21, 26]. In the present work, the dependency of the carbonyl complex formation probability on the carbon monoxide concentration was also measured and was found to be in good agreement, cf. Fig. 4.6, and Figure 9 in [26].

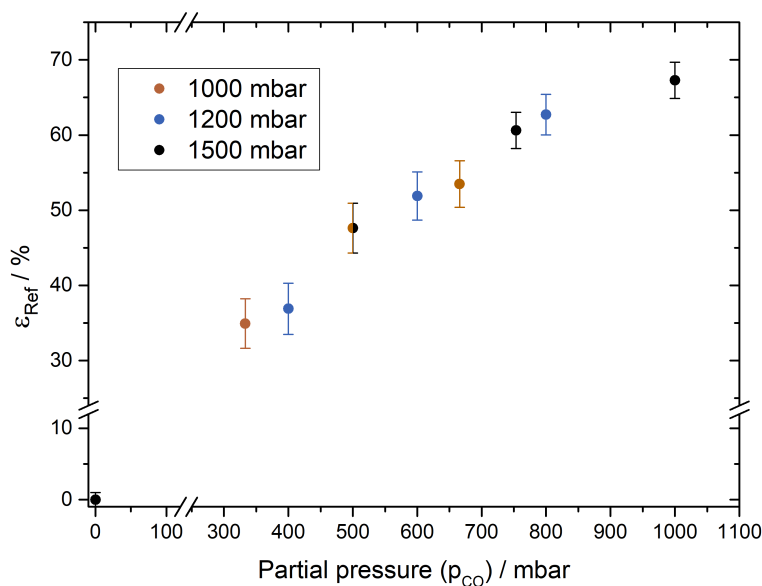


Fig. 4.6: Measured ϵ_{Ref} for ^{101}Mo in a N_2/CO gas mixture as a function of the carbon monoxide partial pressure. The total gas flow rate was 1500 mL/min and p_C was in the range of (1000-1500) mbar. Absolute efficiencies were calculated by using the daughter nuclide ^{101}Tc as an indicator for ^{101}Mo . The different pressures inside the TC, p_{p_C} , are depicted by different colours.

At high carbon monoxide concentrations (p_{CO} : 1000 mbar) in the bulk gas, absolute reference yields of $(67.3 \pm 8.2)\%$ were achieved. With decreasing carbon monoxide content, a decreasing efficiency for the transport of volatile compounds was observed.

4.2.2 Discussion

The CO concentration influences the reaction probability directly, since in case of carbonyl complexes, the corresponding transition metal has to repeatedly collide with carbon monoxide molecules to form a homoleptic carbonyl complex. In case of, e.g., molybdenum, at least six collisions are required, before collisions with either the wall or any reactive impurity (e.g., oxygen) occurs. The probability to form carbonyl complexes thus directly depends on the partial pressure of carbon monoxide within the bulk gas. This explains why the chemical yield increases with increasing carbon monoxide partial pressure [16, 37].

4.3 The flush-out efficiency ϵ_{Flush}

In this section, the results for the flush-out efficiency ϵ_{Flush} will be presented. As described before, the ^{248}Cm -source was mounted in the TC for this measurements. During these

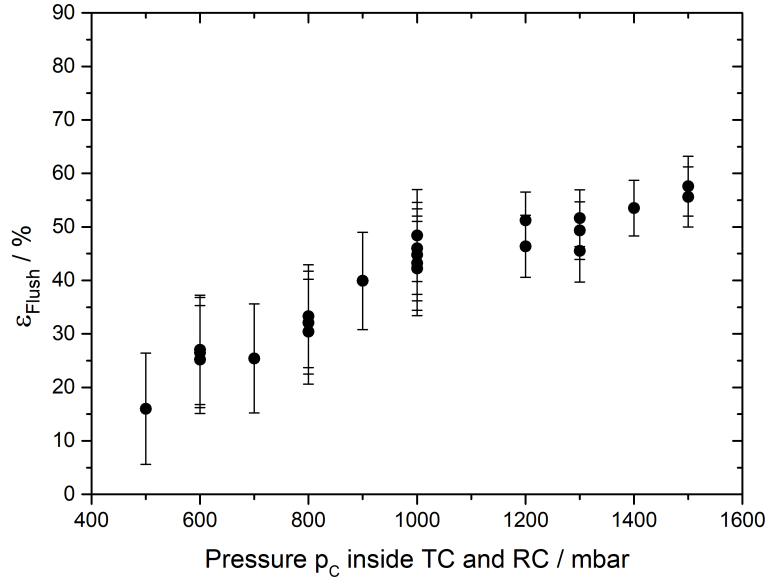


Fig. 4.7: Measured values for ϵ_{Flush} as function of the pressure p_C . Total flow rate was $1 L \min^{-1}$.

measurements N_2 was fed into both chambers. The data presented in this section was collected during the measurement sequences $p_{p_C}(\text{Flush})$ I-X, which in total consists of 60 different data points. For details see Tab. 4.1. ϵ_{Flush} describes the flush-out process for non-volatile fission products from the TC into the RC.

4.3.1 Results

In Fig. 4.7, the flush out efficiency for ^{101}Tc as a function of the pressure p_C inside the chamber is shown. In these measurements, ϵ_{Flush} reveals a dependence on the pressure of the bulk gas in the TC. At low pressure (around 500 mbar) only $(16.0 \pm 3.1) \%$ of ^{146}Pr could be transferred to the entrance of the reaction chamber. After increasing the pressure in the thermalization chamber, higher yields of ϵ_{Flush} of up to $(53.5 \pm 6.9) \%$ at $p_C=1400$ mbar could be achieved. The maximum value of ϵ_{Flush} is in the range of $(55 \pm 5) \%$. The slope of the curve flattens in the direction of $\epsilon_{Flush} = 60 \%$, which can be assumed to be the maximum in ϵ_{Flush} for the given experimental setup.

4.3.2 Discussion

The transfer of fission products emerging from the ^{235}U -target or the ^{248}Cm -source into the RC using inert gas is independent of volatile molecule formation. To ensure that such processes do not influence our determination of ϵ_{Flush} , we used ^{146}Pr , which does not form volatile carbonyl complexes. First, the fission fragments have to be stopped inside the gas volume behind the source. This occurs with a partial efficiency $\epsilon_{Stop} \lesssim 1$, which is finite

as a fraction of ^{146}Pr may implant into the wall of the TC. In a second step, all fission fragments stopped in the gas have to be transferred through the narrow connection between both chambers. Any wall-contacts before a volatile compound is formed in the RC will lead to a loss of the corresponding fission fragments, reducing this transfer efficiency to $\varepsilon_{\text{Diff}}$.

The thermalization efficiency $\varepsilon_{\text{Stop}}$

To evaluate the $\varepsilon_{\text{Flush}}$, the γ spectrum depicted in Fig. 4.4 was evaluated relative to the direct catch measurement shown in Fig. 4.3 (b). An uncovered ^{248}Cm -source was used and the γ lines of the non-volatile ^{146}Pr ($E_{\text{kin}} \lesssim 74\text{ MeV}$) from the heavy mass branch were chosen for the evaluation of $\varepsilon_{\text{Flush}}$. ^{146}Pr ($T_{1/2} = 24.15\text{ min}$) can be easily detected in the γ spectra ($I_{\gamma}(453\text{ keV}): 48\%$ [156]). Its precursors ^{146}La ($T_{1/2} = 10\text{ s}$) and ^{146}Ce ($T_{1/2} = 13.5\text{ min}$) are the dominant primary fission products in the $A=146$ isobar. Neither is volatile, so no losses are expected. Isotopes from the light mass branch, such as ^{101}Mo and ^{101}Tc were not suitable for the analysis in the ^{248}Cm -based measurements due to their undegraded high initial kinetic energies of $\approx 107\text{ MeV}$ and their corresponding long projected stopping ranges leading predominantly to implantation inside the TC.

The computer program TRIM [144] was used for the simulation of the range distribution of ^{101}Mo from the $^{235}\text{U}(\text{n},\text{f})$ and the $^{248}\text{Cm}(\text{sf})$ reactions and ^{146}Pr from the $^{248}\text{Cm}(\text{sf})$ reaction. For example, post-neutron emission kinetic energies (KE_{F}) for the fission products of the spontaneous fission source ^{248}Cm were calculated [165] to be $\approx 96\text{ MeV}$ for $^{101}\text{Mo}^{\text{Cm}}$ and $\approx 74\text{ MeV}$ for $^{146}\text{Pr}^{\text{Cm}}$, respectively, which were reduced by interaction with half of the target thickness, the Al degrader foil in case of ^{101}Mo from the $^{235}\text{U}(\text{n},\text{f})$ reaction, and the gas inside the TC.

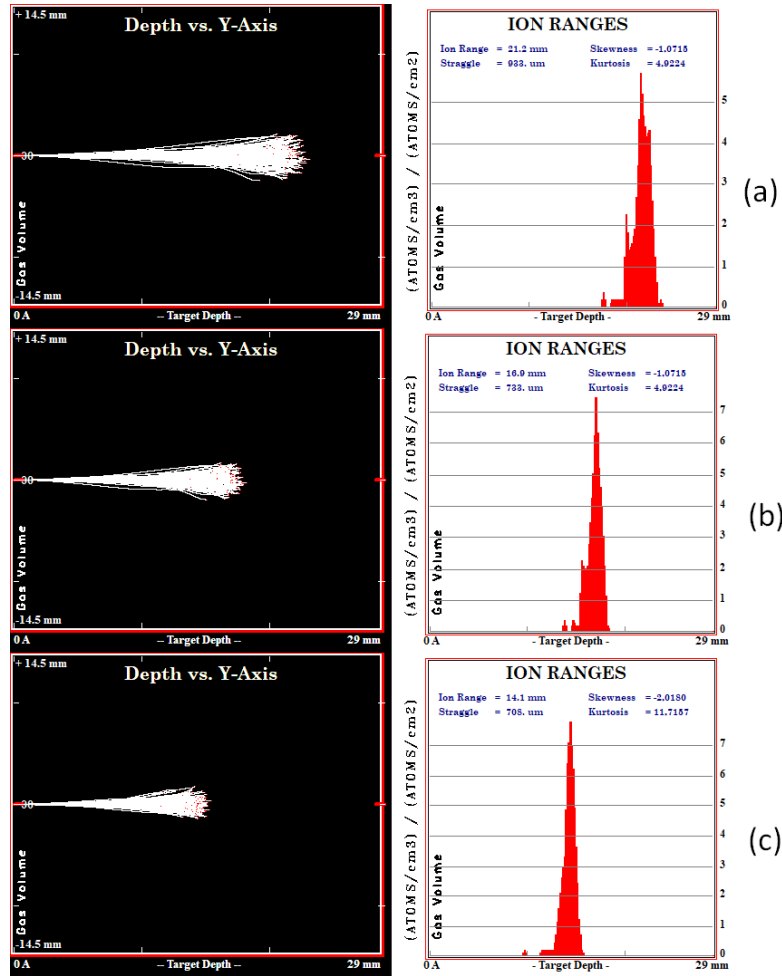


Fig. 4.8: Simulations of the range of fission products, performed with SRIM2013 [144]. For all simulations, 200 ^{146}Pr ions with an initial kinetic energy of 74 MeV were used, whereby the effect of self-absorption in the ^{248}Cm -source was taken into account. (a) The ions were stopped in 800 mbar N₂. (b) The ions were stopped in 100 mbar N₂. (c) The ions were stopped in 1200 mbar N₂.

In the following step, the simulated ranges were compared to the dimensions of the TC and the thermalization efficiency ϵ_{Stop} was calculated based on a geometric model. The spontaneous fission will distribute the fission products equally among all angles and therefore the fission geometry could be considered to be spherical with a total surface of A_{Sp} as shown in Fig. 4.9.

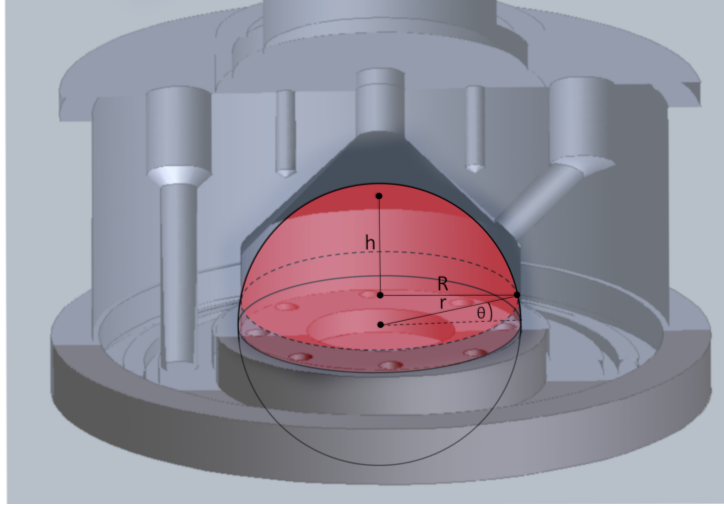


Fig. 4.9: Schematic to illustrate the calculation of ε_{Stop} . The target was considered to be a point source and the chamber exit was described in spherical segments, whereas θ describes the angle of emission where implantation started.

The radius of the fission geometry r , which was simulated with TRIM and refers to the maximum range in the respective stopping medium, was then compared with the distance to the nearby surface of the TC R . By emitting in larger angles of θ , the radius r could be increased until thermalization into the surface could be excluded. Therefore, the percentage of implanted fission products could be calculated by the fraction of the spherical surface A_{Tz} with emission angles $\leq \theta$ as given in Eq. 4.3:

$$A_{Tz} = 2\pi rh = \pi(R^2 + h^2) \quad (4.3)$$

The distance h to the exit of the chamber could be calculated with the following equation Eq. 4.4:

$$h = r(1 - \cos(90 - \theta)) \quad (4.4)$$

In Tab. 4.5 an overview over the simulated ranges (sim. range (TRIM)) and their corresponding ε_{Stop} are given. The simulated ranges have been modified by a correction factor for gaseous targets, due to a general overestimation of the stopping powers evaluated in [166]. However, since the Work of Wittwer et al. is based on simulations with the previous TRIM version (TRIM-2008), the ranges were corrected by a factor of 1.15 only, taking into account the improvements towards TRIM-2010, which is also corresponding to the published uncertainties by Ziegler et al. [144].

For the final calculation of ε_{Stop} , the effective surface of the sphere A_{Eff} for stopping has to be calculated, since only particles emitted in forward direction, which are capable of

leaving the source holder, could be stopped in the corresponding gas volume. Therefore, the shape of the source holder A_{SH} was taken into account, as this already limited the emission angle of fission products as shown in Eq. 4.5 and Eq. 4.6:

$$A_{Eff} = 50 - A_{SH} \quad (4.5)$$

The ϵ_{Stop} now refers to the fraction of particles entering the gas volume and which are additionally emitted at angles $> \theta$ to avoid implantation at the surface of the chamber, which can be described as shown in Eq. 4.6:

$$\epsilon_{Stop} = \frac{(A_{Eff} - (A_{Tz-A_{SH}}))}{A_{Eff}} \quad (4.6)$$

In Tab. 4.5 the values for ϵ_{Stop} been summarized in reference to their corresponding p_C values and their simulated ranges (sim. range) using TRIM2013 [144]. All simulated ranges are corrected (cor. range) by the previously introduced correction factor, to compensate the range underestimation of TRIM as described previously. No implantation is expected for $p_C \geq 1100$ mbar.

Tab. 4.5: Calculated values for ϵ_{Stop} , based on their simulated ranges and p_C .

p_C / mbar	si. range / mm	cor. range / mm	A_{Tz} / %	ϵ_{Stop} / %
800	21.2(3.2)	24.4(3.7)	31.3(4.7)	68.7(4.7)
900	18.9(2.8)	21.6(3.2)	20.9(3.1)	79.1(3.1)
1000	16.9(2.5)	19.5(2.9)	7.3(1.1)	94.7(1.1)
1100	15.3(2.3)	17.6(2.6)	-	100
1200	14.0(2.1)	16.1(2.4)	-	100
1300	13.2(2.0)	15.2(2.2)	-	100
1400	12.2(1.8)	14.1(2.1)	-	100
1500	11.4(1.7)	13.1(2.0)	-	100

The simulations yielded the fractions of these isotopes thermalized inside the TC (I_s). Results of the simulations are given in Tab. 4.6. Even if the kinematics of the chosen ^{146}Pr still differs from that of ^{101}Mo from $^{235}\text{U}(n,f)^{101}\text{Mo}$ ($E_{kin} \lesssim 12$ MeV, after passing the aluminum degrader), the flush-out behaviour for the non-volatile elements stopped in the gas volume inside the TC is expected to be similar. The simulation results for the mean ranges for the ions of interest produced in the $^{235}\text{U}(n,f)$ reaction were typically within the range of ≤ 10 mm, with the closest wall of the TC about 16 mm away from the target. Therefore, stopping losses were neglected in the case of the covered ^{235}U -target.

Tab. 4.6: Simulated stopping ranges for ^{146}Pr and ^{101}Mo produced by spontaneous fission of ^{248}Cm ($^{146}\text{Pr}^{Cm}$, $^{101}\text{Mo}^{Cm}$) and ^{101}Mo produced by neutron induced fission of ^{235}U ($^{101}\text{Mo}^U$) estimated using the TRIM software package. Post-neutron emission total kinetic energies (KE_F) are given, as well as the kinetic energies of the respective ions before entering the stopping gas in the TC ($KE(\text{gas})$), which includes losses caused by interaction with half of the target thickness (and the $10\ \mu\text{m}$ Al degrader in case of $^{101}\text{Mo}^U$). In the last column, the estimated fraction (I_{Is}) of fission products stopped in the bulk gas is given.

Isotope	KE_F /MeV	$KE(\text{gas})$ /MeV	p_C /mbar	Stop. Range /mm	I_{Is} /%
$^{101}\text{Mo}^U$	96(5)	$\lesssim 12(2)$	800 - 1500	≤ 10	100 ^a (-)
$^{146}\text{Pr}^{Cm}$	74(4)	$\lesssim 72(4)$	800	24.4(4.4)	68.7(9.6)
			900	21.6(3.9)	79.1(6.4)
			1000	19.5(3.5)	92.7(2.2)
			1100	17.6(3.2)	97.8(0.7)
			1200 - 1500	< 16.0	100 ^a (-)
$^{101}\text{Mo}^{Cm}$	107(6)	$\lesssim 104(6)$	800	27.1(5.3)	60.4(12.0)
			900	25.5(5.0)	63.6(11.1)
			1000	22.9(4.5)	70.2(8.8)
			1100	20.8(3.7)	79.2(6.4)
			1200	18.9(3.4)	94.7(1.6)
			1300	17.3(3.1)	98.2(0.6)
			1400 - 1500	< 16.0	100 ^a (-)

^a The simulated ranges are shorter than the distance to the closest wall. Therefore, no losses caused by implantation are expected.

The transfer efficiency ϵ_{Diff}

To estimate the losses caused by the lateral diffusion of the non-volatile fission fragments during the flush-out process, a Monte Carlo simulation based on the method developed by Zvara [130] was used. The 6-mm long connection piece between the thermalization- and the reaction chamber had an inner diameter of 4 mm and was considered as a chromatography column, collisions with which will lead to a loss of the corresponding atom due to the strong interaction leading to irreversible adsorption. The simulation also takes into account diffusion, which depends on p_C and the gas flow rate. The experimental conditions present in the connection piece suggest that transfer occurs in the laminar flow regime.

Both, the stopping power of a gas and the diffusion-related movement are pressure-dependent processes. The stopping power of a gas is described by the Bethe-Formula [167]. For non-relativistic ions it is directly proportional to $1/v^2$ and the density of the stopping gas (electron density). The diffusion is based on a statistical movement which is described within the kinetic gas theory and depends on other parameters, including the molecular volumes of the specific gases, which are pressure dependent [168]. The influence of the pressure on both

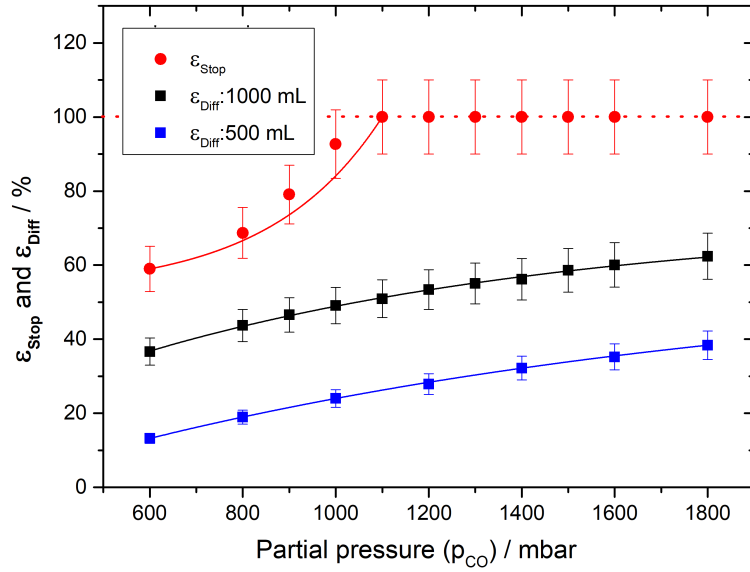


Fig. 4.10: Transfer- and stopping efficiency from the TC to the RC of ^{101}Tc produced by spontaneous fission from a ^{248}Cm source as a function of p_{C} . The stopping efficiency (red circles) was simulated with the computer program TRIM and the transfer efficiency (squares), at a flow rate of 0.5 L/min and 1.0 l/min, was calculated based on the MCS introduced in chapter 3.2.2.. The lines are intended to guide the readers eyes.

processes is shown in Fig. 4.10.

Additional measurements were performed after changing the geometry from the transition in between both chambers after introducing a small aperture. Hereby, the length of the transition got extended from 6 mm to 8 mm, whereby the diameter of the transition got reduced from 6 mm to 4 mm. By this change, the influence of the length of the connection on ϵ_{Flush} could be investigated. Details on the introduced aperture are shown in Fig. 4.11.

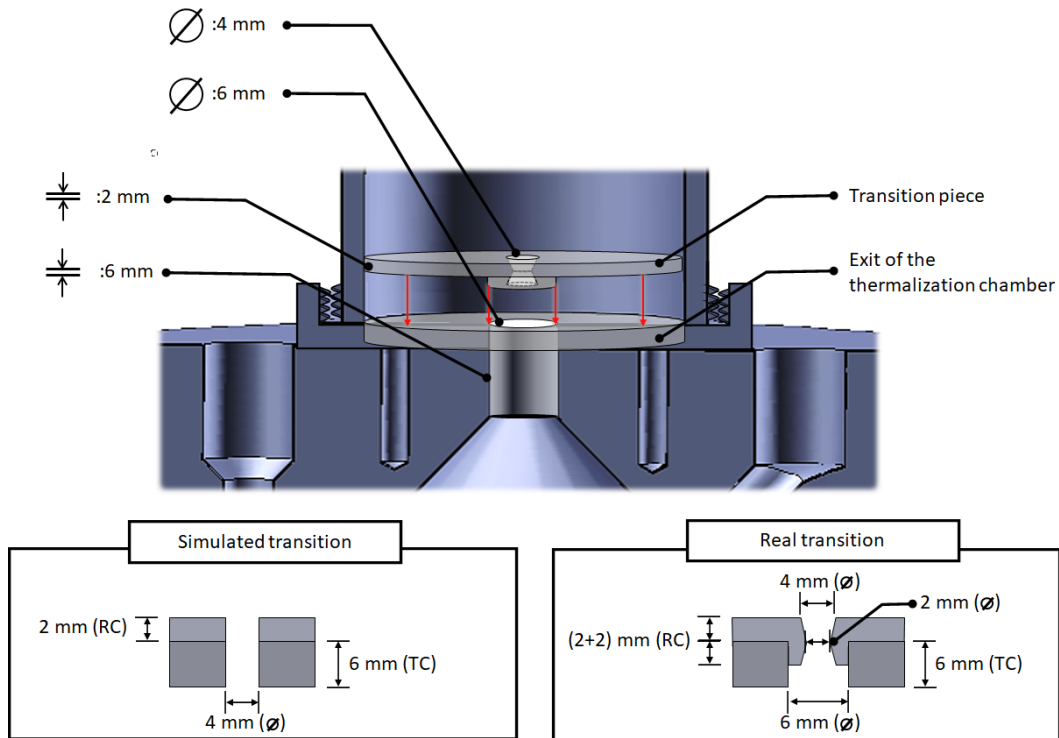


Fig. 4.11: Schematic of the transition piece used in between TC and RC. In addition, the dimensions are given to visualize the change in geometry by introducing this aperture. In the final assembly, the transition piece is mounted directly on the TC and the protrusion is inserted into the into the outlet of the TC.

In Fig. 4.12 the direct comparison of ϵ_{Diff} of both tested geometries is depicted. In the results of the MCS, the negative influence of the longer connection between both chambers leads to a reduction in ϵ_{Diff} of $\approx 20\%$ over the investigated pressure regime. The influence of the shape of the connection could not be simulated within the MCS and were therefore not considered.

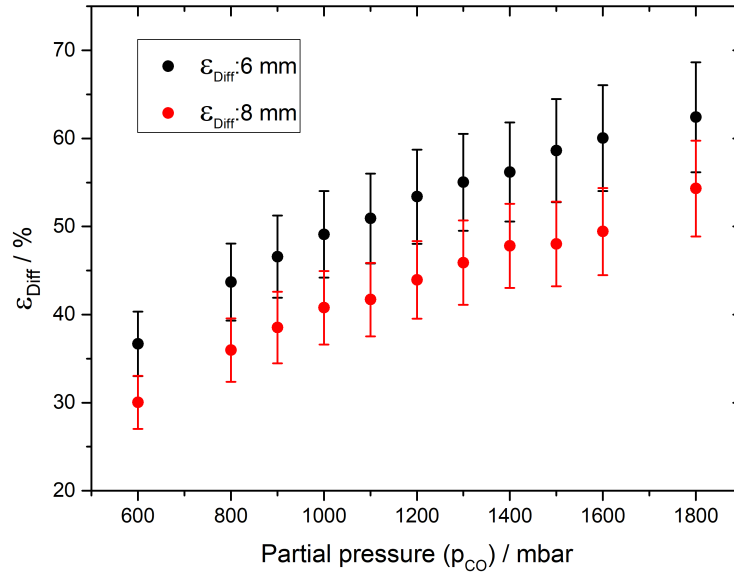


Fig. 4.12: Comparison of ϵ_{Diff} simulated with the MCS approach provided by Zvara et al. [37] for different lengths of the transition piece.

Theoretical modeling the flush-out efficiency ϵ_{Flush}

Based on the fraction of fission fragments stopped inside the gas volume (cf. Sec. 4.3.2 The thermalization efficiency ϵ_{Stop}) and the corresponding diffusion losses (cf. Sec. 4.3.2 The transfer efficiency ϵ_{Diff}), a theoretical value for ϵ_{Flush} was calculated. In Fig. 4.13 the theoretical calculation (red line) is shown together with the experimental values (black symbols). The good agreement supports the validity of our assumption that both finite thermalization efficiency ϵ_{Stop} as well as diffusion-related losses ϵ_{Diff} effect ϵ_{Flush} .

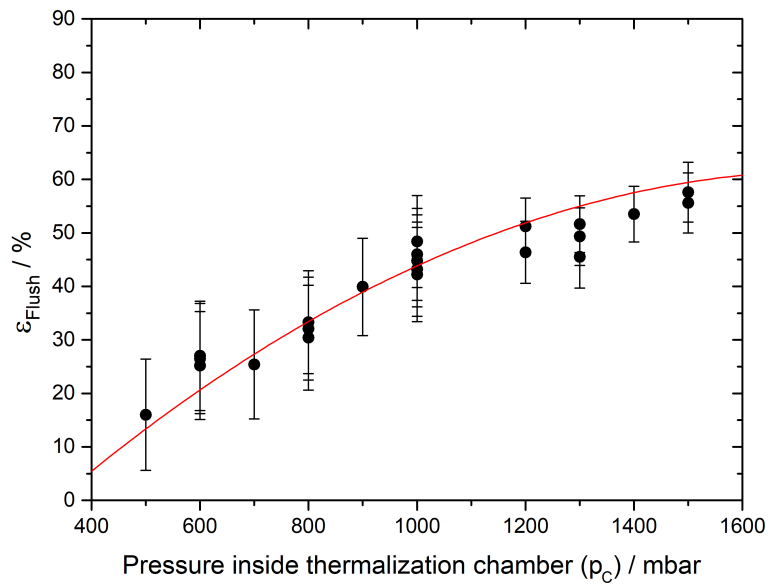


Fig. 4.13: Comparison of the measured ϵ_{Flush} (black circles) with the theoretical predictions (red line). For the calculated values, the respective diffusion- and implantation losses were taken into account.

In order to aid clarity, only mean values of ϵ_{Flush} are depicted. The influence of the slightly conical shape of the aperture was not considered within the simulation as shown in Fig. 4.11. Additionally, the expected losses caused by implantation are assumed to be identical in both theoretical predictions.

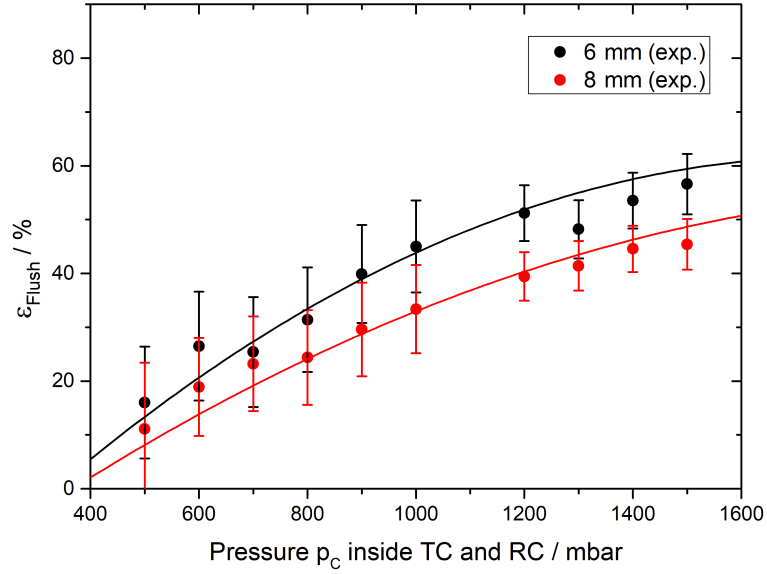


Fig. 4.14: Comparison of the measured ϵ_{Flush} for the 6 mm (black circles) and the 8 mm (red circles) transition, depicted together with their corresponding theoretical predictions (lines). For the calculated values, the respective diffusion- and implantation losses were taken into account.

4.4 The overall efficiency ϵ_{Tot}

In this section, the results for the overall efficiency ϵ_{Tot} will be presented. As described before, the ^{235}U -target was mounted in the TC for these measurements. During these measurements N_2 was fed into the TC, whereas CO was fed into the RC. The data presented in this section were collected during the measurement sequences $p_{p_c}(\text{Tot})$ I-III, which in total consists of 18 different data points. For details see Tab. 4.1. ϵ_{Tot} describes the overall performance of the two-chamber approach. ϵ_{Tot} includes the flush-out of non-volatile fission products from the TC into the RC, the formation of volatile carbonyl complexes, and finally the transport to the detector. Therefore, ϵ_{Tot} is the product of the partial efficiencies, as given in Eq. 4.1 and Eq. 4.2. We employ the ϵ_{Flush} values from the theoretical modelling (red line in Fig. 4.13). Tab. 4.7 lists the average values of all these measurements, including the partial efficiencies ϵ_{Flush} and ϵ_{Chem} . The ϵ_{Chem} was deduced as given in Eq. 4.7:

$$\epsilon_{Chem} = \frac{\epsilon_{Tot}(\text{exp.})}{\epsilon_{Flush}(\text{calc.})} \quad (4.7)$$

4.4.1 Results

An inspection of the dependence of ϵ_{Flush} , ϵ_{Chem} and ϵ_{Tot} on the parameters p_{C} and p_{CO} reveals the following: (i) ϵ_{Flush} and also ϵ_{Chem} increase with increasing p_{C} and (ii) ϵ_{Flush} is independent of p_{CO} , which is natural as processes in the RC, into which CO is fed, are not affecting ϵ_{Flush} ; and (iii) ϵ_{Chem} increases with increasing p_{CO} . This is in line with results obtained in the one-chamber approach within the present work (ϵ_{Ref} vs. p_{CO} shown in [Tab. 4.7](#)) as well as documented in [[21](#), [24–26](#), [164](#)]. As both partial efficiencies ϵ_{Flush} and ϵ_{Chem} show identical trends, also their product, ϵ_{Tot} , shows this trend. [Fig. 4.15](#) shows that ϵ_{Flush} increases with increasing p_{C} and ϵ_{Chem} , which is directly connected to the carbon monoxide concentration in the TC. This explains why high overall efficiencies of ($\epsilon_{\text{Tot}} = 49.5 \pm 7.2$) % could be achieved for the two-chamber approach with high carbon monoxide partial pressures.

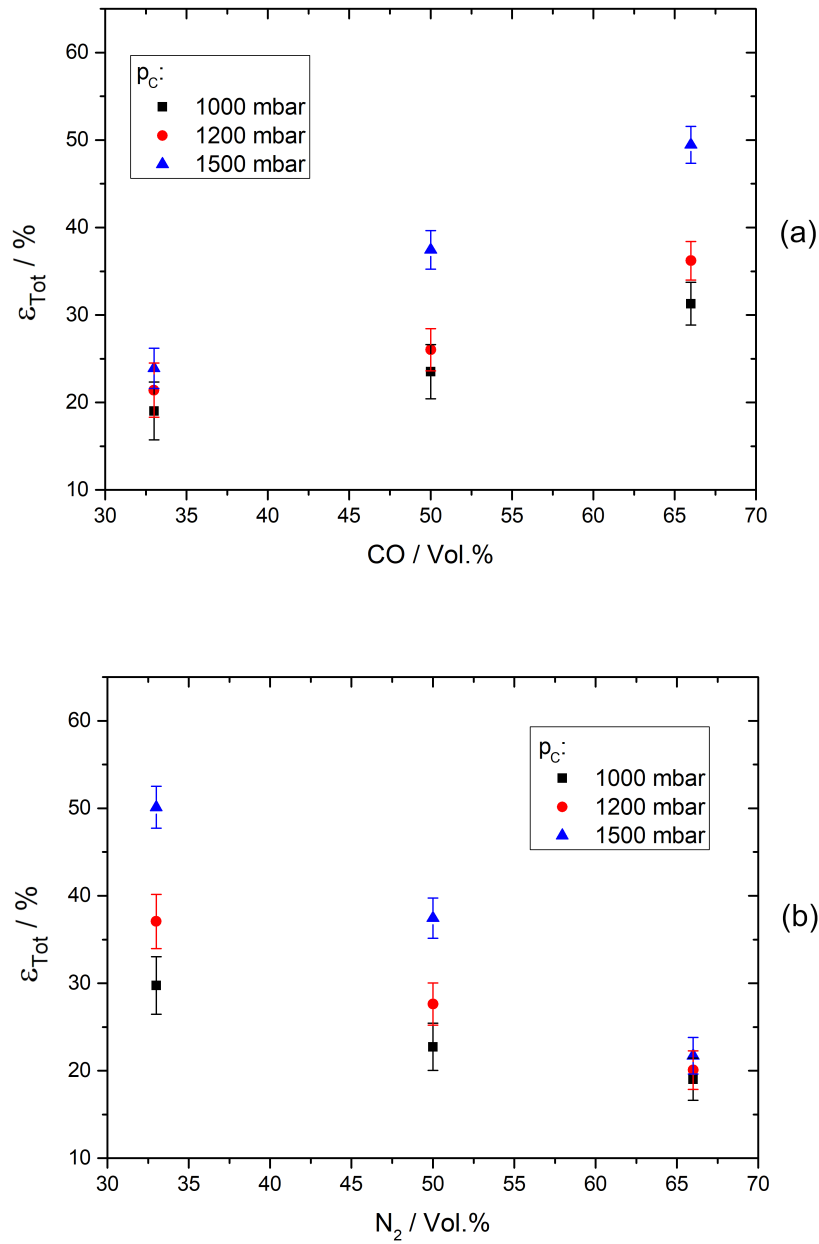


Fig. 4.15: (a) Measured ϵ_{Tot} for ^{101}Mo in a N_2/CO gas mixture as a function of the carbon monoxide content and p_C . (b): Same as (a), but shown as a function of the nitrogen content and p_C . The total gas flow rate was $750\text{-}1500\text{ mL min}^{-1}$ in both measurements, whereas the nitrogen flow rate was kept constant at 500 mL min^{-1} in (a) and the carbon monoxide flow rate was kept constant at 500 mL min^{-1} in (b). Absolute efficiencies were calculated by the detection of the daughter nuclide ^{101}Tc . In the absence of carbon monoxide, no ^{101}Tc was detected.

4.4.2 Discussion

To assess the performance of the two-chamber approach, we first look at the behaviour of ϵ_{Flush} . This partial efficiency only depends on the p_{C} (which was established in the TC purely with N_2 for the measurements of ϵ_{Flush} and ϵ_{Tot} , but by a mixture of N_2 and CO for the measurement of ϵ_{Ref}), but naturally not on the composition of the gas in the RC. ϵ_{Flush} increases with increasing p_{C} . We ascribe this to increases in both, ϵ_{Stop} as well as ϵ_{Diff} . The increased stopping power of the bulk gas reduces the probability for implantation in the surface of the chamber, since a larger fraction of the fission products is stopped in the centre of the gas volume. In our case, the higher pressure leads to a reduced number of collisions in the transition piece, connecting TC and RC, since the lateral diffusion is hindered, thus reducing the losses on the wall in this process. An inspection of ϵ_{Chem} reveals that also this increases with increasing pressure, suggesting that higher pressure will also benefit the ϵ_{Tot} , which indeed is the case. The ϵ_{Chem} depends on the composition of the gas in the chamber where the complex formation takes place (the TC in the case of ϵ_{Ref} measurements and the RC in the case of ϵ_{Tot} measurements). In agreement with literature data, the ϵ_{Chem} increases with increasing fraction of CO, cf. Fig. 4.15 (a), and reaches a value of 85(8)% for the highest measured p_{C} and p_{CO} .

Let us first look at ϵ_{Tot} for a gas composition of $\text{CO}:\text{N}_2 = 2:1$. When comparing the ϵ_{Tot} obtained at conditions, where the gas composition shows the same CO and N_2 ratio but differs in doubling the flow rate of nitrogen fed into the TC, no influence of the higher N_2 flow rate - known to lead to increase in ϵ_{Flush} - on ϵ_{Tot} is seen. We ascribe this to the shorter residence time in the RC at the higher total gas flow rate. Now, let us look at the trend of ϵ_{Tot} as a function of the N_2 -fraction in the RC, which reflects the N_2 applied for the transfer from TC to RC. This is expressed in the trend of ϵ_{Flush} , which is known to increase with increasing p_{C} . However, Fig. 4.15 (b) shows that ϵ_{Tot} drops with increasing N_2 fraction: at 67 %, the ϵ_{Tot} -values at all pressures are below the ϵ_{Tot} values at 33 %. This indicates the carbonyl complex formation step to be more relevant for a high ϵ_{Tot} than the flush-out process. The pressure dependence comes from the sensitivity of ϵ_{Stop} on the pressure. The high values of ϵ_{Tot} , which substantiate the high values of ϵ_{Chem} , also indicate the efficient gas-phase synthesis of single transition-metal carbonyl complexes in a regime different from that of a hot-atom scenario. Note that a potential back-diffusion of CO into the TC, leading to a CO-content $\leq 1\%$ could not explain the measured high yields, because at such low CO-concentrations, metal carbonyl complex formation is inefficient (cf. Fig. 4.6).

4.5 The investigation of CO back diffusion

In this section, the results for the back diffusion tests will be presented. As described in [Sec. 4.1.5](#), no source was mounted in the TC for these measurements. N_2 was fed into the TC, whereas CO were fed into the RC. The data presented in this section were collected during the measurement sequences BDiff_{CO}, BDiff_{TF}, and BDiff_{PC}. For details see [Tab. 4.2](#). This measurements were performed to exclude back diffusion of the reactive gas into the TC.

4.5.1 Results

During this first series of measurements, the influence of the CO flow rate on the back diffusion of carbon monoxide from the RC into the TC was investigated. Therefore, an identical experimental setup as described in [Sec. 3.1](#) was used. By excluding back diffusion, the formation of volatile carbonyl complexes in the TC could be excluded, which was essential for later efficiency calculations. During these measurements the CO flow rate was gradually increased from 0 mL min^{-1} up to 1000 mL min^{-1} , whereas the total flow rate was kept constant at 1500 mL min^{-1} . The results of these measurement series are summarized in [Fig. 4.16](#).

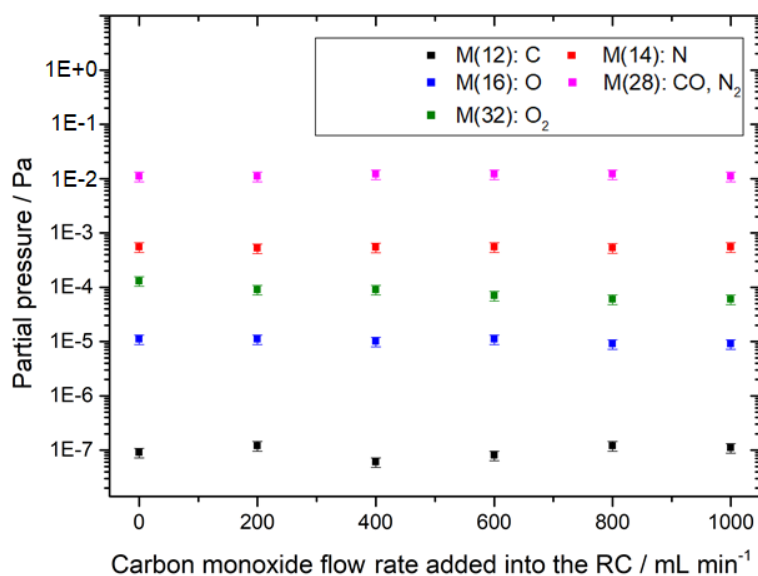


Fig. 4.16: Composition of the gas mixture inside the TC analyzed with the QMS. The signals of different masses are shown as a function of the carbon monoxide flow rate. The total flow rate was 1500 mL min^{-1} and p_C was kept constant at 1000 mbar .

Additional measurements were performed to investigate (a) the influence of the total flow rate on the back diffusion and (b) to investigate the influence of p_C and the ratio of the gas mixture on the back diffusion. For the former, the gas mixture of N_2 to CO was kept

constant at a ratio of 1:1 and the total flow rate was gradually increased from 500 mL/min to 1500 mL/min. The results of both measurement series are summarized in Fig. 4.17 and Fig. 4.18.

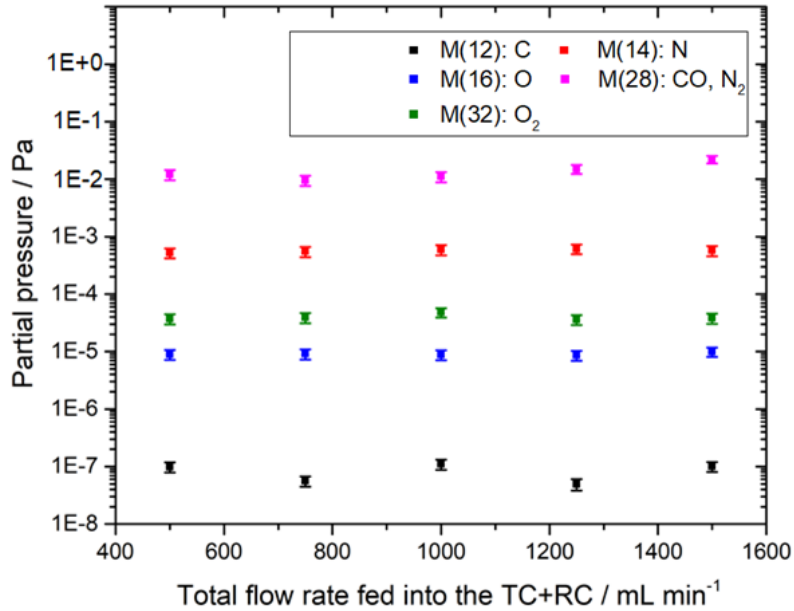


Fig. 4.17: Composition of the gas mixture inside the TC analyzed with the QMS. The signals of different masses are shown as a function of the total flow rate ($N_2 + CO$). The gas mixture of N_2 to CO was kept at a ratio of 1:1 and p_C was kept constant at 1000 mbar.

Besides changes in the gas composition ($N_2:CO$, 2:1, 1:1, 1:2), the total chamber pressure p_C was increased from 500 mbar to 1500 mbar. The masses are shown on the left of each measurement series.

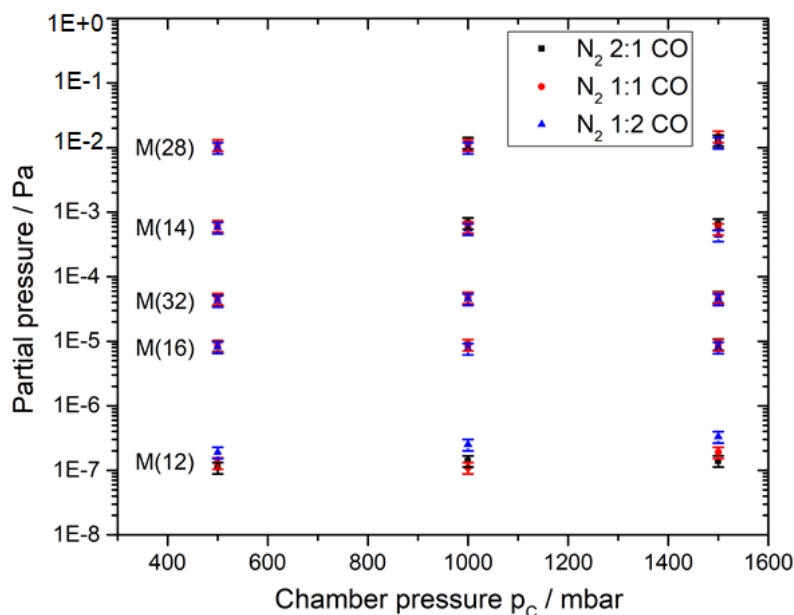


Fig. 4.18: Composition of the gas mixture inside the TC analyzed with the QMS. The signals of different masses are shown as a function of p_c . The gas composition of N_2 to CO and p_c were gradually changed. The total flow rate was kept constant at 1000 mL min^{-1} .

It should be noted that the masses of CO and N_2 are identical. However, when CO-decomposes inside the QMS an increase in the masses 12 and 16 is expected, which could not be observed during these measurements. The QMS used during the experiments was sensitive to the presence of 1% or more CO in pure N_2 . During all performed measurement sequences, no significant increase in the masses of 12 and 16 could be observed, which allows to place an upper limit of 1% CO-content in the N_2 inside the TC. Only during the measurement sequence BDiff_{PC} at a gas composition ratio of CO to N_2 2:1 at high $p_c = 1500 \text{ mbar}$ a small increase in the mass of 12 (carbon) could be observed <1% compared to the mass of 14 (nitrogen). It should be noted, that even without any addition of carbon monoxide the background level of the signal mass 12 was in the order of 10^{-7} Pa .

4.5.2 Discussion

During the first part of the QMS measurements the influence of three different parameters on a possible back diffusion of carbon monoxide from the RC into the TC were investigated. In the first measurement sequence BDiff_{CO} the carbon monoxide partial pressure was gradually increased as (0/13/26/40/53/66)%. Despite the higher partial pressure of CO in the RC in the later measurements, no significant increase in mass 12 could be ascertained during the mass spectrometric investigation.

In the second measurement sequence BDiff_{TF} the influence of the total flow rate on the back diffusion was investigated, whereby a total flow rate of (500 - 1500) mL gas mixture of N₂ and CO in a 1:1 gas mixture was applied. Similarly to the previous measurement sequence BDiff_{CO}, no increase in mass 12 could be observed in these measurements either. Accordingly, it can be assumed that neither an increased total flow rate nor an increase in carbon monoxide partial pressure led to back diffusion of CO from the RC into the TC.

In the last measurement sequence BDiff_{PC} the influence of the pressure inside the TC p_C on the back diffusion in combination with different gas mixtures was investigated. Therefore, the overall pressure in the TC was gradually increased by closing the needle valves in front of the membrane pump. It can be assumed that this directly increased the residence time of one carbon monoxide molecule in the RC, which increases its chance for back diffusion. Nonetheless, no significant increase in the signal of mass 12 could be observed. Even after an additional increase in the partial pressure of CO (1:2/1:1/2:1), no significant increase could be observed. Summarizing all measurements, no significant increase in the signal of mass 12 (carbon) could be observed, which leads to the conclusion that back diffusion of carbon monoxide within the given chamber design is unlikely.

4.6 The influence of the GPS on the gas purity

With a total of 23 different measurements during the measurement sequences GPur₁(15) and GPur₂(8), the influence of the GPS and its containing cartridges on the gas purity was examined. In addition, the influence of different cartridges on the quality of the gas purification could be investigated. These measurements also attempted to investigate the presence of oxygen for the formation of volatile transition metal complexes. Therefore, different combinations were tested by the removal of specific cartridges from the original GPS depicted in Fig. 3.9. Details on the different measurement sequences are given in Tab. 4.3 and Tab. 4.4.

4.6.1 Results

During the measurements the signals for the masses 12(C), 14(N), 18(H₂O), and 28(N₂, CO) usually fluctuated in the order of less than 10 %, (m(16): $2.05 \cdot 10^{-5} \text{ Pa} \pm 11 \%$, m(32): $6.63 \cdot 10^{-5} \text{ Pa} \pm 9 \%$). A similar trend applies to the masses 16(O) and 32(O₂) for the measurement sequences x_i (i = 1-3, 6-8, 11-13). The blue and green dotted lines in Fig. 4.19 visualize the maximum values for these masses. By applying these lines it can be seen that the signals increase for the measurements x_i (i = 4-5, 9-10, 14-15) by a factor of ≤ 1.25 ($\approx 25 \%$). Since the increase in the signals of the masses 16 and 32 follow similar trends this behaviour of the corresponding signals can be attributed to an increased proportion of oxygen in the gas mixture, although it should be noted that the increase in oxygen (m = 16) also refers to CO-decomposition. In Fig. 4.19 and Fig. 4.20 the results of the different measurement sequences are summarized.

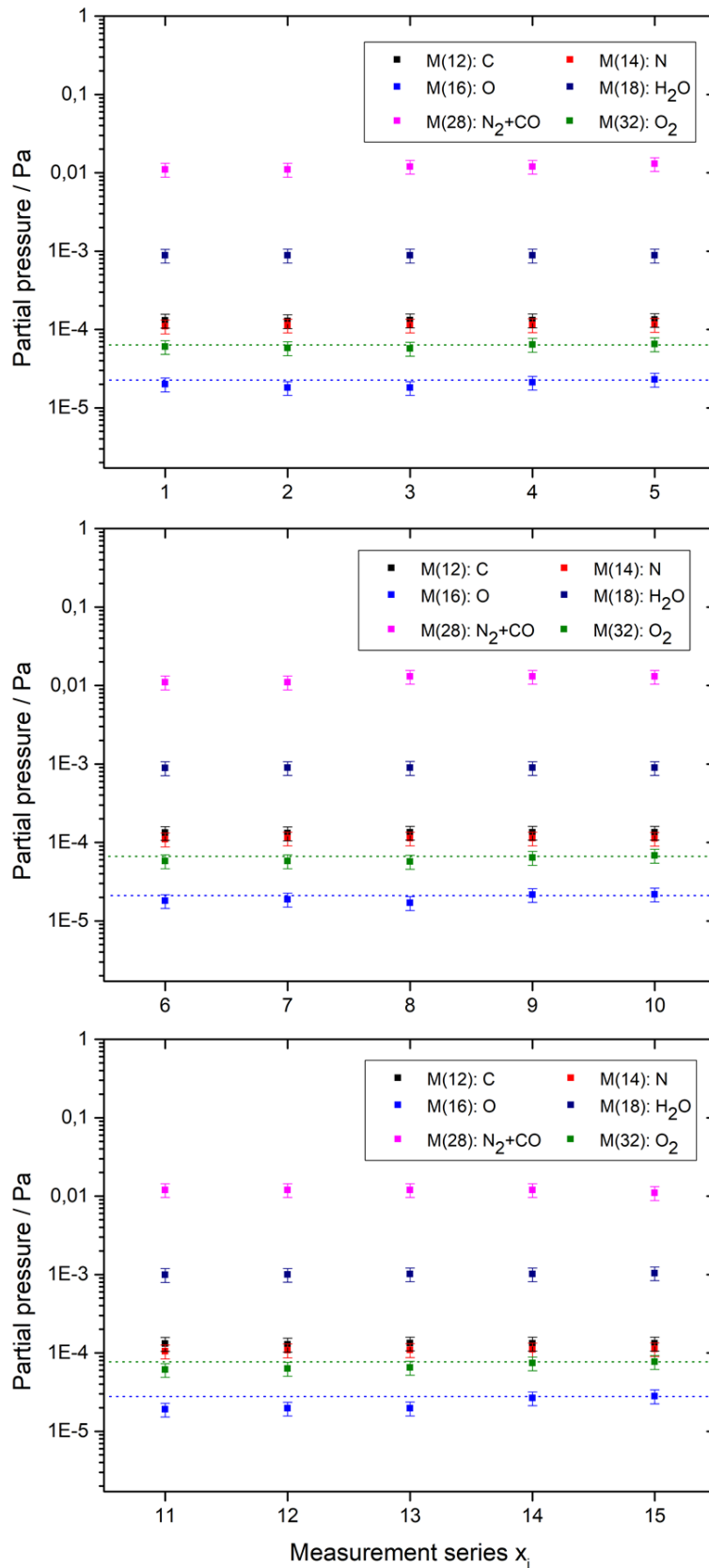


Fig. 4.19: Composition of the gas mixture inside the TC analyzed with the QMS. The signals of different masses are shown for different cartridge combinations as shown in [Tab. 4.3](#). Measurements were performed at $p_C = 1500$ mbar with a total flow rate of 1000 mL min^{-1} of a 1:1 N₂ to CO gas mixture. The lines at masses 16 and 32 are intended to guide the readers eyes.

In Fig. 4.20 the ϵ_{Ref} values as a function of different cartridge combinations are depicted (measurement sequence: GPur₂). Utilizing a different combination of cartridges for the carbon monoxide purification results in a fluctuation of $\leq 8\%$ in ϵ_{Ref} for any combination including the oxisorb cartridge. By removing the oxisorb cartridge, as shown in the measurements y_i ($i = 5-8$), ϵ_{Ref} shows a significant growth $\geq 15\%$. This gap can be reproduced with any combination of cartridges excluding the oxisorb cartridge and therefore the effect can clearly be referred to the absence of oxisorb in the GPS.

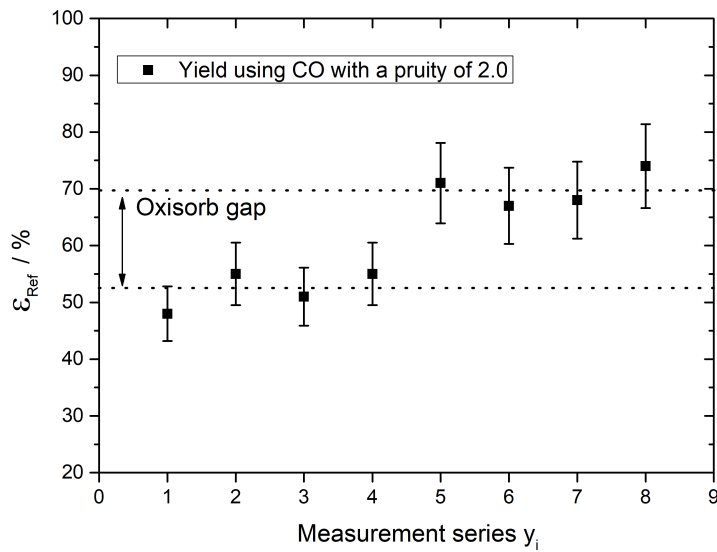


Fig. 4.20: Measured ϵ_{Ref} as a function of the cartridge combination of the GPS. Both gases were fed into the TC with a flow rate of 500 mL min^{-1} each (details for parameters cf. Tab. 4.2 and Tab. 4.4). Measurements were performed at $p_C = 1000 \text{ mbar}$. Carbon monoxide of a purity of 2.0 (99%) was used during this measurement sequence.

4.6.2 Discussion

The motivation for this measurement sequence were observations made during online measurements described in Chapter 4. In these measurements it could be shown, that if the respective gases were not purified by the GPS, but instead fed directly into the TC, ϵ_{Ref} and ϵ_{Tot} increase by a factor ≤ 1.8 . Similar observations were made by Even et al. during carbonyl experiments utilizing carbon monoxide of purity 2.0 (99%) and 3.7 (99.97%) [39] shown in Fig. 4.21.

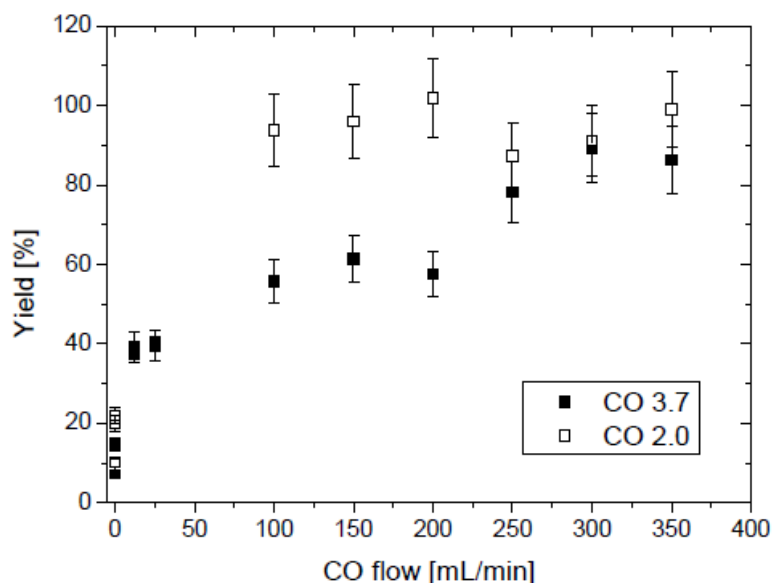


Fig. 4.21: The jet yields of ^{84}Se transported in a N_2/CO gas mixture normalized on a N_2 KCl-cluster jet depending on the amount of CO in the gas stream. The total gas flow was kept at 500 mL min^{-1} . Two different CO gas bottles were used – 2.0 (99%) and 3.7 (99.97%) purity. The spectra were measured 120 s after the pulse. The 407 keV γ -line was analysed and normalized to the live time of the measurement and the reactor pulse. The graph is taken from [39].

In the measurements (GPur₁) shown in Fig. 4.19 only a barely noticeable increase in the masses 16 and 32 during the measurements x_i ($i = 4-5, 9-10, 14-15$) can be observed, which can be referred to the absence of the oxisorb cartridge in the GPS. This observation agrees well with the results of measurement sequence GPur₂, where a significant increase in ϵ_{Ref} could be observed, when no oxisorb cartridge was included. The presence of already a small amount of impurity (e.g.: oxygen, hydrogen) inside the chambers seems to increase the formation of volatile transition metal species. Since the QMS measurements (cf. Fig. 4.19) do not clearly show a significant increase in the masses of 16 and 32 the increased yield in transported transition metals in Fig. 4.21 cannot clearly be attributed to the formation of volatile compounds, e.g. the CO_2 equivalent molecule COSe . However, given the fact that the increase seems to be related to the removal of the oxisorb cartridge, whereby the increase is especially noticeable, the formation of volatile oxides or mixed oxides is likely. This observation agrees with the results of the measurement sequence (GPur₂) shown in Fig. 4.20. The removal of oxisorb cartridge increases ϵ_{Ref} significantly. This is a strong indication, that a specific impurity (oxygen, moisture, non-saturated hydrocarbons), which is removed by the oxisorb cartridge, can be referred to the noticeable growth in ϵ_{Ref} .

However, it should be noted that from literature [169] the formation of technetium pentacarbonyl radical in Szilard-Chalmers reactions is known. It cannot be excluded that mixed

technetium carbonyl complexes (e.g.: hydro or hydrocarbon carbonyl complexes) were formed, as well as volatile pentacarbonyl radical-type complexes [170], since the used oxisorb cartridges from SPECTROMOL are applicable for H₂ and saturated hydrocarbon gases (cf. appendix for more information on the spectromol cartridges).

4.7 Summary of Part I: Carbonyl experiments at the TRIGA Mainz

A novel concept for the in-situ carbonyl-complex synthesis based on a spatial separation of recoil-ion thermalization and complex formation in two separate, but directly connected chambers has been developed and successfully tested at the research reactor TRIGA Mainz. During the first quantitative measurement, promising overall yields of almost 50 % could be achieved for fission-produced Mo radioisotopes. For this experiment, the original thermalization chamber has been successfully modified and tested in the context of the novel two chamber approach with the aim to establish a method with a total efficiency superior of that of physical preseparation. Therefore, detailed transfer studies from the first into the second chamber have been performed with ¹⁴⁶Pr, produced in the spontaneous fission of ²⁴⁸Cm. Experimental efficiencies have been compared with TRIM-simulations to determine pressure-dependent implantation losses in regard to the geometric dimensions of the used thermalization chamber. Monte Carlo simulations have been used for the calculation of diffusion losses inside the transition piece connecting the two chambers. By means of these simulations, the pressure-dependency of the transfer behaviour of non-volatile fission products, represented by ¹⁴⁶Pr, could be described adequately. Short-lived isotopes of technetium and molybdenum, produced in the neutron induced fission of ²³⁵U were used for the investigation of the carbonyl formation process. It could be shown that the chemistry efficiency for the synthesis of carbonyl complexes is favoured by high carbon monoxide partial pressures, in agreement with literature data. The highest efficiencies for the two chamber-approach were obtained by using high bulk gas pressures and high carbon monoxide partial pressures inside the second chamber. They are also promising for experiments with carbonyl-complexes of Sg and potentially heavier transactinides available at smaller rates. Preparatory work, e.g., using group-7 elements, which are known to also form volatile mononuclear carbonyl species [26] are already under way [29, 34, 164]. In Tab. 4.7 the results for all partial efficiencies are summarized.

Tab. 4.7: Experimental (*exp.*) and calculated (*calc.*) efficiencies under various conditions. p_C refers to the pressure present in the TC and in the RC, which were always identical. p_{CO} is the partial pressure of CO i) inside the TC for the determination of $\epsilon_{Ref}(exp.)$, and ii) inside the RC for the determination of $\epsilon_{Tot}(exp.)$. In the measurements of $\epsilon_{Tot}(exp.)$, pure N_2 was present in the TC, which was diluted in the RC by adding the appropriate amount of CO and adjusting the pumping capacity to maintain the desired p_C .

p_C	p_{CO}	ϵ_{Flush}	ϵ_{Flush}^a	ϵ_{Ref}	ϵ_{Chem}	ϵ_{Tot}	ϵ_{Tot}^b
/ mbar	/ mbar	(exp.)	(calc.)	(exp.)	(calc.)	(exp.)	(calc.)
		/ %	/ %	/ %	/ %	/ %	/ %
1000	333	45(9)	44(9)	35(3)	43(12)	19(4)	19(7)
1200	400	49(8)	52(7)	37(3)	46(10)	24(3)	25(6)
1000	500	45(9)	44(9)	48(3)	54(13)	24(3)	23(7)
1200	600	49(8)	52(7)	52(3)	50(11)	26(3)	28(7)
1000	666	45(9)	44(9)	53(3)	70(15)	31(3)	30(9)
1500	750	57(5)	59(4)	62(3)	61(8)	36(3)	37(6)
1200	800	49(8)	52(7)	63(3)	73(13)	38(3)	40(9)
1500	1000	57(5)	59(4)	67(2)	83(8)	49(2)	51(6)

^a The uncertainties have been calculated according to the work of Wittwer et al.[166] for the stopping of ions in gaseous targets using TRIM

$$^b \epsilon_{Tot}(calc.) = \epsilon_{Flush}(calc.) \cdot \epsilon_{Chem}$$

5.1 Experimental parameters

In the previous chapter (cf. [Chapter 4](#)), detailed investigations of the flush-out and carbonyl complex formation processes have been performed using fission products of the $^{235}\text{U}(\text{n},\text{f})$ and $^{248}\text{Cm}(\text{sf})$ processes. As a next step towards transactinide experiments with this "two-chamber" approach, experiments with radioisotopes of 5d elements produced in fusion-evaporation reactions have been performed. Therefore, short-lived fusion products were produced in ^{19}F bombardments of different lanthanide targets at the tandem accelerator facility at JAEA Tokai.

Similar to the preparatory experiments at the TRIGA Mainz, evaporation residues of the transition metals W, Re and Os, were thermalized in a first chamber (TC) mounted directly behind the target, as shown in the schematic of the experimental setup depicted in [Fig. 3.15](#). Suitable radioisotopes were produced in the fusion-evaporation reactions given in [Tab. 5.1](#). The chamber was flushed with inert gas, with the aim to transport evaporation residues into a second, directly connected chamber (RC), where no beam was present. The reactive carbon monoxide gas was added to the RC to facilitate carbonyl complex formation.

The tandem accelerator of JAEA Tokai provided a $^{19}\text{F}^{7+}$ beam at an energy of 6.1 MeV/u, with beam intensities of $(9.4 \pm 0.5) \cdot 10^{11} \text{ s}^{-1}$. The corresponding lab-frame energies in the half-thickness of the targets ($E_{\text{lab, cot}}$) and kinetic energies of the isotopes produced in the reactions (E_{ER}) can also be found in [Tab. 5.1](#). All targets were produced by thermal evaporation [[171](#)] at the GSI target laboratory and covered with a thin carbon layer ($< 5 \mu\text{g}/\text{cm}^2$) to avoid oxidation.

Tab. 5.1: Properties of reactions and evaporation residues (ER) used for the experiment. Beryllium was used as backing material. The beam energy in the laboratory system in the half-thickness of target $E_{lab, cot}$ and the kinetic energy E_{ER} of each isotope produced in the indicated reaction were calculated using Stopping Forces and Ranges of Ions in Matter (SRIM) from Ziegler et al. [144]. For the calculation, the 2- mg cm^{-2} thick beryllium window was taken into account.

Reaction	ER	Target thickness / $\mu\text{g cm}^{-2}$	Backing thickness / mg cm^{-2}	$E_{lab, cot}$ / MeV	E_{ER} / MeV
$^{nat}\text{Tb}(^{19}\text{F}, 5\text{n})$	^{173}W	944	1.68	97.9	10.1
$^{nat}\text{Dy}(^{19}\text{F}, 5\text{n})$	$^{175-178}\text{Re}$	644	1.60	98.6	10.1
$^{nat}\text{Ho}(^{19}\text{F}, 5\text{n})$	^{179}Os	684	1.52	98.9	9.9

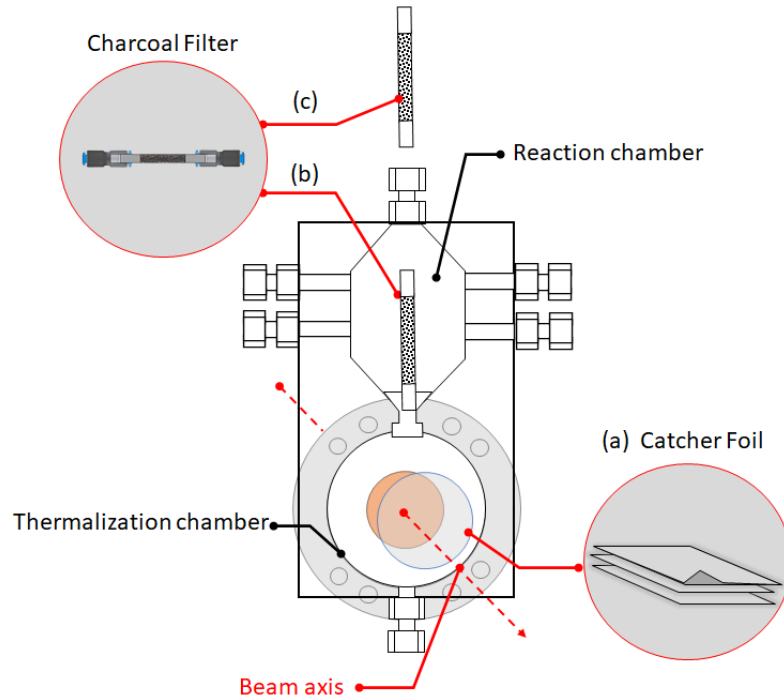


Fig. 5.1: Schematic of all measurement positions where samples could be taken. For details see text.

Samples were collected with a 20 μm Al catcher foil (position (a) in Fig. 5.1) mounted directly behind the target to measure production rates. This foil was thick enough to stop all ER. For the flush-out efficiency measurements from the TC into the RC, self-made charcoal filters that consisted of activated charcoal filled into a piece of Teflon tubing and held in place by quartz wool on both sides as used in [26, 54] could be inserted at the exit of the TC (position (b) in Fig. 5.1). This allowed measuring the fraction of all ERs that was

thermalized and flushed out of the TC (partial efficiency ϵ_{Flush}). The reactive gas (carbon monoxide) was injected directly into the reaction chamber, thus bypassing the TC. Carbonyl complexes were formed in the RC where no beam was present; this is crucial, as beam presence would have prevented the formation of the complexes. Nuclear fusion products, which were volatile or formed volatile carbonyl complexes in the CO-containing atmosphere, were transported with the gas stream from the RC through a 15-m long teflon capillary with an inner diameter of 4 mm to a chemistry laboratory. There, the products were trapped on a charcoal filter (position (c), (total efficiency ϵ_{Tot}) in Fig. 5.1) placed in front of a HPGe detector. The decaying isotopes were identified by γ spectrometry. For the quantitative evaluations, all measured values were normalized using their corresponding beam integral. The determination of the irradiation time (60 s) was performed automatically with a deviation ± 1 s ($< 3\%$). The measurement was performed after the end of irradiation. Unless otherwise specified, the actual start of the measurement began after a 10 min interruption for sample collection and the disassembly process of the chamber. The performed measurement series are summarized in Tab. 5.3. Usually the five-minute measuring time was sufficient to collect suitable statistics on the interesting peaks. Good care was taken to maintain this pattern, so that deviations did not play any significant role in the evaluation of yields. All errors have been calculated by Gaussian error propagation. The most significant contribution comes from the error in the corresponding beam-integral normalized number of net counts in the peaks in the gamma spectra. For measurements with small statistics ($\epsilon_{\text{Tot}} < 30\%$), the relative systematic uncertainty was increased by 25 %.

5.1.1 Isotope production and direct catch measurements

Tab. 5.2: Reaction products and their respective γ lines, chosen for the calculation of the absolute yields. Additionally, the half-lives and the respective gamma intensities of the specific lines $I\gamma$ (%) are given.

Reaction	ER	Gamma line(s) keV ($I\gamma$ / %)	Half-life min
$^{159}\text{Tb}(^{19}\text{F}, 5\text{n})$	^{173}W	457.7 (100) 130.2 (31.5) 174.8 (29.1)	7.6
$^{\text{nat}}\text{Dy}(^{19}\text{F}, 5\text{n})$	$^{176,178}\text{Re}$	^{176}Re :	5.3
			240.2 (48.0) 109.1 (25.0)
		^{178}Re :	13.2
			237.3 (45.0) 105.9 (23.0)
$^{165}\text{Ho}(^{19}\text{F}, 5\text{n})$	^{179}Os	218.6 (100) 165.7 (43.0) 310.0 (29.0)	6.5

The transition metals ^{173}W , $^{175-178}\text{Re}$ and ^{179}Os were produced in the $^{19}\text{F}+^{159}\text{Tb}$, $^{19}\text{F}+^{\text{nat}}\text{Dy}$ and $^{19}\text{F}+^{165}\text{Ho}$ reactions. To facilitate the measurements of the ER production rates, two 20- μm thick Al catcher foils were mounted ≈ 1 mm behind the target. Prior and during irradiation, the TC was flushed with 200 mL min^{-1} He/Ar mixture to reduce oxygen contamination during the subsequent disassembling of the chamber to remove the catcher foils. The pumping capacity was adjusted to maintain a pressure of 1000 mbar inside the TC. The recoil range of ERs in this gas atmosphere was (10-13) mm [167]. For each measurement, the target was irradiated for 1 min, before the chamber assembly was opened and the catcher foils were retrieved. Counting of the foils started 10 min after the end of irradiation. The γ lines, which have been evaluated for the calculation of absolute efficiencies are given in Tab. 5.2, together with the half-lives of the isotopes. In order to compare measurements, which were carried out in two different geometries (charcoal filters vs. foils), the difference in geometry factor was determined. For this, we performed similar measurements using identical aliquots of a gamma standard that were placed on a catcher foil and on a charcoal filter. The difference in geometric efficiency was a factor of 1.05. The uncertainty of this factor is 30 % of the 5 % difference; this was included via Gaussian error propagation in the calculation of all respective yields.

5.1.2 Measurements of the flush-out efficiency $\varepsilon_{\text{flush}}$

The radioisotopes ^{173}W and ^{179}Os were used for optimizing the parameters of flush out from the TC into the RC. A charcoal filter was positioned at position (b) (cf. Fig. 5.1) inside the RC. Tab. 5.3 provides an overview of the used TC conditions and the changes during all measurement sequences. During the first sequence (Flush₁, cf. Tab. 5.3) the optimal gas

composition of the carrier gas was determined by flushing the TC with different gas mixtures of He/Ar at a constant total flow rate of 1000 mL min⁻¹ at 1000 mbar inside the TC. Starting with pure helium, the argon fraction inside the bulk gas was increased stepwise (from 19:1 (5%), 9:1 (10%), 4:1 (20%) to 2.3:1 (30%)) in this measurement sequence. For each step, after 1 min of irradiation the RC was dismantled and the charcoal trap was removed and placed in front of a HPGe detector. The geometric efficiency was about 5 % smaller than for the measurements of the catcher foils; this difference has been taken into account in the data evaluation. We estimate the uncertainty of the difference in geometry factor as being less than 10 %. During the mounting and dismantling process, the TC was flushed with 100 mL min⁻¹ of the inert carrier gas to reduce oxygen contamination. Counting started 10 min after the end of irradiation and lasted for 5 min. The radioactive isotopes were identified by their γ lines. The optimum gas composition for the following experiments was found to be a mixture of He:Ar 9:1 (cf. Sect. 3.1). This ratio was maintained for the rest of the experiments. Before each measurement, the TC was flushed for at least 10 min to reduce the oxygen content inside the two chambers.

In the measuring sequence Flush₂, the total flow rate of the He/Ar mixture was varied in the range of (100 - 1500) mL min⁻¹. In the measurement sequence Flush₃, the investigated flow regime was reduced to (100 - 500) mL min⁻¹. The production and flush-out behaviour of ¹⁷³W and ¹⁷⁹Os were studied in these sequences, respectively.

Tab. 5.3: TC conditions used during the flush-out optimization measurements. The pumping capacity was changed before each measurement sequence to maintain a total pressure of 1000 mbar in the TC. The flow regime shows the total flow rate introduced into the TC. The carrier gas composition remained unchanged at He/Ar = 9:1 in sequences Flush₂ and Flush₃.

Measurement sequence	Investigated isotope	Flow rate / mL min ⁻¹	Studied parameter
Flush ₁	¹⁷³ W	He/Ar: 1000	Ar/He ratio
Flush ₂	¹⁷³ W	He/Ar: 100 - 1500	ϵ_{Flush}
Flush ₃	¹⁷⁹ Os	He/Ar: 100 - 500	ϵ_{Flush}
Total ₁	¹⁷³ W	He/Ar: 85 - 300 CO: 100 - 500	ϵ_{Tot}
Total ₂	¹⁷⁹ Os	He/Ar: 85 - 300 CO: 200 - 500	ϵ_{Tot}
Total ₃	¹⁷⁵⁻¹⁷⁸ Re	He/Ar: 85 - 150 CO: 170 - 300	ϵ_{Tot}
Total ₄	¹⁷⁹ Os	He/Ar: 85 CO: -	Oxygen influence
Total ₅	¹⁷³ W	He/Ar: 85 CO: 500	Oxygen influence

foil and the $^{27}\text{Al}(n,\alpha)^{24}\text{Na}$ reaction, were also present in the spectrum. These were absent in the spectra of charcoal filters.

5.2 The flush-out efficiency $\varepsilon_{\text{Flush}}$

In this section, the results for the flush-out efficiency $\varepsilon_{\text{Flush}}$ will be presented. During these measurements only the gas mixture of He/Ar was fed into the chambers. The data presented in this section were collected during the measurement sequences Flush₁-Flush₃. For details see Tab. 5.3. $\varepsilon_{\text{Flush}}$ describes the flush-out process for non-volatile fission products from the TC into the RC.

5.2.1 Results

In the first part of the experiment, the optimal carrier gas ratio of He:Ar was determined. Fig. 5.3 depicts the $\varepsilon_{\text{Flush}}$ depending on the Ar-content in the carrier gas for a combined He + Ar flow rate of 1000 mL min^{-1} . The maximum value of $\varepsilon_{\text{Flush}}$ of $(34.8 \pm 6.8)\%$ was obtained at a ratio of He:Ar= 9:1.

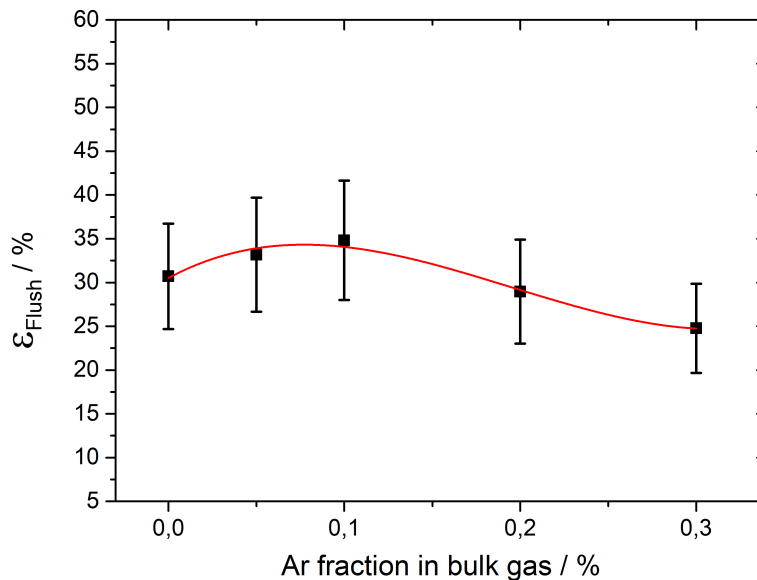


Fig. 5.3: Measured flush-out efficiencies for ^{173}W as a function of the Ar-content of the carrier gas. The total gas flow rate was 1000 mL min^{-1} and the pressure inside the thermalization chamber was 1000 mbar. The line is intended to guide the eye.

In Fig. 5.4 the flush-out efficiencies for ^{173}W are depicted as a function of the carrier gas (He:Ar=9:1) flow rate inside the TC. The ϵ_{Flush} for ^{173}W was relatively stable around 40 % for flow rates $<500 \text{ mL min}^{-1}$. At higher flow rates, ϵ_{Flush} slightly decreases to $(34.8 \pm 6.8)\%$. For ^{179}Os , values of ϵ_{Flush} of around 100 % were measured at flow rates below 400 mL min^{-1} . At higher flow rates, ϵ_{Flush} is reduced to similar values as measured for ^{173}W . No direct transport measurements have been performed for the $^{nat}\text{Dy}(^{19}\text{F}, 5n)^{175-178}\text{Re}$ reaction.

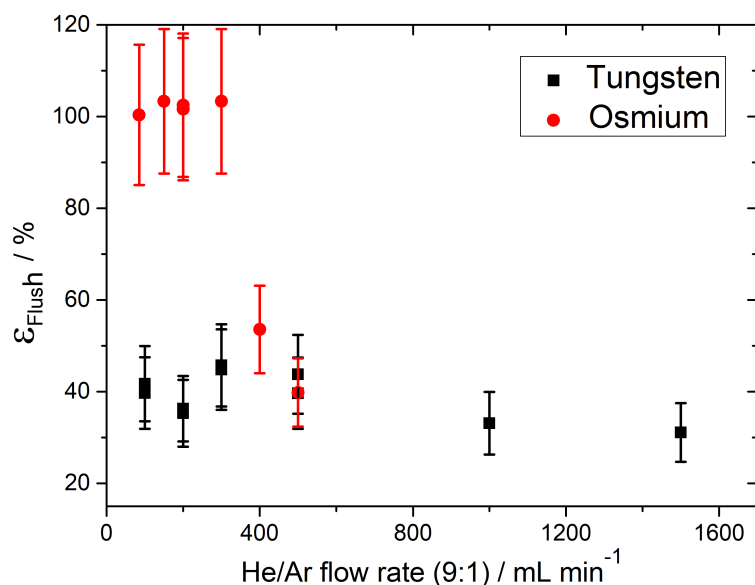


Fig. 5.4: Measured flush-out efficiencies for ^{173}W and ^{179}Os as a function of the carrier gas (He:Ar=9:1) flow rate inside the TC. The pressure inside the thermalization chamber was 1000 mbar.

5.2.2 Discussion

As discussed in the previous chapter (cf. Sec. 5.2), the transport process can be described as a two step process, in which the isotope of interest first needs to be stopped in the gas volume in the TC and will then be flushed through the nozzle into the RC. Due to the non-volatile nature of the transition metals, any wall-collision will reduce the number of reaction products available for carbonyl complex formation. ERs, which are not stopped inside the gas, will be lost by implantation into the TC. The stopping process of the reaction products is influenced by the carrier gas composition. In Fig. 5.3 the flush-out efficiency of ^{173}W is depicted as a

function of the He/Ar gas composition.

According to TRIM [144] simulations the average stopping position of the ERs thermalized in 1000 mbar He:Ar = 9:1 gas is in the centre of the TC. Increasing the Ar content of the carrier gas will lead to shorter ranges, moving the stopping position further away from the entrance to the nozzle. Therefore, a higher argon fraction can be expected to reduce the ϵ_{Flush} . On the other hand, reducing the Ar content will increase the range. In the extreme case of pure helium this reaches values of (16-17) mm, and implantation of a fraction of the reaction products into the TC cannot be excluded.

In Fig. 5.4 the measured ϵ_{Flush} of ^{173}W is depicted as a function of the carrier gas flow rate. In the previous section Sec. 4.3.2, we used a Monte Carlo simulation in the spirit of the microscopic model developed by Zvara [130] to describe the experimental behaviour inside the nozzle by treating this as an isothermal-chromatography process in an open column with laminar flow. The number of collisions as well as the mean jump length were obtained from this simulation. In a chromatography process, higher flow rates would result in a reduction of diffusion-related losses. This behaviour could not be observed during the present experiment. This validates the design of the connection via two touching tapered shapes between the two chambers, which suppresses diffusion-related losses inside the nozzle. The slight reduction of ϵ_{Flush} with increasing carrier gas flow rates could be related to changes in dead volume, due to the flush out process perpendicular to the beam axis.

The flush-out efficiencies determined for osmium are quite different from the results obtained for tungsten. The high Os yields obtained in some measurements, i.e., those performed at low flow-rates, might be connected to the ability of Os to form a volatile compound also in the absence of carbon monoxide, namely the tetroxide OsO_4 . This is impossible for W, which features no highly volatile oxide.

In contrast, potentially, Os atoms can be oxidized and transported as tetroxide, as shown in Fig. 5.5. (a) The fusion products can be guided through the TC without any collisions with either, impurities which may influence the chemical properties of the metal atom, or the surface of the TC itself. This is the optimal case for our flush-out measurements. (b) The fission product may collide with specific impurities on their way through the TC. Oxygen impurities would be of particular importance, since they are capable of forming different oxides $(\text{M}(\text{O})_x, x=1-4)$ with transition metals [172, 173] depending on the oxygen content inside the TC. Due to the fact that the chamber had to be opened to position the charcoal filter inside the RC, the oxygen contamination inside the chamber could be rather high, despite the fact that the TC was continuously flushed with carrier gas during the dismounting process. Therefore, the chamber was flushed with carrier gas for 10 min before a measurement sequence was started, which was intended to suppress scenario (b) which is most likely to happen at high oxygen concentrations. Scenario (c) describes the adsorption of transition metals on the

surface of the TC, which is typically contaminated with oxygen after the chamber opening. After the adsorption, the metal atom will most likely form an oxide which may be volatile (e.g.: OsO_4), or non-volatile (e.g.: WO_2). From (d) it may fly into the RC following the path shown as (e) or it remains sitting on the surface (d). Due to the high volatility of the formed osmium tetroxide, the high flush-out yields are most likely distorted by these oxides and the shown yields cannot exclusively be referred to transported non-volatile osmium atoms. This could also explain the high difference in transport efficiency between osmium and tungsten, since tungsten oxides are non-volatile and thus, remain on the surface of the target chamber.

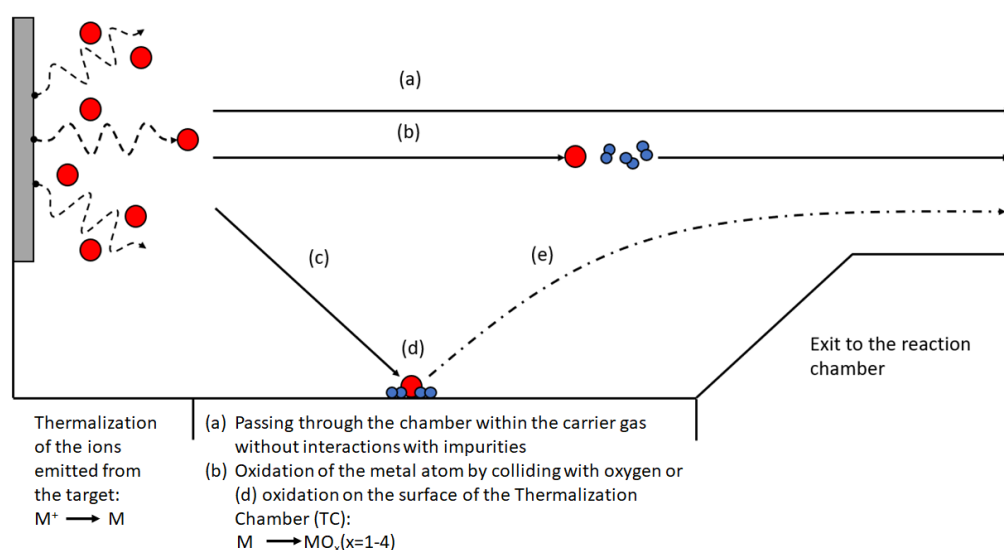


Fig. 5.5: Schematic of different scenarios for the fusion products inside the thermalization chamber. The fusion products are depicted in red, impurities are shown in blue. For details see text.

For the formation of OsO_4 to take place, a source of oxygen needs to be present, beyond that remaining in gases after their purification. An important potential source may be residual oxygen remaining inside the chambers after their opening, due to, e.g., placing or removing catcher foils in position (a) and charcoal traps in position (b) during the measurement series $\text{Flush}_1 - \text{Flush}_3$ (cf. **Tab. 5.3**). To minimize this effect, the TC was continuously flushed with carrier gas while the RC was open. After closing the RC and the tubing, this was flushed with carrier gas for 10 min before a measurement sequence was started. A longer waiting time was not afforded due to the limited beamtime available for these studies. A more aggressive oxygen removal sequence involving evacuation of the whole system was impossible due to the stress this would impose on the vacuum window. Evidently, even during 10 min of flushing with purified, oxygen-free gas, oxygen levels did not reach the low levels of the purified gas. Therefore, the reduction of ϵ_{Flush} for Os shown in **Fig. 5.4** at flow rates $>350 \text{ mL min}^{-1}$ can be referred to (i) a more efficient purification of the chamber at higher gas flow

rates and (ii) a slight reduction caused by the potential occurrence of some turbulence at the transition between TC and RC. The W transport shows only a slight reduction from $(48.0 \pm 8.9)\%$ at 300 mL min^{-1} to $(32.7 \pm 6.4)\%$ at 1500 mL min^{-1} , which is in agreement with the data collected at the TRIGA Mainz [174]. We assume that the formation of volatile species of OsO_4 significantly influences the Os data, and that the maximum ϵ_{Flush} for non-volatile species is in the order of $(50 \pm 10)\%$. The applied flow rate in the TC in the chosen flow regime of this experiment ($< 1000 \text{ mL min}^{-1}$) has only a minor influence.

5.3 The overall efficiency ϵ_{Tot}

In this section, the results for the overall efficiency ϵ_{Tot} will be presented. During these measurements, only the gas mixture of He/Ar was fed into the TC, whereas CO was fed into the RC. The data presented in this section were collected during the measurement sequences Total₁ - Total₅. For details see Tab. 5.3. ϵ_{Tot} describes the overall performance of the two-chamber approach. ϵ_{Tot} includes the flush-out of non-volatile fission products from the TC into the RC, the formation of volatile carbonyl complexes, and finally the transport to the detector. Therefore, ϵ_{Tot} is the product of the partial efficiencies ϵ_{Flush} and ϵ_{Chem} , which have been already presented in Sec. 5.2 and will be discussed in the course of this chapter respectively.

5.3.1 Results

In Fig. 5.6 the measured total efficiency ϵ_{Tot} as a function of the carbon monoxide partial pressure p_{CO} inside the RC is shown for each investigated isotope. All three curves show a direct dependence from the carbon monoxide partial pressure, whereby with increasing fraction of CO inside the gas mixture, ϵ_{Tot} is growing.

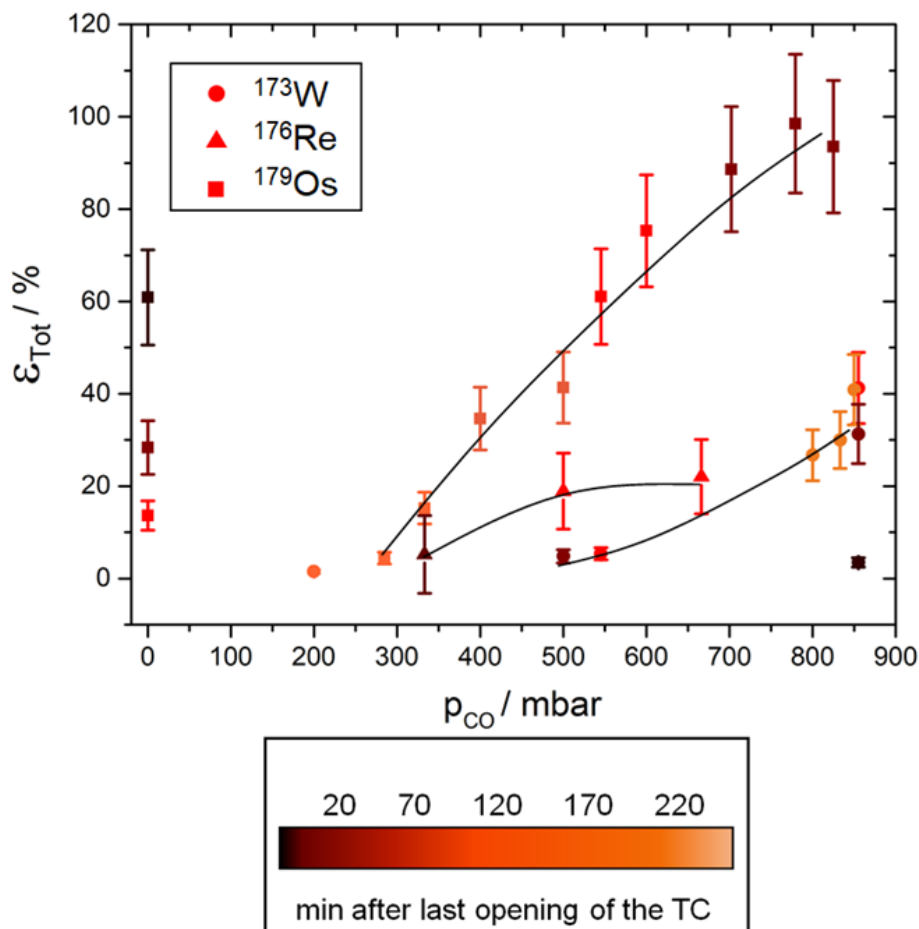


Fig. 5.6: Measured total efficiencies for ^{173}W (circles), ^{176}Re (triangles) and ^{179}Os (squares) as a function of the carbon monoxide partial pressure (p_{CO}) inside the RC. Due to the limited collection efficiency of the Re species on our charcoal traps (cf. Fig. 5.7) the values given for Re represent lower limits. The pressure inside the TC was kept at 1000 mbar. The total flow rates are given in Tab. 5.3. The colour of the data points indicates the time which was elapsed since the last opening of the chamber. The lines are intended to guide the eyes.

Values up to $(98.5 \pm 15.0)\%$ and up to $(41.3 \pm 7.7)\%$ were measured for ^{179}Os and ^{173}W , respectively. The values for ^{176}Re were consistently higher than those for ^{173}W for p_{CO} in the range of $p_{\text{CO}} \leq 700$ mbar, where Re measurements were performed. These experimental series for all three elements show a pronounced dependence on p_{CO} . In Tab. 5.4 the highest values of ϵ_{Flush} and ϵ_{Tot} obtained for all evaluated measurement series are summarized.

In addition, three measurements were performed for the collection of ^{179}Os without feeding CO ($p_{\text{CO}} = 0$ mbar) into the RC (Total₄), to investigate the potential influence on ϵ_{Tot} of a transport of Os in the form of its highly volatile tetroxide OsO_4 [175]. Therefore, the data points given in Fig. 5.6 were colour-coded, with the colour representing the elapsed time

after the last opening of the chamber assembly. In these measurements the amount of ^{179}Os reaching the charcoal trap at position (c) decreased steadily from initially $(60.9 \pm 10.3)\%$ to $(13.7 \pm 3.2)\%$ after continuously flushing both chambers for 45 min.

A similar measurement sequence (Total_5) was performed for the investigation of the influence of the presence of traces of oxygen on the carbonyl complex formation of ^{173}W . Therefore, measurements at identical conditions with $p_{\text{CO}} = 855$ mbar were performed, first directly after the last chamber opening and then after continuous flushing of the chamber assembly for 32 min and 50 min. In this measurement sequence, ε_{Tot} increased successively from initially $(3.4 \pm 1.0)\%$ to $(41.3 \pm 7.7)\%$.

The measurements with ^{176}Re proved to be unexpectedly difficult. The volatile ^{176}Re species could only be retained insufficiently on only one of the used charcoal traps. To address this, four charcoal traps were connected in a series to increase the catching efficiency. The fraction collected on each single charcoal filter, when the filters were arranged in a series, is shown in Fig. 5.7. For W and Os, no breakthrough after one charcoal trap was observed, as verified in separate measurements.

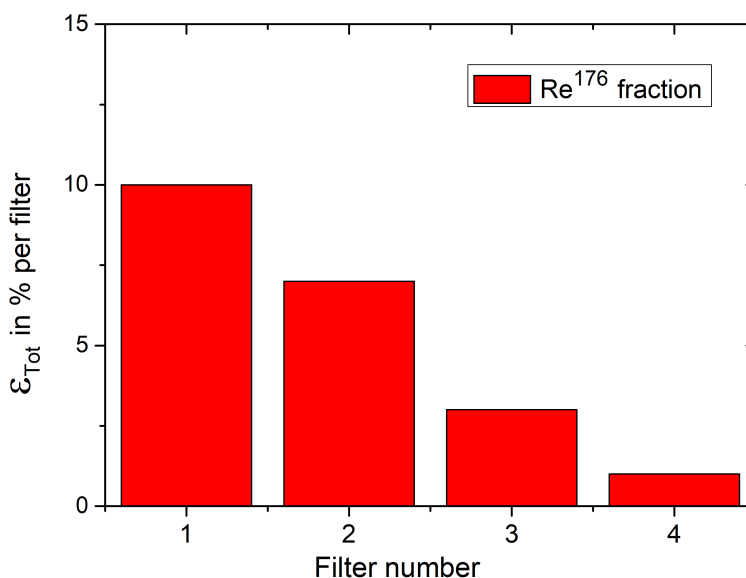


Fig. 5.7: Fraction of collected ^{176}Re on individual charcoal traps, when a total of four charcoal traps were used in a series to collect volatile Re carbonyl complexes. During the measurement p_{CO} was 1000 mbar with 200 mL min^{-1} carbon monoxide fed into the RC and 100 mL min^{-1} carrier gas ($\text{He}:\text{Ar}=9:1$) fed into the TC.

Since breakthrough of volatile rhenium carbonyl complexes could not be fully excluded the values for ϵ_{Tot} of ^{176}Re shown in Fig. 5.6 have been assumed as lower limits. However, ϵ_{Tot} for Re was observed to be consistently higher than for W and lower than for Os in the window of $p_{\text{CO}} = (333\text{-}667)$ mbar. The maximum ϵ_{Tot} value was about $(22.1 \pm 7.0)\%$ at $p_{\text{CO}} = 667$ mbar.

5.3.2 Discussion

In Fig. 5.6 a strong relation between the amount of collected volatile transition metal compounds and the carbon monoxide partial pressure is observed for all three elements. The amount of transported ^{179}Os increases with the carbon monoxide content in the bulk gas, which was already reported in several experiments [21, 24, 25, 27]. The total performance of the two-chamber approach was described by the partial efficiencies of the flush-out and the chemical compound formation process $\epsilon_{\text{Tot}} = \epsilon_{\text{Chem}} \cdot \epsilon_{\text{Flush}}$.

The ϵ_{Flush} was described as mostly dependent on the pressure inside the thermalization chamber and the stopping probability (gas composition) of the fusion products in the TC. Since the pressure was kept at 1000 mbar in all measurements, the difference in flush-out efficiency is expected to be rather small over all measurements, which indeed can be seen in Fig. 5.4 for the flush out efficiency of ^{173}W . The highest overall yields were measured at lower carrier-gas flow rates introduced into the TC ($<500 \text{ mL min}^{-1}$). In the next step, by measuring ϵ_{Tot} with charcoal traps at position (c), ϵ_{Chem} can be deduced by the following equation:

$$\epsilon_{\text{Chem}} = \frac{\epsilon_{\text{Tot}}}{\epsilon_{\text{Flush}}} \quad (5.1)$$

The ϵ_{Chem} depends on the composition of the gas in the RC where the complex formation takes place [174]. In agreement with literature data [16, 21, 27, 164], ϵ_{Chem} increases with an increasing fraction of CO, cf. Fig. 5.6, and reaches its maximum at highest p_{CO} .

The influence of the oxygen content inside the thermalization chamber can be inferred from the data shown in Fig. 5.6. Data points in dark colour indicate measurements taken shortly after the last chamber opening, where the oxygen contamination is expected to be highest.

The effect of the oxygen impurities in the cases of tungsten and osmium was studied in more detail within the measurement sequences Total₄ and Total₅. In Total₄ a measurement sequence for the detailed investigation of ^{179}O was started without addition of carbon monoxide to examine the fraction of ϵ_{Tot} , which can be referred to the transport of volatile OsO_4 over time since the last chamber opening. The results of these measurements are depicted in Fig. 5.6 at $p_{\text{CO}} = 0$ mbar. In Total₅ the influence of oxygen on the transport of ^{173}W was

investigated. This element is known to be susceptible to react with oxygen, however in this case this prevents the formation of volatile species. Therefore, for the measurement sequence Total₅, five different samples were taken whereby only the time elapsed since the last chamber opening varied, while all other conditions were kept identical. In Fig. 5.6 this measurement sequence is depicted at $p_{\text{CO}} = 855$ mbar. The trend of these measurements is depicted in Fig. 5.8 in more detail. The steady increase of ϵ_{Tot} with the elapsed time after the last chamber can be attributed to a reduction in the formation of W oxides and therefore, an increased possibility for carbonyl complex formation in the RC. The change in ϵ_{Tot} for ^{173}W and ^{179}Os indicates the formation of their corresponding oxides and verifies the need for oxygen-free conditions to study carbonyl complexes.

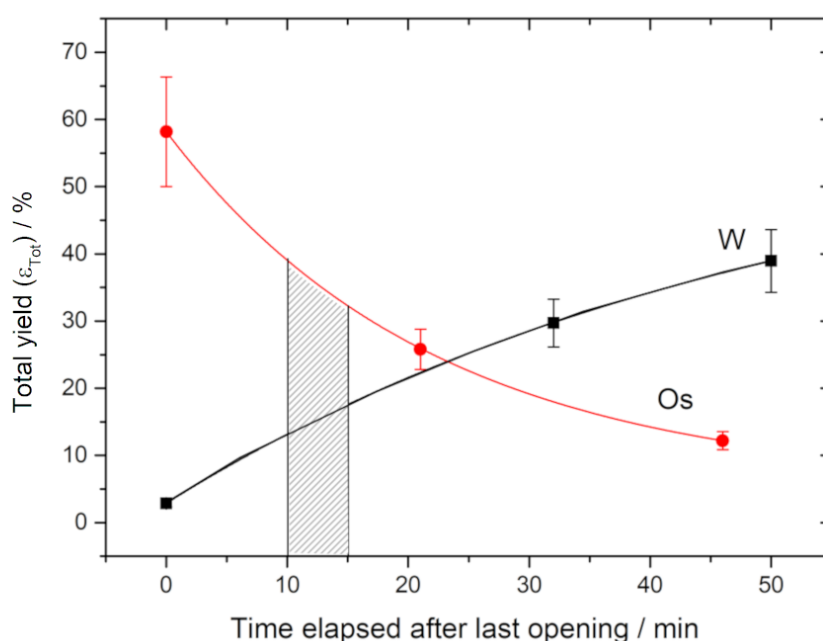


Fig. 5.8: Influence of the oxygen impurities on ϵ_{Tot} . In case of Os a separate measurement sequence was started (Total₄) without the addition of CO inside the RC. In case of W, specific measurements (Total₅) were repeated with identical conditions. Typically measurement sequences were started (10-15) min after the chamber was last opened, indicated with the grey box.

Fig. 5.8 shows that ϵ_{Tot} for ^{179}Os is including approximately 40% of volatile oxides at the beginning of a measurement sequence, which is reduced by the continuous flushing to $\approx 10\%$ after 50 min of operation. In regard to Fig. 5.6 and Fig. 5.4 the maximum efficiencies measured for ϵ_{Tot} and ϵ_{Flush} could be estimated to be around 50-60% rather than almost 100%, which is by far more reasonable. If we assume, that the corresponding efficiencies for ^{173}W are also still negatively influenced by the oxygen impurities, the ϵ_{Tot} is estimated to be $> 38\%$ and therefore is similar to the values for osmium.

The strong decrease in ϵ_{Tot} for Os with increasing elapsed time since the last opening is attributed to the effect of continuously rinsing the chambers, which reduced the oxygen contamination significantly. However, it can also be seen that the rinsing process was not yet complete after 10 to 15 minutes. In contrast, with $\epsilon_{\text{Tot}} \approx 10\%$, the total efficiency measurements were influenced by oxygen transport even after 40 to 50 min of flushing. Similar observations but with an opposite trend were made in the case of ^{173}W . The steady increase of ϵ_{Tot} with the elapsed time after the last chamber opening indicates a reduction in the formation of W oxides and therefore, an increased possibility for carbonyl complex formation in the RC. The change in ϵ_{Tot} for ^{173}W and ^{179}Os indicates the formation of their corresponding oxides and verifies the need for oxygen-free conditions to study carbonyl complexes.

Incidentally, this pronounced decrease in the overall efficiency for the formation of volatile osmium carbonyl complexes can also be observed in Fig. 5.4. However, there was only the corresponding ϵ_{Flush} shown, which also indirectly indicates an oxygen influence. If the values for ϵ_{Flush} is put into the context of the respective rinsing time, as shown in Fig. 5.6, this effect could be reproduced, and the respective values for ϵ_{Tot} observed during the osmium measurements, successively approached to the respective ϵ_{Tot} values observed during the tungsten measurements, if the rinsing time was sufficiently long. Therefore, the strong decrease in ϵ_{Tot} for Os with increasing elapsed time since the last opening (cf. Fig. 5.8) is attributed to the effect of continuously rinsing the chambers, which reduced the oxygen contamination significantly. However, it can also be seen that the rinsing process was not yet complete after 10 to 15 minutes. In contrast, with $\epsilon_{\text{Tot}} \approx 10\%$, the total efficiency measurements were influenced by oxygen transport even after 40 to 50 min of flushing. Similar observations but with an opposite trend were made in the case of ^{173}W . The steady increase of ϵ_{Tot} with the elapsed time after the last chamber opening indicates a reduction in the formation of W oxides and therefore, an increased possibility for carbonyl complex formation in the RC. The change in ϵ_{Tot} for ^{173}W and ^{179}Os indicates the formation of their corresponding oxides and verifies the need for oxygen-free conditions to study carbonyl complexes.

In context to the yields shown in Tab. 5.4 and to the discussed transport yields in the previous chapter, the losses in the second chamber, referring to the unsuccessful formation of a volatile carbonyl complex within the reaction gas, are quite low. In both cases, osmium and tungsten, the chemistry efficiency was observed to be higher than $>85\%$.

In Tab. 5.4 the measured maximum values of ϵ_{Flush} , ϵ_{Chem} and ϵ_{Tot} are summarized. The results shown for ^{173}W indicate that carbonyl experiments without a physical pre-separation step are feasible even in accelerator based experiments. The chemical identification of

Tab. 5.4: Summary of the highest values of the ϵ_{Flush} and ϵ_{Tot} measurements for the given isotopes. The values given for ϵ_{Chem} were calculated according to Eq. 5.1.

Reaction	ϵ_{Flush} / %	ϵ_{Chem} / %	ϵ_{Tot} / %
$^{159}\text{Tb}(^{19}\text{F}, 5\text{n})^{173}\text{W}$	46(5)	85(16)	39(6)
$^{165}\text{Ho}(^{19}\text{F}, 5\text{n})^{179}\text{Os}^a$	98(10)	96(14)	94(10)
$^{\text{nat}}\text{Dy}(^{19}\text{F}, 5\text{n})^{175-178}\text{Re}$	(-)	(-)	(>20)
$^{235}\text{U}(\text{n},\text{f})^{101}\text{Mo}^b$	57(5)	83(8)	49(2)

^a Os data are influenced by the formation of volatile OsO₄.

^b Data shown for ¹⁰¹Mo are taken from Tab. 4.7

carbonyl complexes for the group 8 elements remains problematic due to the high volatility of OsO₄ and already small oxygen concentrations can significantly influence chemical studies of group 8 carbonyl complexes. However, the values for ϵ_{Chem} deduced from W(CO)₆ formation reached $\approx 85\%$ after 50 min of flushing, which corresponds with the results for Mo measured in our previous work [174]. Values of up to 41(8)% for ϵ_{Flush} in the first carbonyl experiments utilizing the two-chamber approach without physical preseparation are also promising for future studies of transactinide elements. Whereas the production of group 7 carbonyl complexes utilizing fission products at the TRIGA Mainz was strongly influenced by precursor effects, the successful production of volatile Re carbonyl complexes in the $^{\text{nat}}\text{Dy}(^{19}\text{F}, 5\text{n})^{175-178}\text{Re}$ reaction confirms that the formation of group 7 carbonyl complexes is viable. Our lower limit for ϵ_{Tot} of 20 % points at a considerable volatility of the group 7 carbonyl complexes. The considerably small lower limits for ϵ_{Tot} can be referred to the high volatility of the group 7 carbonyl complexes and potentially also to a lower ϵ_{Chem} for these non-saturated 17 valence electron complexes. However, the formation of unsaturated 17 valence electron carbonyl complexes agrees with theoretical predictions [17]. Despite that radical-type complexes are not common, their existence was reported already in Szilard Chalmers type experiments leading to the formation of radical-type rhenium pentacarbonyl complexes [176].

5.4 Summary of Part II: Carbonyl experiments at the Tandem research facility

At the JAEA tandem accelerator facility, the first in-beam studies for the in-situ carbonyl complex synthesis using the novel two-chamber approach have been successfully performed. W, Re, and Os fusion-evaporation products were thermalized in the inert-gas-filled first chamber (TC) and flushed to a second chamber (RC) into which carbon monoxide was fed. This maintains a spatial decoupling of beam-environment behind the target and beam-free environment at the site of chemical complex formation, as was established in the previous studies of carbonyl complexes using the approach of physical preseparation. We observed the formation and transport of volatile carbonyl complexes of ¹⁷³W and ¹⁷⁵⁻¹⁷⁸Re. ¹⁷⁹Os was also transported, but this was probably at least partially due to the formation of volatile OsO₄ facilitated by the presence of trace amounts of oxygen impurity in the carrier gas.

An influence of this oxygen contamination was also observed in the results obtained for W, where it reduced the formation of W carbonyl complexes. The overall efficiencies reached in our studies exceed those of the approach of physical preseparation. Thus, the results are very promising for extending studies of carbonyl complexes of transactinides to elements beyond Sg. As a next step, studies with alpha-decaying isotopes especially of Re appear necessary to study kinetic aspects as well as the interaction with hetero-surfaces; these will provide important data on complex stability and adsorption properties of this nearest homolog of Bh. However, experiments with superheavy elements performed at a one-atom-at-a-time level depend on sufficiently low background due to, e.g., species transported via aerosol-transport. More sensitive studies in this regard are ideally carried out with alpha-decaying isotopes of the 5d homologs.

In 2014, the successful synthesis of $\text{Sg}(\text{CO})_6$ was reported [22], thus opening up experimental studies of transactinides to this compound class, which was previously inaccessible due to technical limitations of previously used approaches. This was not only the first reported transactinide carbonyl complex, furthermore it was an exciting new development, which paves the way to metal-organic compounds of superheavy elements. The breakthrough was achieved by using a physical preseparator, which allows the collection coupled with a chemical reaction of single atoms of the SHE in a RTC, without the destructive interference from primary particle beams.

Promising preparatory were performed in the run-up with 4d and 5d elements, which showed that carbonyl complexes are accessible for a wide range of elements (transition metals) [21, 24–27, 29, 164]. However, the synthesis of superheavy elements and the studies of their chemical properties are more challenging due to their low production rates at the one-atom-at-a-time level, and due to their short half-lives. The seaborgium carbonyl experiments were performed with the cryo-thermochromatography detector COMPACT [108] coupled to the GARIS recoil separator of RIKEN [177], whereby ^{265}Sg was produced at a rate of about one atom-per-hour for chemical investigations [12]. Unfortunately, despite promising theoretical predictions for the feasibility and stability of group 7 - 9 carbonyl complexes [17, 34, 35], the synthesis for bohrium-, hassium-, and meitnerium carbonyl complexes is unlikely with the current method of choice of using physical preseparation and the given productions rates as already described in Sec. 1.2.

6.1 Conclusions

For the feasibility of chemical investigations of heavier transactinide carbonyl complexes than Sg in a similar one atom-per-(X)hours rate, it would be essential to overcome the limitations caused by the physical preseparation step ($\epsilon_{\text{GARIS}} \approx 13\%$ [40]). To avoid the yield-reducing isolation in a recoil separator, further possibilities for the chemical investigation of carbonyl complexes without a physical preseparation stage are explored. This work reports on experiments using a so called "two-chamber" approach. The synthesis of carbonyl complexes of short-lived radioisotopes of transition elements using this technique was studied at TRIGA Mainz and at JAEA Tokai. Both experiments verify that the chemical

synthesis of the carbonyls is possible within this approach. The first results are encouraging: the results from the TRIGA experiment suggest that up to almost 50% of the produced Mo isotopes could be delivered from the target chamber to the second chamber, where the chemical reaction took place, yielding the volatile carbonyl complexes. The subsequent experiments at the JAEA TANDEM accelerator facility with fusion products confirm this. Promising results were obtained for long-lived isotopes of W, Re, and Os produced in nuclear fusion reactions. Our results imply that the production of thermally less stable volatile carbonyl compounds is feasible without a physical pre-separation step. Furthermore, the systematic investigation of the transport-, formation-, and overall efficiencies during the experimental series performed at the TRIGA Mainz revealed substantial dependencies from experimental parameters like the carbon monoxide partial pressure or the bulk gas pressure regime. A next step should focus on the study of carbonyl complexes using the two-chamber system with short-lived products of nuclear fusion reactions.

Tab. 6.1: Efficiencies for carbonyl-complex studies of group 6 elements using different techniques. Calculated values are shown in italics, whereas measured values are shown in bold.

	¹⁰¹ Mo at TRIGA ^a / %	¹⁷³ W at JAEA ^b / %	²⁶⁵ Sg at GARIS ^c / %	²⁶⁵ Sg future / %
ϵ_{Flush} :	57	46(5)	(-)	46(5)
ϵ_{GARIS} :	(-)	(-)	13	(-)
ϵ_{Chem} :	85	85(16)	$\gtrsim 8$	$\gtrsim 8$
ϵ_{Tot} :	49	39(6)	≈ 1	≈ 3.7

^aData taken from [174].

^bThis work

^cData taken from [22, 40]

In table Tab. 6.1, the performance of the two-step approach is summarized and compared with that of physical pre-separation, as it was used in studies of the group-6 hexacarbonyl complexes [23, 25–28] including Sg(CO)₆ at the RIKEN GARIS separator [22, 28]. In the experiments by Even et al. in total 18 atoms of ²⁶⁵Sg were observed [22]. Considering the beam integral, target thickness and cross section of the given reaction, the ϵ_{Tot} behind GARIS was $\leq 1\%$. Experiments by Haba et al. [40] verified a ϵ_{GARIS} of 13 %, which describes the amount of ERs reaching the RTC and therefore the number of Sg atoms which will be available for carbonyl complex formation. Comparing these numbers for ϵ_{Flush} with efficiencies obtained for tungsten within our experiment: $\epsilon_{\text{Flush,W}} = (46 \pm 5) \%$ a significant increase (by a factor of ≈ 3.7) in efficiency could be observed. Under the assumption of identical ϵ_{Chem} this would directly translate into an improvement in $\epsilon_{\text{Tot, 265Sg}}$ for seaborgium by a factor of $\epsilon_{\text{Flush}}/\epsilon_{\text{GARIS}} \approx 3.7$ (cf. Tab. 6.1).

6.2 Future studies

Future carbonyl chemistry experiments with transactinide elements like Bh and Hs seem to be feasible by enhancing production rates without a physical pre-separation step. The products of the $^{22}\text{Ne}+^{249}\text{Bk}$ reaction ($\sigma(^{267}\text{Bh}) = 25\text{-}250\text{ pb}$, $T_{1/2} = 17_{-6}^{+14}\text{ s}$) [42] and of the $^{26}\text{Mg}+^{248}\text{Cm}$ reaction ($\sigma(^{269-271}\text{Hs}) = 7_{-3}^{+3}\text{ pb}$, $T_{1/2}(^{269}\text{Hs}) \approx 9.7\text{ s}$) [43, 178], and of the $^{48}\text{Ca}+^{226}\text{Ra}$ reaction ($\sigma(^{270}\text{Hs}) = 16_{-7}^{+13}\text{ pb}$, $T_{1/2} = 7.7_{-2}^{+5}\text{ s}$) [44] could be particularly suitable here. It is still not completely understood, why the transition metals of group 7 and 9 form volatile homoleptic carbonyl complexes of the radical type. Additional experiments, coupled with QMS measurements may be able to investigate the formation of metal carbonyl hydrides, whereas mass analytic experiments, e.g., at FIONA (For the Identification Of Nuclide A) [179] could be used to investigate the metal carbonyl bonding and their corresponding bond strengths. The bond strength, in turn, is suitable for investigating the influence of relativistic effects on the transactinides, since the bond strength in the carbonyl complexes is directly connected to the orbital energies (cf. Sec. 2.4.2).

Nevertheless, the carbonyl synthesis of superheavy elements holds promises for the investigation also of metall-organic complexes in the superheavy element region. A fast and quantitative formation of carbonyl complexes could be used for the first chemical experiments with different isotopes of meitnerium, which are difficult to access with typical chemical experiments like oxides and chlorides [180]. A new isothermal chromatography detector called AlBeGa (Alpha Beta Gamma), which is shown in Fig. 6.2 [181] could be used for nuclear spectroscopy methods and the investigation of isomeric states of volatile species like carbonyl complexes via detailed spectroscopy, e.g., of ^{261}Rf , which have been observed in different reactions, e.g.: ($^{244}\text{Pu}(^{22}\text{Ne}, 5\text{n})$ [182] and $^{248}\text{Cm}(^{18}\text{O}, 5\text{n})$ [96]) or even ^{265}Sg with its two isomeric states (cf. Fig. 6.1), which can be produced in the $^{248}\text{Cm}(^{22}\text{Ne}, 5\text{n})$ reaction.

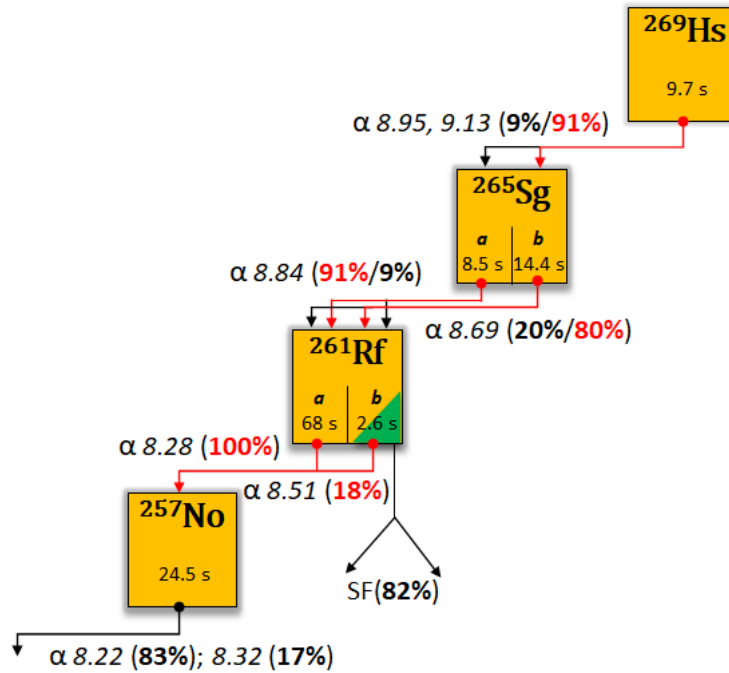


Fig. 6.1: Decay pattern of the chain starting from ^{269}Hs and their corresponding daughters, the two isomeric states of $^{265}\text{Sg}^{a,b}$, which then pass by means of another α -decay into the two isomeric states of $^{261}\text{Rf}^{a,b}$, followed by another α -decay into the ^{257}No . The dominant transitions are shown in red, with the respective energies given in MeV. The picture is taken and adapted from [40].

The significant benefit would result from avoiding the unbeneficial physical pre-separation, which would be replaced with a chemical pre-separation step, the chemical conversion to a volatile carbonyl complex. The change to a chemical pre-separation step is expected to improve the statistics for experiments with production rates in the one atom-at-a-time regime, where $\epsilon_{\text{Chem}}/\epsilon_{\text{Trans}}(\text{separator}) \gg 1$ could be applied. Typically, the sample would be created by the deposition of the volatile carbonyl complex on a cold α -detector surface, e.g.: AlBeGa. Improved statistics could be used to investigate the chemical behavior of these two different isomeric states by their probability of forming carbonyl complexes, as well as the influence, if any, of the respective isomeric state on the corresponding complex stability.

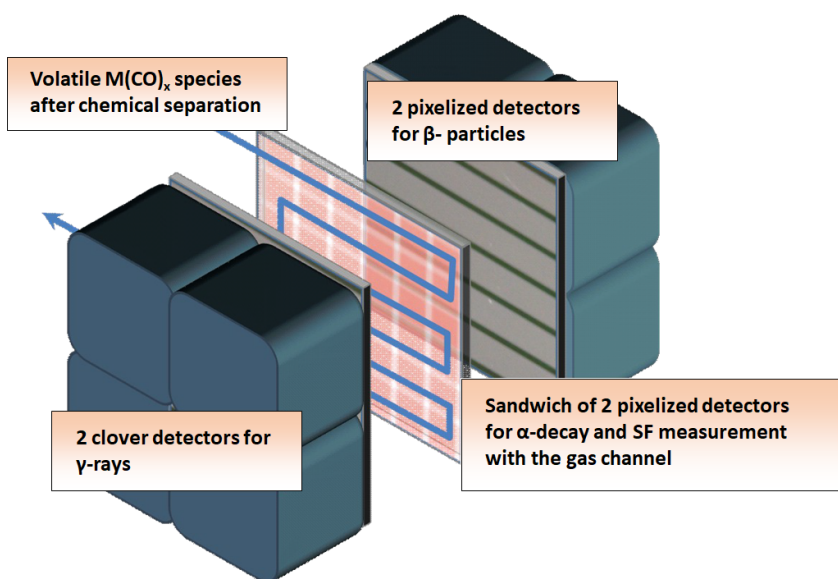


Fig. 6.2: Schematic drawing of the ALBeGa detector. The chromatography channel is made of pixelized detectors for α and SF measurement. This detector plate is cooled by liquid nitrogen. The α detectors are in between a “sandwich” of two pixelized β - detectors. The outer shell consists of two clover detectors for γ and X-ray measurements. The picture is taken from [23].

The ALBeGa detector consists of a meander formed chromatography channel, which is surrounded by two pixelized α -detectors, which are typically cooled by ethanol. These two detectors are "sandwiched" by two detectors panels, sensitive to β -particles and two additional germanium clover detectors for the identification of *gamme*-rays. For this system to operate, volatile compounds or complexes are needed, which can deposition on a detector surface at specific temperatures. These nuclear spectroscopy experiments are also of high interest for elements like Db and Bh, as these elements are expected to have a high chance to observe isomeric states. Since the products of these very asymmetric reactions are hard to study in the focal plane of a physical preseparator, the two-chamber system, which is viable for carbonyl systems could be the method of choice. By providing higher transport rates than physical pre separators, the chemical separation system provided by the formation of volatile carbonyl complexes could be the method of choice for upcoming experiments with elements produced in asymmetric reactions, which provide only small cross sections, and are chemically accessible for carbonyl formation, e.g. bohrium up to meitnerium.

7.1 List of Tables

Tab. 2.1:	Target(Tar.) and projectile(Proj.) combinations for the synthesis of nuclides from nuclear fusion reactions used in transactinide chemistry are shown with their cross sections (σ), neutron evaporation channels(NEC) and estimated production rates (Prod. rate).	24
Tab. 2.2:	Stable, neutral binary metal-carbonyl complexes. Data taken from [16].	25
Tab. 2.3:	The change of bond length d and stretching frequencies ν , when the CO molecule is getting bonded to a transition metal. CO describes the ground state ($X^1\Sigma^+$), whereas CO* describes the electronically excited state in $a^3\Sigma^+$ (TS), and $a^3\Pi_r$ (TP). Data taken from [130] . .	27
Tab. 3.1:	Thermal neutron fluxes at different irradiation positions at the TRIGA MARK II research reactor in Mainz.	50
Tab. 4.1:	Overview of the performed parameter studies, listing measurement sequence and gas flow rates of N_2 and/or CO entering the thermalization chamber (TC) and reaction chamber (RC), respectively. All given positions refer to Figure 4.2.	68
Tab. 4.2:	Overview of the measurement sequences performed during the back diffusion tests. The carbon monoxide fraction in the gas mixture was gradually increased during the BDiff _{CO} measurement sequence, whereas the N_2 to CO ratio was kept at 1:1 during BDiff _{TF} , GPur ₁ and GPur ₂ . In the sequence BDiff _{PC} the N_2 to CO ratio was changed in the ratio of 1:2/1:1/2:1.	73

Tab. 4.3:	Detailed overview of the measurement sequences performed during the gas purification tests GPur ₁ . Cartridges included into the purification system are marked with ✓, whereas cartridges which were excluded from the system are marked with ✗. The influence of the following cartridges was investigated: Sicapent (S), Hydrosorb (M) and Oxisorb (O)	73
Tab. 4.4:	Detailed overview of the measurement sequences performed during the gas purification tests GPur ₂ . Cartridges included into the purification system are marked with ✓, whereas cartridges which were excluded from the system are marked with ✗. The influence of the following cartridges was investigated: Sicapent (S), Hydrosorb (M) and Oxisorb (O)	74
Tab. 4.5:	Calculated values for ϵ_{Stop} , based on their simulated ranges and p_C	80
Tab. 4.6:	Simulated stopping ranges for ^{146}Pr and ^{101}Mo produced by spontaneous fission of ^{248}Cm ($^{146}\text{Pr}^{Cm}$, $^{101}\text{Mo}^{Cm}$) and ^{101}Mo produced by neutron induced fission of ^{235}U ($^{101}\text{Mo}^U$) estimated using the TRIM software package. Post-neutron emission total kinetic energies (KE_F) are given, as well as the kinetic energies of the respective ions before entering the stopping gas in the TC ($\text{KE}(\text{gas})$), which includes losses caused by interaction with half of the target thickness (and the $10\ \mu\text{m}$ Al degrader in case of $^{101}\text{Mo}^U$). In the last column, the estimated fraction (I_{Is}) of fission products stopped in the bulk gas is given.	81
Tab. 4.7:	Experimental (exp.) and calculated (calc.) efficiencies under various conditions. p_C refers to the pressure present in the TC and in the RC, which were always identical. p_{CO} is the partial pressure of CO i) inside the TC for the determination of $\epsilon_{\text{Ref}}(\text{exp.})$, and ii) inside the RC for the determination of $\epsilon_{\text{Tot}}(\text{exp.})$ In the measurements of $\epsilon_{\text{Tot}}(\text{exp.})$, pure N_2 was present in the TC, which was diluted in the RC by adding the appropriate amount of CO and adjusting the pumping capacity to maintain the desired p_C	98
Tab. 5.1:	Properties of reactions and evaporation residues (ER) used for the experiment. Beryllium was used as backing material. The beam energy in the laboratory system in the half-thickness of target $E_{\text{lab, cot}}$ and the kinetic energy E_{ER} of each isotope produced in the indicated reaction were calculated using Stopping Forces and Ranges of Ions in Matter (SRIM) from Ziegler et al. [144]. For the calculation, the 2-mg cm^{-2} thick beryllium window was taken into account.	100
Tab. 5.2:	Reaction products and their respective γ lines, chosen for the calculation of the absolute yields. Additionally, the half-lives and the respective gamma intensities of the specific lines $I\gamma$ (%) are given.	102

Tab. 5.3:	TC conditions used during the flush-out optimization measurements. The pumping capacity was changed before each measurement sequence to maintain a total pressure of 1000 mbar in the TC. The flow regime shows the total flow rate introduced into the TC. The carrier gas composition remained unchanged at He/Ar = 9:1 in sequences Flush ₂ and Flush ₃	103
Tab. 5.4:	Summary of the highest values of the ϵ_{Flush} and ϵ_{Tot} measurements for the given isotopes. The values given for ϵ_{Chem} were calculated according to Equation 5.1.	115
Tab. 6.1:	Efficiencies for carbonyl-complex studies of group 6 elements using different techniques. Calculated values are shown in italics, whereas measured values are shown in bold.	118

7.2 List of Figures

Fig. 1.1:	Schematic of the direct and indirect relativistic effect and the influence of the radial distribution of the 7s valence electrons in element 105, Db. The relativistic calculations are shown as solid line, whereas the non-relativistic distribution is shown as dashed line. Figure adapted from [3].	2
Fig. 1.2:	Periodic table of elements. The transactinices (Superheavy elements, $Z < 104$) are shown in red. Elements, for which successful gas- and liquid phase experiments have been performed are indicated by violet and blue boxes. Elements supposed to be accessible with carbonyl experiments are indicated with green boxes.	3
Fig. 1.3:	Schematic of the experimental setup used for the $^{248}\text{Cm}(^{22}\text{Ne},5n)^{265}\text{Sg}$ reaction at the recoil separator GARIS at RIKEN. The reaction products are transported through GARIS, and slowed down in the recoil transfer chamber (RTC), where they react with the carbon monoxide. The resulting $\text{Sg}(\text{CO})_6$ products are transported to the thermochromatography apparatus COMPACT for analysis. Picture is taken from [22].	6
Fig. 1.4:	Production cross sections for the $^{248}\text{Cm}(X,5n)$ reactions for the elements nobelium up to meitnerium. Cross sections were taken from references [40, 43, 45–49].	7
Fig. 2.1:	Binding energies and β decays of nuclides with even mass number. ^{64}Ni (even-even), is the minimum of the mass parabola, which undergoes no further decay as a stable nucleus. Data adapted from [10].	11
Fig. 2.2:	Differences between experimental atomic masses and the LDM drop model masses as a function of their proton (top)- and neutron (bottom) numbers. A noticeable difference is pronounced at the numbers 28, 50, 82 and 126. Picture taken and adapted from [10].	12

Fig. 2.3:	The approach along the x-axis of a neutron (orange) to a ^{116}Sn nucleus. The single-neutron levels in the potential well are indicated. The neutron is trapped at a certain energy level. The distance r_n indicates the range of the cohesive forces at which the approach neutron is adsorped and pulled inside the potential well. Adapted from [62].	13
Fig. 2.4:	Single-particle levels of a deformed harmonic oscillator as a function of the deformation. The graph is taken from [10].	14
Fig. 2.5:	Schematic representation of the prolate and oblate deformations, compared to a spherical nucleus.	15
Fig. 2.6:	Double humped fission barrier (solid line) as a function of the deformation parameter ε_D . The fission barrier equals the deformation energy and can be calculated as shown in Equation 2.4. E_{LDM} shows the deformation of the nucleus, which leads a split in energy levels, shown by E_{Shell} . The sum of these two energies gives the fission barrier and characterizes the stability of the nucleus against fission. For details, see text above. Picture adapted from [10].	16
Fig. 2.7:	Double humped fission barrier (solid line) as a function of the deformation parameter ε_D . The fission barrier equals the deformation energy and can be calculated as shown in Equation 2.4. Picture adapted from [10].	17
Fig. 2.8:	Excerpt from the upper end of the Chart of Nuclei and the shell corection energies calculated for the given area of interest. Estimated magic numbers are highlighted in red. Picture adapted from [73] with calculations taken from Möller et al. [74, 75].	18
Fig. 2.9:	Calculated fission barriers for ^{250}Cf (actinide), ^{268}Sg (transactinide) and ^{298}Fl (spherical transactinide). The macroscopic fission barrier is shown as a red dotted line. The ground state deformation is shown based on calculations performed by A. Sobiczewski. Pictured adapted from [77].	19
Fig. 2.10:	Plot of the observed cross section for the production of heavy elements by cold and hot fusion reactions with $Z \geq 102$ in the 1n (cold fusion) and 5n (hot fusion) evaproation channel. Figure taken from [12] and adapted with values from Ref. [81]	20
Fig. 2.11:	The sketch of the sequences of the nuclear reaction mechanism in heavy ion collisions. When the projetile (P) collides with the Target (T), the formation of a compound nucleus (CN) competes always with other reaction channels, e.g.: nucleon transfer, quasi-fission and fission [82]	21
Fig. 2.12:	Classification of heavy-ion collisions. Figure adapted from Ref. [88]	23

Fig. 2.13:	(left)Schematic of the molecular orbital diagram of carbon monoxide before and after s-p mixing. With quantum mechanical calculations the contour-line (right) diagrams for the orbitals can be visualized, which are used to describe the shape of the M-C-O bond. Picture adapted from [16].	26
Fig. 2.14:	Scheme of synergistic σ -donation, π -donation and π -backbonding in the transition metal carbon monoxide bonding. The bond strength of the C-O bond is influenced by the difference in charge between the oxygen and carbon atom, therefore moving electrons away in a donation to the transition metal will strengthen the C-O bond, whereas the addition of electrons has the opposite effect. Picture adapted from [16].	27
Fig. 2.15:	Calculated Bond dissociation energies (kcal/mol) as a function of the charge of the complex for isoelectronic $M(CO)_6^q$ ($M^q = Hf^{2-}, Ta^-, W, Re^+, Os^{2+}, Ir^{3+}$) hexacarbonyl complexes [122].	28
Fig. 2.16:	Splitting of the orbital energy levels of an octahedral d^6 transition metal complex ML_6 , where the ligand L has occupied donor orbitals with σ symmetry and empty acceptor orbitals with π symmetry [16].	29
Fig. 2.17:	Orbital interaction diagram of the splitting d, s, p valence orbitals of a transition metal in an octahedral ligand field [16].	30
Fig. 2.18:	Trend of the covalent- and electrostatic energy contributions to the interaction energy between $TM(CO)_5^q$ and CO. The numbers in brackets indicate the interatomic distances. Data taken from [122].	31
Fig. 2.19:	Trend of the frontier orbital energy levels of the pentacarbonyls. Data taken from [122].	32
Fig. 2.20:	Trend of the radii of maximum charge density of group 8 elements. Data taken from [35].	34
Fig. 2.21:	SO ZORA energies of the ns and (n-1)d valence AOs of group 8 elements. Data taken from [35].	35
Fig. 2.22:	Schematic of the $M(CO)_5$ bond formation of group 8 transition metals. Picture adapted from [35].	36
Fig. 2.23:	Schematic of the σ -interactions in the D_{3h} representation. Figure is adapted from [126].	36
Fig. 2.24:	Schematic of the π -interactions in the D_{3h} representation. Figure is adapted from [126].	37
Fig. 2.25:	(a) Calculated first bond dissociation energies of group-8 $M(CO)_5$ carbonyl complexes and (b) predicted adsorption enthalpies via ADF (SO) on quartz and teflon surfaces. Data taken from [35]	38
Fig. 2.26:	Schematic of the different steps during nuclear fission. After neutron capture, the fission products will gain kinetic energy of up to 100 MeV, emit neutrons and γ rays until they end as stable nuclei.	40

Fig. 2.27:	Aysmmetric thermal neutron fission yields of ^{235}U . The thermal neutron induced fission yield mass distribution shows a ratio of the heavy to light mass >1.0 for the fission of most nuclei [10].	41
Fig. 2.28:	Schematic of the description of a molecule in the downstream migration inside a chromatography column. Picture taken from [37].	42
Fig. 2.29:	Stopping Powers for silicion ions in a silicon target as a function of the ion velocity and the ion energy. The ion velocity is given in the units of Bohr velocity v_B . The picture is adapted from [138].	45
Fig. 2.30:	Schmatic trajectory of a particle passing through a stopping medium. The electronic stopping affects the ion both during the collision and thereafter. Between two collisions, the ion is slowed by a constant force owing to the momentum exchange with the electrons in the material (1). The energy loss during a collision is connected to electron exchange (4)+(5) between the ion and the target. In addition, charge-exchange events will occur (2)+(3)+(6).	46
Fig. 3.1:	Schematic of the beam tube arrangement at the reasearch reactor TRIGA Mainz. The experiments described in the thesis were performed at beamport A, which offers the possibility for long-term experiments. The thermal neutron flux among the beamports varies significantly, for instance beamport D points directly at the reactor core and therefore, the neutron flux is substantially higher than at the others. The picture was taken and adapted from [148, 149]	49
Fig. 3.2:	Schematic of the original target chamber which is placed inside of beamport A close to the core. The carrier gas (red line) enters the chamber through a lateral inlet. The fission products (green circles) produced by neutron induced fission will be extracted through the central exit port.	51
Fig. 3.3:	Target-holder of the TRIGA Mainz. The front- and back-plate of the target-holder hold the target in place between of each other. The eight surrounding holes, which offer a possibility for the gas to enter the target chamber are also visible.	51
Fig. 3.4:	Shematic of the target-holder in side- and isometric view. The target-holder consists of two parts: (1) Back-plate and (2) Front-plate.) . . .	52
Fig. 3.5:	Schematic of the modified thermalization chamber which is placed inside of beamport A. The thermalization chamber can be flushed with a carrier gas (nitrogen) and the reactive gas can be introduced seperately into the reaction chamber, which can be mounted on the former exit of the thermalization chamber.	53

Fig. 3.6:	(a): The modified target chamber consists of 7 main elements shown in its disassembled state: (1) Aluminum shell of the chamber (2) Screw bracket of the aluminum shell (3) Aluminum shells for the connection ports of the chamber (4) Back-plate of the target chamber (5) Thermalization chamber (6) Reaction chamber (7) Connections for the gas inlets of the reaction chamber (b) Target chamber in its assembled state.	54
Fig. 3.7:	Simplified schematic of the experimental setup used for the experiments at the TRIGA Mainz. The respective gases were introduced via the gas purification system (GPS). Nitrogen and carbon monoxide could be fed into the TC, whereas the RC could only be flushed with carbon monoxide. The pressure was monitored inside the GPS and both chambers. For more details, see text.	55
Fig. 3.8:	The pneumatic fitting type QSM-6 provides a leakproof sealing up to 14 bar. A collet keeps the capillary in position by the help of small stainless steel teeth.	56
Fig. 3.9:	Schematic of the experimental setup used for the mass spectrometry measurements. The respective gases were either introduced: (a) via the gas purification system (GPS) used during the experiments at TRIGA or (b) via a bypass, which either allowed the installation of specific purification cartridges or any combination of them (b.1) or was directly connected to the two-chamber system (b.2). The nitrogen gas was introduced into the thermalization chamber (TC), whereas the carbon monoxide gas was connected to the reaction chamber (RC). Samples could be extracted from either, the TC and the RC and were transported to the quadrupole mass analyzer (QMS).	57
Fig. 3.10:	Schematic of the used charcoal filters, plugged into two push-in fittings from FESTO. The filters could be used up to flow-rates of 1500 mL min^{-1}	58
Fig. 3.11:	Simplified schematic of the tandem accelerator facility. Ions will be produced by a pellet chain and will be accelerated in two stages. First, in the form of negative ions up to the high voltage terminal and after electron stripping, downwards as positively charged ions. Figure taken and adapted from Ref. [161]	59
Fig. 3.12:	Schematic of the JAEA tandem research facility. The tandem accelerator provides ion beams ten beam lines, distributed among 5 different research rooms. The JAEA tandem accelerator also includes a LINAC booster, which can be used as an additional "third" acceleration step for heavy ions. Figure was adapted from [161].	60

Fig. 3.13:	Isometric view of the thermalization- (TC) and the reaction chamber (RC). The TC is mounted perpendicularly to the beam axis and flushed with the carrier gas (He/Ar in a mixture of 9:1, shown as blue dots). The gas is guided into a conically-shaped nozzle. Carbon monoxide was introduced through gas inlets inside the nozzle directly behind the tapering (shown as orange dots). Additional carbon monoxide was introduced to the RC over two further inlets in the middle of the chamber.	61
Fig. 3.14:	Isometric view of the thermalization- (TC) and the reaction chamber (RC) in conjunction with the newly designed nozzle connecting the two chambers. The gas flow of the reactive gas (CO) is shown in orange.	62
Fig. 3.15:	Simplified schematic of the experimental setup used for the experiments at the JAEA tandem accelerator. The respective gases were introduced via the gas purification systems (GPS-Reactive gas, GPS-Carrier gases). A mixture of helium and argon was used as carrier gas, whereas carbon monoxide remains the reactive gas. The pressure was monitored inside the gas system and both chambers. For more details, see text.	64
Fig. 4.1:	Cut-out of the chart of nuclides, including their half-lives and independent-, as well as cumulative yields in the neutron induced fission reaction of ^{235}U . Data is taken from the ENDF/B-VI fission library.	65
Fig. 4.2:	Schematic of all measurement positions where samples could be taken. For details see text.	66
Fig. 4.3:	(a) γ -ray spectrum observed for the direct catch measurement with a teflon disc using the Al-covered ^{235}U -target. Counting started 47 min after the end of irradiation and lasted for 30 min. This spectrum was used as a reference measurement for the calculation of absolute yields, referring to the amount of ^{101}Tc entering the TC. (b) γ -ray spectrum for the direct catch measurement using the non-covered ^{248}Cm -source. Counting started 5 min after the sample collection ended and lasted for 90 min. Both measurements were performed under similar conditions with 500 mL/min of nitrogen flow and $p_{\text{C}} = 1000$ mbar.	69
Fig. 4.4:	γ -ray spectrum of ^{248}Cm fission products of the $p_{\text{C}}(\text{Flush})$ I-X measurement sequence transported in 500 mL/min N_2 fed into the TC and 500 mL/min N_2 fed into the RC, collected on a quartz fibre filter at $p_{\text{C}} = 1000$ mbar. The sample was measured 5 min after 90 min of collection.	70

Fig. 4.5:	γ -ray spectrum of fission products of the $p_{p_C}(\text{Tot})$ I-III measurement sequence transported in 500 mL min^{-1} nitrogen and 500 mL min^{-1} carbon monoxide, collected on a charcoal filter at $p_C = 1000 \text{ mbar}$. The charcoal filters were measured 5 min after the end of irradiation.	71
Fig. 4.6:	Measured ϵ_{Ref} for ^{101}Mo in a N_2/CO gas mixture as a function of the carbon monoxide partial pressure. The total gas flow rate was 1500 mL/min and p_C was in the range of (1000-1500) mbar. Absolute efficiencies were calculated by using the daughter nuclide ^{101}Tc as an indicator for ^{101}Mo . The different pressures inside the TC, p_{p_C} , are depicted by different colours.	75
Fig. 4.7:	Measured values for ϵ_{Flush} as function of the pressure p_C . Total flow rate was 1 L min^{-1} .	76
Fig. 4.8:	Simulations of the range of fission products, performed with SRIM2013 [144]. For all simulations, $200 \text{ }^{146}\text{Pr}$ ions with an initial kinetic energy of 74 MeV were used, whereby the effect of self-absorption in the ^{248}Cm -source was taken into account. (a) The ions were stopped in 800 mbar N_2 . (b) The ions were stopped in 100 mbar N_2 . (c) The ions were stopped in 1200 mbar N_2 .	78
Fig. 4.9:	Schematic to illustrate the calculation of ϵ_{Stop} . The target was considered to be a point source and the chamber exit was described in spherical segments, whereas θ describes the angle of emission where implantation started.	79
Fig. 4.10:	Transfer- and stopping efficiency from the TC to the RC of ^{101}Tc produced by spontaneous fission from a ^{248}Cm source as a function of p_C . The stopping efficiency (red circles) was simulated with the computer program TRIM and the transfer efficiency (squares), at a flow rate of 0.5 L/min and 1.0 l/min , was calculated based on the MCS introduced in chapter 3.2.2.. The lines are intended to guide the readers eyes.	82
Fig. 4.11:	Schematic of the transition piece used in between TC and RC. In addition, the dimensions are given to visualize the change in geometry be introducing this aperture. In the final assembly, the transition piece is mounted directly on the TC and the protrusion is inserted into the into the outlet of the TC.	83
Fig. 4.12:	Comparison of ϵ_{Diff} simulated with the MCS approach provided by Zvara et al. [37] for different lengths of the transition piece.	84
Fig. 4.13:	Comparison of the measured ϵ_{Flush} (black circles) with the theoretical predictions (red line). For the calculated values, the respective diffusion- and implantation losses were taken into account.	85

Fig. 4.14:	Comparison of the measured ϵ_{Flush} for the 6 mm (black circles) and the 8 mm (red circles) transition, depicted together with their corresponding theoretical predictions (lines). For the calculated values, the respective diffusion- and implantation losses were taken into account.	86
Fig. 4.15:	(a) Measured ϵ_{Tot} for ^{101}Mo in a N_2/CO gas mixture as a function of the carbon monoxide content and p_{C} . (b): Same as (a), but shown as a function of the nitrogen content and p_{C} . The total gas flow rate was $750\text{-}1500\text{ mL min}^{-1}$ in both measurements, whereas the nitrogen flow rate was kept constant at 500 mL min^{-1} in (a) and the carbon monoxide flow rate was kept constant at 500 mL min^{-1} in (b). Absolute efficiencies were calculated by the detection of the daughter nuclide ^{101}Tc . In the absence of carbon monoxide, no ^{101}Tc was detected.	88
Fig. 4.16:	Composition of the gas mixture inside the TC analyzed with the QMS. The signals of different masses are shown as a function of the carbon monoxide flow rate. The total flow rate was 1500 mL min^{-1} and p_{C} was kept constant at 1000 mbar.	90
Fig. 4.17:	Composition of the gas mixture inside the TC analyzed with the QMS. The signals of different masses are shown as a function of the total flow rate ($\text{N}_2 + \text{CO}$). The gas mixture of N_2 to CO was kept at a ratio of 1:1 and p_{C} was kept constant at 1000 mbar.	91
Fig. 4.18:	Composition of the gas mixture inside the TC analyzed with the QMS. The signals of different masses are shown as a function of p_{C} . The gas composition of N_2 to CO and p_{C} were gradually changed. The total flow rate was kept constant at 1000 mL min^{-1} .	92
Fig. 4.19:	Composition of the gas mixture inside the TC analyzed with the QMS. The signals of different masses are shown for different cartridge combinations as shown in Table 4.3. Measurements were performed at $p_{\text{C}} = 1500\text{ mbar}$ with a total flow rate of 1000 mL min^{-1} of a 1:1 N_2 to CO gas mixture. The lines at masses 16 and 32 are intended to guide the readers eyes.	94
Fig. 4.20:	Measured ϵ_{Ref} as a function of the cartridge combination of the GPS. Both gases were fed into the TC with a flow rate of 500 mL min^{-1} each (details for parameters cf. Table 4.2 and Table 4.4). Measurements were performed at $p_{\text{C}} = 1000\text{ mbar}$. Carbon monoxide of a purity of 2.0 (99 %) was used during this measurement sequence.	95

Fig. 4.21:	The jet yields of ^{84}Se transported in a N_2/CO gas mixture normalized on a N_2 KCl-cluster jet depending on the amount of CO in the gas stream. The total gas flow was kept at 500 mL min^{-1} . Two different CO gas bottles were used – 2.0 (99 %) and 3.7 (99.97 %) purity. The spectra were measured 120 s after the pulse. The 407 keV γ -line was analysed and normalized to the live time of the measurement and the reactor pulse. The graph is taken from [39].	96
Fig. 5.1:	Schematic of all measurement positions where samples could be taken. For details see text.	100
Fig. 5.2:	γ -ray spectra from the $^{19}\text{F}+^{159}\text{Tb}$ reaction. The γ -lines in the direct catch collected at position (a), see Figure 5.1 (black line) are shown in comparison with those in the charcoal filter measurement collected at position (c) (red line).	104
Fig. 5.3:	Measured flush-out efficiencies for ^{173}W as a function of the Ar-content of the carrier gas. The total gas flow rate was 1000 mL min^{-1} and the pressure inside the thermalization chamber was 1000 mbar. The line is intended to guide the eye.	105
Fig. 5.4:	Measured flush-out efficiencies for ^{173}W and ^{179}Os as a function of the carrier gas (He:Ar=9:1) flow rate inside the TC. The pressure inside the thermalization chamber was 1000 mbar.	106
Fig. 5.5:	Schematic of different scenarios for the fusion products inside the thermalization chamber. The fusion products are depicted in red, impurities are shown in blue. For details see text.	108
Fig. 5.6:	Measured total efficiencies for ^{173}W (circles), ^{176}Re (triangles) and ^{179}Os (squares) as a function of the carbon monoxide partial pressure (p_{CO}) inside the RC. Due to the limited collection efficiency of the Re species on our charcoal traps (cf. Figure 5.7) the values given for Re represent lower limits. The pressure inside the TC was kept at 1000 mbar. The total flow rates are given in Table 5.3. The colour of the data points indicates the time which was elapsed since the last opening of the chamber. The lines are intended to guide the eyes. . .	110
Fig. 5.7:	Fraction of collected ^{176}Re on individual charcoal traps, when a total of four charcoal traps were used in a series to collect volatile Re carbonyl complexes. During the measurement p_{CO} was 1000 mbar with 200 mL min^{-1} carbon monoxide fed into the RC and 100 mL min^{-1} carrier gas (He:Ar=9:1) fed into the TC.	111

Fig. 5.8:	Influence of the oxygen impurities on ε_{Tot} . In case of Os a separate measurement sequence was started (Total ₄) without the addition of CO inside the RC. In case of W, specific measurements (Total ₅) were repeated with identical conditions. Typically measurement sequences were started (10-15) min after the chamber was last opened, indicated with the grey box.	113
Fig. 6.1:	Decay pattern of the chain starting from ^{269}Hs and their corresponding daughters, the two isomeric states of $^{265}\text{Sg}^{a,b}$, which then pass by means of another α -decay into the two isomeric states of $^{261}\text{Rf}^{a,b}$, followed by another α -decay into the ^{257}No . The dominant transitions are show in red, with the respective energies given in MeV. The picture is taken and adapted from [40].	120
Fig. 6.2:	Schematic drawing of the AlBeGa detector. The chromatography channel is made of pixelized detectors for α and SF measurement. This detector plate is cooled by liquid nitrogen. The α detectors are in between a “sandwich” of two pixelized β - detectors. The outer shell consists of two clover detectors for γ and X-ray measurements. The picture is taken from [23].	121
Fig. 9.1:	Specifications of Hydrosorb gas purifications cartridges of the company Spectromol.	152
Fig. 9.2:	Specifications of Oxysorb gas purifications cartridges of the company Spectromol.	153
Fig. 9.3:	Specifications of the Big Moisture Trap BMT-4 of the company Agilent.	154
Fig. 9.4:	Specifications of the Big Oxygen Trap BOT-4 of the company Agilent.	154
Fig. 9.5:	Specifications of the Molecular Sieve MT400-4 of the company Agilent.	154

- (1) Pyykkö, P.; Desclaux, J. P. Relativity and the periodic system of elements. *Acc. Chem. Res.* **1979**, *12*, 276–281.
- (2) Pershina, V. In Schädel, M., Ed., 2nd, Erratum, pp. E1-E3; Springer: 2014; Chapter Theoretical chemistry of the heaviest elements, pp 135–239.
- (3) Schädel, M. Chemistry of the superheavy elements. *Philos. Trans. R. Soc. London, Ser. A* **2015**, *373*, 1–15.
- (4) Pitzer, K. S. Relativistic effects on chemical properties. *Acc. Chem. Res.* **1979**, *12*, 271–276.
- (5) Vandenbosch, R. Angular Momentum Distributions in Subbarrier Fusion Reactions. *Annu. Rev. Nucl. Part. Sci.* **1992**, *42*, 447–481.
- (6) Schädel, M. Chemistry of Superheavy Elements. *Angew. Chem. Int. Ed.* **2006**, *45*, 368–401.
- (7) Hoffman, D. C.; Lee, D. M. Chemistry of the Heaviest Elements- One Atom at a Time. *J. Chem. Educ.* **1999**, *76*, 331–347.
- (8) Schädel, M., *The Chemistry of Superheavy Elements*; Springer: 2007.
- (9) Türler, A. Advances in chemical investigations of the heaviest elements. *EPJ Web of Conf.* **2016**, *131*, 07001.
- (10) Kratz, J.-V., *The Chemistry of Superheavy Elements*; Springer-Verlag GmbH: 2013.
- (11) Vertes, A. et al., *Handbook of Nuclear Chemistry*; Springer US: 2010; 3440 pp.
- (12) Türler, A.; Pershina, V. Advances in the Production and Chemistry of the Heaviest Elements. *Chem. Rev.* **2013**, *113*, 1237–1312.
- (13) Türler, A. et al. Chemical studies of elements with $Z \geq 104$ in gas phase. *Nucl. Phys. A* **2015**, *944*, 640–689.
- (14) Loveland, W. Superheavy carbonyls. *Science* **2014**, *345*, 1451–1452.
- (15) Baumgärtner, F.; Reichold, P. Zur Chemie bei Kernprozessen. *Z. Naturforsch., A: Phys. Sci.* **1961**, *16*, 945–948.
- (16) Elschenbroich, C., *Organometallchemie*; Teubner B.G. GmbH: 2008; 764 pp.
- (17) Iliáš, M.; Pershina, V. Carbonyl compounds of Rh, Ir, and Mt: electronic structure, bonding and volatility. *Phys. Chem. Chem. Phys.* **2020**, *22*, 18681–18694.
- (18) Pershina, V.; Hoffman, D. C. In *Theoretical Chemistry and Physics of Heavy and Superheavy Elements*; Springer Netherlands: 2003, pp 55–114.
- (19) Pershina, V. In *Theoretical and Computational Chemistry*; Elsevier: 2004, pp 1–80.
- (20) Pershina, V. In *Challenges and Advances in Computational Chemistry and Physics*; Springer Netherlands: 2010, pp 451–520.
- (21) Even, J. et al. Rapid synthesis of radioactive transition-metal carbonyl complexes at ambient conditions. *Inorg. Chem.* **2012**, *51*, 6431–6433.
- (22) Even, J. et al. Synthesis and detection of a seaborgium carbonyl complex. *Science* **2014**, *345*, 1491–1493.
- (23) Even, J. Developments for transactinide chemistry experiments behind the gas-filled separator TASCA, Ph.D. Thesis, Johannes Gutenberg University Mainz, Germany, 2011.

- (24) Cao, S. et al. Gas-phase chemistry of ruthenium and rhodium carbonyl complexes. *Phys. Chem. Chem. Phys.* **2016**, *18*, 119–125.
- (25) Wang, Y. et al. Gas-phase chemistry of Mo, Ru, W, and Os metal carbonyl complexes. *Radiochim. Acta* **2014**, *102*, 69–76.
- (26) Even, J. et al. In-situ formation, thermal decomposition, and adsorption studies of transition metal carbonyl complexes with short-lived radioisotopes. *Radiochim. Acta* **2014**, *102*, 1093–1110.
- (27) Even, J. et al. In situ synthesis of volatile carbonyl complexes with short-lived nuclides. *J. Radioanal. Nucl. Chem.* **2014**, *303*, 2457–2466.
- (28) Usoltsev, I. Methodical Developments for Future Chemical Investigations of Superheavy Elements, Ph.D. Thesis, Departement für Chemie und Biochemie der Universität Bern, Switzerland, 2014.
- (29) Wang, Y. et al. The study of rhenium pentacarbonyl complexes using single-atom chemistry in the gas phase. *Phys. Chem. Chem. Phys.* **2019**, *21*, 7147–7154.
- (30) Usoltsev, I. et al. Decomposition studies of group 6 hexacarbonyl complexes. Part 1: Production and decomposition of Mo(CO)₆ and W(CO)₆. *Radiochim. Acta* **2016**, *104*, 141–151.
- (31) Usoltsev, I. et al. Decomposition studies of group 6 hexacarbonyl complexes. Part 2: Modelling of the decomposition process. *Radiochim. Acta* **2016**, *104*, 531–537.
- (32) Nash, C. S.; Bursten, B. E. Prediction of the Bond Lengths, Vibrational Frequencies, and Bond Dissociation Energy of Octahedral Seaborgium Hexacarbonyl, Sg(CO)₆. *J. Am. Chem. Soc.* **1999**, *121*, 10830–10831.
- (33) Davidson, E. R. et al. The transition metal-carbonyl bond. *Acc. Chem. Res.* **1993**, *26*, 628–635.
- (34) Pershina, V.; Iliaš, M. Carbonyl compounds of Tc, Re, and Bh: Electronic structure, bonding, and volatility. *J. Chem. Phys.* **2018**, *149*, 204306–204320.
- (35) Pershina, V.; Iliaš, M. Penta- and tetracarbonyls of Ru, Os, and Hs: Electronic structure, bonding, and volatility. *J. Chem. Phys.* **2017**, *146*, 184306–184318.
- (36) Düllmann, Ch. E. et al. Heavy-ion-induced production and physical preseparation of short-lived isotopes for chemistry experiments. *Nucl. Instrum. Methods Phys. Res., Sect. A* **2005**, *551*, 528–539.
- (37) Zvára, I., *The Inorganic Radiochemistry of Heavy Elements*; Springer-Verlag GmbH: 2008.
- (38) Düllmann, Ch. E. Physical preseparation: A powerful new method for transactinide chemists. *Eur. Phys. J. B* **2007**, *45*, 75–80.
- (39) Even, J. et al. The recoil transfer chamber—An interface to connect the physical preseparator TASCA with chemistry and counting setups. *Nucl. Instrum. Methods Phys. Res., Sect. A* **2011**, *638*, 157–164.
- (40) Haba, H. et al. Production of ²⁶⁵Sg in the ²⁴⁸Cm(²²Ne,5n)²⁶⁵Sg reaction and decay properties of two isomeric states in ²⁶⁵Sg. *Phys. Rev. C* **2012**, *85*, 024611-1–024611-11.
- (41) Haba, H. et al. Production of ²⁶⁶Bh in the ²⁴⁸Cm(²³Na,5n)²⁶⁶Bh reaction and its decay properties. *Phys. Rev. C* **2020**, *102*, 024625.
- (42) Wilk, P. A. et al. Evidence for new isotopes of element 107: ²⁶⁶Bh and ²⁶⁷Bh. *Phys. Rev. Lett.* **2000**, *85*, 2697–2700.
- (43) Dvorak, J. et al. Observation of the 3n Evaporation Channel in the Complete Hot-Fusion ²⁶Mg + ²⁴⁸Cm Leading to the New Superheavy Nuclide ²⁷¹Hs. *Phys. Rev. Lett.* **2008**, *100*, 132503-1–132503-4.
- (44) Oganessian, Y. T. et al. Synthesis and study of decay properties of the doubly magic nucleus ²⁷⁰Hs in the ²²⁶Ra + ⁴⁸Ca reaction. *Phys. Rev. C* **2013**, *87*, 034605-1–034605-8.

- (45) Sikkeland, T. et al. Analysis of Excitation Functions in Cm(C,xn)No Reactions. *Phys. Rev.* **1968**, *172*, 1232–1238.
- (46) Eskola, K. et al. Studies of Lawrencium Isotopes with Mass Numbers 255 Through 260. *Phys. Rev. C* **1971**, *4*, 632–642.
- (47) Murakami, M. et al. Excitation functions for production of Rf isotopes in the $^{248}\text{Cm} + ^{18}\text{O}$ reaction. *Phys. Rev. C* **2013**, *88*, 024618.
- (48) Haba, H. et al. Production of ^{262}Db in the $^{248}\text{Cm}(^{19}\text{F},5\text{n})^{262}\text{Db}$ reaction and decay properties of ^{262}Db and ^{258}Lr . *Phys. Rev. C* **2014**, *89*, 024618.
- (49) Morita, K. et al. Decay properties of ^{266}Bh and ^{262}Db produced in the $^{248}\text{Cm} + ^{23}\text{Na}$ reaction. *J. Phys. Soc. Japan* **2009**, *78*, 064201-1–064201-6.
- (50) Zvára, I. et al. Experiments on chemistry of element 104-kurchatovium V. *J. Inorg. Nucl. Chem.* **1970**, *32*, 1885–1894.
- (51) Zvára, I. et al. Chemical separation of kurchatovium. *Inorg. Nucl. Chem. Lett.* **1971**, *7*, 1109–1116.
- (52) Timokhin, S. N. et al. Chemical identification of element 106 by thermochromatography. *J. Radioanal. Nucl. Chem.* **1996**, *212*, 31–34.
- (53) Zvára, I. et al. Chemical Identification of Element 106 (Thermochromatography of Oxochlorides). *Radiochim. Acta* **1998**, *81*, 179–187.
- (54) Düllmann, Ch. E. et al. Gas chemical investigation of hafnium and zirconium complexes with hexafluoroacetylacetone using pre-separated short-lived radioisotopes. *Radiochim. Acta* **2009**, *97*, 403–418.
- (55) V. Weizsäcker, C. F. Zur Theorie der Kernmassen. *Z. Phys.* **1935**, *96*, 431–458.
- (56) Bethe, H.; Bacher, R. F. Nuclear Physics A. Stationary States of Nuclei. *Rev. Mod. Phys.* **1936**, *8*, 82–229.
- (57) Mayer, M. G. On Closed Shells in Nuclei. II. *Phys. Rev.* **1949**, *75*, 1969–1970.
- (58) Bohr, N.; Wheeler, J. A. The Mechanism of Nuclear Fission. *Phys. Rev.* **1939**, *56*, 426–450.
- (59) Rösch, F., *Nuclear- and radiochemistry*; De Gruyter: Berlin, Germany Boston, Massachusetts, 2016.
- (60) Loveland, W., *Modern nuclear chemistry*; Wiley-Interscience: Hoboken, N.J., 2006.
- (61) Haxel, O. et al. On the "Magic Numbers" in Nuclear Structure. *Phys. Rev.* **1949**, *75*, 1766–1766.
- (62) Nilsson, S. G. Binding states of individual nucleons in strongly deformed nuclei. *Kgl. Danske Videnskab. Selskab., Mat.-fys Medd.* **1955**, *29*.
- (63) Mayer, M. G. Nuclear Configurations in the Spin-Orbit Coupling Model. I. Empirical Evidence. *Phys. Rev.* **1950**, *78*, 16–21.
- (64) Mayer, M. G. Nuclear Configurations in the Spin-Orbit Coupling Model. II. Theoretical Considerations. *Phys. Rev.* **1950**, *78*, 22–23.
- (65) Strutinsky, V. Shell effects in nuclear masses and deformation energies. *Nucl. Phys. A* **1967**, *95*, 420–442.
- (66) Strutinsky, V. Shells in deformed nuclei. *Nucl. Phys. A* **1968**, *122*, 1–33.
- (67) Hamilton, J. H. et al. Search for Superheavy Nuclei. *Annu. Rev. Nucl. Part. Sci.* **2013**, *63*, 383–405.
- (68) Oganessian, Y. T. et al. Heavy element research at Dubna. *Nucl. Phys. A* **2004**, *734*, 109–123.
- (69) Sobiczewski, A. Structure of Heaviest Nuclei. *Acta Phys. Pol. B* **1998**, *29*, 2191.
- (70) Sobiczewski, A.; Pomorski, K. Description of structure and properties of superheavy nuclei. *Prog. Part. Nucl. Phys.* **2007**, *58*, 292–349.

- (71) Lalazissis, G. et al. Superheavy nuclei in the relativistic mean-field theory. *Nucl. Phys. A* **1996**, *608*, 202–226.
- (72) Cwiok, S. et al. Shell structure of the superheavy elements. *Nucl. Phys. A* **1996**, *611*, 211–246.
- (73) Experiments at the limits of stability: exploring physical and chemical properties of super-heavy elements last checked: 28.11.2020, https://www.superheavies.de/english/research_program/general.htm.
- (74) Möller, P.; Nix, J. R. Nuclear Ground-State Masses and Deformations. *Atom. Data Nucl. Data Tabl.* **1995**, *59*, 185–381.
- (75) Möller, P. et al. Nuclear Ground-State Masses and Deformations. *Phys. Rev. C* **2009**, *79*, 064304.
- (76) Münzenberg, G. In Schädel, M., Ed., 1st; Vieweg: 1996; Chapter Kapitel 21: Etwas Theorie zur Kernstabilität, pp 201–217.
- (77) Hoffmann, S. Synthesis and properties of isotopes of the transactinides. *Radiochim. Acta* **2019**, *107*, 879–915.
- (78) Seaborg, G.; Loveland, W., *Elements Beyond Uranium*; John Wiley Sons: 1990; 376 pp.
- (79) Silva, R. J. In Morss, L. R. et al., Eds., 4th; Springer: 2008; Chapter Fermium, Mendelevium, Nobelium, and Lawrencium, pp 1621–1651.
- (80) Zagrebaev, V. I. et al. Production of heavy and superheavy neutron-rich nuclei in neutron capture processes. *Phys. Rev. C* **2011**, *84*, 044617–044626.
- (81) Oganessian, Y. T. Heaviest Nuclei from ^{48}Ca -induced Reactions. *J. Phys. Conf. Ser.* **2011**, *312*, 082003–082082.
- (82) Nasirov, A. K. et al. Mass and angular distributions of the reaction products in heavy ion collisions. *J. Phys. Conf. Ser.* **2018**, *1014*, 012009.
- (83) Back, B. B. Complete fusion and quasifission in reactions between heavy ions. *Phys. Rev. C* **1985**, *31*, 2104–2112.
- (84) Cherepanov, E. et al. Systematics of the effective ratio (Γ_n/Γ_f) of neutron emission and fission partial widths for transcurium nuclei. *J. Phys. G Nucl. Partic.* **1999**, *9*, 931.
- (85) Moller, P. et al. Nuclear Ground-State Masses and Deformations. *At. Data Nucl. Data Tables* **1995**, *59*, 185–381.
- (86) Zagrebaev, V. I. et al. Fusion-fission dynamics and perspectives of future experiments. *Phys. At. Nucl.* **2003**, *66*, 1033–1041.
- (87) Hoffmann, D. C. et al. In Morss, L. R. et al., Eds., 4th; Springer: 2008; Chapter Transactinide Elements and Future Elements, pp 1652–1752.
- (88) Hodgson, P. E., *Introductory nuclear physics*; Clarendon Press Oxford University Press: Oxford New York, 1997.
- (89) Malli, G. L. In *Fundamental World of Quantum Chemistry*; Springer Netherlands: 2004, pp 323–363.
- (90) Hoffman, D. C. Atom-at-a-Time Chemistry. *Radiochim. Acta* **1993**, *61*, 169–176.
- (91) Kratz, J. V. In *Handbook of Nuclear Chemistry*; Springer US: 2011, pp 925–1004.
- (92) Dragojević, I. et al. Influence of projectile neutron number in the $^{208}\text{Pb}(^{48}\text{Ti},n)^{255}\text{Rf}$ and $^{208}\text{Pb}(^{50}\text{Ti},n)^{257}\text{Rf}$ reactions. *Phys. Rev. C* **2008**, *78*, 024605–024615.
- (93) Gates, J. M. et al. Synthesis of rutherfordium isotopes in the $^{238}\text{U}(^{26}\text{Mg},xn)^{264-x}\text{Rf}$ reaction and study of their decay properties. *Phys. Rev. C* **2008**, *77*, 034603.
- (94) Kadkhodayan, B. et al. On-line Gas Chromatographie Studies of Chlorides of Rutherfordium and Homologs Zr and Hf. *Radiochim. Acta* **1996**, *72*, 169–178.
- (95) Dvorak, J. et al. Doubly Magic Nucleus $^{270}_{108}\text{Hs}_{162}$. *Phys. Rev. Letters* **2006**, *97*, 242501.

- (96) Haba, H. et al. Production and decay properties of the 1.9-s isomeric state in ^{261}Rf . *Phys. Rev. C* **2011**, *83*, 034602.
- (97) Kratz, J. V. et al. New nuclide ^{263}Ha . *Phys. Rev. C* **1992**, *45*, 1064–1069.
- (98) Nagame, Y. et al. Production Cross Sections of ^{261}Rf and ^{262}Db in Bombardments of ^{248}Cm with ^{18}O and ^{19}F Ions. *J. Nucl. Radiochem. Sci.* **2002**, *3*, 85–88.
- (99) Ghiorso, A. et al. Element 106. *Phys. Rev. Letters* **1974**, *33*, 1490–1493.
- (100) Düllmann, Ch. E.; Türler, A. $^{248}\text{Cm}(^{22}\text{Ne},\text{xn})^{270}\text{Sg}$ reaction and the decay properties of ^{265}Sg reexamined. *Phys. Rev. C* **2008**, *77*, 064320.
- (101) Morita, K. et al. In AIP: 2010.
- (102) Eichler, R. et al. Chemical characterization of bohrium (element 107). *Nature* **2000**, *407*, 63–65.
- (103) Türler, A. et al. On the decay properties of ^{269}Hs and indications for the new nuclide ^{270}Hs . *Eur. Phys. J. A* **2003**, *17*, 505–508.
- (104) Graeger, R. et al. Experimental study of the $^{238}\text{U}(^{36}\text{S},3\text{-5n})^{269-271}\text{Hs}$ reaction leading to the observation of ^{270}Hs . *Phys. Rev. C* **2010**, *81*, 061601-1–061601-5.
- (105) Eichler, R. et al. Thermochemical and Physical Properties of Element 112. *Angew. Chem. Int. Ed.* **2008**, *47*, 3262–3266.
- (106) Aksenov, N. V. et al. On the volatility of nihonium (Nh, $Z = 113$). *Eur. Phys. J. A* **2017**, *53*, 158–162.
- (107) Dmitriev, S. N. et al. Pioneering experiments on the chemical properties of element 113. *Mendeleev Commun* **2014**, *24*, 253–256.
- (108) Yakushev, A. et al. Superheavy Element Flerovium (Element 114) Is a Volatile Metal. *Inorg. Chem.* **2014**, *53*, 1624–1629.
- (109) Yakushev, A.; Eichler, R. Gas-phase chemistry of element 114, flerovium. *EPJ Web Conf.* **2016**, *131*, ed. by Rudolph, D., 07003–07008.
- (110) Guillaumont, R. et al. Kinetic and Thermodynamic Aspects of Tracer-Scale and Single Atom Chemistry. *Radiochim. Acta* **1989**, *46*, 169–176.
- (111) Guillaumont, R. et al. Sub-tracer Scale Behaviour of Radionuclides. Application to Actinide Chemistry. *Radiochim. Acta* **1991**, *54*, 1–16.
- (112) Herrmann, W. A. 100 years of metal carbonyls: a serendipitous chemical discovery of major scientific and industrial impact. *J. Organomet. Chem.* **1990**, *383*, 21–44.
- (113) Mond, L. et al. Einige neue Metallcarbonyle. *Z. Anorg. Allg. Chem.* **1910**, *68*, 207–219.
- (114) Hieber, W.; Romberg, E. Über Metallcarbonyle. XX. Die Metallhexacarbonyle der Chromgruppe, ihre Bildungsweise und der Reaktionsmechanismus derselben. *Z. Anorg. Allg. Chem.* **1935**, *221*, 321–331.
- (115) Hieber, W.; Lagally, H. Über Metallcarbonyle. XXXV. Über Iridiumcarbonyl. *Z. Anorg. Allg. Chem.* **1940**, *245*, 321–333.
- (116) Manchot, W.; Manchot, W. J. Darstellung von Rutheniumcarbonylen und -nitrosylen. *Z. Anorg. Allg. Chem.* **1936**, *226*, 385–415.
- (117) McIntosh, D.; Ozin, G. A. Synthesis of binary gold carbonyls, $\text{Au}(\text{CO})_n$ ($n = 1$ or 2). Spectroscopic evidence for isocarbonyl(carbonyl)gold, a linkage isomer of bis(carbonyl)gold. *Inorg. Chem.* **1977**, *16*, 51–59.
- (118) Darling, J. H.; Ogden, J. S. Spectroscopic studies on matrix-isolated metal carbonyls. Part II. Infrared spectra and structures of $\text{Pd}(\text{CO})_4$, $\text{Pd}(\text{CO})_3$, $\text{Pd}(\text{CO})_2$, and PdCO . *J. Chem. Soc., Dalton Trans.* **1973**, 1079.
- (119) Frenking, G.; Fröhlich, N. The Nature of the Bonding in Transition-Metal Compounds. *Chem. Rev.* **2000**, *100*, 717–774.

- (120) Chatt, J.; Duncanson, L. A. 586. Olefin co-ordination compounds. Part III. Infra-red spectra and structure: attempted preparation of acetylene complexes. *J. Chem. Soc.* **1953**, 2939.
- (121) Szilagyi, R. K.; Frenking, G. Structure and Bonding of the Isoelectronic Hexacarbonyls $\text{Hf}(\text{CO})_6^{2-}$, $\text{Ta}(\text{CO})_6^-$, $\text{W}(\text{CO})_6$, $\text{Re}(\text{CO})_6^+$, $\text{Os}(\text{CO})_6^{2+}$, and $\text{Ir}(\text{CO})_6^{3+}$: A Theoretical Study. *Organometallics* **1997**, *16*, 4807–4815.
- (122) Diefenbach, A. et al. The Nature of the Transition Metal-Carbonyl Bond and the Question about the Valence Orbitals of Transition Metals. A Bond-Energy Decomposition Analysis of $\text{TM}(\text{CO})_6^q(\text{TM}^q) = \text{Hf}^{2-}$, Ta^- , W , Re^+ , Os^{2+} , Ir^{3+} . *J. Am. Chem. Soc.* **2000**, *122*, 6449–6458.
- (123) Pershina, V. Relativistic effects on the electronic structure of the heaviest elements. Is the Periodic Table endless? *Comptes Rendus. Chimie* **2020**, *23*, 255–265.
- (124) Pershina, V. Relativistic electronic structure studies on the heaviest elements. *Radiochim. Acta* **2011**, *99*, 459–476.
- (125) Nash, C. S.; Bursten, B. E. Spin-Orbit Effects, VSEPR Theory, and the Electronic Structures of Heavy and Superheavy Group IVA Hydrides and Group VIIIA Tetrafluorides. A Partial Role Reversal for Elements 114 and 118. *Am. J. Phys. Chem. A* **1999**, *103*, 402–410.
- (126) Ziegler, T. et al. Thermal stability and kinetic lability of the metal carbonyl bond. A theoretical study on $\text{M}(\text{CO})_6$ (M = chromium, molybdenum, tungsten), $\text{M}(\text{CO})_5$ (M = iron, ruthenium, osmium), and $\text{M}(\text{CO})_4$ (M = nickel, palladium, platinum). *J. Am. Chem. Soc.* **1987**, *109*, 4825–4837.
- (127) Aumann, D. C. Was wissen wir heute über die Kernspaltung? *Angew. Chem.* **1975**, *87*, 77–97.
- (128) Newson, H. W. Symmetric and Asymmetric Fission. *Phys. Rev.* **1961**, *122*, 1224–1226.
- (129) Lieser, K., *Einführung in die Kernchemie*; VCH: Weinheim Germany New York, 1991.
- (130) Zvára, I. Simulation of thermochromatographic processes by the monte carlo method. *Radiochim. Acta* **1985**, *38*, 95–101.
- (131) Gäggeler, H. W. On-line gas chemistry experiments with transactinide elements. *J. Radioanal. Nucl. Chem.* **1994**, *183*, 261–271.
- (132) Türler, A. Gas Phase Chemistry Experiments with Transactinide Elements. *Radiochim. Acta* **1996**, *72*, 7–17.
- (133) Türler, A. et al. On-line Gas Phase Chromatography with Chlorides of Niobium and Hahnium (Element 105). *Radiochim. Acta* **1996**, *73*, 55–66.
- (134) Eichler, B.; Kratz, J. V. Electrochemical deposition of carrier-free radionuclides. *Radiochim. Acta* **2000**, *88*, 475–482.
- (135) Gilliland, E. R. Diffusion Coefficients in Gaseous Systems. *Ind. Eng. Chem.* **1934**, *26*, 681–685.
- (136) Geissel, H. Untersuchungen zur Abbremsung von Schwerionen in Materie im Energiebereich von (0,5-10) MeV/u, Dissertation, Gesellschaft für Schwerionenforschung, Darmstadt, 1982.
- (137) Riese, B. Abbremsung relativistischer Schwerionen in Materie, Diplomarbeit, FB7 der Justus-Liebig-Universität Giessen, 2008.
- (138) Keinonen, J. In *Particle Acceleration and Detection*, Hellborg, R., Ed., 1st; Springer: 2005; Chapter Atomic Collisions in Matter, pp 486–505.
- (139) Nankov, N. Untersuchung der Abbremsung von Schwerionen in Materie im Energiebereich (40-400) MeV/u, Dissertation, FB7 der Justus-Liebig-Universität Giessen, 2002.
- (140) Bohr, N. LX. On the decrease of velocity of swiftly moving electrified particles in passing through matter. *London Edinburgh Philos. Mag. J. Sci.* **1915**, *30*, 581–612.
- (141) Bohr, N. The penetration of atomic particles through matter. *Dan. Mat. Fys. Medd.*, **1948**, (8)18.

- (142) Bethe, H. Theory of the Passage of Fast Corpuscular Rays Through Matter. *Ann. Phys.*, **1930**, 5, 325.
- (143) Bethe, H. Braking Formula for Electrons of Relativistic Speed. *Z. Phys.*, **1932**, 76, 293.
- (144) Ziegler, J. Computer Code SRIM-2013 last checked: 03.02.2021, <http://www.srim.org/>.
- (145) Fouquet, D. M. et al. TRIGA research reactors: A pathway to the peaceful applications of nuclear energy. *Nuc. Phys. News* **2000**, 46, 46–56.
- (146) Uddin, M. S. et al. Fast neutron spectrum unfolding of a TRIGA Mark II reactor and measurement of spectrum-averaged cross sections: integral tests of differential cross sections of neutron threshold reactions. *Radiochim. Acta* **2013**, 101, 613–620.
- (147) Hampel, G. et al. Irradiation facility at the TRIGA Mainz for treatment of liver metastases. *Appl. Radiat. Isot.* **2009**, 67, S238–41.
- (148) Eberhardt, K.; Geppert, C. The research reactor TRIGA Mainz – a strong and versatile neutron source for science and education. *Radiochim. Acta* **2019**, 107, 535–546.
- (149) Schmitz, T. ESR-Dosimetry in Thermal and Epithermal Neutron Fields for Application in Boron Neutron Capture Therapy, Dissertation, Institute for Chemistry, University Mainz, 2016.
- (150) Menke, H. et al. Irradiations by means of reactor pulses. *Kerntechnik* **1975**, 7, 281–286.
- (151) Eberhardt, K.; Kronenberg, A. Research reactor TRIGA Mainz - a neutron source for versatile applications in research and education. *Kerntechnik* **2000**, 65, 269–274.
- (152) The TIGA Mark-II Reactor last checked: 22.06.2021, https://ati.tuwien.ac.at/fileadmin/t/ati/ati/files/reaktor/beschreibung/E_Text__Bilder.pdf.
- (153) Parker, W.; Falk, R. Molecular plating: A method for the electrolytic formation of thin inorganic films. *Nucl. Instrum. Methods* **1962**, 16, 355–357.
- (154) Vascon, A. et al. Elucidation of constant current density molecular plating. *Nucl. Instrum. Methods Phys. Res., Sect. A* **2012**, 696, 180–191.
- (155) Chu, S. et al. The Lund/LBNL Nuclear Data Search last checked: 03.01.2021, <http://nucleardata.nuclear.lu.se/toi/>.
- (156) The Lund/LBNL Nuclear Data Search last checked: 03.02.2021, <http://nucleonica.com>.
- (157) England, T.; Rider, B. Thermal Neutron Induced Fission. *Progress in Nuclear Energy* **1993**, LA-UR-94-3106.
- (158) Minehara, E. The JAERI tandem accelerator facility. *Nucl. Instrum. Methods. Phys. Res. B* **1986**, 244, 13–19.
- (159) Stock, R., *Encyclopedia of Nuclear Physics and its Applications*; Wiley VCH Verlag GmbH: 2013; 796 pp.
- (160) Takeuchi, S. et al. In *The eighth international conference on heavy-ion accelerator technology*, ASCE: 1999.
- (161) The tandem accelerator facility last checked: 28.11.2020, https://www.jaea.go.jp/english/04/ntokai/kasokuki/kasokuki_04.html.
- (162) Wachsmuth, M. et al. Chemical characterization of short-lived selenium and their daughter isotopes from thermal neutron induced fission of ²³⁵U at a gas-jet facility. *J. Radioanal. Nucl. Chem.* **2002**, 254, 201–208.
- (163) Nucleonica Fission Yields++ last checked: 21.01.2021, <http://www.nucleonica.com/>.
- (164) Wang, Y. et al. Gas-phase chemistry of technetium carbonyl complexes. *Phys. Chem. Chem. Phys.* **2015**, 17, 13228–13234.
- (165) Zhao, Y. et al., Eds., New formulas for TKE release in nuclear fission process, Proceedings of the 1999 symposium on nuclear data, JAERI-Conf-2000-005, Fukahori, Tokio, 2000.

- (166) Wittwer, D. et al. Gas phase chemical studies of superheavy elements using the Dubna gas-filled separator – Stopping range determination. *Nucl. Instrum. Methods Phys. Res., Sect. B* **2010**, *268*, 28–35.
- (167) Ziegler, J. F., *The Stopping and Ranges of Ions in Matter*; Pergamon Press: 2013.
- (168) Chen, N. H.; Othmer, D. F. New generalized equation for gas diffusion coefficient. *J. Chem. Eng. Data* **1962**, *7*, 37–41.
- (169) Jong, I. G. D.; Wiles, D. R. Pentacarbonyltechnetium radical. *Inorg. Chem.* **1973**, *12*, 2519–2522.
- (170) Chellappa, R.; Chandra, D. Assessment of vapor pressure data of solid metal carbonyls. *J. Chem. Thermodyn.* **2005**, *37*, 377–387.
- (171) Stolarz, A. Target preparation for research with charged projectiles. *J. Radioanal. Nucl. Chem.* **2013**, *299*, 913–931.
- (172) Domanov, V. Thermochromatographic Isolation of Os, Ru, Re, and Tc Radioisotopes in the Form of Lower Oxides. *Radiochemistry* **2002**, *44*, 109–113.
- (173) Düllmann, Ch. E. et al. On the Stability and Volatility of Group 8 Tetroxides, MO₄(M = Ruthenium, Osmium, and Hassium (Z= 108)). *J. Phys. Chem. B* **2002**, *106*, 6679–6684.
- (174) Götz, M. et al. Gas phase synthesis of 4d transition metal carbonyl complexes with thermalized fission fragments in single-atom reactions. *Radiochim. Acta* **2021**, *109*, 153–165.
- (175) Düllmann, Ch. E. et al. IVO, a device for In situ Volatilization and On-line detection of products from heavy ion reactions. *Nucl. Instrum. Methods Phys. Res., Sect. A* **2002**, *479*, 631–639.
- (176) Webber, I.; Wiles, D. Radiochemical reactions in rhenium carbonyls—I: Re₂(CO)₁₀. *J. Inorg. Nucl. Chem.* **1976**, *38*, 1103–1107.
- (177) Haba, H. et al. RIKEN Gas-filled Recoil Ion Separator (GARIS) as a Promising Interface for Superheavy Element Chemistry—Production of Element 104,261Rf, Using the GARIS/Gas-jet System—. *Chem. Lett.* **2009**, *38*, 426–427.
- (178) Graeger, R. Reaction studies about the Q-value in uence on the production of superheavyelements, Dissertation, Technical University Munich, 2010.
- (179) Gates, J. et al. First Direct Measurements of Superheavy-Element Mass Numbers. *Phys. Rev. Letters* **2018**, *121*, 222501.
- (180) Haenssler, F. Thermochromatographische Untersuchungen von inaktivem undradioaktivem Rhodium (Rh-107) mit verschiedenen Trägergasen, Diploma Thesis, University Bern, 2001.
- (181) Di Nitto, A. et al. ALBEGA: A decay spectroscopy setup for chemically separated samples. **2015**, DOI: [10.15120/GR-2015-1-MU-NUSTAR-SHE-C-06](https://doi.org/10.15120/GR-2015-1-MU-NUSTAR-SHE-C-06).
- (182) Gorshkov, A. A new focal plane detector for the gas-filledseparator TASCA, Dissertation, Technical University Munich, 2010.

The Monte Carlo codes presented in this section were used for the Theoretical modelling the flush-out efficiency $\varepsilon_{\text{Flush}}$ (cf. Sec. 4.3.2).

9.1 Python code: Monte Carlo simulation

```
#!/usr/bin/env python
#
# Monte Carlo simulation of thermotography using a
# microscopic model proposed by. I. Zvara. in
# Simulation of Thermochromatographic Process by the Monte Carlo Method),
# Radiochimica Acta 38, 95-101 (1985)
#
# Original BASIC program made by A. Tuerler from 10/05/94
# rewritten by J. Dvorak in Python 30/05/2005
#
# Changes made to use numpy instead of ScientificPython, which is
# incompatible with python 2.5 under Windows
#
#####
#Some definitions
#####

from Scientific.Functions.LeastSquares import *
from numpy import *
from random import random
from math import *
from thermochem_module import *

#####
#Main body
#####

# Get input data
arg = get_arguments()
if "output_file" in arg.keys():
    output_file = arg["output_file"]
    print("Using output file"), output_file
if "input_file" in arg.keys():
    input_file=arg["input_file"]
    print("Reading parameters from input file"), input_file
    avar = read_input_file(input_file)
if avar.has_key("M2"): M2 = float(avar["M2"])
else: M2 = 6.8
if avar.has_key("d2"): d2 = float(avar["d2"])
else: d2 = 0.303
if avar.has_key("P"): P = float(avar["P"])
else: P = float(1)
if avar.has_key("p0"): p0 = float(avar["p0"])
else: p0 = 0.2
if avar.has_key("particles"): particles = avar["particles"]
else: particles = 10
if avar.has_key("Q"): Q = float(avar["Q"])
else: Q = float(25)
if avar.has_key("halflife"):halflife = float(avar["halflife"])
else: halflife = float(15)
if avar.has_key("M1"): M1 = float(avar["M1"])
else: M1 = float(333)
if avar.has_key("d1"): d1 = float(avar["d1"])
```

```

else: d1 = 6.4
if avar.has_key("dHa1"): dHa1 = avar["dHa1"]
else: dHa1 = -10
if avar.has_key("dHa2"): dHa2 = avar["dHa2"]
else: dHa2 = -100
if avar.has_key("dHastep"): dHastep = avar["dHastep"]
else: dHastep = 5
if avar.has_key("length"): length = float(avar["length"])
else: length = 40
if avar.has_key("shape"):
if avar["shape"] == "rectangle":
shape="rectangle"
if avar.has_key("side_a"): side_a = float(avar["side_a"])
else: side_a = 1
if avar.has_key("side_b"): side_b = float(avar["side_b"])
else: side_b = 0.05
if avar.has_key("mean_path"): mean_path = float(avar["mean_path"])
else: mean_path = mean_path_calculation2(side_a,side_b)
elif avar["shape"] == "circle":
shape="circle"
if avar.has_key("radius"): radius = float(avar["radius"])
else: radius = 0.178
else: raise IOError, "Column shape must be given (circle or rectangle)"
if avar.has_key("hist_steps"): hist_steps = avar["hist_steps"]
else : hist_steps = 32
if avar.has_key("temp_data"):
temp_data = avar["temp_data"]
#Temp_parameters = polynomialLeastSquaresFit( (1,1,1),
str_to_data(avar["temp_data"]))
Temp_parameters = polyfit(str_to_data_for_numpy(temp_data)[0],
str_to_data_for_numpy(temp_data)[1],2)
# fit the temperature profile with polynom of 2nd order

else:
#Temp_parameters = polynomialLeastSquaresFit( (1,1,1), str_to_data())
Temp_parameters = polyfit(str_to_data_for_numpy("")[0],
str_to_data_for_numpy("")[1],2)
# fit the temperature profile with polynom of 2nd order

else:
M2 = get_param("Mass of gas in amu (Ar = 39.948): ", 28)
d2 = get_param("Density of gas (Ar = 1.784): ", 0.77114)
P = get_param("Pressure of gas in atm (1): ", 0.6)
p0 = get_param("Period of oscilation in 10e-12 s (0.2): ", 0.2)
particles = get_param("Number of particles : ", 10000,'i')
Q = get_param("The STP flow rate of gas through column (cm3/s): ", 16.66)
halflife = get_param("Halflife of the nuclide: ", 10)
M1 = get_param("Molecular weight of the substance: ", 146)
d1 = get_param("Density of the substance: ", 6.475)
dHa1 = get_param("The adsorption enthalpy to start with: ", -1000)
dHa2 = get_param("The adsorption enthalpy to stop with: ", -100)
dHastep = get_param("How many steps in enthalpy (5): ",5,'i')
length = get_param("Length of column (120): ",0.8)
shape = "circle"
radius = get_param("Radius of column in cm (0.175): ", 0.2)
#if yes_not("Column profile (Circle or Rectangle): ", "circle", "rectangle")
== 1:
#Column has circle profile
#shape = "circle"
#radius = get_param("Radius of column in cm (0.175): ",0.3)
#else:
#column has rectangular profile
#shape = "rectangle"
#side_a = get_param("Dimension of side a in cm: ", 1)
#side_b = get_param("Dimension of side b in cm: ", 0.5)
#if yes_not("Do you know the mean path? (Yes or Not): ") == 1:
#mean_path = get_param("Enter mean path: ", 0.0668)
#else :
#print "Calculating mean path, it can take a while...."
#mean_path = mean_path_calculation2(side_a,side_b)
#print "Done, mean path is ", mean_path

```

```

hist_steps = get_param("How many values in result histogram (25): ",24,'i')
temp_data = raw_input("Temperature data (in format {x1,y1 x2,y2 ...}): ")
    #Temp_parameters = polynomialLeastSquaresFit( (1,1,1),
    str_to_data(temp_data) )
Temp_parameters = polyfit(str_to_data_for_numpy(temp_data)[0],
    str_to_data_for_numpy(temp_data)[1],2)
    # fit the temperature profile with polynom of 2nd order

R = 8.31432e+7 #Universal gas constant cgs

prog = progressBar(0, particles, 77) #Inicialise progress bar
oldprog = str(prog)

print "-----"

#Calculate some values
if shape == "circle":
cross_section = pi*pow(radius,2)
mean_path=radius
else:
cross_section = side_a*side_b

D298 = 0.0043 * pow(298.15,1.5) * sqrt(1.0/float(M1)+1.0/float(M2)) /
    (float(P)*pow(pow(float(M1)/float(d1),1.0/3)
    +pow(float(M2)/float(d2),1.0/3),2))
    # Calculate diffusion coefficient using proper Gillilands formula
#D298 = 0.0043 * pow(298.15,1.5) * sqrt(1/M1+1/M2) /
    (P*sqr(pow(M1/d1,1/3)+pow(M2/d2,1/3)))
    # Calculate diffusion coefficient using Gillilands formula
#D298 = 0.001 * pow(298.15,1.75) * sqrt(1.0/M1+1.0/M2) /
    (float(P)*sqr(pow(float(M1)/d1,1.0/3)+pow(float(M2)/d2,1.0/3)))
    # Calculate diffusion coefficient using the
    Fuller-Schettler-Giddings formula
T0 = temp_numpy(0, Temp_parameters)
    #Temperature at the entry of the column
TE = temp_numpy(length, Temp_parameters)
    #Temperature at the end of the column
#T0 = 298.15
#TE = 298.15
print "T0: ", T0-273.15, "TE: ", TE-273.15

#Prepare array of results
results=[]
hist=[]
for k in range(hist_steps+1):
hist.append(0)

#Simulation
for j in range(dHastep+1):
dHa = dHa1+(dHa2-dHa1)/dHastep*j

for k in range(hist_steps+1): # Setting hist to zero
hist[k] = 0
print ""
print "Calculating enthalpy",dHa,": "

for n in range(particles): # For all particles
#print "New particle"
prog.updateAmount(n) #make progress bar
if oldprog != str(prog):
print prog, "\r",
oldprog=str(prog)

xi = float(0) # Starting at zero
tf = float(0) # Time of jump
tt = float(0) # Processing time of particle
ta = float(0) # Time the particle spends staying on the surface

```

```

td = -halflife / log(2)*log(1-random())
    # Generate random life time for nuclide
#print "\nParticle #",n,"Half-life je ",td
Ro = float(1)
while tt < td :
T1 = temp_numpy(xi, Temp_parameters) # Calculate temperature in xi
Dcoff = D298*pow(T1/298.15,1.5)
    # Calculate Diffusion coefficient at the T(xi)
if tf > 0 :
Ro = tf / (tf + ta)
    # Calculate Ro - ratio of the velocity of the carrier
    gas to the mean migration velocity of the zone

# Particle jumps
Nm = cross_section * Dcoff / (4*Q*T1/273.15) +
    (11 - 16*Ro+6*pow(Ro,2)) * ((Q*T1/273.15)/(48*pi*Dcoff))
    # Calculate mean jump length
Ni = - Nm * log(1-random()) # Generate random jump length
xi = xi + Ni # Calculate new position
if xi > length : break
    # If particle flies through the column,
    we will find it in the filter
T2 = temp_numpy(xi, Temp_parameters)
    # Calculate temperature in new position
tf = 2 * cross_section * Ni / ((Q*T1/273.15)+(Q*T2/273.15))
# Calculate flight time
    (assume that flight time was Ni/Velocity; Velocity= Qi/cross_section
tt = tt + tf # Processing time of particle increases
#print "Time after flight: ", tt
if tt > td: break # particle decays

# Particle stays on the surface for some time
tm = p0 * (1e-12) * exp((-dHa*(1e10))/(R*T2))
    # Mean time to stay on surface
vi = mean_path /((Q*T2/273.15) * sqrt(2*pi*R*T2/M1)
    #Mean number of collisions
ta = -vi * tm * Nm * log(1-random())
    # Generate random time the particle spends staying on the surface
tt = tt + ta # Processing time of particle increases
#print "Dcoff: ", Dcoff, "Colisions:",vi, "Mean stay:",tm,
    "Mean jump :",Nm, "Time of stay: ", ta

if xi > length :
    # If particle flies through the column,
    we will find it in the filter
k = len(hist) - 1
hist[k] = hist[k] + 1
else :
#print "T2: ",T2-273.15
for k in range(hist_steps +1):
    # Particle is somewhere in the column, calculate where
if ((T2 < ((TE-T0)/hist_steps*k+T0)) and
    (T2 > ((TE-T0)/hist_steps*(k+1)+T0)) ):
#print "Fitting temperature: ", k,
    ((TE-T0)/hist_steps*k+T0-273.15), "--" ,
    ((TE-T0)/hist_steps*(k+1)+T0-273.15)
hist[k] = hist[k] + 1
results.append(map(int,hist))
    # Save results for this enthalpy in the array of results

#Results
#print results
print D298
part_ord = int(0.5+log10(particles))
divider = "+"*8*"-"+"+"+("-"*4+"+")*hist_steps+7*"-"+"+"
print divider
print "|Enthalpy"+"|",
for k in range(hist_steps):
print "%3d|" %(k+1),
print "Filter|"

```

```

print divider

for j in range(dHastep+1):
dHa = dHa1+(dHa2-dHa1)/dHastep*j
line = results[j]
print "|%8.1f|" %(dHa),
for k in range(hist_steps):
print "%3d|" %(line[k]),
print "%6d|" %(line[k+1])
# print "Enthalpy:",dHa,":",results[j]
print divider

#create output file
if "output_file" in arg.keys():
f = open(output_file, 'w')
f.write("# Output file from MCS of Thermochromatography.\n#\n")
f.write("# Used Parameters: \n# \n")
f.write("#M2 = %f # Mass of gas in amu\n" % M2 )
f.write("#d2 = %f # Density of gas\n" %d2)
f.write("#P = %.1f # Pressure of gas in atm \n" %P)
f.write("#p0 = %.1f # Period of oscilation in 10e-12 s \n" %p0)
f.write("#particles = %d # Number of particles \n" %particles)
f.write("#Q = %3f # The STP flow rate of gas in cm3/s \n" %Q)
f.write("#halflife = %f # Halflife of the nuclide in s \n" %halflife)
f.write("#M1 = %d # Molecular weight of the substance \n" %M1)
f.write("#d1 = %f # Density of the substance \n" %d1)
f.write("#dHa1 = %d # The adsorption enthalpy to start with \n" %dHa1)
f.write("#dHa2 = %d # The adsorption enthalpy to stop with \n" %dHa2)
f.write("#dHastep = %d # How many steps in enthalpy \n" %dHastep)
f.write("#length = %d # Length of column in cm \n" %length)
f.write("#shape = %s # Profile of column \n" %shape)
if shape == "circle" :
f.write("#radius = %f # Radius of column in cm \n" %radius)
else:
f.write("#side_a = %f # Dimension of side a in cm \n" %side_a)
f.write("#side_b = %f # Dimension of side b in cm \n" %side_b)
f.write("#mean_path = %f # Mean path in cm \n" %mean_path)
f.write("#hist_steps = %d # How many values in histogram \n" %hist_steps)
f.write("#temp_data = %s # Measured values for temperature \n" %temp_data)
t_param = Temp_parameters [0]
f.write("#temperature(x) = %f + %fx + %fx^2 # Interpolation
of temperature profile\n" %(t_param[0],t_param[1],t_param[2]))
f.write("#\n#\n")

f.write("\n\tTemp\t")
for j in range(dHastep+1):
dHa = dHa1+(dHa2-dHa1)/dHastep*j
f.write("%.2f\t" %dHa)
f.write("\n")
for k in range(hist_steps+1):
if k == (hist_steps):
f.write("\nfilter\t\t")
else:
temp_k = temp_numpy(((k+0.5)*length/hist_steps),Temp_parameters)-273.15
f.write("%d\t%5.2f\t" %(k+1,temp_k))
for j in range(dHastep+1):
res_line = results[j]
f.write("%d\t" %res_line[k])
f.write("\n" )

f.close()

#####

#!/usr/bin/env python
#
# Collection of modules used in script thermochromatography.py
# Written by J. Dvorak in Python 14/06/2005
#

```



```

#####

from random import random
from math import *
from string import *
import sys

def sqr(x):
    """Make x^2. """
    return x*x

def mean_path_calculation(a,b,n=10e5):
    """Calculating mean flight path in rectangular channel."""
    sum = 0

    for i in range(int(n)):
        xi = (random()-0.5)*a
        yi = (random()-0.5)*b
        alfa = random()*2*pi
        alfa1 = atan((b*0.5-yi)/(a*0.5-xi))
        alfa2 = pi - atan((b*0.5-yi)/(a*0.5+xi))
        alfa3 = pi + atan((b*0.5+yi)/(a*0.5+xi))
        alfa4 = 2*pi-atan((b*0.5+yi)/(a*0.5-xi))
        x=0
        y=0
        if (alfa > alfa1) and (alfa < alfa2) :
            #alpha goes in the top detector
            x = xi+(b/2-yi)/tan(alfa)
            y = b/2
        elif (alfa > alfa2) and (alfa < alfa3):
            #alpha goes in the left side
            x = -a/2
            y = yi-tan(alfa)*(a/2+xi)
        elif (alfa > alfa3) and (alfa < alfa4):
            #alpha goes in the bottom detector
            x = xi-(b/2+yi)/tan(alfa)
            y = -b/2
        elif ((alfa > alfa4) and (alfa < 2*pi)) or ((alfa>0) and (alfa < alfa1)):
            #alpha goes in the right side
            x = a/2
            y = yi+tan(alfa)*(a/2-xi)
        else: raise ValueError, 'Particle not hitte wall!'
        l = sqrt(sqr(x-xi)+sqr(y-yi))
        sum = sum+l
    average = sum/n
    return average

#Parsing data from format x1,y1 x2,y2 x3,y3 ...
    to [(x1,y1),(x2,y2),(x3,y3),...] for the polynomial fit
def str_to_data_for_numpy(data_str):
    """Function to parse string to data format for Polynomial fit"""
    if data_str == "":
        #return [0,20,40], [20,-60,-140]
        return [0, 120, 240], [25, 24.5, 24]
    else :
        x=[]
        y=[]
        a = data_str.strip().split()
        for i in range(len(a)) :
            b = map(float,a[i].split(',') )
            x.append(b[0])
            y.append(b[1])
        return x,y

#Parsing data from format x1,y1 x2,y2 x3,y3 ...
    to [(x1,y1),(x2,y2),(x3,y3),...] for the polynomial fit
def str_to_data(data_str):
    """Function to parse string to data format for Polynomial fit"""
    if data_str == "":
        #return [(0,20),(20,-60),(40,-140)]

```

```

return [(0, 20), (120, 24.5), (240, 24)]
else :
data_arr=[]
a = data_str.strip().split()
for i in range(len(a)) :
b = map(float,a[i].split(','))
c = b[0], b[1]
data_arr.append(c)
return data_arr

#Asking for parameters
def get_param(message="Enter value: ",
              default=0, int_or_float="f", repeat=3, warning="Wrong value! "):
    """Function asking for parameters

    Asks for parameter, checks if OK and returns.
    """
    while 1:
        r_param = raw_input(message)
        try:
            if int_or_float == "i" :
                param = int(r_param)
            elif int_or_float == "f" :
                param = float(r_param)
            else : raise IOError, 'Not integer or float.'
            return param
        except ValueError:
            if r_param == "":
                param = default
                return param
            else:
                print warning
                repeat = repeat - 1
                if repeat < 0:
                    raise IOError, 'Wrong value entered as an answer. '

def temp_numpy(x,Temp_parameters):
    """Function for calculation of temperature in x. """
    param=Temp_parameters
    return (param[2]+param[1]*x+param[0]*x*x + 273.15)

def temp(x, Temp_parameters):
    """Function for calculation of temperature in x. """
    param=Temp_parameters[0]
    return (param[0]+param[1]*x+param[2]*x*x + 273.15)

def sqr(x):
    """Function returning square."""
    return x*x

def yes_not(message, yes_string="yes",no_string="no",
            repeat=4, warning='Wrong entry'):
    """Function asking question yes or not and returning 1 or 0."""
    while 1:
        ok = raw_input(message)
        if ok in (yes_string[0], yes_string): return 1
        if ok in (no_string[0], no_string): return 0
        repeat = repeat - 1
        if repeat < 0: raise IOError, 'Wrong value entered as an answer'
        print warning

class progressBar:
def __init__(self, minValue = 0, maxValue = 10, totalWidth=12):
self.progBar = "[" # This holds the progress bar string
self.min = minValue
self.max = maxValue
self.span = maxValue - minValue

```

```

self.width = totalWidth
self.amount = 0      # When amount == max, we are 100% done
self.updateAmount(0) # Build progress bar string

def updateAmount(self, newAmount = 0):
if newAmount < self.min: newAmount = self.min
if newAmount > self.max: newAmount = self.max
self.amount = newAmount

# Figure out the new percent done, round to an integer
diffFromMin = float(self.amount - self.min)
percentDone = (diffFromMin / float(self.span)) * 100.0
percentDone = round(percentDone)
percentDone = int(percentDone)

# Figure out how many hash bars the percentage should be
allFull = self.width - 2
numHashes = (percentDone / 100.0) * allFull
numHashes = int(round(numHashes))

# build a progress bar with hashes and spaces
self.progBar = "[" + '#' * numHashes + ' ' * (allFull - numHashes) + "]"

# figure out where to put the percentage, roughly centered
percentPlace = (len(self.progBar) / 2) - len(str(percentDone))
percentString = str(percentDone) + "%"

# slice the percentage into the bar
self.progBar = self.progBar[0:percentPlace] +
               percentString + self.progBar[percentPlace+len(percentString):]

def __str__(self):
return str(self.progBar)

def read_input_file(f_name):
"""Function for reading values from input file."""
f = open(f_name, 'r')
first_line = f.readline().strip()
#print first_line
if first_line != "
        # Input file for MCS of thermochromatography.":
f.close()
raise IOError, 'Wrong input file'
else:
entries = f.readlines()
f.close()
var_inp = {} #Make a dictionary for variables

for ent in entries :
ent_str = ent.strip()
ent_str_spt = split(ent_str, '#')

if ent_str_spt[0] != "":
val = split(ent_str_spt[0])
if val[0] in ['M2', 'm2']: var_inp["M2"] = float(val[(len(val)-1)])
elif val[0] in ['D2', 'd2']: var_inp["d2"] = float(val[(len(val)-1)])
elif val[0] in ['P', 'p']: var_inp["P"] = float(val[(len(val)-1)])
elif val[0] in ['P0', 'p0']: var_inp["p0"] = float(val[(len(val)-1)])
elif val[0] in ['particles', 'Particles']: var_inp["particles"]
        = int(val[(len(val)-1)])
elif val[0] in ['Q', 'q']: var_inp["Q"] = float(val[(len(val)-1)])
elif val[0] in ['halflife', 'Halflife']: var_inp["halflife"]
        = float(val[(len(val)-1)])
elif val[0] in ['M1', 'm1']: var_inp["M1"] = float(val[(len(val)-1)])
elif val[0] in ['d1', 'D1']: var_inp["d1"] = float(val[(len(val)-1)])
elif val[0] in ['dHa1', 'DHa1', 'DHA1', 'dha1']: var_inp["dHa1"]
        = float(val[(len(val)-1)])
elif val[0] in ['dHa2', 'DHa2', 'DHA2', 'dha2']: var_inp["dHa2"]
        = float(val[(len(val)-1)])
elif val[0] in ['dHastep', 'DHastep', 'DHASstep', 'dhastep']: var_inp["dHastep"]

```

```

        = int(val[(len(val)-1)])
elif val[0] in ['length', 'Length']: var_inp["length"]
    = float(val[(len(val)-1)])
elif val[0] in ['circular', 'circle', 'Circular', 'Circle']: var_inp["shape"]
    = 'circle'
elif val[0] in ['rectangular', 'rectangle', 'rect']: var_inp["shape"]
    = 'rectangle'
elif val[0] in ['radius', 'Radius']: var_inp["radius"]
    = float(val[(len(val)-1)])
elif val[0] in ['side_a', 'Side_a']: var_inp["side_a"]
    = float(val[(len(val)-1)])
elif val[0] in ['side_b', 'Side_b']: var_inp["side_b"]
    = float(val[(len(val)-1)])
elif val[0] in ['mean_path', 'Mean_path']: var_inp["mean_path"]
    = float(val[(len(val)-1)])
elif val[0] in ['hist_steps', 'Hist_steps']: var_inp["hist_steps"]
    = int(val[(len(val)-1)])
elif val[0] in ['temp_data', 'Temp_data']:
temp_li_str = split(join(val), "[")
temp_str = temp_li_str[1]
var_inp["temp_data"] = temp_str[:-1]
else: print "I Don't Understand", val[(len(val)-1)]
return var_inp

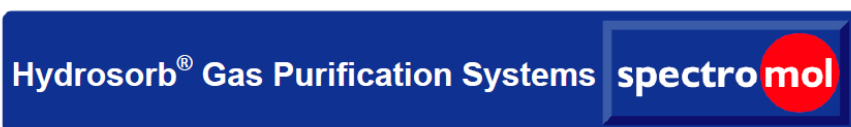
def usage():
print "Possible arguments are: \n -h
      help \n -i   input file \n -o   output file"

def get_arguments():
args = sys.argv[1:]
arguments={}
for arg_nr in range(len(args)):
if args[arg_nr] in ["-h", "--help"]:
usage()
sys.exit(2)
elif args[arg_nr] in ["-i", "--input"]:
arguments['input_file'] = args[arg_nr+1]
elif args[arg_nr] in ["-o", "--output"]:
arguments['output_file'] = args[arg_nr+1]
return arguments

def mean_path_calculation2(a,b):
mean_path = 1/pi*(b*log(fabs(tan(atan(a/b)*0.5+pi*0.25)))+
    a*log(fabs(tan(atan(b/a)*0.5+pi*0.25))))
return mean_path

```

9.2 Specifications gas purification cartridges



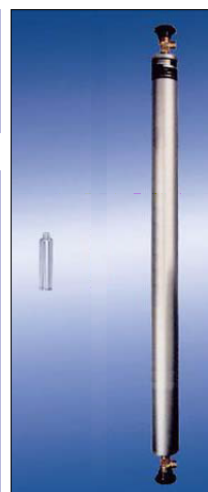
Hydrosorb® gas purification systems are designed for the removal of moisture from gas flows.

The applied process is based on **physisorption**:

Physisorption: moisture (and carbon dioxide) are physically bound to a porous mass and therefore permanently removed from the gas flow. Molecular sieve 5A is used as absorption material.

Hydrosorb®	
Applicable for	Rare gases, N ₂ , H ₂ , CO, CO ₂ , saturated HC halogenated HC, N ₂ O, O ₂ and compressed air
Removed contaminants	Moisture (and carbon dioxide)
Process	physisorption
Final purity	Moisture < 20 ppb

Hydrosorb®		
	Small cartridge	Large cartridge
Shield gas	Helium	Argon
Capacity	moisture 1 Ltr	Moisture 100 Ltr
Optical indication	no	no
Max. gas flow	1 m ³ /h	10 m ³ /h
Max. working pressure		10 bar ¹⁾
Length	125 mm	1.170 mm
Diameter	29 mm	71 mm
Material	Aluminium	Aluminium
Remarks	-	Complete with 2 diaphragm type valves Connections: NPTF 1/4"
Delivery	2-pack	single
Part no.	123326	123348



1) Small cartridges can be applied with high pressure housing PN200 for working pressure up to 200 bar.

For removal of oxygen and moisture:

see Oxisorb®

For removal of HC and oil vapour:

see Accosorb®

For removal of mercaptan, COS, SC, H₂S, SO₂, und NO:

see Sulfosorb®

For removal of Fluoride

see Excisorb®-F

For holders, purge systems and accessories:

see Spectromol accessories

Fig. 9.1: Specifications of Hydrosorb gas purifications cartridges of the company Spectromol.

Oxisorb® gas purification systems are designed for the removal of oxygen and moisture from gas flows.

The applied processes are **chemisorptions** and **physisorption**:

Chemisorptions: Oxygen is chemically bound to the absorption material and therefore permanently removed from the gas flow. Silica gel with chromium oxide is used as absorption material. As a side affect, moisture is removed by physisorption.

Physisorption: Moisture is being physically bound to Silica gel and therefore removed from the gas flow.

Oxisorb®	
Applicable for	rare gases, N ₂ , H ₂ , CO, CO ₂ , saturated HC
Not applicable for	O ₂ , compressed air, non-saturated HC
Removed contaminants	oxygen, moisture
Process	O ₂ : chemisorptions H ₂ O: physisorption
Final purity	O ₂ < 5ppb H ₂ O < 30 ppb

Oxisorb®			
	Small cartridge		Large cartr.
	Aluminium	Glass	Aluminium
Capacity	O ₂ : 0,1 Ltr H ₂ O: 0,5 Ltr		O ₂ : 9 ltr H ₂ O: 45 Ltr
Optical indication	no	blue - brown	no
Max. gas flow	1 m ³ /h		10 m ³ /h
Max. working pressure	10 bar ¹⁾		
Length	125 mm	130 mm	1.170 mm
Diameter	29 mm	30 mm	71 mm
Material	Aluminium	Glass ²⁾	Aluminium
Remarks	-	-	Complete with 2 diaphragm type valves connections: NPTF ¼"
Delivery	2-pack		single
Part no.	123325	123342	123311



¹⁾ Small cartridges can be applied with high pressure housing PN200 for working pressure up to 200 bar.

²⁾ Attention: Glass cartridges must be applied with a „splinter protection“ only!

For removal of moisture: see Hydrosorb®
 For removal of HC and oil vapour: see Accosorb®
 For removal of mercaptan, COS, SC, H₂S, SO₂, und NO: see Sulfosorb®

For removal of Fluoride see Excisorb®-F

For holders, purge systems and accessories: see Spectromol accessories

Fig. 9.2: Specifications of Oxysorb gas purifications cartridges of the company Spectromol.

Hydrosorb Big Moisture trap



Fitting Size	1/4 in
Includes Indicator	No
Length	17.5 in
Gas Filter Type	Moisture
Substance Concentration	0.1 ppm
Trap Capacity	750 cc
UNSPSC Code	41115700
Diameter	2.3 in
Maximum Pressure	250 psig



Fig. 9.3: Specifications of the Big Moisture Trap BMT-4 of the company Agilent.

Oxisorb Big Oxygen trap



Fitting Size	1/4 in
Includes Indicator	No
Length	17.5 in
Gas Filter Type	Oxygen
Substance Concentration	50 ppb
Trap Capacity	750 cc
UNSPSC Code	41115700
Diameter	2.3 in
Maximum Pressure	250 psig



Fig. 9.4: Specifications of the Big Oxygen Trap BOT-4 of the company Agilent.

Molecular Sieve 13X Moisture trap



Fitting Size	1/4 in
Includes Indicator	Yes
Length	17.5 in
Gas Filter Type	Moisture, indicating
Trap Capacity	400 cc
UNSPSC Code	41115700
Diameter	1.75 in
Maximum Pressure	125 psig



Fig. 9.5: Specifications of the Molecular Sieve MT400-4 of the company Agilent.

Persönliche Daten

Name Michael Götz
Anschrift Darmstädter Straße 269b, 64625 Bensheim
Geburtsdaten 6. März 1986 in Mainz
Geburtsort Wiesbaden-Dotzheim

Bildungsweg

- 03/2015 – heute **Promotionsstudium**, *GSI Helmholtzzentrum für Schwerionenforschung*, Darmstadt.
Schwerpunkt: Nuklear- und Kernchemie - Arbeitskreis Prof. Dr. Düllmann
Titel: In-situ synthesis of volatile transition-metal carbonyl complexes produced in nuclear fusion reactions without physical presparation.
- Arbeit mit Radioaktivität und radioaktiven Proben
 - Umgang mit Detektoren zur Messung von radioaktiver Strahlung (α , β , γ)
 - Arbeiten in Kontrollbereichen und Sicherheitsprotokolle
 - Berechnung von radioaktiven Zerfallsprozessen
- Abschluss: voraussichtlich 05/2021
- 10/2006 – 03/2015 **Studium: Diplom Chemie**, *Johannes Gutenberg Universität*, Mainz.
Schwerpunkt der Diplomarbeit: Nuklear- und Kernchemie - Arbeitskreis Prof. Dr. Düllmann
Titel: Radiochemische Untersuchung der Kinematik von Multinukleonentransferreaktionen in Kollisionen von $^{48}\text{Ca} + ^{248}\text{Cm}$ 10 Prozent über der Coulombbarriere.
Abschlussnote: gut
- 07/2002 – 07/2005 **Abitur**, *Friedrich-List-Gymnasium*, Wiesbaden.
Schwerpunkt: Informatik und Chemie
Abschlussnote: 1,5

Auslandserfahrung

- 03/2018 – 05/2018 **Experiment am RIKEN Nishina Center for Accelerator-Based Science**, *Wako, Saitama*, Japan.
Arbeitsgruppe: Nuclear Chemistry Research Team - Dr. Hiromitsu Haba
- 02/2019 – 04/2019 **Experiment am Nuclear Science Research Institute der Japan Atomic Energy Agency**, *Tokai-mura, Ibaraki*, Japan.
Arbeitsgruppe: Heavy Element Nuclear Science - Prof. Dr. Yuichiro Nagame

Sprachkenntnisse

Deutsch Muttersprache
Englisch Verhandlungssicher

IT-Kenntnisse

- Anwendungen **Officeanwendungen (sehr gut), CAD (einfach), Photoshop (gut), Programmierung (gut)**
Weit umfassende Kenntnisse im Umgang mit Officeanwendungen und umfangreiche Kenntnisse in Grafikbearbeitung mit Adobe Photoshop sowie der Java und LaTeX Programmierung. Grundlegende Kenntnisse im Umgang mit digitalen Konstruktionsmodellen.

Außeruniversitäre Tätigkeiten

- Fortbildung Teilnahme an Soft-Skill Kursen im Rahmen der HGS-HIRE Graduate School
- Werksstudent British Telecom, Migration von Datenbanken und Portierung von Telefonaufträgen (2008-2010)

Ausgewählte Publikationen

- 2017 M.Götz et al. **Radiochemical study of the kinematics of multi-nucleon transfer reactions in $^{48}\text{Ca} + ^{248}\text{Cm}$ collisions 10% above the Coulomb barrier** In *Nuclear Physics A*, Volume 961, 1-21 (2017), DOI: 10.1016/j.nuclphysa.2017.02.006
- 2020 M.Götz et al. **Gas phase synthesis of 4d transition metal carbonyl complexes with thermalized fission fragments in single-atom reactions** In *Radiochim. Acta*, Volume 109(3), 153-165 (2020), DOI: <https://doi.org/10.1515/ract-2020-0052>
- 2021 M.Götz et al. **A novel approach to gas phase synthesis of accelerator-produced 5d transition metal carbonyl complexes** In *Radiochim. Acta*, In press

Konferenzen und Workshops

- 05/2015 M.Götz et al. **Radiochemical Investigation of the Kinematics of Multinucleon Transfer Reactions in $^{48}\text{Ca} + ^{248}\text{Cm}$ Collisions 10 % above the Coulomb Barrier** In *5th International Conference in the Chemistry and Physics of the Transactinide Elements*, Fukushima, Japan, 2015.
- 08/2015 M.Götz et al. **In-situ Darstellung von Carbonylkomplexen kurzlebiger Übergangsmetall-Isotope ohne physikalische Vorseparation** In *GDCh Wissenschaftsforum 2015*, Dresden, Deutschland, 2015.
- 10/2015 M.Götz et al. **Radiochemical Investigation of the Kinematics of Multinucleon Transfer Reactions in $^{48}\text{Ca} + ^{248}\text{Cm}$ Collisions at 1.1 x B** In *14th Workshop on Recoil Separator for Superheavy Element Chemistry*, Darmstadt, Deutschland, 2015.
- 08/2016 M.Götz et al. **Radiochemical investigation of the kinematics of multi-nucleon transferreactions** In *9th International Conference on Nuclear and Radiochemistry*, Helsinki, Finnland, 2016.
- 09/2016 M.Götz et al. **In-situ synthesis of carbonyl complexes with short-lived isotopes of group VI, VII and VIII elements** In *15th Workshop on Recoil Separator for Superheavy Element Chemistry*, Darmstadt, Deutschland, 2016.

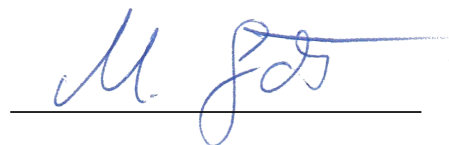
Darmstädter Straße 269b – 64625 Bensheim

☎ 01608114312 ✉ migoetz@students.uni-mainz.de

- 09/2017 M.Götz et al. **On-line studies with carbonyl complexes at TRIGA Mainz** In *16th Workshop on Recoil Separator for Superheavy Element Chemistry*, Darmstadt, Deutschland, 2017.
- 09/2017 M.Götz et al. **Die in-situ Darstellung von Carbonylkomplexen kurzlebiger Übergangsmetall-Isotope ohne physikalische Vorseparation** In *GDCh Wissenschaftsforum 2017*, Berlin, Deutschland, 2017.
- 10/2017 M.Götz et al. **On-line studies with carbonyl complexes at TRIGA Mainz** In *9th Workshop on the Chemistry of the Heaviest Elements*, Ascona, Schweiz, 2017.

Technical Reports

- 2016 M.Götz et al. **Radiochemical investigation of the kinematics of multi-nucleon transfer reactions** In *GSI Scientific Report 2015*, MU-NUSTAR-SHE-C-3
- 2017 M.Götz et al. **Radiochemical investigation of the kinematics of multi-nucleon transfer reactions** In *GSI Scientific Report 2016*, RESEARCH-NUSTAR-SHEC-5



Michael Götz
Idstein, 6. November 2021

Darmstädter Straße 269b – 64625 Bensheim

01608114312 ■ migoetz@students.uni-mainz.de